

## Liquid noble gas detectors for low energy particle physics

---

Vitaly Chepel<sup>a\*</sup> and Henrique Araújo<sup>b</sup>

<sup>a</sup>*LIP–Coimbra & Department of Physics, University of Coimbra,  
P-3004-516 Coimbra, Portugal*

*Email: vitaly@coimbra.lip.pt*

<sup>b</sup>*High Energy Physics Group, Imperial College London,  
Blackett Laboratory, London SW7 2AZ, United Kingdom*

**ABSTRACT:** We review the current status of liquid noble gas radiation detectors with energy threshold in the keV range, which are of interest for direct dark matter searches, measurement of coherent neutrino scattering and other low energy particle physics experiments. Emphasis is given to the operation principles and the most important instrumentation aspects of these detectors, principally of those operated in the double-phase mode. Recent technological advances and relevant developments in photon detection and charge readout are discussed in the context of their applicability to those experiments.

**KEYWORDS:** Noble liquid detectors (scintillation, ionization, double phase); Dark matter detectors (WIMPs, axions, etc.); Neutrino detectors; Charge transport, multiplication and electroluminescence in rare gases and liquids.

---

\*Corresponding author.

---

## Contents

<b>1. Introduction</b>	<b>2</b>
<b>2. Elastic scattering of dark matter particles and neutrinos off nuclei</b>	<b>2</b>
<b>3. Overview of detection principles</b>	<b>4</b>
<b>4. Relevant properties of the liquefied rare gases</b>	<b>13</b>
4.1 Particle energy transfer to the liquid	13
4.2 Primary scintillation	15
4.2.1 Emission mechanism and yields	15
4.2.2 The role of recombination	26
4.2.3 Light propagation	32
4.3 Ionization charge	34
4.3.1 Ionization yields and transport properties in the liquid	34
4.3.2 Liquid purity	38
4.4 Combined signal	39
4.5 Electron emission from liquid to gas	40
4.6 Electrons in the gas phase	43
<b>5. State-of-the-art technologies and methods</b>	<b>47</b>
5.1 Detection of the VUV light	47
5.1.1 Photomultiplier tubes	47
5.1.2 Large area avalanche photodiodes	51
5.1.3 Silicon photomultipliers	53
5.1.4 Hybrid devices	56
5.2 Alternative techniques for light and charge signal detection	58
5.2.1 Electron multiplication with micro-pattern structures	58
5.2.2 Photon detection with micro-pattern structures	63
5.2.3 Optical readout from micro-pattern structures	66
5.2.4 Back to single phase?	68
<b>6. Direct dark matter search experiments</b>	<b>70</b>
6.1 Liquid xenon detectors	70
6.2 Liquid argon detectors	78
<b>7. Detecting coherent neutrino scattering with the noble liquids</b>	<b>85</b>
<b>8. Conclusion</b>	<b>90</b>

---

## 1. Introduction

Liquefied noble gases have attracted the attention of experimental physicists since the middle of the 20th century [1, 2, 3, 4]. The unique combination of their scintillation properties with the fact that electrons released in the ionization process can remain free to drift across long distances favorably distinguishes these liquids from other dense detector media. Another notable property of the ‘noble liquids’ is the possibility of extracting electrons to the gas phase, where the ionization signal can be amplified through secondary scintillation or avalanche mechanisms. These properties have been extensively studied over the years and significant progress has been made in understanding the underlying physics as well as on development of the associated technologies, notably gas purification, material cleaning, cooling, photon and charge detection, and low noise electronics. A wide spectrum of applications has been considered involving both precise particle tracking (owing to the low electron diffusivity) and calorimetry/spectroscopy (good energy resolution): in high energy physics,  $\gamma$ -ray astronomy, neutrinoless  $\beta\beta$ -decay, medical imaging and, more recently, dark matter (DM) searches and coherent neutrino scattering (CNS) detection.

The latter two applications have much in common from the instrumentation point of view, as we shall discuss below: a low energy threshold and low intrinsic background are important requirements in both cases. In addition, both are low energy processes which benefit from coherence of the scattering across all nucleons in the nucleus, thus enhancing expected event rates very significantly. For that reason, we shall consider them in close connection, despite the fact that direct DM searches are more mature than CNS experiments: while large scale DM detectors using liquid xenon and argon are already running or in advanced stage of construction, the possibility of detecting CNS with those media is still under consideration, and several important questions remain open.

Although this review gives a reasonably comprehensive account of efforts to measure low energy signals with liquefied noble gas detectors, its main aim is to show how the noble liquid technology works for this purpose and to discuss some recent advances and improvement attempts. The authors apologize in advance for inevitable incompleteness. More information can be found in other recently published monographs and review papers [5, 6, 7, 8, 9, 10].

The article is organized as follows. After motivating the search for particle dark matter and coherent neutrino-nucleus scattering in Section 2, we examine in the following section the main characteristics of the signals expected in liquid xenon and liquid argon targets and how those interactions might be detected. We devote Section 4 to a detailed description of the physics involved in the response mechanisms. In Section 5 we review the devices used to detect scintillation light and ionization charge, both those which are well established as well as others under development. In Section 6 we examine how the different DM search programs have implemented the noble liquid technologies and indicate their status at the time of writing. A brief overview of ongoing efforts towards a first detection of CNS is presented in Section 7. We conclude in Section 8, highlighting the progress in sensitivity achieved by direct DM searches with noble liquids in the last two decades.

## 2. Elastic scattering of dark matter particles and neutrinos off nuclei

There are several observational evidences for the existence of non-luminous (i.e. not observable electromagnetically), non-baryonic matter in the Universe. The exact nature of this dark matter

is not known yet. It is recognized that it may exist in various hypothetical forms; one possibility — favored by current cosmological models — is a new, neutral particle, frozen-out as a thermal relic in the early Universe, with mass in the GeV–TeV range and interacting with ordinary matter through the weak force. These so-called Weakly Interacting Massive Particles (WIMPs) might be the lightest supersymmetric particles; in particular, the neutralino — arising in some flavors of Supersymmetry — is the prime candidate for direct detection.

A simple model for the distribution of this ‘cold’ dark matter in our galaxy suggests that WIMPs should gather in a spherical isothermal halo — much larger than the visible baryon disc — with a mean particle speed of 270 km/s. The solar system moves through this halo with a speed of  $\simeq 220$  km/s. Therefore, in the Earth’s frame one should observe WIMPs coming preferentially from a certain direction in the sky, with that velocity on average (plus a small seasonal variation due to the Earth’s rotation around the Sun with a speed of about 30 km/s). Since the WIMP velocity dispersion is comparable to our orbital velocity around the galactic center, such directional effects are not large, and even a stationary observer in the DM halo might be able to detect WIMPs.

Naturally, this ‘canonical’ dark halo offers too simplistic a view of galaxy dynamics, one which has been questioned by n-body simulations in particular. These propose a more ‘lumpy’ distribution of galactic dark matter and the possibility that the dark component may be co-rotating with the baryon disc to some degree. However, we adopt the simpler halo model for the purpose of this article. For a recent and comprehensive review of dark matter the reader is referred to [11].

Elastic scattering of WIMPs off the atomic nuclei of a target material should result in nuclear (atomic) recoils [12]. With an adequate detection technique, the minute energies transferred to recoiling nuclei can be measured, allowing WIMPs to be observed. This method is usually referred to as *direct dark matter detection* (reviewed also, e.g., in [13, 14, 15, 16, 17]). In contrast, *indirect detection* relies on the observation of WIMP annihilation products arising elsewhere in the Milky Way or beyond [16, 18]. Discovery of the nature of dark matter would not only solve an astrophysical puzzle dating back to the early 1930s — and change radically how we view our own galaxy — but it would arguably be one of the most important steps in our understanding of the Universe.

In turn, the interest in measuring coherent neutrino scattering off atomic nuclei is twofold. From a fundamental physics viewpoint, it is important to observe a process for which the Standard Model offers a concrete prediction. This would allow several tests of the theory. For example, observation of neutrino oscillations with CNS would provide evidence for the existence of sterile neutrinos, since this is a flavor-blind process. Measurement of the CNS cross section could shed light on the value of the neutrino magnetic momentum, and so reveal how neutrinos couple to the high magnetic fields which exist in some astrophysical environments. It would contribute to our understanding of neutrino dynamics in neutron stars and supernovae, where CNS adds to the neutrino opacity, besides providing a high-rate mechanism for supernova detection. Many other applications could be listed (see [19], for example). In addition to these scientific applications, detection of neutrinos through this scattering mechanism could bring about new neutrino technologies, such as nuclear reactor monitoring (nuclear safety, non-proliferation), geological prospecting and perhaps even neutrino telecommunications.

The effect of coherence over all nucleons in the nucleus is the enhancement of the scattering cross section by a factor of  $N^2$  ( $N$  is the neutron number) with respect to neutrino-nucleon scattering [20]. If the coherence condition  $qR \lesssim 1$  is fulfilled, with  $R$  the nuclear radius and  $q$  the transferred

momentum, then one can gain a factor of  $N \sim 100$  in scattering rate by using a neutron rich target. However, this enhancement works well only for low energy neutrinos, roughly  $\lesssim 50$  MeV. The CNS cross section (and the rate per kg) is also several orders of magnitude higher than that of elastic neutrino-electron scattering — the process used in several neutrino detectors. The relatively large cross section allows consideration of kg-scale, rather than tonne-scale, detectors. This is what makes coherent scattering on nuclei so attractive in spite of the challenge of measuring extremely low recoil energies. The search for a spin-independent WIMP-nucleus interaction benefits from the coherence enhancement in a similar way, as outlined in the next section.

### 3. Overview of detection principles

A nuclear recoil with energy in the keV range is the only signature of the interaction of both WIMPs and neutrinos scattering elastically off atomic nuclei. The recoil energy spectrum due to galactic WIMPs is approximately exponential. Although it depends on the (unknown) WIMP mass and atomic number of the target, most recoils have energies well below  $\sim 100$  keV [21]. Therefore, expected WIMP count rates depend critically on the detector energy threshold, which must be as low as possible. The recoil spectrum expected from coherent neutrino scattering has roughly a similar shape and can extend up to tens of keV for higher energy neutrinos (from decay of relativistic ions or decay of stopped pions, for example [22, 23]); on the other hand, the spectrum lies mostly in the sub-keV region in the case of the reactor antineutrinos [24].

Liquid xenon (LXe) and liquid argon (LAr), as well as liquid neon (LNe), have been proposed for direct dark matter search detectors. At present, several liquid xenon detectors (with target masses of order 10–100 kg) have been built and operated for dark matter searches and larger ones are in the process of construction or underground deployment. Liquid argon projects have made slower progress after initial demonstration of capability for WIMP searches, but systems are now under construction with tonne-scale targets. Neon offers some interesting complementarity in direct searches and is the subject of R&D work. We review briefly some of the existing projects in Section 6.

The present predominance of liquid xenon detectors is explained by several advantages of this medium, namely higher WIMP-nucleus interaction cross section (the spin-independent cross section  $\sigma_{\chi, \text{Xe}}^{\text{SI}}$  includes a factor of  $A^2$ , where  $A$  is the atomic number), absence of long-lived radioisotopes in natural xenon<sup>1</sup> and presence of odd-neutron isotopes with non-zero nuclear spin, which makes the detector sensitive also to a spin-dependent interaction component. High  $Z$  and density combined into a continuum (unsegmented) active medium allow for a compact self-shielding detector geometry. In turn, liquid argon detectors benefit from higher electron recoil discrimination capability due to a large difference between the decay times of the two scintillation components (expanded in Section 4.2.1 in more detail). The much lower cost of argon and the relative ease of contaminant purification are the other advantages of liquid argon. Unfortunately, natural atmospheric argon contains the radioisotope  $^{39}\text{Ar}$ , with a specific activity of 1 Bq/kg; sourcing from specific underground sites is required to mitigate against this problem [29].

---

<sup>1</sup>The  $2\nu\beta\beta$ -decay mode of  $^{136}\text{Xe}$  has been measured recently [25, 26], but this produces an extremely low event rate at energies relevant for DM and CNS searches. Also,  $^{85}\text{Kr}$  ( $\beta$ -decay,  $T_{1/2} \sim 10.8$  years) is a common contaminant, but can be removed by cryogenic distillation [27] or adsorption-based chromatography [28].

As for coherent scattering neutrino experiments, low  $A$  liquids (argon and especially neon) are favored for low neutrino energies, due to the fact that the nuclear recoil energy is inversely proportional to the mass of the target nucleus,  $E_r^{max} \propto E_\nu^2/A$ . For example, for neutrinos with energy  $E_\nu = 3$  MeV (close to the average energy of reactor antineutrinos) the maximum recoil energy is  $\approx 1$  keV for neon,  $\approx 0.5$  keV for argon and merely  $\approx 150$  eV for xenon. This means that the signals one can expect from ionization or scintillation detectors are of the order of a few electrons or photons, respectively. Thus, the requirement of a low detection energy threshold is even more demanding for CNS than for DM search experiments, unless WIMPs are much lighter than presently thought. On the other hand, the scattering cross section increases with the square of the neutron number  $N$  in the nucleus,  $\sigma_\nu \propto E_\nu^2 N^2$ , thus giving advantage to xenon as far as the interaction probability is concerned. For a given target mass, the scattering rate is proportional to  $E_\nu^2 N^2/A$ . Xenon detectors can be advantageous if the source provides neutrinos with energy above  $\sim 30$  MeV, so that the maximum recoil energy becomes  $> 15$  keV [22], [23].

By any standard, scattering cross sections are small for both processes. The scalar WIMP-nucleon cross section is unknown, but from existing experimental constraints it is smaller than  $\sigma_{\chi,n} \sim 2 \cdot 10^{-45} \text{ cm}^2$  ( $2 \cdot 10^{-9}$  pb). Due to coherence, the cross section scales up with  $A^2$  for the whole nucleus and gains also a kinematic factor  $(A(m_n + m_\chi)/(Am_n + m_\chi))^2$ , where  $m_n$  is the nucleon mass and  $m_\chi$  is the WIMP mass. Assuming  $m_\chi = 100$  GeV, present experimental limits imply  $\sigma_{\chi,\text{Xe}} < 10^{-37} \text{ cm}^2$  and  $\sigma_{\chi,\text{Ar}} < 2 \cdot 10^{-39} \text{ cm}^2$  for scattering off the two nuclei.<sup>2</sup>

At the same WIMP mass of 100 GeV, a simple estimate of expected scattering rates can be obtained from the particle flux in our galactic neighbourhood, where the WIMP density is  $\rho_0 \sim 0.3 \text{ GeV/cm}^3$  [30] and the mean particle speed is  $\bar{v}_\chi \sim 270 \text{ km/s}$  (assuming a stationary Earth in the galactic frame for simplicity). The WIMP flux is therefore  $\Phi_\chi \sim \rho_0 \bar{v}_\chi / m_\chi \sim 10^5 \text{ s}^{-1} \text{ cm}^{-2}$ . From this one can calculate the expected total scattering rate for a given target species  $T$  as  $R_T = \sigma_{\chi,T} \Phi_\chi N_A / A_T$ , which results in a maximum of  $\sim 0.1$  event per year per 1 kg of xenon, and nearly an order of magnitude lower for argon. The left panel in Figure 1 shows scattering rates above detection threshold for several noble gas elements and for germanium, the most competitive cryogenic bolometer material.

These calculations must take into account the weak nuclear form factor, which decreases with transferred momentum much more rapidly for xenon than for argon [21, 31, 32, 33]. The Xe form factor drops practically to zero for recoil energies of 100 keV, while it is still  $\approx 0.5$  for argon recoils of that energy — this behavior is apparent in Figure 1 (left), where the full calculations following [21] are presented. This is fortunate since WIMP-search thresholds are anyway higher in LAr as discussed later. Such low scattering rates justify why dark matter search experiments require large detector masses, with tonne-scale experiments being built at present. It is also important to keep in mind that these estimates are made under the assumption that the WIMP mass is about 100 GeV. One must also point out that the rates mentioned above are *scattering* rates. Actual *detection* rates will also depend on detector efficiency (and energy resolution) as a function of recoil energy.

For neutrinos, the scattering cross section can be calculated in the Standard Model framework [20, 35]. It is different for neutrons and protons due to different coupling to up and down

---

<sup>2</sup>In reality, this is measured in the opposite way: the scattering cross section on xenon ( $\sigma_{\chi,\text{Xe}}$ ) provides the present experimental constraint, and the WIMP-nucleon cross section ( $\sigma_{\chi,n}$ ) is calculated via a hypothetical particle model (typically a neutralino); scattering rates on other nuclei, such as argon, can then be inferred.

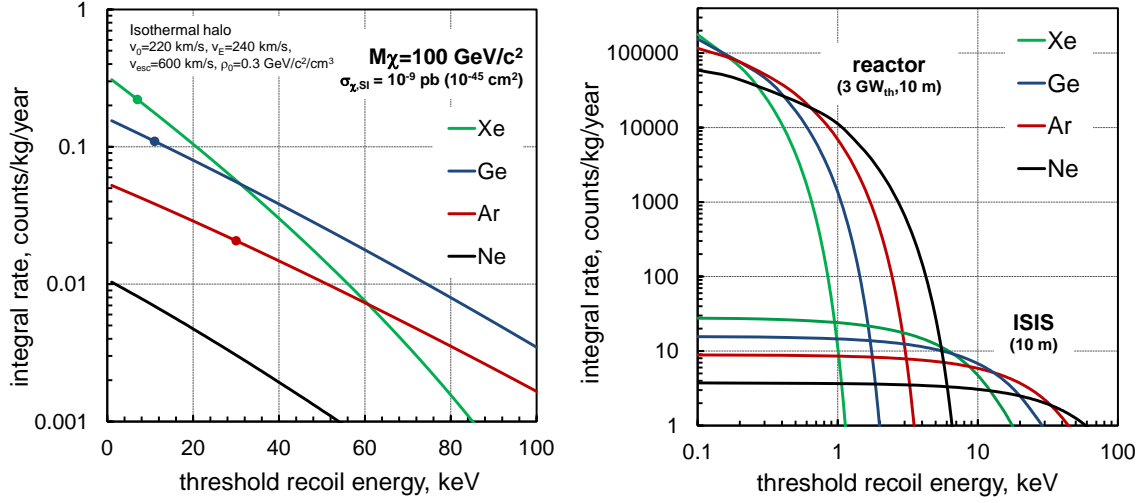


**Figure 1.** Predicted integral spectra for WIMP elastic scattering (left) and for coherent neutrino-nucleus elastic scattering (right) for Xe, Ge, Ar and Ne (in order of decreasing rate at zero threshold). Both plots assume perfect energy resolution. Dark matter rates are for a 100 GeV/ $c^2$  WIMP with  $10^{-45}\text{cm}^2$  ( $10^{-9}$  pb) interaction cross section per nucleon, calculated as per [21] with the halo parameters shown; the markers indicate typical WIMP-search thresholds for each technology. CNS rates are calculated at 10 m from a 3  $\text{GW}_{\text{th}}$  nuclear reactor ( $4 \cdot 10^{13}$   $\nu/\text{cm}^2/\text{s}$ ) and at the same distance from the ISIS neutron spallation source (thanks to E. Santos), where 3 neutrino flavors result from pion and muon decay at rest ( $1 \cdot 10^7$   $\nu/\text{cm}^2/\text{s}$  for all flavors [34]).

quarks: for neutrons it is  $\sigma_{\nu,n} \approx 0.42 \cdot 10^{-44} (E_\nu/\text{MeV})^2 \text{cm}^2$ , whereas for protons it is a factor of  $\sim 200$  smaller. Therefore, the effect of coherence over the whole nucleus is an enhancement factor of  $N^2$ . For example, for 10 MeV neutrinos, the cross section for scattering on a Xe nucleus is  $\sigma_{\nu,\text{Xe}} \sim 2 \cdot 10^{-39} \text{cm}^2$ ; for Ar it is an order of magnitude smaller,  $\sigma_{\nu,\text{Ar}} \sim 2 \cdot 10^{-40} \text{cm}^2$ . Although these values are even smaller than those expected for WIMPs, significantly higher fluxes can be obtained with neutrinos from artificial sources ( $\sim 10^{13} \text{cm}^{-2}\text{s}^{-1}$  at a distance of  $\sim 10$  m from a nuclear reactor, to give one example). Calculated rates as a function of threshold for two neutrino sources are shown in Figure 1 (right). In addition, ‘on/off’ experiments are also possible in this instance, which is a significant advantage for controlling systematic uncertainties. Therefore, detectors with a mass of the order of kilograms can, in principle, provide a reasonable rate. However, one must not neglect the fact that, contrary to WIMP searches, where only a few events with correct signature could constitute a discovery in a nearly background-free experiment conducted underground, a neutrino experiment in a surface laboratory must accumulate enough recoil signals to produce a statistically significant distribution in energy (or in the number of ionization electrons, as only few-electron signals can be expected for MeV neutrinos [24, 36, 37]).

The low scattering rate makes the background issue of extreme importance. Background reduction (passive shielding, low radioactivity environment and radio-clean construction) and its active discrimination in the experimental setup are essential. In the case of direct dark matter searches in underground laboratories, two kinds of background can be distinguished: one resulting in electron recoils and the other leading to production of nuclear (atomic) recoils in the sensitive

volume of the detector. Most electron recoils are produced by  $\gamma$ -ray interactions, both from the environment and from radioactivity of detector components, and from decays within the detector or contamination of internal surfaces. The intrinsic radioactivity is mostly due to the U/Th decay chains, but other radioisotopes can be important (e.g.  $^{40}\text{K}$ ,  $^{60}\text{Co}$ ,  $^{137}\text{Cs}$ ). Ultimately, elastic scattering of solar p-p neutrinos off electrons will provide a challenging background for next-generation detectors, with hundreds of events/year expected in a tonne-scale target (see, e.g. [38, 39]).

Nuclear recoil background is the most dangerous one since some of the resulting signals are indistinguishable from those that WIMPs or neutrinos would produce. The dominant source is the elastic scattering of neutrons arising from either ( $\alpha$ ,n) reactions (induced by  $\alpha$ -particles from the U and Th decay chains) or from spontaneous fission of  $^{238}\text{U}$ . Trace amounts of these nuclides are naturally present in the surrounding environment and in detector components, despite careful screening and purification of materials. Another source of neutrons is the interaction of atmospheric muons, some of which penetrate deep underground, in the rock and  $\gamma$ -ray shielding around the experiment. Low-A shielding is essential for moderation of external neutrons; an active neutron veto surrounding the detector (e.g. Gd-loaded scintillation counters [40, 41]) can also be very effective at tagging radioactivity as well as muon-induced neutrons.

Fiducialization of the sensitive volume by excluding from the data interactions in the outer regions of the target is crucial for background reduction, not only those effects mentioned above but also nuclear recoils from  $\alpha$ -decays on detector surfaces. This relies on the ability to reconstruct particle interaction sites in three dimensions. Owing to their high spatial resolution, double-phase noble element detectors are capable of very effective fiducialization even in modest-sized targets.

While elastic neutron single-scatter events cannot be discriminated from WIMP or CNS signals in the detector, electron recoils have a different signature and therefore can be identified and rejected to a significant extent. The early dark matter detectors relied on the fact that the relative contributions of slow and fast components to the observed scintillation signal are different for nuclear recoils and for electrons. This was the case in the DAMA/LXe and ZEPLIN-I liquid xenon scintillation detectors [42, 43, 44]. The difference between the two effective decay time constants in liquid xenon is not large:  $\sim 32$  ns and  $\sim 18$  ns were measured for electrons and for nuclear recoils, respectively, in the energy range of 10 keV to 20 keV [44, 45]. Considering, in addition, the small number of scintillation photons and the relatively small VUV light detection efficiency, it is understandable that a discrimination efficiency of only  $\sim 50\%$  was achieved. The current generation of liquid xenon detectors does not rely on pulse shape discrimination for the primary scintillation signal. However, for liquid argon targets this method is much more effective and can increase the discrimination power very significantly. Indeed, the two scintillation decay time constants differ very much in liquid argon:  $\sim 1,600$  ns versus  $\sim 7$  ns (see Section 4.2.1).

Much higher discrimination efficiency can be achieved if, in addition to primary scintillation, the ionization signal is also measured. Most noble liquid detectors dedicated to dark matter searches share a common operation principle. It is based on electron emission from the liquid, followed by secondary scintillation (also known as electroluminescence) in the uniform electric field in the gas phase, as illustrated in Figure 2. The foundations for this technology were laid by Dolgoshein, Lebedenko and Rodinov in 1970 [46], who demonstrated the possibility of particle detection in a double-phase argon chamber; by Barabash and Bolozdynya some two decades later [47], who first proposed the use of double-phase detectors for WIMP searches; and in work of



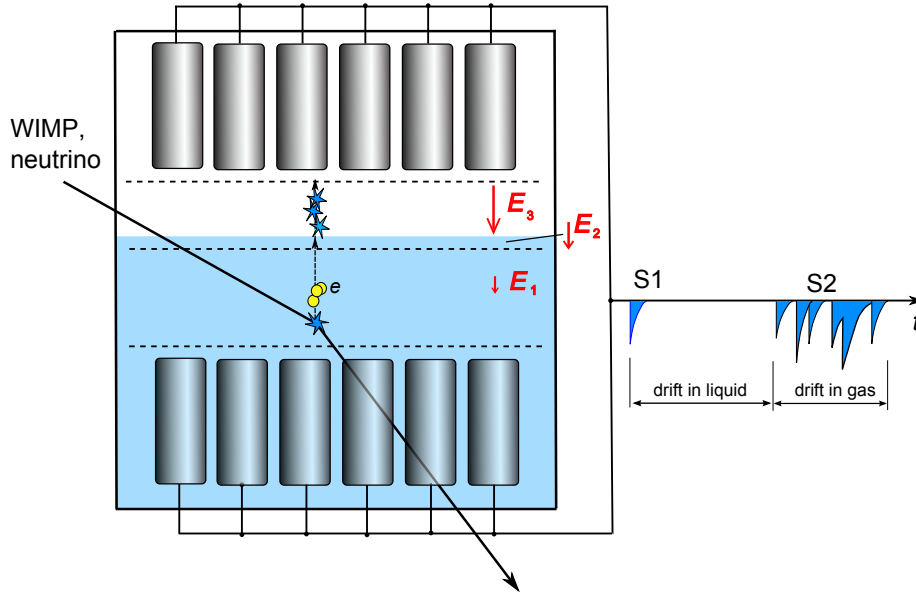


**Figure 2.** Illustration of the operation principle of a double-phase electroluminescence detector. The number of electrodes may vary: some detectors do not feature a grid under the liquid surface; additional grids are often placed in front of the photomultipliers in order to shield them from the external electric field. Only one array of photomultipliers is used in some chambers: either immersed into the liquid and looking upwards, or placed in the gas phase viewing downward.

the ICARUS group at CERN, who proposed to measure both scintillation and ionization signals for background discrimination of WIMP signals from electron and  $\gamma$ -ray background in the early 1990s [48]. Following preliminary work with several small prototype chambers built by different groups, these three crucial components were implemented in ZEPLIN-II — the first double-phase dark matter search detector operated underground [49].

The interaction of a dark matter particle with the detector takes place in the bulk of the liquefied xenon or argon. The particle scatters elastically off an atomic nucleus transferring to it part of its kinetic energy. In the energy range considered ( $\sim 1$ – $100$  keV) the initial velocity of the nuclear recoil is comparable to that of the atomic electrons, so that the recoiling atom conserves most of its electrons and moves through the liquid as a positive ion with low effective charge (or even as a neutral atom). The moving ion continuously exchanges electrons with other atoms along its way and its average charge in xenon is  $\sim 0.1e$  at 1 keV and  $\sim 1e$  for 100 keV (for argon and neon these values are approximately twice as large). As the medium consists of atoms of the same species, the primary recoil can transfer a significant fraction of its kinetic energy in each collision, thus losing rapidly its ‘projectile’ identity and producing a cascade of secondary recoils of comparable energy which interact with the medium in the same way.

The interaction mechanism of nuclear recoils with matter differs from that of electrons, as besides the energy loss to atomic electrons it involves energy transfer to atomic nuclei (essentially generating heat, which does not contribute to the observed signal in these detectors). Consequently, the track structure is different for electrons and nuclear recoils and one can expect that the charge recombination along the particle track also behaves differently. This is indeed veri-

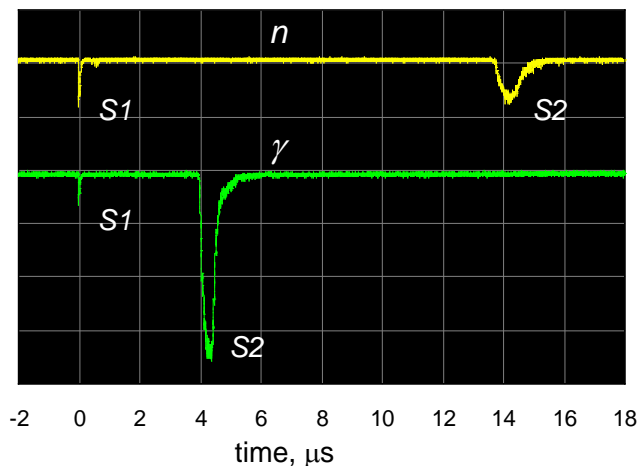


**Figure 3.** Signals from a xenon nuclear recoil after elastic scattering of a neutron (upper trace) and from a  $\gamma$ -ray (lower trace) measured in ZEPLIN-III [50]. The label ‘S1’ designates prompt scintillation in the LXe, while ‘S2’ denotes secondary scintillation produced in the gas phase by the electrons extracted from the liquid. (Courtesy ZEPLIN-III Collaboration.)

fied experimentally. For a given electric field strength, the fraction of electrons escaping recombination with positive ions is higher for electrons than for nuclear recoils. This affects directly the size of the ionization signals but also influences, in the opposite way, the amplitude of the scintillation signal. Therefore, one can roughly say that in the case of nuclear recoils more energy is drawn into the luminous signal than into the (observable) ionization signal, while for electrons the situation is reversed, as shown in Figure 3. The plot shows two signals measured by an array of photomultipliers (PMTs) with an Am-Be neutron source. The lower trace corresponds to a  $\gamma$ -ray interaction and the upper one is due to a neutron elastically scattered on a nucleus. The first short pulse in each signal (usually known as ‘S1’) is due to primary scintillation of the liquid xenon, while the second one (‘S2’) corresponds to the secondary scintillation produced in the gas by the electrons extracted from the liquid. Although both signals are detected in the form of light, S2 is frequently called the ‘ionization’ signal to stress that its origin is in the ionization process and its size (pulse area) is proportional to the number of electrons extracted from the particle track. Note that the time delay between these two signatures provides a very accurate measurement of the depth of the interaction site in the liquid.

A complete picture of the energy transfer mechanisms as well as energy sharing between different channels for low energy particles is still missing, both for nuclear recoils and for electrons. However, it is well established experimentally that the distributions of the collected charge versus the number of detected primary scintillation photons (both depending on the deposited energy) appear quite different for the two particles (see Figure 4). This constitutes the basis for discrimination of the electron/ $\gamma$ -ray background in the current double-phase dark matter detectors. This method was initially tested with  $\alpha$ -particles and  $\gamma$ -rays in liquid xenon [48], with the ionization signal observed through secondary scintillation in the liquid; it was further investigated with double-phase xenon in [51] and [52], until it was conclusively demonstrated in [53].

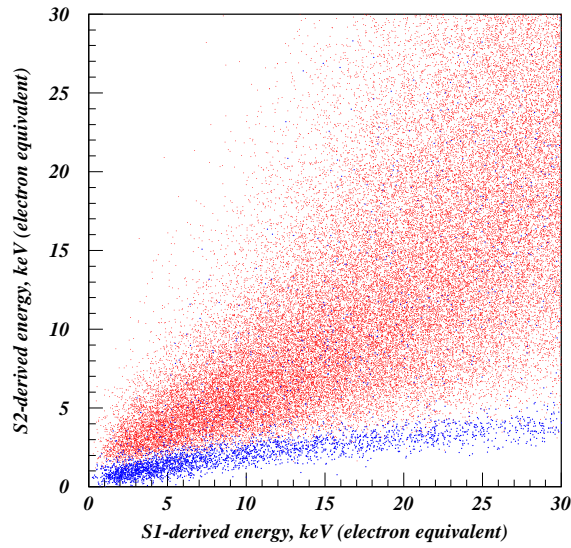


**Figure 4.** Scatter plot of the ionization signal measured from proportional scintillation (S2) versus the prompt scintillation signal (S1), both expressed in electron equivalent energy, for Compton-scattered  $^{137}\text{Cs}$   $\gamma$ -rays (upper population, in red) and for xenon recoils induced by elastic scattering of Am-Be neutrons (blue), acquired during the ZEPLIN-III calibration runs at 3.9 kV/cm drift field in the liquid. (Courtesy ZEPLIN-III Collaboration.)

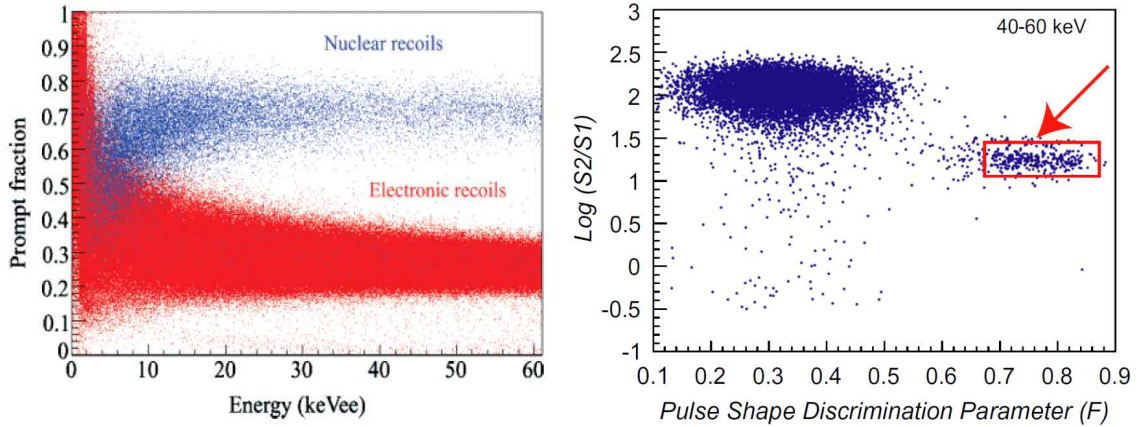


**Figure 5.** Discrimination in liquid argon. Left: pulse shape discrimination in a single-phase chamber yielding 4.85 photoelectrons per keV (electron equivalent); the nuclear recoils are produced with a D-D neutron generator [54]. (Courtesy D. McKinsey; copyright (2008) by The American Physical Society.) Right: dual parameter discrimination in the 2.3-liter WARP detector; nuclear recoils with energy 40–60 keV from an Am-Be neutron source are indicated by the red region (from [55]; with permission from Elsevier). In both panels the scintillation pulse shape is described by a ‘prompt fraction’, i.e. the ratio of signal integrated within a narrow prompt window (90 ns and 200 ns, respectively) to the total pulse area (several  $\mu\text{s}$ ).

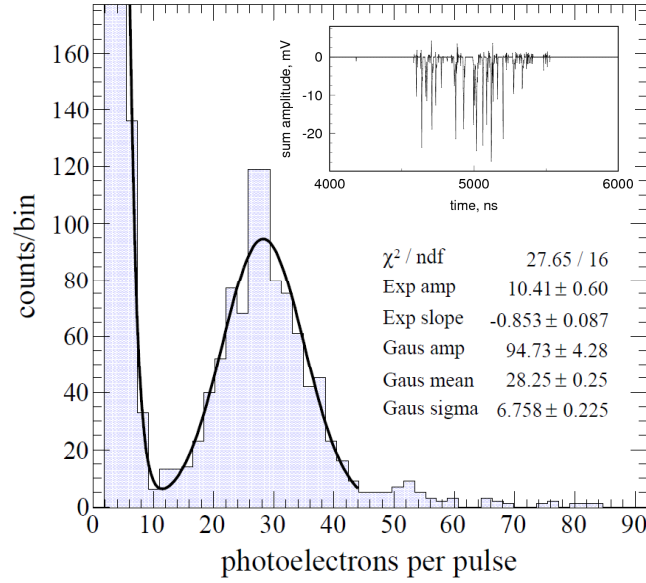


**Figure 6.** Pulse size distribution of the secondary scintillation signal due to cross-phase emission of a single electron in ZEPLIN-III (adapted from [37]); the mean signal contains 28 photoelectrons. The inset shows the summed waveform from 31 photomultipliers; each pulse of  $\sim 10$  ns width represents a single photoelectron measured at the output of one PMT. (Courtesy ZEPLIN-III Collaboration; with permission from Springer Science and Business Media.)

In liquid argon, pulse shape discrimination on the primary scintillation signal is extremely effective at rejecting electronic interactions above  $\sim 10$  keV; this is confirmed by data from a single phase detector shown in Figure 5 (left). In addition, the charge/light ratio measured in double-phase configuration can be used to enhance the electron recoil rejection, as illustrated in Figure 5 (right). Very high discrimination efficiency is essential in LAr to mitigate against the  $^{39}\text{Ar}$  background.

The sensitivity of the scintillation channel is lower than that of the ionization by as much as an order of magnitude. Therefore, the minimum detectable energy is limited by the S1 signal in experiments where the presence of both signals is required. Strictly, the minimum detectable energy is not well defined: due to significant dispersion at low energies, the probability to observe energy depositions below an established energy threshold is not zero. The nuclear recoil energy threshold for the purpose of WIMP searches is chosen by each experiment as a compromise between the count rate expected in the signal region and acceptable background discrimination efficiency (which decreases for low energies, as illustrated in Figures 4 and 5. For example, the ZEPLIN-III and XENON100 experiments used similar thresholds of  $\approx 10$  keV for nuclear recoils [56, 57]. Recoil energy can be reconstructed both from S1 and S2 signals, none of the methods being straightforward. Since direct, *in situ* calibration of the nuclear recoil response with MeV neutrons has so far proved impractical, the energy scale is usually obtained indirectly by irradiating the detector with 122 keV  $\gamma$ -rays from  $^{57}\text{Co}$ . If primary scintillation is used as a measure of recoil energy, the relative scintillation efficiency for electrons and nuclear recoils must be known, from ancillary measurements, as well as its dependence on the recoil energy and field strength (see

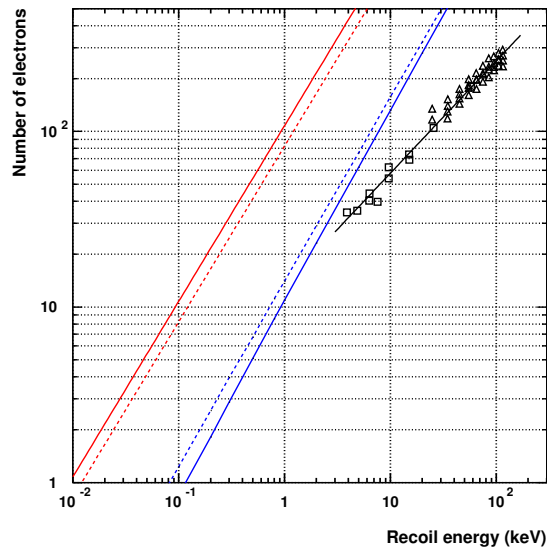


**Figure 7.** Number of electrons extracted from tracks of Xe recoils in liquid xenon. Experimental data from [53] (triangles) and [61] (squares); the black line is an empirical fit. Electric field strength varies from 0.1 kV/cm to 4 kV/cm. Color lines: red – ionization potential (band gap) limit; blue – SRIM [62] prediction for the energy transferred to atomic electrons. Solid lines correspond to the solid state model (band gap  $E_g=9.62$  eV); dashed lines are for a gas model (ionization potential  $I=12.13$  eV). The ionization potential and band gap values are from [63].

Section 4.2). In the case of the S2 signal, one has to correct the energy scale for the differences in charge yield from electron and nuclear recoil tracks, also dependent on the field and energy.<sup>3</sup>

Remarkably, the ionization signal measured through secondary scintillation in the gas is sensitive to single electrons extracted from the liquid [64, 65, 37]. An example of such a signal in ZEPLIN-III is shown in the inset of Figure 6. Each pulse on the waveform corresponds to a single photoelectron emitted from a PMT photocathode (outputs of all PMTs are summed in this plot). On average, about 30 photoelectrons are detected per extracted electron [37]. The main histogram in the same figure shows the size distribution of those signals, very clearly separated from the exponential-like noise.

In order to express the sensitivity to single electrons in terms of recoil energy, the electron extraction efficiency from the recoil tracks must be known; this includes the probability to escape recombination and the transfer efficiency from liquid to gas. Both are functions of electric field strength; recombination depends also on the recoil energy. Any losses during the charge drift to the liquid surface must also be considered. Using  $\sim 7$  e/keV as a reference for LXe [53, 66, 61, 67], one can estimate that the nuclear recoil threshold in the ionization channel could be as low as a few hundred eV (Figure 7).

<sup>3</sup>In the large detectors now under construction, calibration with  $^{57}\text{Co}$  becomes problematic due to thicker vessels and self-shielding of the inner detector volume. It may become necessary to refer the nuclear recoil response to short-lived, internally-dispersed sources, e.g.  $^{83\text{m}}\text{Kr}$  ( $T_{1/2}=1.8$  hr), which emits 32.1 keV and 9.4 keV conversion electrons [58, 59]. However, an anomalously high yield was recently measured for the 9.4 keV electrons at zero field, explained by the presence of positive ions left over in LXe after the preceding 32.1 keV transition [60]; further study of the  $^{83\text{m}}\text{Kr}$  source is therefore desirable.

## 4. Relevant properties of the liquefied rare gases

### 4.1 Particle energy transfer to the liquid

The energy transferred by a particle to the medium,  $E_0$ , is split between three channels — ionization, excitation and heat. For electrons, the following equation can be written [68]:

$$E_0 = N_i E_i + N_{ex} E_{ex} + N_i \varepsilon, \quad (4.1)$$

where  $E_i$  and  $E_{ex}$  are the mean energies spent to ionize or to excite an atom;  $N_i$  and  $N_{ex}$  are the mean numbers of ionized and excited atoms, respectively; and  $\varepsilon$  is the mean energy of sub-excitation electrons immediately after the last collision to result in either excitation or ionization. Below such energy free electrons will participate only in elastic collisions with atoms, thus increasing the temperature of the medium. The value of  $\varepsilon$  has been estimated to lie between 6.3 eV and 7.7 eV for LAr and between 4.65 eV and 5.25 eV for LXe, depending on the theoretical model [69]. In more recent work, the lowest of the two values for each liquid has been adopted (e.g. [63]).

In the case of nuclear recoils, a significant fraction of the particle energy is spent in nuclear collisions which do not result in excitations or ionizations. Therefore, an additional term should be considered in equation (4.1) to account for recoil elastic scattering. We shall discuss various aspects related to this topic in Sections 4.2, 4.3 and 4.4.

Returning to equation (4.1) for electrons, one notices that, in the gas phase, the energy quantities can be conveniently referred to the atomic ionization potential,  $I = 15.75$  eV for argon and  $I = 12.13$  eV for xenon:

$$\frac{E_0}{I} = N_i \frac{E_i}{I} + N_{ex} \frac{E_{ex}}{I} + N_i \frac{\varepsilon}{I}. \quad (4.2)$$

It has been found that the ratio  $E_i/I$  exceeds unity by a few percent due to a small probability to produce multiple ionizations or to form an excited ion.

The liquefied noble gases (Ar, Kr and Xe, at least) exhibit a band structure of electronic states, so that the atomic ionization potential should be replaced by the band gap,  $E_g$ , and equation (4.2) can be rewritten for the liquid phase as:

$$\frac{E_0}{E_g} = N_i \frac{E_i}{E_g} + N_{ex} \frac{E_{ex}}{E_g} + N_i \frac{\varepsilon}{E_g}. \quad (4.3)$$

The band gap was found to be  $E_g = 14.2$  eV for solid Ar and 9.28 eV for solid Xe [70] (see also Table 2 in Section 4.3, where ionization processes are discussed in more detail). For liquid xenon a band gap of 9.22 eV was measured [71].

Using the definition of the  $W$ -value,  $W = E_0/N_i$ , equation (4.3) can now be written as:

$$\frac{W}{E_g} = \frac{E_i}{E_g} + \frac{E_{ex}}{E_g} \cdot \frac{N_{ex}}{N_i} + \frac{\varepsilon}{E_g}. \quad (4.4)$$

These ratios for liquid argon, krypton and xenon were evaluated by several authors. Although a general agreement seems to have been achieved, some values are not concordant. In particular, a ratio  $N_{ex}/N_i = 0.06$  has been calculated for LXe, although 0.2 is more consistent with experimental data. Their average, 0.13, is often used for some estimates. For LAr better agreement has been obtained around the ratio  $N_{ex}/N_i \approx 0.2$ . We refer the reader to Refs. [63, 72, 73] for a comprehensive set of parameters, some of which are reproduced in Table 2 in this work.

For nuclear recoils, the ratio of the number of primary excitations to that of ionizations in liquid xenon was found to be much higher than for electrons:  $N_{ex}/N_i \sim 1$  [74, 75].

In the condensed medium, charge recombination along the particle track plays a very important role in determining the response to radiation. Therefore, the observable ionization and scintillation signals depend on the applied electric field and, in most cases, are not equal to those that one might expect on the basis of the  $N_i$  and  $N_{ex}$  values. Due to recombination, the number of electrons collected at an anode is  $< N_i$  and depends both on the ionizing particle (species and energy) and on the applied electric field. For some particles, such as 1 MeV electrons, the number of collected electrons approaches  $N_i$  already at fields of  $\sim 1$  kV/cm, while for heavily ionizing particles ( $\alpha$ -particles, for example) it can be significantly smaller even at some tens of kV/cm. For the very low particle energies relevant to DM and CNS searches — both regarding electron and nuclear recoils — it is found that the dynamics of the recombination process becomes qualitatively different from that described by the models applicable to MeV particles and above.

In the absence of electric field and for medium ionization density, which on a first approach can be characterized by the linear energy transfer (LET), practically all electron-hole pairs created initially recombine and give rise to recombination luminescence; in this instance, the scintillation yield is at its maximum, and the number of emitted photons is  $N_{ph} \approx N_i + N_{ex}$ . For low density tracks, some electrons escape recombination even at zero field, and so  $N_{ph} < N_i + N_{ex}$ . On the other extreme are the tracks surrounded by a high density of ionized and excited species. In this region, the luminescence signal can be suppressed because of a high probability of collision between excited species, leading to so-called ‘bi-excitonic quenching’ [76, 77]. We shall discuss these effects in more detail in Sections 4.2.1 and 4.2.2.

Regarding the energy transfer from nuclear recoils, two substantial differences with respect to high energy particles must be stressed. Firstly, although some of the energy of the impinging ion goes ultimately into electronic excitations and ionization, a large fraction is spent in collisions in which the target atom recoils as a whole. Therefore, a significant fraction of the particle energy appears as kinetic energy of the target atoms (i.e. heat) and is not visible either as light or as charge. This mechanism of energy transfer is referred to as nuclear energy loss. In the formalism of stopping power it is described by a separate term:  $dE/dx = (dE/dx)_e + (dE/dx)_n$ , where the index  $n$  denotes energy losses through nuclear collisions and  $e$  refers to the electronic component. The second difference lays in a distinct ionization/excitation pattern that exists in the medium at the instant when the energy of all secondary particles drops below the excitation threshold — frequently called the ‘track structure’, except that in the case of very low energies this pattern does not resemble a track, but rather a cloud of electrons, positive ions and excited species (see Section 4.2.2).

A comprehensive theory of the energy loss of ions with velocity comparable to that of atomic electrons is not sufficiently developed to provide a solid theoretical background for exact calculations [78]. This certainly constitutes a handicap in understanding the physics associated with WIMP detection. The theoretical basis was laid out by Lindhard *et al.* [79, 80], who calculated the nuclear stopping power using the Thomas-Fermi screened potential to describe the interaction between the ion and a target atom. The electronic stopping was obtained by considering an ion moving through a constant density electron gas. The dependence on the ion and target atom charge was included again using the Thomas-Fermi description. Lindhard himself considered the treat-

ment of electronic stopping the most approximate of the two. In fact, the charge of an ion moving through a medium is not constant due to electron exchange with other atoms and accurate determination of the effective charge is a difficult task. This formulation is usually referred to as the Lindhard–Scharff–Schjøtt (LSS) theory.

As in WIMP detectors the medium consists of atoms of the same species as the nuclear recoil, the latter very rapidly loses its ‘projectile’ identity producing a cascade of secondary recoils which undergo the same interactions as the primary particle. In order to evaluate the total energy partition between the electronic and nuclear components for an impinging recoil of a given energy (Lindhard’s partition function [81]), the whole cascade must be taken into account. In spite of all difficulties, the LSS theory provides a useful framework and describes reasonably well the energy losses by nuclear recoils, at least in what the scintillation efficiency of LXe is concerned (see [82, 78]). We recommend [78] for a concise analysis of Lindhard’s model and more recent works related to it, in view of WIMP detection with liquefied noble gases.

The SRIM/TRIM code [62] provides information on ranges and stopping powers,  $(dE/dx)_e$  and  $(dE/dx)_n$ , using parameterizations adjusted to the existing experimental data, mostly for light ions; it can also simulate the whole cascade. For xenon, it results in somewhat low values for the electronic-to-nuclear loss ratio, which predicts a lower-than-observed scintillation yield for nuclear recoils even if no quenching is taken into account. A comparative analysis of SRIM/TRIM and LSS model predictions can be found in [78].<sup>4</sup>

## 4.2 Primary scintillation

### 4.2.1 Emission mechanism and yields

The emission mechanisms and scintillation yields have been studied primarily (and better understood) for particles of relatively high energies:  $\sim 1$  MeV electrons and  $\gamma$ -rays as well as  $\alpha$ -particles and relativistic ions. Information is rather scarce in the range  $\lesssim 100$  keV, although some progress has been made in recent years. Therefore, we begin by discussing the results obtained with fast electrons and  $\alpha$ -particles and then move to low-energy electrons and nuclear recoils.

In general terms, the mechanism of primary scintillation is similar for liquid argon and xenon. Imagining the liquid as a compressed gas (which is not strictly correct given the acknowledged existence of a band structure), one can say that most of the observed light is emitted by diatomic excited molecules which are formed in two distinct processes. One is excitation of rare gas atoms by electron impact with subsequent formation of strongly bound diatomic molecules in the excited state (excimers), similarly to what happens in the gas phase (using the terminology of solid state physics, one would refer to these states as ‘excitons’):



Here,  $R = \text{Ar}$  or  $\text{Xe}$  and the superscript  $\nu$  is used to distinguish excited states with vibrational excitation ( $R_2^{*,\nu}$ ) from purely electronic excitation with  $\nu = 0$  ( $R_2^*$ ). The vibrational relaxation is

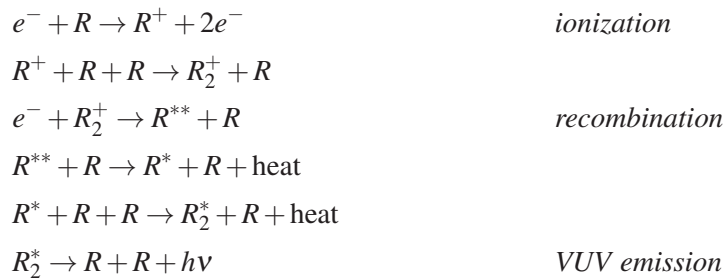
<sup>4</sup>The 2003 version of SRIM/TRIM code was used in [78]; newer versions are now available.



mostly non-radiative, as shown in the above equations, but emission of infrared photons is also possible. The scintillation photons, with wavelength in the vacuum ultraviolet (VUV) region for all rare gases, are emitted in a transition from one of the two lowest electronic excited states  $^3\Sigma_u^+$ , or  $^1\Sigma_u^+$  with  $v = 0$ , to the ground state  $^1\Sigma_g^+$ . The transition occurs at short interatomic distances, where the ground state potential is repulsive, resulting in dissociation of the molecule. Although the two transitions are spectroscopically indistinguishable, their decay times are quite different, especially in liquid argon. Direct transition from the triplet state  $^3\Sigma_u^+$  is forbidden, but the decay becomes possible owing to the mixing between  $^3\Sigma_u^+$  and  $^1\Pi_u$  states through spin-orbital coupling [83]. This can result in rather long life-times as is the case in LAr ( $\sim 1 \mu\text{s}$ ). As the coupling becomes stronger for molecules with higher atomic number, the decay time is significantly shorter for LXe ( $\sim 27 \text{ ns}$ ). Conversely, the triplet lifetime is even longer in LNe ( $15 \mu\text{s}$  [84]) and reaches  $\sim 13$  seconds in LHe [85].

Emission in the visible and near infrared (NIR) wavelength region (up to 2000 nm) has also been observed in LAr and LXe [86, 87, 88, 89].<sup>5</sup> Its intensity, however, is much lower than in the VUV region in those liquids (and falls also far short of the NIR emission in the respective gas). For liquid argon, emission in the range 400 – 1000 nm represents only  $\sim 1\%$  of the VUV yield [88]. In [89], a value of  $0.51 \pm 0.09$  infrared photons per keV is reported for LAr for  $\lambda = 690 - 1000 \text{ nm}$ , a result generally consistent with that in [88]. For LXe, an estimate of  $\gtrsim 0.2$  photons/keV can be obtained combining results from [87] and [92].

The alternative VUV luminescence process to direct excitation involves recombination of the ionization electrons with positive ions. The recombination occurs mostly with molecular ions formed shortly ( $\sim \text{ps}$ ) after ionization of atoms of the liquid by a particle [73, 93]:



The final stage of this sequence is similar to the direct excitation channel and consequently wavelengths and decay times are similar. However, the relative population of the singlet and triplet excited states is not necessarily the same. Moreover, the recombination process preceding the excimer formation can introduce a considerable time delay. This is the case in liquid xenon, where recombination is rather slow compared with the excimer de-excitation times, which leads to the appearance of a non-exponential third component in the decay curve. For liquid xenon, apparent time constants of 34 ns to 45 ns have been reported [83, 76] (see Figure 8). However, a longer tail

---

<sup>5</sup>The origin of the emission in the near UV, visible and infrared regions in these liquids is not fully understood. Observed spectra bear some similarity to those measured in the gas phase, where some lines have been identified as due to atomic transitions from the higher excited levels to the first excited state  $3p^54s$  [90, 91], but with significant suppression of the intensity for  $\lambda > 1300 \text{ nm}$  [87]. A weaker intensity (by a factor of  $\sim 100$ ) in LAr and LXe compared to that in the gas may be understood in view of the much higher collision rate in the condensed phase, leading to efficient non-radiative quenching of the highly excited states.

of up to  $\sim 2 \mu\text{s}$ , at the level of  $\sim 1\%$  of the initial amplitude of the scintillation signal, could also be observed in the study reported in [94]. This component disappeared completely when an electric field of a few kV/cm was applied, which confirms its recombination origin.

In liquid argon no significant changes in the shape of the decay curve under electric field have been observed — a fact explained by the relatively fast ( $\sim 1 \text{ ns}$ ) recombination, so that the timing of the photon emission is mostly determined by the decay time of excitons formed shortly after ionization [94]. Measurements of the electron thermalization time (0.9 ns for LAr and 6.5 ns for LXe [95]) support this conclusion. We point out that the recombination dynamics is especially sensitive to the purity of the liquid, as contaminant atoms and molecules can provide more effective thermalization of ionization electrons than elastic scattering off xenon atoms — thus hindering their escape from the influence of the positive ions.

It has long been observed that, for electrons under a field of the order of  $\sim 10 \text{ kV/cm}$ , the scintillation yield decreases by a factor of up to  $\approx 3$  in both liquids, which means that only  $\approx 1/3$  of the scintillation light emitted in the absence of an applied field is due to direct excitation, the remaining  $\approx 2/3$  resulting from recombination. The relative contribution of the recombination component to the total light yield was measured to be  $(67 \pm 2)\%$  for liquid argon and  $(74 \pm 2)\%$  for liquid xenon [96]. Similar results, 64% and 71% for argon and xenon, respectively, were obtained in [94]. The observed light yield decreases with field more rapidly in xenon than in argon. For example, in xenon it drops by a factor of 2 already at  $\sim 250 \text{ V/cm}$ , while in argon  $\sim 1 \text{ kV/cm}$  is necessary to produce the same effect.

The diagram shown in Figure 8 represents the distribution of the total number of emitted scintillation photons between different excitation channels when the liquid is excited by fast electrons with typical energies from 0.5 MeV to 1 MeV. The diagram is based on data published in [83, 94, 97]; other results are referred in the figure caption. Note the small contribution of the transitions from the singlet state to the direct excitation channel (only about 1.5% of the total number of emitted photons). In argon, the fast component is enhanced through the recombination channel resulting in about 8% of the total number of photons emitted at zero field. In LXe, however, the fast component is practically unobservable for electrons unless an electric field is applied to suppress recombination luminescence. It is important to point out again that impurities can affect (sometimes significantly) the luminescence properties of the medium, namely the light yield, emission spectrum and observed decay times. This may explain some discrepancies (especially noticeable for the slow component in liquid argon) between the early measurements and more recent ones, when more advanced purification techniques and better control of the impurity content were employed. This was observed in [99, 100] where the addition of small concentrations of  $\text{N}_2$  and  $\text{O}_2$  ( $\gtrsim 0.1 \text{ ppm}$ ) effectively quenched  $\text{Ar}_2^*$  triplet states and significantly shortened the observed decay time for the slow component, reducing the overall light yield (especially significant in the case of nitrogen).

For particles with higher LET, such as  $\alpha$ -particles or fission fragments, no difference in the decay time constants has been observed compared to those for electrons [101, 97, 76]. This means that the species emitting the scintillation photons are the same for all exciting particles. It also indicates that there is no substantial non-radiative quenching of the  $^3\Sigma_u^+$  and  $^1\Sigma_u^+$  states (which, being present, would shorten their effective lifetimes). However, the relative contribution of each component to the observed scintillation signal does depend on the particle type and energy. A

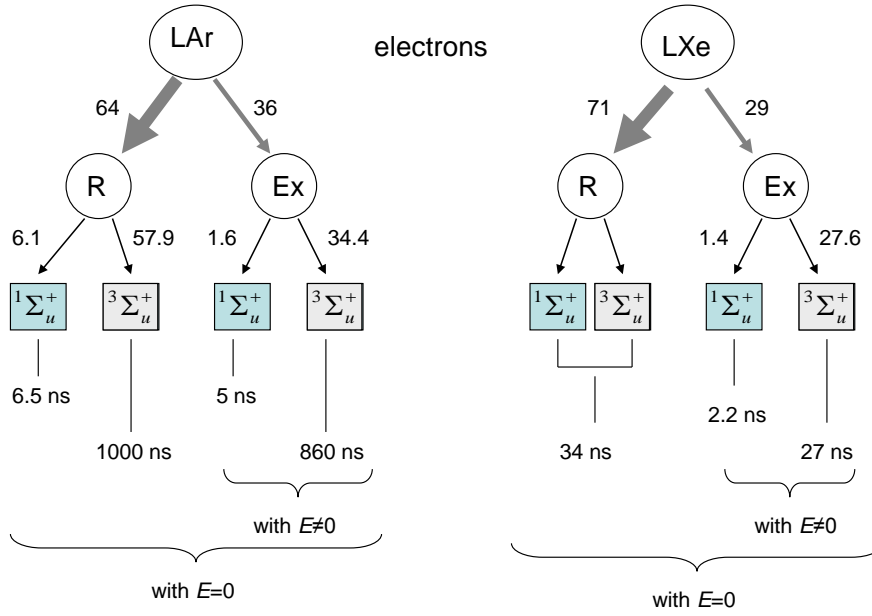


**Figure 8.** Observable distribution (percent) of the luminous energy for fast electrons.  $R$  and  $Ex$  stand for recombination and direct excitation channels, respectively. Estimates are from data in [83] and [97]. The share between the direct excitation and the recombination channel is from [94].

\*) Other values can be found in the literature (see also [98] for earlier measurements). On time constants, 7.0 ns has been reported for the fast component in LAr [76], whereas the slow component has been also measured as 1600 ns [76], 1463 ns [54] and 1260 ns [99] (all at zero electric field); for LXe, singlet and triplet decay times of 4.3 ns and 22.0 ns were reported in [76] along with an apparent scintillation decay time of 45 ns also at zero field. Other singlet/triplet intensity ratios have been published: 0.31/0.69 [94] and 0.23/0.77 [76] in LAr, and 0.36/0.64 in LXe [94].

strong enhancement of the fast component with respect to the slow one has been observed with 5 MeV  $\alpha$ -particles in liquid xenon [101, 97, 76] (see Figure 9).

The linear energy transfer for  $\alpha$ -particles is higher by a factor of  $\sim 100$  than for fast electrons. Therefore, the density of the ionized and excited species along the particle track is also much higher for  $\alpha$ -particles, which leads to stronger and faster recombination. No long ( $\sim \mu s$ ) tail nor the  $\sim 40$  ns recombination component have been observed in LXe with  $\alpha$ -particles, which means that, in this instance, the recombination time is shorter than the excimer decay time constants even in liquid xenon, contrary to what happens for electrons [101]. Moreover, it is an experimental fact that only a few percent of the charge initially created along  $\alpha$ -particle tracks can be extracted even with fields of  $\sim 10$  kV/cm (for electrons, this would collect nearly 100% of the ionization). Therefore, the two scintillation mechanisms (direct excitation and recombination) cannot be distinguished in practice. This is represented in the diagram in Figure 9 by the joining of the two channels together.

Strong recombination does not explain *per se* why the relative contribution of the fast component is enhanced for  $\alpha$ -particles. To our knowledge, a comprehensive explanation for this observation is still missing, although a number of hypotheses have been suggested [76]. One of the plausible mechanisms is quenching of singlet states in superelastic collisions with thermal elec-

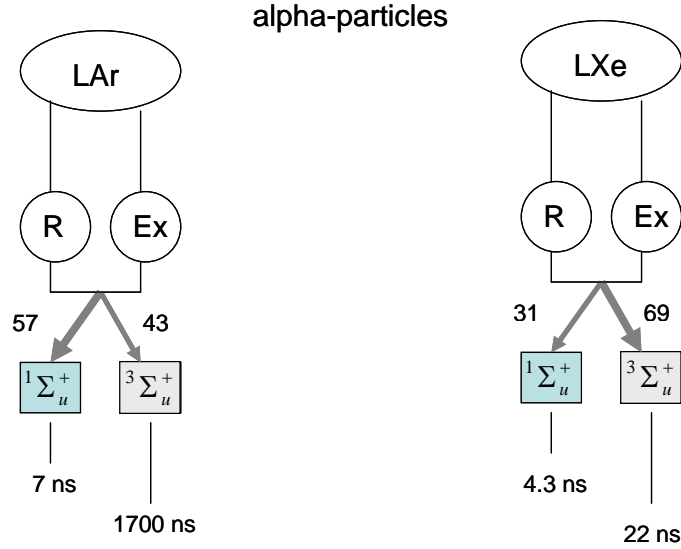


**Figure 9.** Observable distribution (percent) of the luminous energy for  $\alpha$ -particles, based on results in [76]. For liquid xenon, different estimates for the fast/slow intensity ratio have also been obtained: 0.53/0.47 from [101] and 0.77/0.23 from [97].

trons resulting in transitions from the singlet to triplet state. These transitions are more probable in the case of electrons than for  $\alpha$ -particles due to slower recombination along the electron tracks.

An even stronger contribution of the fast component to the total light yield was found for fission fragments, which have LET values  $\sim 10^5$  times higher than those for electrons. According to [76], in liquid argon the number of photons emitted in transitions from the singlet state for electrons,  $\alpha$ -particles and fission fragments is about 23%, 57% and 75% of the total, respectively. In liquid xenon, the singlet component contributes with about 60% in the case of  $\alpha$ -particles and fission fragments and only  $\sim 5\%$  in the case of relativistic electrons.

With regard to the scintillation decay time, a similar situation is found in the case of low energy nuclear recoils: the effective decay time for recoils is also shorter than that for electrons and  $\gamma$ -rays. This was the basis of  $\gamma$ -ray background discrimination in early dark matter detectors using liquid xenon as a target [44, 42]. For example, decay times of 33 ns and 19 ns were observed for  $\sim 20$  keV electrons and xenon recoils (after elastic scattering of neutrons), respectively [44]. In liquid argon, the enhancement of the singlet component for nuclear recoils is of the same order of magnitude as in xenon (or even less significant) but the very large difference between the singlet and triplet time constants allows much more efficient pulse shape discrimination to be used [54, 102]. (Liquid neon and helium are even more promising from this point of view.)

In general, the liquefied noble gases are very good scintillators. For 1 MeV electrons and  $\gamma$ -rays, yields of 40 to 50 photons/keV, i.e. comparable to that of NaI(Tl), have been reported for LXe (see [73, 104] and references therein). At lower energies, the light yield increases rather significantly, especially in xenon: in the energy region between 10 and 100 keV LXe can produce nearly 70 photons/keV. A comprehensive analysis of the existing data for  $\gamma$ -ray scintillation in liquid xenon has been presented in [103]. Those authors also developed a simulation model

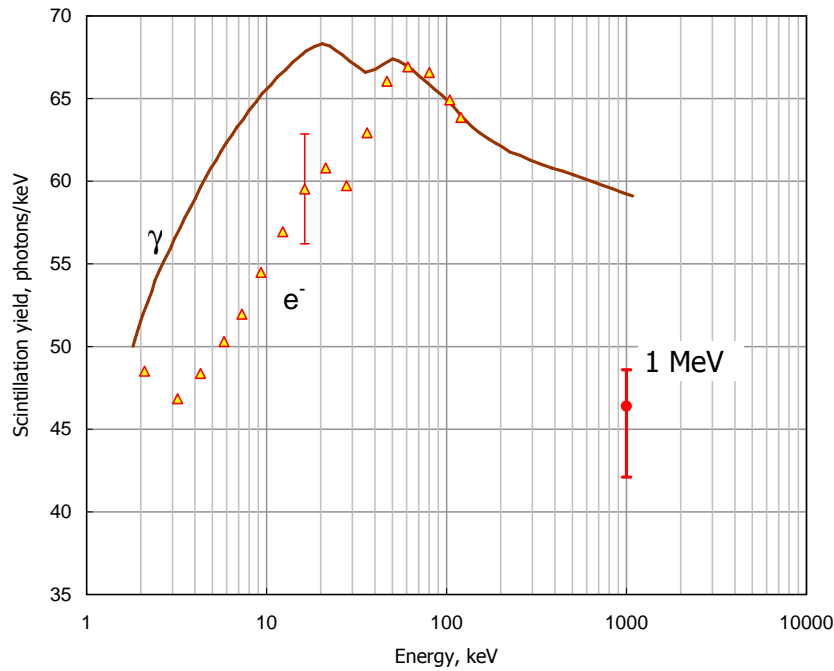


**Figure 10.** Scintillation yield of LXe as a function of energy for electrons and  $\gamma$ -rays. Solid line – evaluated yield (absolute) for  $\gamma$ -rays based on a comprehensive analysis of the existing experimental data in [103]. Triangles – relative measurements with Compton electrons in [60]; these data were re-normalized by us to the evaluated curve at  $\approx 120$  keV (see main text). The circle is for 1 MeV electrons from [73].

consistently describing most of the available datasets. Their results are shown by the brown curve in Figure 10. Recently, the relative scintillation efficiency for low energy electrons has also been reported [60]. The electrons were produced in Compton scattering of 662 keV  $\gamma$ -rays in a liquid xenon target. These data, re-normalized by us to the absolute light yield from [103] at  $\approx 120$  keV, are also shown in Figure 10 (red yellow-filled triangles). When considering these two datasets one must bear in mind that absorption of  $\gamma$ -rays in the liquid results in not one but several electrons of different energies (photoelectron, those resulting from absorption of xenon fluorescence, Auger electrons). Therefore, direct comparison of the light yields for electrons and  $\gamma$ -photons of the same energy is not generally correct at low energies<sup>6</sup>. However, the similarity of the trends with energy between the two datasets gives an important insight into the physics of the scintillation process, as we shall discuss in the context of recombination in Section 4.2.2. There are also important practical implications that follow from the comparison shown in Figure 10: the difference in light yields must be taken into account when performing detector calibration with low energy electrons or  $\gamma$ -rays.

It should be remarked that absolute measurements of the scintillation yield in liquefied rare gases are difficult, in large part due to the short wavelength of scintillation photons (178.1 nm for liquid xenon and 129.6 nm for argon — excited with  $\alpha$ -particles [105]). For xenon, quartz-windowed PMTs can be used, but for argon wavelength shifters are usually required (*p*-terphenyl,

<sup>6</sup>Although it actually works out correctly at  $\approx 120$  keV for xenon.

tetraphenyl butadiene (TPB) or other). Poor knowledge of the angular reflectivity of different materials in this wavelength region and absolute calibration of the VUV photon detectors pose additional difficulties. (See Section 4.2.3 for more information on material reflectivities.)

The scintillation efficiency, or the number of photons per unit deposited energy, is frequently expressed via its reciprocal quantity, the  $W_s$ -value, similarly to the  $W$ -value for charge.  $W_s$  is defined by dividing the energy deposited by a particle in the liquid,  $E_0$ , by the number of emitted photons, i.e.  $W_s = E_0/N_{ph}$ . The number of scintillation photons emitted from a particle track depends strongly on the electric field, being maximum at  $E = 0$ . Therefore,  $W_s$  is defined for zero field (contrary to the  $W$ -value, which is defined for an infinite field).

Assuming that all the excited atoms give one VUV photon (after undergoing the excimer formation<sup>7</sup> phase described above) and that all initially created electron-ion pairs recombine and also give a photon, one can write for the number of emitted photons  $N_{ph} = N_{ex} + N_i$ . From this equation, and recalling that  $W = E_0/N_i$ , one can establish a simple relationship between the two  $W$ -values:

$$W_s^{min} = \frac{W}{1 + N_{ex}/N_i}. \quad (4.5)$$

This  $W_s^{min}$  corresponds to the minimum possible energy needed to produce a scintillation photon (maximum  $N_{ph}$ ) when there are no quenching processes, which depends very much on the track structure and ionization/excitation density on its different parts. We also note that  $W_s$  reflects the efficiency of energy transfer to the medium through both direct excitation and ionization (in contrast with the  $W$ -value for ionization, which determines  $N_i$  only). This has important consequences for improving energy resolution and linearity of detector response to electrons, as discussed in Section 4.4.

The available data on  $W_s$  for different particles are shown in Table 1. Compilations of the existing experimental and theoretically estimated  $W_s$  values for liquid xenon can be found in [106, 104, 103, 67]. One can see that, in spite of the existence of a few discordant points, there is a general agreement, within  $\approx 10\%$ , between the various datasets, except probably for low energy nuclear recoils, where some significant statistical and systematic uncertainties still remain (although the situation has improved in recent times).

Figure 11 shows a compilation of scintillation yields of LXe and LAr for various particles of different energies as a function of LET. Although no unified picture on the LET dependence of the scintillation efficiency emerges from the figure, some observations can be made. It is apparent that a  $dE/dx$ -based model is at odds with the experimental data for low energy electrons. The behavior of low energy nuclear recoils is similarly discrepant; an indicative curve for the scintillation yield of Xe recoils with energy  $\lesssim 100$  keV is also shown in Figure 11 (more precise data are shown in Figure 12 and discussed later in this section). A significant reduction of scintillation yield is obvious in this case.

The LET dependence of the scintillation efficiency of liquid argon and xenon for high energy particles is discussed in [73, 106, 120, 107, 122]. The scintillation yield is approximately constant for intermediate LET values, in the range between  $\sim 10^2$  and  $\sim 10^3$  MeV/(g-cm<sup>2</sup>), but decreases for lower and higher ionization densities. This trend can be observed both in LXe and LAr. According

---

<sup>7</sup>Formation of self-trapped excitons, using the terminology of solid state physics.

**Table 1.** Energy expended per scintillation photon for different particles.

Particle	Energy	LET, MeV/(g·cm <sup>2</sup> )	$W_s$ , eV (LAr)	$W_s$ , eV (LXe)
No quenching; $W_s^{min}$	–	–	$19.5 \pm 1.0$ <sup>a)</sup> $19.8$ <sup>b)</sup> $18.4$ <sup>b)</sup>	$13.8 \pm 0.9$ <sup>a)</sup> $13.0$ <sup>b)</sup> $14.7 \pm 1.5$ <sup>c)</sup> $13.45 \pm 0.29$ <sup>d)</sup> $13.7 \pm 0.2$ <sup>e)</sup>
Relativistic electrons	1 MeV	$\approx 1$	$25.1 \pm 2.5$ <sup>c)</sup> $24.4$ <sup>a)</sup>	$23.7 \pm 2.4$ <sup>c)</sup> $21.6$ <sup>a)</sup> $22.5 \pm 2.5$ <sup>f)</sup> $< 35$ <sup>g)</sup> $42 \pm 6$ <sup>h)</sup> $67 \pm 22$ <sup>i)</sup>
Low energy electrons	20 – 100 keV	$\sim 7$ to 2	–	$18.3 \pm 1.5$ <sup>f)</sup> $14.2$ <sup>j)</sup> $12.7 \pm 1.3$ <sup>k)</sup> $29.6 \pm 1.8$ <sup>l)</sup>
$\alpha$ -particles	$\approx 5$ MeV	$\sim 4 \times 10^2$	$27.1$ <sup>a)</sup> $27.5 \pm 2.8$ <sup>c)</sup>	$17.9$ <sup>a)</sup> $19.6 \pm 2.0$ <sup>c)</sup> $16.3 \pm 0.3$ <sup>m)</sup> $17.1 \pm 1.4$ <sup>f)</sup> $39.2$ <sup>n)</sup>
Relativistic heavy ions	$\sim 1$ GeV/amu	$\sim 10^2$ to $10^3$	$19.4 \pm 2.05$ <sup>c)</sup>	$14.7 \pm 1.5$ <sup>c)</sup>
Nuclear recoils*	60 keV	$2.9/4.0 \times 10^3$	$\sim 100$ <sup>p)</sup> (exp) $\sim 90$ <sup>q)</sup> (theor)	$95 \pm 20$ <sup>r)</sup> (exp) $\sim 77$ <sup>s)</sup> (theor)
	20 keV	$2.6/2.7 \times 10^3$	$\sim 100$ <sup>p)</sup> (exp) $\sim 105$ <sup>q)</sup> (theor)	$110 \pm 20$ <sup>r)</sup> (exp) $\sim 86$ <sup>s)</sup> (theor)
	5 keV	$1.9/1.5 \times 10^3$	$\sim 100$ <sup>p)</sup> (exp) $\sim 140$ <sup>q)</sup> (theor)	$160 \pm 40$ <sup>r)</sup> (exp) –
Fission fragments	$\sim 1$ MeV/amu	$\sim 10^4$	$\sim 110$ <sup>t)</sup>	$60$ <sup>u)</sup>

\* For nuclear recoils the total LET values, estimated from range tables in [62], are presented; the electronic part can be roughly obtained by multiplying by  $\sim 0.2$ . Values in column 3 are for argon/xenon.

<sup>a)</sup> From [73]: evaluated from several estimates and considered by those authors to be the most probable values.

<sup>b)</sup> From [73]: other estimates.

<sup>c)</sup> [106, 107]; <sup>d)</sup> [108]; <sup>e)</sup> [75];

<sup>f)</sup> [104]; <sup>g)</sup> [109]; <sup>h)</sup> [110]; <sup>i)</sup> [111]; <sup>j)</sup> [112]; <sup>k)</sup> [113]; <sup>l)</sup> [114]; <sup>m)</sup> [115]; <sup>n)</sup> [116].

<sup>p)</sup> Using measured scintillation efficiency referred to 122 keV  $\gamma$ -rays [117] and  $W_s^{min}$  from [73].

<sup>q)</sup> Using theoretical quenching factor from [118], [119] and  $W_s^{min}$  from [73].

<sup>r)</sup> Estimated by the authors using the relative scintillation efficiency with respect to 122 keV  $\gamma$ -rays from data compiled in [67] (see our Figure 12), with  $W_s^{min}$  from [73].

<sup>s)</sup> Using a theoretical estimate for the quenching factor from [82] and  $W_s^{min}$  from [73].

<sup>t)</sup> [120] with  $W_s^{min}$  from [73].

<sup>u)</sup> From [106].

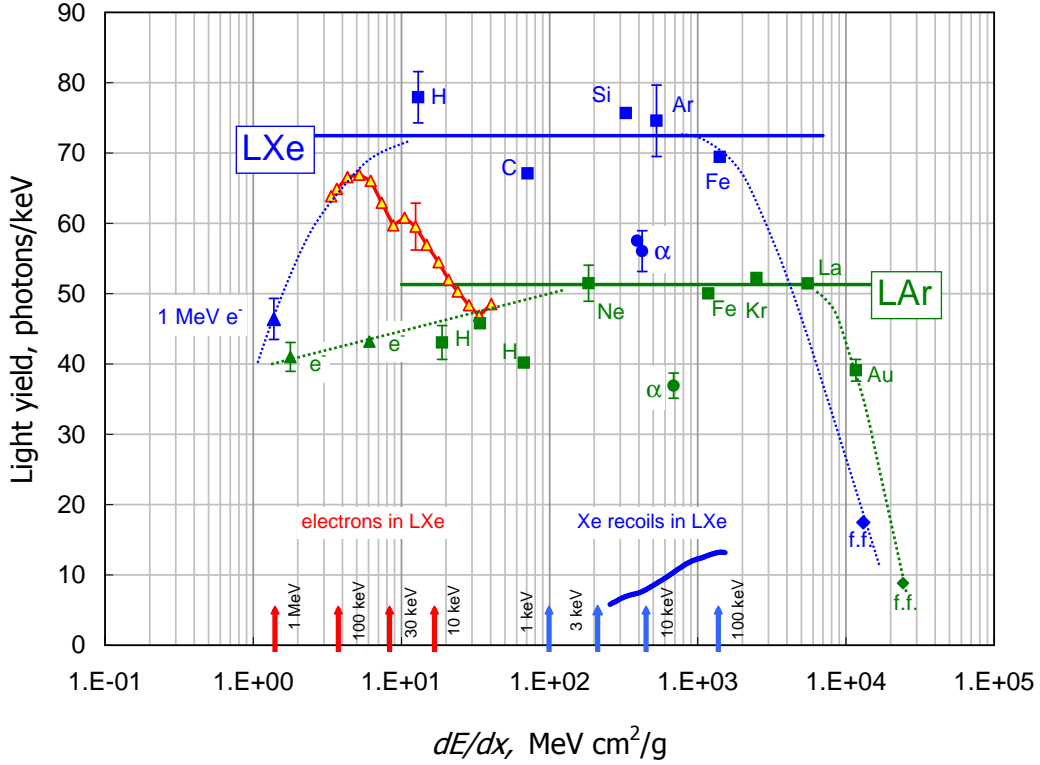


**Figure 11.** Scintillation yield of LXe and LAr as a function of linear energy transfer for various particles. Data points (in blue for LXe, and in green for LAr) are after [73] (Figures 2, 4 and Table III); not all data points are shown for clarity. For the same reason, only a typical error bar is shown for each dataset. Dashed lines are for guiding the eye only, no underlying model is assumed; the top plateau corresponds to a minimum energy to produce a scintillation photon  $W_s^{min}=13.8$  eV for LXe and 19.5 eV for LAr according to [73, 63]. Red arrows indicate average  $dE/dx$  values for electrons in LXe calculated as the initial particle energy (indicated next to arrow) divided by the range from ESTAR [121]; blue arrows indicate  $(dE/dx)_e$  for Xe recoils in LXe calculated in a similar way using stopping power and range tables from SRIM [62] and the Lindhard partition function from [81]. The red yellow-filled triangles represent the relative measurements with Compton electrons reported in [60]; we re-scaled their energy to  $dE/dx$  using ESTAR as above, and re-normalized their response to that of  $\gamma$ -rays at  $\approx 120$  keV using the evaluated curve from [103] as in Figure 10.

to those studies, the ‘flat-top response’ in the region of intermediate LET corresponds to the situation when each of the excited and ionized species created by a particle gives a photon, and therefore  $W_s = W_s^{min}$  in this region. The  $W_s^{min}$  value for LAr was calculated to be  $19.5 \pm 1.0$  eV, in good agreement with experiment (see Table 1). In LXe  $W_s^{min}$  is lower and, furthermore, some disagreement remains between the values obtained from theoretical estimates and experimental data. Assuming  $N_{ex}/N_i = 0.06$ , a value of  $W_s^{min} = 14.7 \pm 1.5$  eV was calculated in [73] while experimental data point to about 13.0 eV, which translates to a ratio of  $N_{ex}/N_i \approx 0.20$  instead. Therefore, an evaluated value of  $W_s^{min} = 13.8 \pm 0.9$  eV was presented by those authors. More recent measurements resulted in  $13.45 \pm 0.29$  eV [108] and  $13.7 \pm 0.2$  eV [75] for  $W_s^{min}$  in liquid xenon. We refer to Table 1 for other references and also to [103] for a recent compilation.



Reduction of the scintillation yield at low LET values is attributed to a higher probability for an electron to escape recombination even at zero field. This is the case for  $\sim 1$  MeV electrons and  $\gamma$ -rays. In the high LET region above  $\sim 10^3$  MeV/(g $\cdot$ cm $^2$ ) a decrease is observed too, but for a different reason. The density of excited species along the particle track becomes high enough to render non-negligible the probability of collisions between them. The mechanism of bi-excitonic quenching has been proposed in [76]. This mechanism implies autoionization of one of the two colliding free excitons ( $R^* + R^* \rightarrow R + R^+ + e^-$ ) at the beginning of the exciton formation process. Although the formed  $R^+$  ion has a good chance of recombining with an electron to produce a new excited state, this would result, at best, in one emitted photon instead of two — one from each of the two excitons initially created if these underwent a normal process<sup>8</sup>  $R^* + R \rightarrow R_2^* \rightarrow R + R + h\nu$ .

Low energy electrons and nuclear recoils ( $\lesssim 100$  keV) fall out of the trend observed in Figure 11 for higher energies. This fact can be explained by a different track structure and therefore a different recombination mechanism. We shall postpone this discussion until Section 4.2.2, but we do consider here the experimental data (and some interpretations) on the scintillation yield for nuclear recoils — a case of special importance for DM and CNS search experiments.

A significantly reduced light yield has been found for low energy xenon ions traveling in LXe and argon ions in LAr. Xenon recoils below 140 keV are found to expend at least  $W_s \sim 100$  eV per scintillation photon produced, a much higher energy than, for instance, for electrons. In the dark matter community, the recoil scintillation efficiency is usually referenced to the scintillation yield for 122 keV  $\gamma$ -rays from a  $^{57}\text{Co}$  source, a convenient energy for detector calibration (one should, however, keep in mind that the light yield for  $\gamma$ -rays of this energy is  $\approx 12\%$  lower than the maximum possible yield, while quenching calculations usually use the maximum as reference). According to this common definition, the scintillation efficiency is  $L_{eff}(E) = W_{s,e}(122 \text{ keV})/W_{s,Xe}(E)$  at zero electric field (the indices ‘ $e$ ’ and ‘Xe’ correspond to electron and xenon recoils, respectively).

Most experimental measurements of the scintillation efficiency for nuclear recoils to date were carried out with different setups but using the same method — elastic scattering of mono-energetic  $\sim$ MeV neutrons off a LXe target [61, 123, 124, 125, 126, 127, 128]. The scattered neutrons are detected at a fixed angle, thus allowing the energy transferred to Xe atoms to be determined kinematically.

An alternative, indirect method is afforded by modern Monte Carlo codes, notably GEANT4 [129], which can model the elastic scattering of neutrons as well as detector response effects very accurately. The energy-dependent scintillation efficiency can be extracted by fitting the scintillation response obtained with a broadband source (e.g. Am-Be) with simulated spectra of deposited energy folded with all efficiencies and energy resolution (including the sought quenching effect), as demonstrated in [67]. The beam measurements do not rely directly on Monte Carlo, but they require small chambers with high light yield, usually operated at zero electric field to maximize light yield and light collection. The indirect method can be applied to calibration data from real dark matter experiments and provides, therefore, a useful validation of nuclear recoil detection efficiencies. The most recent datasets, namely [61], [127], and [67] report a nuclear recoil scintillation efficiency which decreases gently with energy, as shown in Figure 12.

---

<sup>8</sup>When mentioned in the context of nuclear recoils, this kind of quenching mechanism is usually referred to as ‘electronic quenching’ to distinguish from ‘nuclear quenching’ which is the fraction of the particle energy transferred to atoms of the medium in elastic collisions, i.e. lost to heat.

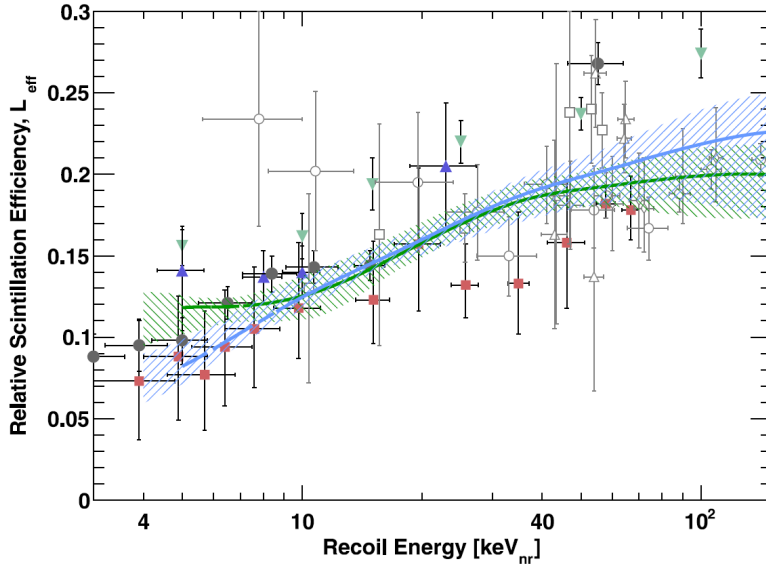


**Figure 12.** Energy-dependent relative scintillation yield for nuclear recoils in liquid xenon; data from mono-energetic neutron beam measurements are labelled by the following markers: (■) [61]; (●) [127]; (▲) [126]; (◊) [123]; (△) [124]; (○) [128]; (□) [125]. Indirect measurements from Monte Carlo: (▼) [66]; the two lines are the indirect measurements obtained from the first and second runs of ZEPLIN-III, with 68% CL bands shown in green (\\) and blue (///), respectively [67]. (From [67]; with permission from Elsevier.)

As far as liquid argon is concerned, fewer experimental data exist on the relative scintillation efficiency for nuclear recoils. A value of 0.28 has been reported for 65 keV argon recoils referred to  $\gamma$ -rays of 20 keV [130]. However, the measurements were carried out with an applied electric field, so that the recombination component of primary scintillation was partly suppressed, the effect being more significant for  $\gamma$ -rays than for nuclear recoils. In more recent measurements, a constant scintillation efficiency of  $0.25 \pm 0.02$  (relative to 122 keV  $\gamma$ -rays) has been obtained for argon recoils in the range from 20 to 250 keV [117]. Even newer results were reported in [131]; these are compatible with a flat interpretation of  $L_{eff}$  with a mean value of  $0.29 \pm 0.03$  above 20 keV. In both cases a slight increase in efficiency was observed below 20 keV (similarly to some measurements in xenon [128]).

Some recent data exist also for liquid neon in the range 30–370 keV [132]; an average efficiency of 0.24 is reported above 50 keV. Similarly to liquid argon, an upturn at low energies is also observed in this work (although the authors point out that the uncertainties on the lowest energy points are also the most significant).

The quenching effect for xenon recoils has been assessed theoretically in [82]. The theoretical prediction, based on the concept of bi-excitonic quenching for the electronic component and using Lindhard's theory [81, 79] to calculate the contribution from nuclear collisions,<sup>9</sup> agrees quite well with experimental data. The model also predicts a gradual decrease of the scintillation efficiency

<sup>9</sup>The observed reduction of the light yield with respect to its maximum value due to the increasing contribution of the nuclear component is sometimes referred to as 'nuclear quenching' (misleadingly, in fact, because strictly speaking there is no quenching of the excited species, only a lower probability for their formation).

with decreasing recoil energy. It was concluded that for 60 keV xenon recoils electronic quenching is responsible for the reduction of the scintillation efficiency by a factor of  $\approx 1.5$ , while nuclear collisions contribute with another factor of  $\approx 3.2$ . Applied to liquid argon, a similar behavior of the quenching factor with recoil energy is predicted [118, 119]:  $\approx 0.26$  for 100 keV recoils with gradual decrease to  $\approx 0.19$  for 20 keV and, further, to  $\approx 0.15$  for 5 keV. We recall that the quenching factor is defined with respect to the maximum scintillation yield, which is observed with relativistic light ions, i.e. at intermediate LET values; the light yield for  $\sim 100$  keV electrons is somewhat lower (Figure 11) thus resulting in an efficiency referred to 122 keV  $\gamma$ -rays of  $L_{eff} \approx 0.32$ ,  $\approx 0.23$  and  $\approx 0.18$  for 100 keV, 20 keV and 5 keV recoil energies, respectively.

Another phenomenological approach to the problem was proposed in [133]. This study combined Lindhard's theory with Birks' saturation law, which was rather successful in describing the LET dependence for organic scintillators. This combination results in a less pronounced dependence of  $L_{eff}$  on recoil energy at higher values. For xenon, the predicted relative scintillation efficiency is constant down to approximately 20 keV recoil energy, at which point it begins to decrease slowly. This approach seems to be better suited to describe experimental data for argon and neon than for xenon.

The authors of [61] have found that their dataset on  $L_{eff}$  for LXe at zero field is better described if, in addition to nuclear and bi-excitonic quenching as proposed in [82], a non-negligible electron escape probability is assumed for nuclear recoils tracks. This assumption was supported by a very weak dependence of the extracted charge on applied electric field (see Figure 13 and Section 4.3.1). Considering a constant ratio  $N_{ex}/N_i = 0.06$ , both for electrons and nuclear recoils, they arrived at rather high values for the fraction of escaping electrons,  $N_{esc}/N_i$ , which increases with decreasing recoil energy from  $\sim 0.15$  for 70 keV up to  $0.7 \pm 0.2$  for 4 keV.

None of the above models foresees an increase of the scintillation efficiency at low recoil energies as observed in LAr.

#### 4.2.2 The role of recombination

In view of the previous discussion, it is manifest that the recombination light contributes significantly to the total scintillation yield in the liquefied noble gases. Recombination in these liquids is rather strong and it is a complex process which depends on a large number of factors: the initial distribution of ions and electrons immediately after the particle passage, including all secondary ionizations and in some cases also excitations; the speed with which subexcitation electrons lose their energy to phonons and the distance traveled to reach thermal equilibrium with the medium; electron mobility and diffusion rate; collision frequency and the probability of recombination to occur when an electron encounters a positive ion. In this section the interested reader will find a more detailed discussion of recombination models which describe the scintillation and ionization responses.

The scintillation efficiency as a function of LET for different particles and energies shown in Figure 11 reflects well the complexity associated with recombination. For high energy particles a general trend was recognized early on (see [73, 106] and references therein): a flat-top response at intermediate values of LET with some reduction in the low LET region and a significant drop for high LET fission fragments, similar for LXe and LAr. Clearly, low energy electrons — and  $\gamma$ -rays — as well as nuclear recoils fall out of that trend, and this has been recognized only recently. In

this section we search for an explanation for such irregular behavior starting, as before, from higher energies since recombination along the tracks of these particles is better understood.

A common feature of the interaction of high energy particles with matter is a relatively well defined track along which the ionizations and excitations are distributed. The distribution of ionization electrons, ions and excited species at the instant when all electrons slow down to sub excitation energy is frequently called the ‘track structure’ and this determines to a large extent the subsequent behavior of the charge carriers. The track structure varies significantly for different particles and LET values, thus hindering the development of a universal theory of recombination in liquid radiation detectors. Nevertheless, one can always distinguish a cylindrically symmetric principal trace and secondary branches due to  $\delta$ -rays; these can be partially cylinder-shaped or form more complex structures, especially around the end point.

Thus, according to [94], the track of a 1 MeV electron (low LET) can be regarded as a column of widely spaced positive ions with average distance between them close to the Onsager radius,  $r_c = e^2/(4\pi\epsilon_0\epsilon kT)$  ( $r_c = 125$  nm for liquid argon and 49 nm for xenon), where  $\epsilon$  is the dielectric constant and other symbols have their usual meaning. Comparing these values with the mean distance between atoms,  $\sim 0.4$  nm, it is clear that ions are separated from each other by hundreds of neutral atoms. At the surface of a sphere with the Onsager radius, the potential energy of the Coulomb attraction of the electron to its parent ion is equal, by definition, to the kinetic energy of the thermal motion. Thus, the electrostatic attraction to the ion dominates within the sphere, while outside it the thermal motion is likely to draw the electron away from the ion. The thermalization length for electrons is estimated as  $\sim 4.5$   $\mu\text{m}$  in LXe [134] and  $\sim 1.7$   $\mu\text{m}$  in LAr [135], meaning that a good fraction of the electrons can be found out of the reach of positive ions when thermalization is achieved. In the absence of an external electric field, these will partly diffuse to the chamber walls thus escaping recombination (these escaping electrons are considered to be the cause of the decrease in scintillation efficiency at low LET values discussed earlier — see Figure 11). The remaining fraction of electrons governed by diffusion will sooner or later meet an ion and recombine.

The mean volume density of free electrons along the track of 1 MeV electrons can be estimated from [94] as  $\sim 2 \cdot 10^{-7}$   $\text{nm}^{-3}$  for liquid argon and  $\sim 3 \cdot 10^{-6}$   $\text{nm}^{-3}$  for liquid xenon (or even much lower taking into account thermalization distances from [135, 134]). These values are to be compared with densities of up to  $\sim 10^{-2}$   $\text{nm}^{-3}$  to  $\sim 10^{-1}$   $\text{nm}^{-3}$  in the track core of an  $\alpha$ -particle or a fast heavy ion (estimated from [77], [136] and [137]). For these particles, the positive ions form a continuous line of positive charges with a mean separation, projected to the particle trajectory, of about 0.22 nm and 0.13 nm for LAr and LXe, respectively, so that an electron ejected from an atom finds itself in a strong cylindrical field from which it will have difficulty escaping. According to [77], an electron with sub-excitation energy in liquid argon can stray from the track core up to a distance of only some 5 nm, whereupon it turns back, being attracted by the column of positive ions, crosses it and continues to oscillate around the track axis until it recombines with one of the ions. It has been shown in [77] that about 10 passes are sufficient for an electron to recombine with large probability, and this takes in fact a very short time of  $\sim 0.4$  ps. This suggests that, on  $\alpha$ -particle tracks, electrons recombine long before they reach thermal equilibrium with the liquid, in contrast with the low LET particles.

The track structure of  $\alpha$ -particles and fast ions with similar LET values in LAr was analyzed in [77] leading to the conclusion that more energy is deposited in the core track and less in

the penumbra in the case of  $\alpha$ -particles than for ions. Moreover, the core radius was estimated as  $\sim 0.4$  nm for  $\alpha$ -particles versus  $\sim 6$  nm for ions meaning higher ionization/excitation density along  $\alpha$ -particle tracks. This should lead to complete recombination which does not result, however, in maximum scintillation yield in either LAr or LXe — a fact explained by bi-excitonic quenching, similarly to what happens for particles with very high LET values such as fission fragments (note the discordant points for  $\alpha$ -particles in Figure 11).

This shows how much the ionization/excitation pattern at the particle interaction site can influence the observed scintillation signal (as well as the ionization one, since the recombination strength naturally affects the amount of charge that can be extracted from the particle track — we shall discuss this issue in Section 4.3.1).

Concerning the scintillation for low-energy electrons and  $\gamma$ -rays (the former shown as yellow-filled red triangles in Figure 11) we note that the data agree reasonable well with the above trend for energies  $\gtrsim 80$  keV, but this is not so for lower energies. The higher energy part can be suitably fitted with a Birks-type law [103] in terms of LET, as proposed in [120] for light ions and  $\sim 1$  MeV electrons:

$$\frac{dY(E)}{dE} = \frac{A \frac{dE(E)}{dx}}{1 + B \frac{dE(E)}{dx}} + \eta_0. \quad (4.6)$$

In this model, the scintillation yield due to recombination was considered to be a sum of two components: recombination of geminate and non-geminate types. Geminate recombination and the direct excitation component do not depend on LET and are both included in the constant term  $\eta_0$ . An electron is considered to undergo geminate recombination if it thermalizes within the Onsager sphere. Recombination of all remaining electrons is included instead into the first term, which was obtained under the assumption that recombination can be treated in terms of concentrations of electrons ( $n_-$ ) and ions ( $n_+$ ):  $dn_{\mp}/dt = -\alpha n_- n_+$ , where  $\alpha$  is the recombination coefficient, thus presuming that this process is volumetric in nature. Further simplification was made by setting  $n_- = n_+ = n$ . A link to  $dE/dx$  is obtained by assuming proportionality,  $n \propto dE/dx$ , which is, strictly speaking, valid only for a cylindrical geometry (i.e. long tracks). Indeed, a function in the form of equation (4.6) was successfully applied for  $E_\gamma \gtrsim 80$  keV but failed for lower energies where the ionization pattern resembles more a spherical blob than a cylinder [103]. For these energies those authors used the Thomas-Imel box recombination model which was rather successful in parameterizing specifically the charge yield as a function of electric field  $\mathcal{E}$  [138]:<sup>10</sup>

$$\frac{Q(\mathcal{E})}{Q_0} = \frac{1}{\xi} \ln\left(1 + \frac{1}{\xi}\right), \quad (4.7)$$

with  $\xi = N_0 \alpha / 4a^2 \mu \mathcal{E} = \kappa / \mathcal{E}$ ; here,  $N_0$  is the total number of electrons and  $\mu$  is the electron mobility, assumed to be independent of field. In this model, recombination is also described through the term  $\alpha n^2$  and, to provide a connection between the electron/ion concentrations and the total

---

<sup>10</sup>In fact, this model was originally developed to describe the field-dependent charge yield for low-LET particles such as MeV electrons. A better fit of the experimental data was obtained, however, by adding a second term to equation (4.7), similar to the existing one, but depending on an additional recombination parameter  $\xi'$  [139]; this recognizes that the principal trace can appear surrounded by low-energy  $\delta$ -electrons creating ionization ‘blobs’ with a different recombination strength.

charge created by a particle, a box of arbitrary size  $a$  containing that charge (assumed uniformly distributed) is defined. Then,  $\kappa = N_0\alpha/4a^2\mu$  is used as a single adjustable parameter.

The brown curve in Figure 10 corresponds to a combination of these two models — Birks' for 'long' tracks and Thomas-Imel for 'short' ones — with which the authors of [103] succeeded in describing consistently most of the existing data on scintillation yield of liquid xenon for  $\gamma$ -rays. To adapt the Thomas-Imel model to zero-field conditions,  $\mu\mathcal{E}$  was replaced by some constant velocity so that the adjustable parameter becomes  $\xi$  and not  $\kappa$ . In order to account for energy partition between various channels (photo- and Compton electrons, X-rays, Auger electrons) a detailed GEANT4 Monte Carlo simulation was used and the most adequate model was chosen for each electron track having the thermalization length scale as a cross-over distance.

Qualitatively, the decrease in scintillation efficiency on the low energy (high LET) side can be understood as the increasing probability for electrons to escape recombination. For sufficiently low energies, the dimensions of the ionization region are determined by the thermalization length  $r_{th}$  rather than by the electron range and so the charge concentration becomes a linear function of deposited energy  $n_- \approx (E/W)(3/4\pi r_{th}^3)$  (here  $W$  is the  $W$ -value for charge — see Section 4.3.1). However, this simple picture is in tension with the basic presumption of the Thomas-Imel model which considers no electron diffusion. Without diffusion, no escape from recombination is possible unless an electric field is applied.

The combined model was also able to describe the field dependence of the scintillation yield. The geminate (Onsager) recombination component included in the term  $\eta_0$  in equation (4.6) was found to be significant at zero field, but more easily suppressed by an external electric field than the non-geminate part [75, 103].

To reproduce the field dependence in the modified Thomas-Imel parameterization, some field effect on  $\xi$  had to be empirically re-introduced, although it was found to be much weaker than in the original model:  $\xi \propto \mathcal{E}^{-0.1}$ , approximately [75, 103] (originally,  $\xi \propto \mathcal{E}^{-1}$  [138]).

In spite of physical inconsistencies in the existing recombination models, the approach proposed in [103] provides a very useful framework for modeling detector response to low energy backgrounds and to  $\gamma$ -rays used for calibration of DM detectors. These inconsistencies reflect in fact our poor understanding of the recombination process in noble liquids. Critical reviews of these and other models can be found in [140, 141, 142, 143, 75]. Original papers such as [144, 145, 135, 134] may also constitute useful reading.

Even less is known about recombination along nuclear recoil tracks with energy relevant for DM and CNS searches. It is clear that the contribution from nuclear collisions cannot be neglected, especially in liquid xenon, but the details of the track structure are not sufficiently clear. The Bohr impulse principle is not applicable in the case of ions moving through a medium with velocity comparable to, or lower than, that of atomic electrons (see [78]). Besides, as the medium consists of atoms of the same species, the primary recoil can transfer a significant fraction of its kinetic energy in each collision, thus losing rapidly its 'projectile' identity and producing a cascade of secondary recoils of comparable energy which interact with the medium in the same way. Consequently, the spacial distribution of ionizations and excitations will be quite different from what is expected along the tracks of other particles.

Recombination affects both scintillation and charge yields — the two signals that constitute the basis of background rejection in most dark matter detectors. These signals are complemen-

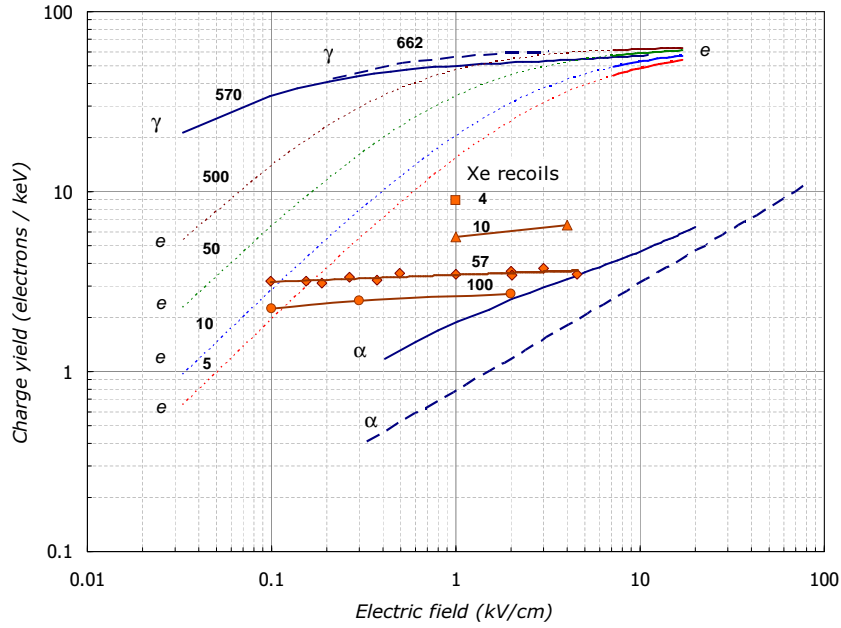


**Figure 13.** Free electron yield from the tracks of different particles as a function of electric field in liquid xenon. Numbers next to the data represent particle energy in keV. For  $\alpha$ -particles the data are: solid line from [147], dashed line from [148]. Red symbols indicate charge yield from xenon recoil tracks from [53] and [61] (not all data are shown). For  $\gamma$ -rays: solid line [149], dashed line [150]. For electrons: calculated using recombination coefficients  $k$  from [151]. The coefficients were determined from the charge yield measurements with  $\mathcal{E}$  in the range 7–15 kV/cm (in this field region, the data are represented by solid lines), assuming  $Q(\mathcal{E}) = Q_0/(1 + k/\mathcal{E})$ . Dotted lines correspond to extrapolation to the lower field region using the above equation. We point out the difference between these calculations for 500 keV and the experimental data for 570 keV and 662 keV, which may indicate a systematic shift. However, the important information here is the dependence of the charge yield on electron energy, which shows the opposite tendency to that observed for nuclear recoils.

tary and depend on electric field in opposite ways. It is therefore important to study them simultaneously. The charge yield from xenon recoils tracks has been measured directly in dedicated experiments [53, 61] and also indirectly assessed from calibration data of real dark matter detectors [66, 146, 67]. A relatively high charge yield and weak electric field dependence has been found, against expectations, as shown in Figure 13. Although data with simultaneous measurement of scintillation and ionization are still scarce and a detailed discussion of this topic is premature, a few interpretations of the existing data can be mentioned.

Most of the energy of a Xe ion or atom moving in liquid xenon (this is what is meant by a ‘nuclear recoil’) is lost in elastic collisions with other atoms. The topology of the cascade represents a complex and very ramified structure with tens or even hundreds of branches formed by secondary recoils (see Figure 14 for some examples). The transverse dimensions of the cascade are, in most cases, comparable to that along the initial direction of primary recoil (although long tracks resembling, to some extent, a high energy particle also can appear with some probability). Therefore, recombination models based on cylindrical symmetry are hardly applicable to nuclear

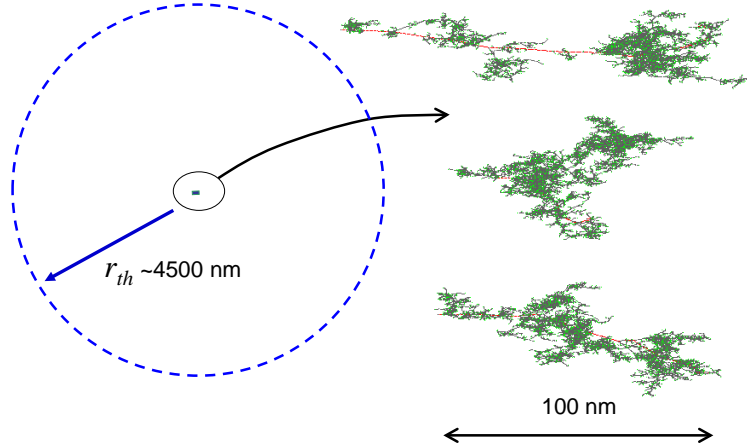


**Figure 14.** Xe recoil tracks in liquid xenon simulated with TRIM [62] compared with the thermalization distance (calculated in [134]). The projectile trajectory is shown in red; trajectories of secondary atoms/ions are in gray with end points in green (this shows the number of secondary atomic recoils in the cascade). No electron tracks are shown.

recoils. The extent of these cascades is in the  $\lesssim 100$  nm scale, which is much smaller than the electron thermalization distance ( $r_{th} \sim 4 \mu\text{m}$  in liquid xenon [134]). Therefore, the distribution of thermalized electrons looks more like a sphere surrounding a tree-like core of positive ions at its center with size  $\lesssim 1/40$  of that of the sphere. In this sense, the recombination should be similar to that for low energy electrons with the difference that, for the same particle energy, only a fraction  $\sim 0.2$  goes into ionizations/excitations in the case of nuclear recoils.

This picture is qualitatively consistent with the trend observed for recoils of different energies in Figure 13. More electrons per keV can be extracted for lower recoil energies because less charge is distributed over approximately a constant volume with radius  $\sim r_{th}$ . Thus, the electron density should be roughly proportional to the recoil energy, something which is not fully confirmed by the data. The energy dependence of Lindhard's energy partition function may partially explain the absence of strict proportionality since the electronic component of the energy losses decreases with decreasing energy [81]).

A loose distribution of the thermalized ionization electrons may explain the relatively large charge yield from nuclear recoil tracks and its weak variation with field: practically all electrons escape recombination even at very low field ( $\sim 0.1$  kV/cm), as argued in [61]. Considering a constant ratio  $N_{ex}/N_i = 0.06$ , both for electrons and nuclear recoils, those authors concluded that the fraction of escaping electrons increases with decreasing recoil energy from  $\sim 0.15$  for 70 keV to  $0.7 \pm 0.2$  for 4 keV.

The measured charge yield, although higher than one might expect on the basis of the  $dE/dx$  argument (cf.  $\alpha$ -particles), is still lower than for electrons even taking into account the energy partition between electronic and nuclear parts. This may be explained by assuming a much higher  $N_{ex}/N_i$  ratio for nuclear recoils as proposed in [75] and [74] where it was estimated to be  $N_{ex}/N_i \sim 1$  (cf.  $\sim 0.1$  for other particles — see Table 2). This would also explain lower S2/S1 ratios observed



for nuclear recoils than in the case of electrons. As remarked in [75], a possible mechanism for more energy to be channeled into excitation than ionization might be the lowering of some atomic levels during the interpenetration of atomic shells of colliding xenon atoms [152]. Hypotheses of possible field or energy dependence of the ratio  $N_{ex}/N_i$  have also been proposed in [75, 153, 74].

Explanation of the trend for the recoil scintillation efficiency observed in Figure 12 in terms of escaping electrons also seems plausible: the lower the recoil energy the more electrons escape recombination and less light is emitted per unit energy. In this respect, the importance of bi-excitonic quenching, proposed to approximate Lindhard’s prediction for the electronic component of energy transfer to the observed scintillation yield [82], might be questioned. On the other hand, one should bear in mind that excitons do not migrate as fast as electrons. Their distribution should accompany the cascade topology and therefore the existence of high excitonic densities locally cannot be excluded.

The possibility of a more complex recombination picture cannot be ruled out either, for example, the existence of regions with very high ionization density from which extraction of electrons with field is difficult. This may be the reason for a weak dependence of the charge yield with field: when all escaped electrons have already been collected and those in highly ionized regions require much higher field to be extracted. A weak dependence of the scintillation signal on the applied field for nuclear recoils [53] can also be qualitatively explained on this grounds. In this case, there may be no need to consider  $N_{ex}/N_i$  to be higher for nuclear recoils than for other particles.

### 4.2.3 Light propagation

Beyond the generation of scintillation photons one must consider which conditions may affect their propagation in the liquid up to their eventual detection. Two processes contribute to a finite photon attenuation length in noble liquids: absorption, which leads to loss of scintillation photons, and Rayleigh scattering, which is an elastic process. Absorption is mostly due to impurities — the excimer-mediated scintillation mechanism described in Section 4.2.1 ensures that self-absorption of VUV photons is very unlikely. Water vapor is one of the main culprits; for example, 1 ppm H<sub>2</sub>O in liquid xenon will absorb most scintillation light in under 10 cm [154] (see Figure 15).

Separate measurement of the two light attenuation components is difficult. Usually, a combined effect is observed, which is characterized by a total attenuation length,  $L$ . The attenuation length is related to the absorption and scattering lengths ( $L_a$  and  $L_s$ , respectively) via the equation  $L^{-1} = L_a^{-1} + L_s^{-1}$ . The value of  $L_a$  can be assessed if reflection on all passive (non-sensitive) surfaces is close to 100%. For example,  $L_a > 100$  cm has been reported for liquid xenon [154]. On the other hand, in experiments where no special provision has been made to enhance reflections, or where these were intentionally suppressed, attenuation lengths between 30 and 50 cm have been obtained by several authors [111, 155, 156, 157]. Assuming that  $L_a > L_s$ , this gives an estimate for the scattering length,  $L_s \approx L$ . It has also been noticed that the measured  $L$  increases if the photon wavelength is shifted to longer values (as observed in [156] when a few percent of Xe was added to LAr or LKr), also indicating a significant contribution from Rayleigh scattering in the pure liquid. For liquid xenon, a Rayleigh scattering length of  $\sim 30$ – $50$  cm is generally accepted, resulting both from the measurements described above and from a calculation of scattering on density fluctuations (30 cm [158]). These values are also consistent with those estimated from the measured refractive

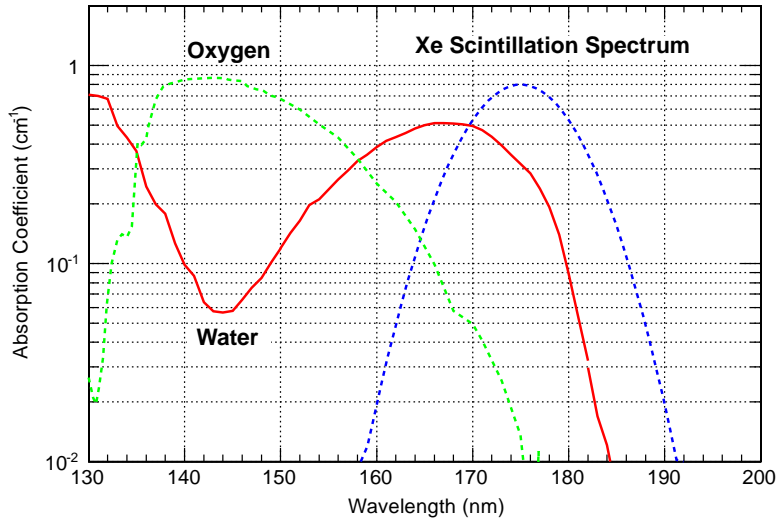


**Figure 15.** VUV absorption coefficients for 1 ppm water vapor and 1 ppm oxygen in liquid xenon calculated in [154] (we note that in the original publication the y-axis is wrongly labelled in ‘ $m^{-1}$ ’ and this is corrected here to ‘ $cm^{-1}$ ’; we thank G. Signorelli for pointing this out). (With permission from Elsevier.)

index [159, 157]. For liquid argon, an experimental value of  $L_s = 66$  cm has been reported [156], while theoretical calculations predict 90 cm [158].

As discussed in Section 4.3.2, the purity requirements demanded by ionization readout are even more stringent, but loss of scintillation performance is increasingly important in large noble liquid detectors. Elastic scattering of scintillation photons is not as problematic in small chambers (the total light yield is preserved), but in very large, scintillation-only systems reconstruction of the interaction position becomes more difficult.

High reflectivity of detector components at the scintillation wavelength is also very important for efficient detection of the scintillation light. Data on reflectivity of some relevant materials for  $\lambda < 200$  nm are shown in Figure 16. Among the metals, freshly deposited Al presents the highest reflectance although this rapidly degrades when exposed to air. A  $MgF_2$  coating can protect the Al surface from oxidation and preserve high reflectance in the VUV for long periods of time. As for dielectric materials, much attention has been paid to PTFE because it is known to be compatible with the high purity and low radioactivity requirements, and is therefore a material of choice for electrical insulation and light enhancement in DM detectors. The exact values of PTFE reflectivity for xenon scintillation light are still being discussed; in fact, they depend on the manufacturing technology and surface treatment. Importantly, it is found that the reflectivity of a PTFE surface in contact with liquid xenon is enhanced quite significantly relative to that in vacuum (see Figure 16, left). Values in excess of 90–95% have been reported for the PTFE/LXe interface [168, 169, 170].

A detailed knowledge of the angular reflectivity profiles is also important for correct modeling of the detector response. Recently, there have been new efforts to determine the reflectivity profiles of some materials of interest for detector construction at the xenon emission wavelength [171, 166, 172]; some results are shown on the right panel of Figure 16.

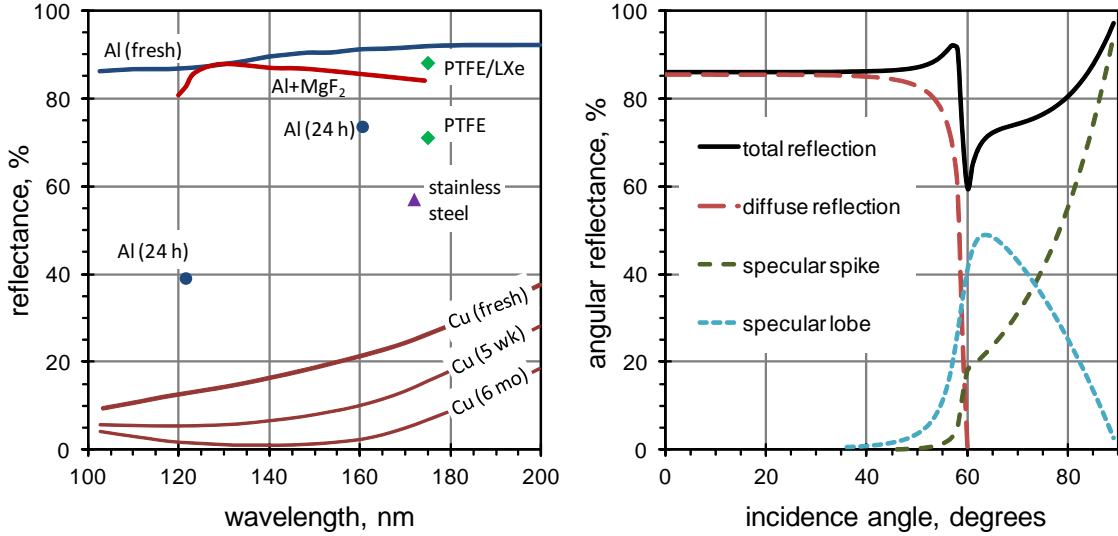


**Figure 16.** The VUV reflectance of some materials employed internally in noble liquid chambers is shown left. Data for Al [160] and Cu [161] are for freshly evaporated films and the ensuing degradation from build-up of the native oxides; a logarithmic decrease of reflectivity up to 3 years after Al evaporation was reported in [162]. Data for Al passivated with MgF<sub>2</sub> (both deposited by evaporation) is from [163]; a similar coating on a chemically-etched surface was used in the 80 kg LXe detector in [164]. Data for stainless steel is from [165]. Measurements with pressed, polished PTFE illuminated with Xe scintillation light in vacuum were reported in [166]; an angle-averaged value is indicated here. A model extrapolation for the angular reflectance of a PTFE/LXe interface is shown on the right ([167], courtesy C. Silva). The increase in specular reflection relative to the interface with vacuum increases the angle-averaged reflectance to approximately 90%. Some experimental measurements suggest even higher reflectivity for the PTFE/LXe interface [168, 169, 170].

### 4.3 Ionization charge

#### 4.3.1 Ionization yields and transport properties in the liquid

The number of primary ionizations,  $N_i$ , created in the liquid by a particle is significantly larger than the number of excitations,  $N_{ex}$ , for electrons and comparable in the case of nuclear recoils (see Table 2). For the ionization signal to be detected, the following conditions must be met: i) charge carriers must escape recombination; ii) their mobility in the electric field must be high; iii) the probability to form low mobility states along the drift path must be low, and iv) a high gain amplification mechanism is required in order to form a measurable signal.

The ionization process results initially in the creation of free electrons and positive ions  $R^+$ ; the treatment of dielectrics in solid state physics provides the relevant framework here, and in this context we would refer to these positive ions as ‘holes’. Holes are rapidly localized through formation of molecular ions  $R_2^+$  within picoseconds (see [94] and references therein). The electrons lose their kinetic energy in inelastic collisions, producing more ionizations and excitations, and in elastic collisions with atoms, producing heat (or ‘phonons’, to carry the solid state analogy further), until thermal equilibrium with the medium is reached.

Recombination prevents some of the charge created initially from being collected by an electric field; this fraction depends very much on the type of particle and its energy, as discussed in

**Table 2.** Some properties of LAr and LXe relevant for particle detection.  $W$  is the  $W$ -value and  $F$  is the Fano factor, both for electrons;  $N_{ex}/N_i$  is the ratio of the number of primary excitations to the number of ionizations in the particle track;  $v_e$  is the electron drift velocity,  $\mu$  is the mobility given for several ions (TMSi stands for trimethylsilane). The ion drift velocity is a linear function of electric field,  $v = \mu \mathcal{E}$ . This is also true for electrons at low field, until their energy begins to deviate from thermal.

	LAr	LXe
$E_g$ , eV		
solid	14.2 <sup>a)</sup>	9.28 <sup>a)</sup>
liquid	–	$9.22 \pm 0.01$ <sup>b)</sup>
$W$ , eV	$23.6 \pm 0.3$ <sup>c)</sup>	$15.6 \pm 0.3$ <sup>d)</sup>
$F$	0.116 <sup>e)</sup>	0.059 <sup>e)</sup>
$N_{ex}/N_i$		
electrons	0.21 <sup>f)</sup>	0.13 <sup>f)</sup>
nuclear recoils	–	$\sim 1$ <sup>g)</sup>
$v_e$ , cm/s		
$\mathcal{E} = 1$ kV/cm	$2.6 \times 10^5$ <sup>h)</sup>	$2.25 \times 10^5$ <sup>h)</sup>
$\mathcal{E} = 10$ kV/cm	$4.9 \times 10^5$ <sup>h)</sup>	$2.8 \times 10^5$ <sup>h)</sup>
$\mu$ , cm <sup>2</sup> /(V·s)		
Ar <sup>+</sup> in LAr or Xe <sup>+</sup> in LXe	$0.2 \times 10^{-3}$ <sup>i)</sup>	$3.5 \times 10^{-3}$ <sup>j)</sup>
TMSi <sup>+</sup>	–	$0.2 \times 10^{-3}$ <sup>k)</sup>
O <sub>2</sub> <sup>–</sup>	$0.2 \times 10^{-3}$ <sup>i)</sup>	$0.7 \times 10^{-3}$ <sup>k)</sup>

<sup>a)</sup>[70]; see [173, 142, 174] for other measurements and references. The agreement between data for the band gap for the solid state is better than 0.5%;

<sup>b)</sup>[71]; <sup>c)</sup>[136]; <sup>d)</sup>[72]; <sup>e)</sup>[69];

<sup>f)</sup>[73]; for LXe, an average value between that expected from theory (0.06) and that suggested by experiment (0.2) is given; for LAr, these values agree;

<sup>g)</sup> [74, 75]; <sup>h)</sup> [175]; <sup>i)</sup> [176]; <sup>j)</sup> [177]; <sup>k)</sup> [178].

Section 4.2.2. For high energy particles,  $\gtrsim 100$  keV, which leave a well-defined ‘long’ track in the liquid, the  $dE/dx$  approach works relatively well: the higher the  $dE/dx$  value the stronger the recombination. Thus, for the low-LET  $\sim 1$  MeV electrons ( $dE/dx \sim 1$  MeV cm<sup>2</sup>/g) about 90% of the charge created initially can be extracted by applying a field of the order of a few kV/cm [94, 150, 149], while for  $\alpha$ -particles ( $dE/dx \sim 500$  MeV cm<sup>2</sup>/g) a field of  $\sim 20$  kV/cm in liquid argon, or  $\sim 80$  kV/cm in liquid xenon, is required to collect about 20% of the charge [148, 147]. Figure 13 on page 30 shows some of the available data on the charge yield as a function of electric field for different particles.

For low energy particles which are of interest for DM and CNS searches, the ionization pattern presents no cylindrical symmetry and therefore  $dE/dx$  is no longer a good parameter to describe

the charge yield. For example, higher yield is observed for nuclear recoils than for  $\alpha$ -particles in liquid xenon in spite of comparable  $dE/dx$  values for both projectiles. The yield dependence on the applied field is also quite different as Figure 13 attests. Although some absolute figures for the charge yield for xenon recoils are known, it is not clear yet how much ionization is originally created in the liquid by these particles.

The usual way to characterize a medium with respect to its ionization ‘capacity’ is through the energy expended per electron-ion or electron-hole pair  $W = E_0/N_i$ , where  $E_0$  is the energy transferred to the medium by a particle and  $N_i$  is the number of initially created electron-hole pairs. The Platzman equation (4.1) allows one to express it through other quantities characterizing the detection medium (see Section 4.1). The  $W$ -value is a convenient practical parameter but its measurement is not easy. Experimentally, absolute charge measurements are inherently challenging for low energy interactions, although the single electron signal measured in double-phase detectors provides an ideal calibration standard. However, the main problem rests with the fact that the charge observed at an electrode is not necessarily equal to that initially created by the passing particle. This can often be due to attachment of electrons to impurities, but the main reason is recombination, which in principle exists at any finite field strength. Therefore, in order to determine the number of electrons created promptly by a particle,  $N_i = Q_0/e$ , one needs to extrapolate the extracted charge, measured as a function of electric field,  $\mathcal{E}$ , to an infinitely large field. In turn, that requires the assumption of a model describing this dependence. In the absence of a complete model, it is generally accepted that the parameterization  $Q(\mathcal{E}) = Q_0/(1 + k/\mathcal{E})$  works well for the purpose, although the physical assumptions made to derive this expression are not strictly valid for liquefied rare gases. This equation was first obtained by Jaff e to describe recombination in a column of positive and negative ions with equal mobilities [179], which is far from being the case for the noble liquids (see Table 2). Besides, recombination is treated as a perturbation in this approach, which might be acceptable for gases but certainly not for liquids.<sup>11</sup>

Assuming the above dependence for  $Q(\mathcal{E})$ , linear fits of  $1/Q$  against  $1/\mathcal{E}$  provide  $1/Q_0$  as the vertical axis intercept, thus allowing  $N_i$  to be determined. The  $W$ -values for liquid argon and xenon have been measured in [136, 72, 181]. Table 2 presents commonly adopted values for  $W$ , although other values have been also reported (for example  $W=13.6\pm 0.2$  eV for liquid xenon [181]).

Electrons which escape recombination drift relatively quickly in heavy noble liquids [175, 182]: at a field of 1 kV/cm their drift velocities in LAr and LXe are very similar (2.6 mm/ $\mu$ s and 2.25 mm/ $\mu$ s, respectively). At higher fields, the drift velocity increases more rapidly in liquid argon, reaching 4.9 mm/ $\mu$ s compared with 2.8 mm/ $\mu$ s in xenon at  $\mathcal{E} = 10$  kV/cm (see Table 2). In argon, it continues to increase at least up to 100 kV/cm, while in xenon it saturates already at 10 kV/cm [175]. (In liquid neon and helium a gas bubble is formed around the drifting electron, thus reducing its mobility dramatically — see [183].)

The drift velocity of positive carriers at ordinary fields is a factor of  $\sim 10^5$  lower than that of electrons and, therefore, their motion is not detectable in most experiments. It has been noticed

---

<sup>11</sup>The constant  $k$  in the above parameterization characterizes the recombination strength. Representative values are: for a few hundred keV electrons and  $\gamma$ -rays  $k \approx 0.56$  kV/cm in LAr and  $\approx 0.42$  kV/cm in LXe [180];  $k \approx 2.4$  kV/cm for 15.3 keV X-rays [151];  $k \sim 470$  kV/cm for  $\alpha$ -particles (obtained with a different parameterization, but one in which  $k$  still combines with the field strength in the same way, i.e. also through the ratio  $k/\mathcal{E}$  [138]). A more complete compilation can be found in [6, p.340].

that the mobility of positive carriers resulting from the ionization of xenon atoms is significantly higher than that of other positive ions — a fact attributed to hole-type conductivity [177, 178]. The same does not happen in liquid argon, in which the same mobility has been measured for positive carriers and  $O_2^-$  ions [176]. This indicates that positive ions actually drift physically in liquid argon, similarly to the transport in gases, while in liquid xenon it is the vacancy that moves, very much like in solids (for comparison, in solid xenon and argon the hole mobility is about  $2 \cdot 10^{-2} \text{ cm}^2/(\text{V}\cdot\text{s})$  for both elements [184]).

The high mobility of negative charge carriers can decrease significantly in the presence of even a very small amount of electronegative impurities, such as  $O_2$ , water and some other molecules. These molecules can capture free electrons and form negative ions with extremely low mobility (for example,  $\mu(O_2^-) \approx 0.2 \cdot 10^{-3} \text{ cm}^2/(\text{V}\cdot\text{s})$  in LAr and  $0.7 \cdot 10^{-3} \text{ cm}^2/(\text{V}\cdot\text{s})$  in LXe [177, 178] — see Table 2 — resulting in drift velocities of a few mm/s at practical electric fields). The probability for an electron to be captured by an impurity species depends on its concentration, the reaction rate constant and the path length of the electron on its way to the anode. Therefore, purification of liquefied rare gases to better than ppb level is a critical issue. (Impurities can also affect the scintillation light yield and time constants as mentioned previously.)

Another aspect to consider is electron diffusion during their drift in the electric field. Diffusion in noble liquids is much lower than in the respective gas and this is why measurements of the diffusion coefficients are difficult. For electrons in thermal equilibrium with the medium and at zero field, diffusion is isotropic and is characterized by a diffusion coefficient  $D$ , which is related to the zero-field electron mobility  $\mu_0$  through the Einstein equation  $eD/\mu_0 = kT$ . With increasing fields, the electron energy rises and their mobility begins to deviate from  $\mu_0$ . The equation can be modified to  $eD/\mu = F\langle\epsilon\rangle$ , where  $\langle\epsilon\rangle$  is the mean electron energy and  $F$  is a constant depending on the electron energy distribution (for example, for Maxwell's distribution function  $F = 2/3$ ). In the presence of an electric field, however, the diffusion process is no longer isotropic and occurs predominantly in the plane perpendicular to the electric field. Two diffusion coefficients are therefore required:  $D_T$  for transverse diffusion, and  $D_L$  for longitudinal diffusion. For liquid xenon, a ratio  $D_L/D_T \sim 0.1$  is rather well verified for fields  $\gtrsim 1 \text{ kV/cm}$  [93]; for a field of  $730 \text{ V/cm}$ ,  $D_L/D_T \sim 0.15$  has been obtained [185]. In the zero-field limit this ratio should approach unity.

Absolute values for diffusion coefficients in liquid xenon are not well measured but some indicative figures can be presented:  $D_T \sim 100 \text{ cm}^2/\text{s}$  has been reported for  $1 \text{ kV/cm}$ , decreasing to  $\sim 50 \text{ cm}^2/\text{s}$  for  $10 \text{ kV/cm}$ ; for  $D_L$  the values are an order of magnitude lower [93, 8]. Theoretical estimates in [186] result in  $D_T \approx 85$  to  $100 \text{ cm}^2/\text{s}$  which vary only very weakly with field in the range from  $100 \text{ V/cm}$  to  $10 \text{ kV/cm}$ . Recent measurements indicate  $D_T \approx 30 \text{ cm}^2/\text{s}$  with variation of about  $\pm 5 \text{ cm}^2/\text{s}$  in the field range of  $0.5$  to  $1.2 \text{ kV/cm}$  [187]. For longitudinal diffusion, a value  $D_L = (12 \pm 1) \text{ cm}^2/\text{s}$  has been reported [185].

Less information is available for liquid argon. Transverse diffusion is studied experimentally in [188]. The authors present values for the characteristic energy of electrons  $eD/\mu$  between  $0.1 \text{ eV}$  and  $0.4 \text{ eV}$  for fields  $2$  to  $10 \text{ kV/cm}$ , which are consistent with some earlier measurements and also with predictions from Lekner's theory. In terms of diffusion coefficient this translates to  $\sim 3 \text{ cm}^2/\text{s}$  for  $1 \text{ kV/cm}$  and  $\sim 16 \text{ cm}^2/\text{s}$  for  $10 \text{ kV/cm}$ . Somewhat higher values were reported in [182] for low fields. Those authors report  $13 \text{ cm}^2/\text{s}$  for  $1 \text{ kV/cm}$  and  $9 \text{ cm}^2/\text{s}$  for  $300 \text{ V/cm}$ . The effect of the liquid temperature was also studied in this work. The ICARUS group reported on the longitudinal

diffusion coefficient in LAr at fields of  $\sim 100$  V/cm :  $D_L = (4.8 \pm 0.2)$  cm<sup>2</sup>/s [189]; this value was also referred in a more recent publication from this group [190].

The impact of electron diffusion on the performance of DM and CNS search detectors is not expected to be very significant (for current designs, at least). For a 1 m drift in LXe in a field of 1 kV/cm one can estimate that an initially point-like electron cloud will spread over a distance  $\sigma_x = (2DL/v_e)^{1/2} \approx 4$  mm. This smearing can even be turned into an advantage when considering very low detection thresholds for nuclear recoils, as argued in [185]: for very low recoil energies with no observable S1 signal, the width of the S2 signal can provide information on the drift time of the electrons and hence help fiducialize the sensitive volume.

### 4.3.2 Liquid purity

From a practical point of view, the purity problem has several facets. Firstly, one must consider the purity of the gas to be liquefied. The purity supplied by the manufacturer is an important starting point but never sufficient — the contamination is usually of order parts per million (ppm). Therefore, additional on-site purification is required. Much effort has been put into this over the last decades and numerous purifiers have been developed; nowadays commercial getters (operating hot or cold) can deliver sufficient purity for most applications: free electron lifetimes of  $\sim 1$  ms can now be achieved, providing  $>1$  m drift distances. There are also a number of distillation and vapor evacuation tricks that can help remove inert impurities present in elevated quantities and which are not removed efficiently by most getters. A common problem, which still has no simple and reliable solution, is to know exactly which impurities actually contaminate the system. The impurity monitoring is best done with a residual gas analyzer using mass spectrometry. Its sensitivity is limited by a high partial pressure of the bulk gas; however, using a cold trap between the gas inlet and the mass spectrometer can improve the sensitivity to ppb levels [191]. Oxygen and water are the most common electronegative contaminants, but it is not unusual to measure electron lifetimes which decrease with electric field, just opposite to what would be expected for these species [192]; N<sub>2</sub>O is often blamed for this behavior but, to our knowledge, the evidence for its presence in most systems is not conclusive. The presence of nitrogen has been detected in some setups where a significant reduction of secondary light in the gas phase was observed; in double-phase systems, a significant nitrogen concentration can build up in the thin gas layer above a large LXe target to quench the secondary scintillation completely.

No less important is the cleanliness of the experimental setup, including detector components and the gas handling system. Standard ultra-high vacuum (UHV) techniques should be adhered to whenever possible, to minimize contamination of the gas due to outgassing of materials, or from inappropriate component handling, cleaning or storage. A rigorous selection of ‘wetted’ materials is essential, and special surface treatment of metallic surfaces to reduce porosity and diffusion is very desirable. The choice of electrical insulators should be subject to special attention: the large surface and bulk porosity of many such components can lead to a high outgassing rate. Implementation of rigorous storage, handling and cleaning protocols is essential: the system must be assembled in a clean environment, after ultrasonic cleaning of all components using the right solvents in the correct sequence.

After ensuring that the system is leak-tight, baking under high vacuum and at maximum allowed temperature for long periods (days to weeks, depending on dimensions and system complexity) is the next important step. This is not always feasible for detectors operated underground (for safety reasons) or when delicate internal components are involved (e.g. some photo-sensors and vacuum seal techniques). Systems built from low-outgassing materials and following strict gas handling procedures have sustained adequately large electron lifetimes for longer than a year without re-purification [193]. On the other hand, some of the largest noble liquid detectors today contain large amounts of fluoropolymers such as PTFE to enhance VUV reflectivity, and this leads to very high outgassing rates. In this instance, continuous pump-driven purification of the gas is often used: some gas is taken from the detector, recirculated through the purification system and condensed into the detector again; purification directly in the liquid phase is also possible but technically more challenging.

Finally, the issue of radio-purity is intimately connected with this discussion. For example, most commercial getters are not suitable for application in rare event searches due to very significant radon emanation rates.  $^{222}\text{Rn}$  atoms wash into the detector where they decay, and (metallic) radioactive progeny will subsequently plate-out internal surfaces; some are  $\alpha$  emitters, which can cause nuclear recoils into the active volume. Radon mitigation is also related to component cleaning and storage (typical Rn concentrations in air give 1–100 Bq/m<sup>3</sup>), especially in systems which cannot fiducialize the active target very accurately (such as those relying only on scintillation).

For further information on purification methods, material selection and techniques for obtaining acceptable purity of the liquid the reader is referred, for example, to [5, 7, 194] and references therein. We can also refer [195, 155, 50, 196, 197] for some gas purification systems.

#### 4.4 Combined signal

When detecting either scintillation or ionization due to a particle, what is actually observed is an electrical signal which is proportional either to the number of emitted VUV photons,  $S1 \propto N_{ph} = N_{ex} + rN_i$ , or the number of free electrons,  $S2 \propto N_e = (1 - r)N_i$ , where  $r$  is the charge recombination fraction for a given particle species, energy and electric field (note that S2 may be measured by means other than proportional scintillation). In the limit of infinite electric field, all initially created electrons escape recombination and therefore direct excitation is the sole mechanism leading to photon emission; in general,  $r > 0$ , i.e. the charge signal is smaller and the scintillation signal is larger due to recombination.

Both  $N_{ph}$  and  $N_e$  are subject to statistical fluctuation — however, not independently. They are constrained by the total energy transferred to the medium by the particle, as indicated by equation (4.1) in the case of electrons. Therefore, fluctuations of a linear combination of S1 and S2 with suitably chosen coefficients are expected to be much smaller than fluctuations of each of the two signals separately. The idea of using the combined signals to form an improved energy estimator was originally proposed in [112] but it was not sufficiently appreciated at the time and was implemented only much later [198]. Presently, LXe dark matter experiments use a combined signal mostly to characterize detector performance and electron backgrounds, exploiting the improved linearity and energy resolution thus made possible.

It has been proposed in [108] that the best estimator for the energy of an electron recoil event can be obtained by recognizing that  $N_i + N_{ex} = N_{ph} + N_e$  for any value of  $r$ . Making this re-



placement in the definition of  $W_s^{min} = E_0/(N_i + N_{ex})$  leads to the recombination-independent sum  $E_0 = (N_{ph} + N_e) \cdot W_s^{min}$ . Note that  $W_s^{min}$  corresponds to the ‘flat top’ response in Figure 11 on page 23, i.e when complete recombination occurs at zero field (see also [73]); it can be measured from fixed energy interactions (e.g.  $^{57}\text{Co}$   $\gamma$ -rays) by varying the electric field applied to the liquid, which effectively scans through  $N_{ph}$  and  $N_e$  whilst keeping their sum constant (see Table 1 for  $W_s^{min}$  values).

As for the energy resolution, we recall that the observables S1 and S2 are proportional — but not identical — to  $N_{ph}$  and  $N_e$ , respectively; the number of quanta actually detected can be substantially lower than the number released at the particle track — especially in the case of scintillation — and this implies that minimizing the variance of the combined signal may require different coefficients to those suggested by the equation for  $E_0$  above. By exploiting a combined energy estimator,  $\sigma/E \approx 3.4\%$  for 122 keV  $\gamma$ -rays [199],  $\sigma/E \approx 3\%$  for 570 keV [198] and  $\sigma/E \approx 1.7\%$  for 662 keV  $\gamma$ -rays [200] have been achieved in liquid xenon. The resolution improvement is more pronounced at high energies but still significant below 100 keV [199, 201, 202, 197]. For example, for 40 keV  $\gamma$ -rays XENON100 reported  $\sigma/E \approx 16.2\%$  when measured with the primary scintillation signal only, and  $\approx 9\%$  for the combined signal [197]. In  $\beta\beta$ -decay experiments any improvement in energy resolution is extremely important; EXO-200 uses the combined scintillation/ionization signal to achieve  $\sigma/E = 1.67\%$  at the  $Q$ -value in  $^{136}\text{Xe}$  (2,458 keV) [203].

In WIMP and CNS searches, precise reconstruction of nuclear recoil energies is even more important, but unfortunately harder to achieve at present. Currently, most double-phase experiments utilize the S1 response together with independent measurements of the relative scintillation efficiency for nuclear recoils in this reconstruction, as discussed in Section 4.2. Therefore, this ignores information encoded in the ionization response. In [74] it is argued that a combined energy scale should also be applied in this instance, but specifically to the fraction  $f_n$  of nuclear recoil energy transferred to electronic excitations (i.e. including ionization and atomic excitation, but excluding the energy lost in elastic collisions with atoms):  $E_0 = (N_{ph} + N_e) \cdot W_s^{min} / f_n$ . In that study the authors find that  $f_n$  as predicted by Lindhard’s theory is in general agreement with experimental data for LXe. More measurements with simultaneous acquisition of scintillation and ionization signals, especially reaching below 4 keV (see Figure 12), are required to consolidate this approach.

#### 4.5 Electron emission from liquid to gas

With double-phase detectors, the combination of large active detector masses with exquisite sensitivity to two response channels — at the level of single carriers in ionization and a few photons in scintillation — is bringing about a steep improvement in sensitivity for dark matter searches and may soon allow a first detection of coherent neutrino scattering. Ultimately, this is due to the possibility to extract electrons across the liquid surface. In addition to providing amplification of the ionization signal in the gas, this also allows the ionization response to be transduced into an optical signal, so that the same photon detectors can be used for both signatures. The fact that free electrons can cross, under moderate electric field, the liquid/gas boundary has been known for more than 60 years [1]. Owing to its application to particle detection, electron emission has been extensively studied for several decades (for example, [46], [204] and many others — see [9] for more references). The decisive impetus to this technique came in the last decade from the growing interest in direct detection of WIMP dark matter, which led to several programs worldwide.

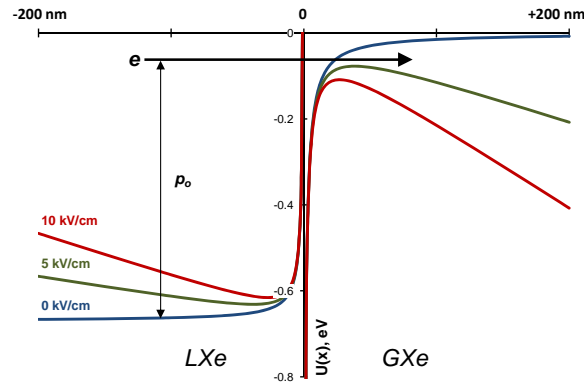


**Figure 17.** Illustration of the electron emission process in double-phase xenon; the figure shows the potential energy of excess electrons near the liquid-gas interface calculated from the model in [206], with different electric field strengths indicated for the liquid.

The potential energy of a free electron in the liquefied heavy rare gases is somewhat lower than in the gas or vacuum (by 0.2 eV in liquid argon and 0.67 eV in xenon — see  $V_0$  value in Table 3). Therefore, it is energetically advantageous for electrons to remain in the liquid phase. However, some electrons in the upper tail of the Maxwellian velocity distribution can overcome the barrier if there is even a weak electric field forcing them to approach the surface. With increasing drift field strength, the thermal equilibrium between electrons and the liquid is broken and the mean electron energy starts to increase — already at a few tens of V/cm [205]. Another effect of the external field is some reduction of the height of the potential barrier at the liquid-gas interface. The barrier is the sum of two components: the potential step of height  $V_0$  and the image potential of a charge placed above the liquid surface. The distance at which the resulting potential curve in the gas phase reaches its maximum also depends on the field strength, as illustrated in Figure 17. The maximum approaches the liquid surface with increasing field, thus reducing the probability of the electron back-scattering into the liquid (for example, at 1 kV/cm the maximum is  $\approx 60$  nm from the surface, while at 5 kV/cm it is only  $\approx 20$  nm away). Finally, under an applied field the electron velocity distribution in the liquid gains some anisotropy towards the surface, also resulting in a higher emission probability.

It is usually considered that electron emission occurs through two mechanisms: emission of ‘hot’ electrons and ‘thermal’ emission. The first mechanism refers to the case when the mean electron energy is higher than the mean thermal energy and also greater than  $V_0$ , so that a significant fraction of the electrons approaching the liquid surface has sufficient kinetic energy to overcome the potential barrier and thus pass immediately into the gas phase. Many electrons, however, do not cross the surface barrier at the first attempt. They are reflected back into the bulk of the liquid and, after a number of scatterings, return to the surface guided by the field. Again, those which do have energy above the barrier cross it, but the remainder return to the bulk and so forth. This process is similar to thermal evaporation from the tail of a Maxwell-Boltzmann distribution, hence the name ‘thermal emission’ for the second mechanism. We note, however, that the mean energy of these electrons is not necessarily equal to the thermal value.

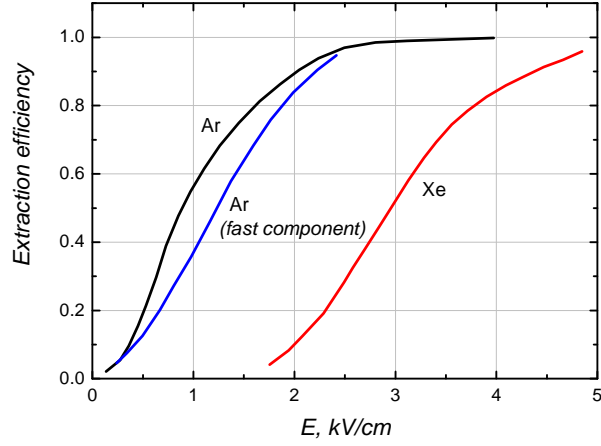


**Figure 18.** Probability of electron emission from liquid to gas as a function of electric field. Re-drawn from data in [207].

The relative contribution from these two processes depends on the  $V_0$  value (Table 3) as well as on the field strength. In liquid argon, two very distinct time constants have been observed for the emission time [207, 208, 209]: a fast component of the order of 1 ns or less and a very slow emission up to  $\sim 1$  ms at  $E \sim 100$  V/cm, the latter explained by electron trapping under the surface [208]. The time constant of the slow component depends on the field as  $1/E$  as suggested by the thermal emission model. A similar phenomenon, although less pronounced, has also been reported in liquid xenon detectors [37, 210]. In liquid xenon, the surface barrier is higher than in argon and, therefore, a lesser contribution from thermal emission is expected, and the longer emission time is limited, in practice, by electron attachment to impurities. A much higher emission threshold for xenon is also consistent with the above considerations (see Figure 18, where the emission efficiency is presented as a function of electric field).

We recommend [204, 206, 9] and references therein for additional information.

**Table 3.** Electron emission coefficients for LAr and LXe.  $V_0$  is the electron energy in the liquid relative to the vacuum level;  $E_{th}$  is the threshold field for electron emission;  $E_c$  is minimum field strength for which the mean electron energy begins to deviate from thermal;  $\langle \epsilon_{th} \rangle$  is the mean electron energy at  $E = E_{th}$ ;  $\langle \epsilon_{sat} \rangle$  is the mean electron energy at the field corresponding to saturation of the emission curve (Figure 18). Data from [142, 204, 205, 207].

	LAr	LXe
$V_0$ , eV	$-0.2 \pm 0.03$ (83 K)	$-0.67 \pm 0.05$ (161 K)
$E_{th}$ , V/cm	250	1750
$E_c$ , V/cm	$\sim 60$	$\sim 20$
$\langle \epsilon_{th} \rangle$ , eV	$\sim 0.02$	$\sim 0.3$
$\langle \epsilon_{sat} \rangle$ , eV	$\sim 0.12$	$\sim 0.4$

## 4.6 Electrons in the gas phase

Once in the gas phase, electrons can easily be accelerated by the applied electric field to sufficient energies to excite the gas atoms (and thus produce secondary scintillation, also known as electroluminescence) or even to ionize them resulting in a cascade of secondary electrons (avalanche). The latter process is widely used in gaseous detectors and has been very well studied in various gas mixtures. It allows very high amplification gains to be achieved and signals due to a single initial electron to be detected (however, not with 100% efficiency). Charge multiplication has also been tried in the gas phase of double-phase systems, but unsuccessfully. Discharging occurred already at gains of a few hundred [211] (see also [212]). As the excitation energy is lower than the ionization potential and Ar and Xe are both very efficient scintillators, plenty of photons are produced in the avalanche. Such VUV photons cause photoelectric feedback effects at cathode electrodes with high probability, resulting in secondary avalanches. Strong purity concerns and low temperature do not allow much scope for traditional solutions — such as adding quenching molecules. Nevertheless, signal amplification through electron multiplication in the gas layer of a double-phase system continues to attract interest. As has been shown recently, structures such as GEM, THGEM, LEM or similar devices may offer a promising solution for this problem. This topic is discussed in Section 5.2.

Contrary to electron multiplication, secondary scintillation does not seem to have any significant drawbacks except the need to detect VUV photons. It does not require any admixtures and is in fact most efficient in the pure rare gases. It was proven to work in medium-sized detectors in the early 1980s [213, 214] (see [9] for more references). The electroluminescence response has now been shown to provide stable operation in underground experiments over periods of  $\sim 1$  year [215, 56].

A single electron extracted from the liquid can produce hundreds of photons along its drift path. In the ZEPLIN-III configuration, for example, one electron extracted into the gas produced some 300 VUV photons, resulting in a total signal of about 30 photoelectrons at the PMT photocathodes [37] (see also Figure 6).

The mechanism of secondary scintillation is well understood and is similar in argon and xenon [216]. Atoms are initially excited by electron impact to one of the lowest excited states,  $^3P_2$ ,  $^3P_1$ ,  $^3P_0$  and  $^1P_1$  (all of these corresponding to the electronic configuration  $3p^54s^1$ ). Excitation to higher levels, namely those corresponding to the configuration  $3p^54p^1$ , is also possible but less probable. Relaxation of these states occurs through the transition  $4p \rightarrow 4s$  with emission of an infrared photon, or non-radiatively via collisions with other atoms. At low gas pressure (less than a few mbar), collisions between atoms are rare so that the excited atoms have enough time to decay to the ground state  $^1S_0$  (if the transition is not forbidden by the selection rules, as is the case of  $^3P_2$  and  $^3P_0$ , which form metastable states). The allowed transitions  $^3P_1 \rightarrow ^1S_0$  and  $^1P_1 \rightarrow ^1S_0$  occur with emission of VUV photons with wavelengths of about 107 nm and 105 nm in argon, and 147 nm and 130 nm in xenon, with a narrow spectrum. As the gas density increases, the collision frequency also increases and formation of diatomic excimers  $\text{Ar}_2^*$  or  $\text{Xe}_2^*$  in  $^3\Sigma_u^+(0_u^+)$  and  $^1\Sigma_u^+(1_u)$  becomes more probable. Therefore, a wider molecular continuum at longer wavelengths starts to appear in the emission spectra [217]. At gas pressures of 1 bar and above the atomic lines are very much suppressed so that the emission spectrum shows only the second continuum, which

corresponds to transitions from the lowest vibrational levels of the  $^3\Sigma_u^+(0_u^+)$  and  $^1\Sigma_u^+(1_u)$  states to the ground level. The observed spectrum is rather similar to that of primary scintillation in the liquid except for a small difference in the peak position and its width, especially in xenon (in argon,  $\lambda_{liq} = 129.6$  nm,  $\Delta\lambda_{liq} \approx 10$  nm,  $\lambda_{gas} = 128$  nm,  $\Delta\lambda_{gas} \approx 10$  nm; in xenon,  $\lambda_{liq} = 178.1$  nm,  $\Delta\lambda_{liq} \approx 14$  nm,  $\lambda_{gas} = 171$  nm,  $\Delta\lambda_{gas} \approx 12$  nm — data from [105] for liquids, and [218] for gases). The difference in wavelength is due to the fact that the exciton energy levels in the liquid are slightly shifted down with respect to the excimer levels in the gas.

The number of photons emitted by an electron in a uniform electric field is proportional to the drift path length. The light yield per cm is well described by a linear function of  $E/n$  [219]:

$$\frac{1}{n} \frac{dN_{ph}}{dx} = a \frac{E}{n} - b \quad [\text{photons}\cdot\text{cm}^2/\text{e}], \quad (4.8)$$

where  $E$  is the field strength (in V/cm) and  $n$  is the number of rare gas atoms per  $\text{cm}^3$  (related to the gas density  $\rho$  through  $n = N_A \rho / A$ , being  $N_A$  Avogadro's number and  $A$  the atomic number);  $a$  and  $b$  are gas-specific empirical coefficients. Secondary scintillation is a threshold process, requiring a minimum field  $E/P \approx 1.0 \pm 0.3$  kV/cm/bar at room temperature (if the temperature is different,  $P$  should be treated as the equivalent pressure at room temperature for the same gas density). In terms of number density, the threshold is  $E/n \approx (4 \pm 1) \cdot 10^{-17}$  V $\cdot\text{cm}^2/\text{atom}$ . The stated uncertainty reflects the variability of data published by different authors. A recent compilation of the coefficients  $a$  and  $b$  for xenon can be found in [220]. Despite more than 30 years of such measurements, the light yields reported by different authors differ by a factor of up to 2 even for recent data, with most lying below the values predicted theoretically [221, 222]. This can be explained by the difficulty in achieving precise absolute calibration of the photon detectors used in the measurements, accounting correctly for light reflections and non-uniformity of both light collection and photoelectric conversion efficiency across the PMT photocathode or photodiode.

The secondary scintillation light yield of xenon was found to increase with decreasing temperature. In saturated xenon gas at  $-90^\circ\text{C}$  it was measured to be a factor of 1.5 higher than at room temperature [223]. This might be attributed to the increasing probability of direct excitation of pre-formed  $\text{Xe}_2$  molecules (and probably more complex aggregates  $\text{Xe}_n$  with  $n > 2$ ), the concentration of which increases when approaching the saturation point [213].

Concerning argon, scarce data are available on secondary scintillation in this gas even at room temperature and no data exist for saturated vapor, to our knowledge. Recent measurements in argon gas at room temperature [224] show that the light yield can also be described by a linear function of  $E/n$ , as above, with coefficients  $a$  and  $b$  given in Table 4. On average, the light yield in argon is a factor of about 2 lower than in xenon.

For practical purposes, a more convenient parameterization of the light yield as a function of field strength and gas pressure is:

$$\frac{dN_{ph}}{dx} = \alpha E - \beta P - \gamma \quad [\text{photons}/(\text{e}\cdot\text{cm})], \quad (4.9)$$

with  $E$  in V/cm and  $P$  in bar. It takes into account the fact that the density of the saturated vapor is described by a linear function of pressure,  $\rho(P) = a_0 + a_1 P$ , which is a good approximation up to at least 10 bar [225]. The coefficients are shown in Table 4, and the number of photons generated by one electron over a distance of 1 cm is plotted as a function of  $E$  in Figure 19.

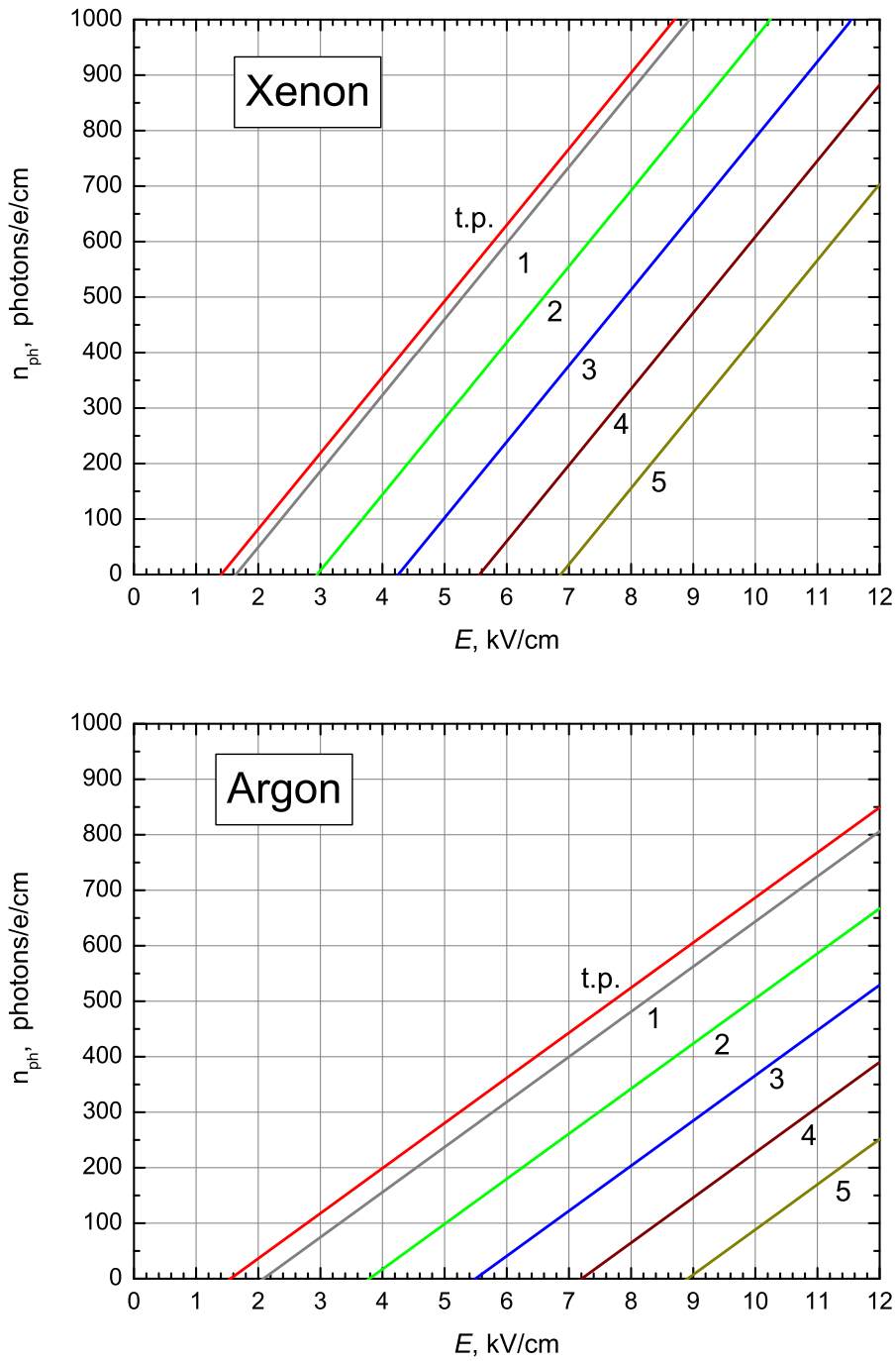


**Figure 19.** Number of secondary scintillation (electroluminescence) photons generated by an electron traveling 1 cm in saturated gas at different gas pressure (indicated next to each curve, in bar) as a function of electric field; ‘t.p.’ stands for triple point and corresponds to a pressure of 0.6889 bar for Ar and 0.8175 bar for Xe). For xenon, the data are from [223], taken in double-phase at  $T = 183$  K; for argon, data are from [224] measured at room temperature. Thermodynamic data are from [225].

**Table 4.** Secondary scintillation coefficients in equations (4.8) and (4.9);  $a$  and  $b$  are according to [224] for argon (measured at room temperature) and [223] for xenon (measured in saturated xenon vapor in a double-phase chamber). The coefficients  $\alpha$ ,  $\beta$  and  $\gamma$  are calculated by the authors with densities and pressure from [225].

	Ar	Xe
$a, \text{V}^{-1}$	0.0813	0.137
$b, \text{cm}^2$	$1.90 \times 10^{-18}$	$4.70 \times 10^{-18}$
$\alpha, \text{V}^{-1}$	0.0813	0.137
$\beta, \text{bar}^{-1} \cdot \text{cm}^{-1}$	139	177
$\gamma, \text{cm}^{-1}$	30.6	45.7

Secondary light emission in pure noble gases in the visible and near infrared regions has recently received some interest in view of advances in solid state photon detectors sensitive at these wavelengths. Published data on the light yield are scarce and not consistent, indicating, however, that it is significantly lower than in the VUV region.

For Ar at atmospheric pressure, a yield of  $\sim 3$  photons/(e·cm) was measured at  $E = 6.3$  kV/cm ( $E/n = 25 \cdot 10^{-17} \text{ V} \cdot \text{cm}^2$ ) in the range 690–1000 nm, in good agreement with calculations [226]. It should be noted that at this field there is already some electron multiplication with a gain of  $\sim 9$ . For unity gain ( $E/n < 7 \cdot 10^{-17} \text{ V} \cdot \text{cm}^2$ , i.e.  $E < 1.7$  kV/cm), the maximum light yield achieved is  $\sim 0.2$  photons/(e·cm). In a more recent study [89], values of  $\sim 60$  and  $\sim 2$  photons/(e·cm) have been reported for  $E/n = 25 \cdot 10^{-17} \text{ V} \cdot \text{cm}^2$  and  $7 \cdot 10^{-17} \text{ V} \cdot \text{cm}^2$ , respectively. The measurements were done at  $T=163$  K and  $P=0.6$  bar, i.e. in argon gas of approximately the same density as in the studies reported in [226]. For comparison, the VUV yield is  $\sim 90$  photons/(e·cm) for  $E/n = 7 \cdot 10^{-17} \text{ V} \cdot \text{cm}^2$  [224].

It was also found that the yield in the NIR region,  $1/n \cdot dN_{ph}/dx$ , as a function of  $E/n$  follows the same linear law which has been established for the VUV light through equation (4.8), but with smaller slope and about three times higher threshold of  $E/n = 6.5 \cdot 10^{-17} \text{ V} \cdot \text{cm}^2$ , i.e.  $E \approx 1.7$  kV/cm (about 570 V/cm for VUV;  $P=1$  bar). Note the proximity of the threshold to the minimum field required for electron multiplication. These facts indicate that the excitation to higher atomic states, resulting in the emission of NIR photons, becomes appreciable only near the ionization threshold.

In Xe gas, secondary scintillation in the wavelength regions 3–14  $\mu\text{m}$  [227] and 0.7–1.6  $\mu\text{m}$  [92] has been observed, but unfortunately not quantified.

## 5. State-of-the-art technologies and methods

### 5.1 Detection of the VUV light

#### 5.1.1 Photomultiplier tubes

All liquefied rare gases scintillate predominantly in the vacuum ultraviolet region. Liquid xenon has the longest wavelength of 178 nm, while argon emits at 130 nm [105] and neon at about 80 nm [228]. Xenon and argon light can be directly detected with photomultiplier tubes (PMTs) if a special entrance window transparent to the short wavelengths is used. For xenon light, a quartz window will be sufficient, while a magnesium fluoride or lithium fluoride window is required to detect the light from liquid argon. Quartz window PMTs are more expensive than ordinary tubes with borosilicate glass window, but not prohibitively so, and can be manufactured with relatively large diameter. Photomultipliers with  $\text{MgF}_2$  window are much more expensive and the window diameter is usually smaller, two inches at most. In addition, no ultra-low background PMTs have been commercialized with these windows.

Therefore, for detection of liquid argon scintillation the most common solution is to use wavelength shifting materials, which absorb VUV and re-emit the light at longer wavelength. For example, *p*-terphenyl emits mostly between 280 nm and 350 nm, diphenyloxazolyl-benzene (POPOP) shifts the light to the region 340–420 nm, diphenyloxazole (PPO) emits between 305 nm and 365 nm [229]. Tetraphenyl butadiene (TPB), which emits in the blue wavelength region from 400 to 470 nm [230, 231, 232], is a popular choice for large liquid argon detectors [233, 234]. A more complete list of wavelength shifting materials can be found in [9, p.76]. The use of a wavelength shifter in liquid xenon detectors can enhance the photon detection efficiency by  $\sim 20\%$ , but it seems that the risk of contamination of the liquid, which can lead to a substantial reduction of the electron lifetime, should not be neglected [235] (this work indeed reports that *p*-terphenyl can dissolve in liquid xenon).

When using photomultipliers for these applications, one should take into account that the electrical resistivity of the photocathode materials increases when the temperature decreases. This can lead to saturation of the photocathode under illumination and to partial or even total loss of sensitivity of the PMT due to photocathode charging. This effect is more accentuated for bialkali materials, which have the highest photocathode sheet resistance, while multialkali photocathodes are affected much less by the low temperature [236]. The critical temperature, at which a sharp drop in sensitivity of bialkali photocathodes is observed, is related to the illumination intensity and the photocathode diameter [237, 238]. For example, it was possible to operate a PMT with 25 mm photocathode diameter at photocurrents of up to 60 pA down to  $-125^\circ\text{C}$ , while for a 2-inch PMT at 6 pA photocurrent the sensitivity started to decrease sharply already at  $-100^\circ\text{C}$ . In spite of that, bialkali photomultipliers were found to be suitable for most applications using liquid xenon as a scintillator. Most photomultiplier tubes intended for low temperature applications were provided until recently with radial metal strips deposited under the photocathode and connecting the central photocathode region with the peripheral conducting ring, to which the power supply is connected (Figure 20 a). This provides a faster compensation of the charge emitted from the photocathode under illumination, so that higher irradiances can be withstood at lower temperatures without degradation of performance. For example, 2-inch PMTs R2154 from Hamamatsu



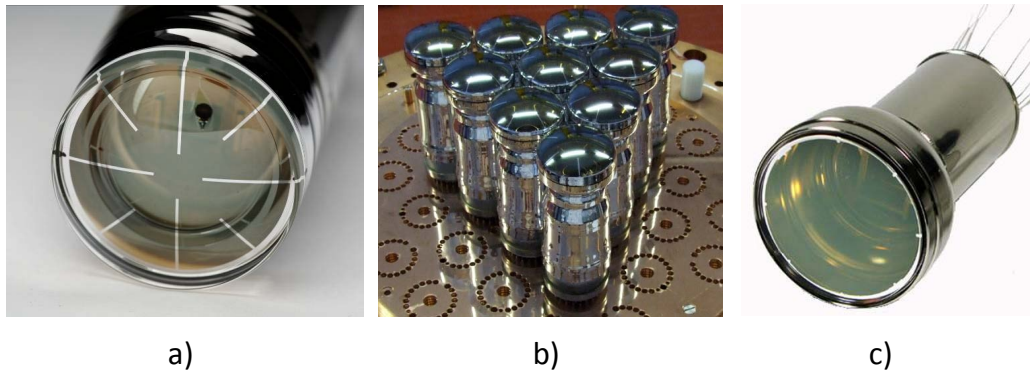


**Figure 20.** (a) Hamamatsu R7724Q-MOD tailored for LXe operation, featuring metal strips evaporated under the quartz window to compensate for the increase in resistivity of the bialkali photocathode at low temperature; (b) ETEL D766Q low background photomultipliers mounted on a stack of voltage distribution plates (courtesy ZEPLIN-III Collaboration); (c) Extremely low radioactivity 3-inch Hamamatsu R11410 (courtesy Hamamatsu Photonics).

Photonics with metal fingers under the bialkali photocathode were successfully operated in liquid xenon [169]; it was shown in [239] that 2-inch photomultipliers with metal fingers from ETEL (model D730Q/9829QA) can withstand a photocurrent of up to  $\sim 100$  pA at LXe temperatures.

The quantum efficiency of the photocathode can also be affected by temperature, the effect being different at different wavelengths. An increase in quantum efficiency by  $\sim 10$ – $20\%$  at xenon wavelength has been observed for a batch of 35 bialkali PMTs (ETEL model D730Q/9829QA) upon cooling to  $-100^\circ\text{C}$  [239]. A similar increase by  $20\%$  had been previously noticed with a R1668 Hamamatsu photomultiplier at  $170$  nm but not at  $185$  nm, for which almost no change was observed [238]. In the same work, a much more significant variation of the radiant sensitivity at  $170$  nm, by up to a factor of 2 (also not present at  $185$  nm) was observed with a Philips XP2020Q tube. A comparable (but wavelength dependent) decrease in the overall PMT response has also been observed for other PMTs (Hamamatsu R8778, ETL D742 [240]). A recent study of the Hamamatsu R8520 1-inch PMT [241] revealed an improvement in QE of  $\sim 5$ – $11\%$  upon cooling. These results highlight the importance of calibration of the photomultiplier tubes under the exact conditions in which they will be used in real experiments.

In spite of the risk of saturation (notably with the higher photon rates required during calibration), bialkali photomultipliers are the most frequent choice in liquid xenon DM search experiments because of their high quantum efficiency and low dark noise. In most cases 1- or 2-inch tubes have been used, usually with conductive metal fingers, for operation while immersed in the liquid phase (ZEPLIN-III [239], XENON10 [242], XENON100 [197], XMASS [243], LUX350 [244]). Larger tubes (130-mm diameter ETEL D742Q) were successfully used in ZEPLIN-II [49]. These had a thin platinum underlay to reduce the effect of photocathode charging at low temperature. Unfortunately, this came at the expense of quantum efficiency (only  $17\%$  for xenon scintillation).

In liquid argon detectors, PMTs have to operate at even lower temperature ( $87$  K). An 8-inch model (ETEL 9357FLA) with platinum underlay as above was successfully used to detect liquid argon scintillation [233]. With a TPB wavelength shifter on the PMT glass window, a quantum

efficiency of  $\sim 20\%$  for liquid argon scintillation light has been reported; a batch of 54 such tubes has been tested with visible light at 77 K in [245]. No dramatic changes were detected for most PMTs. Compared to room temperature, a gain drop was observed at 77 K, varying from sample to sample in the range from 15% up to a factor of 5. It was possible to compensate the gain loss by increasing the anode voltages by  $\approx 100$  V. A 2- to 3-fold increase of the dark count rate was also observed, which led to some deterioration of the peak-to-valley ratio in the single electron response. The transit time jitter was measured to be twice shorter at 77 K than at room temperature; the sensitivity decrease was 20% at 470 nm; good linearity was found up to 300 photoelectrons per 50 ns pulse at 10 kHz repetition rate (corresponding to 4.8 pA average and 1 nA peak photocurrent) both at room and low temperatures.

A similar 8-inch tube with bialkali photocathode and platinum underlay from Hamamatsu Photonics, model R5912-MOD02, was used in contact with liquid argon [54]. This tube was also tested down to 29 K to investigate its applicability to detect liquid neon scintillation [246]. A sharp loss of gain from  $\sim 10^9$  to  $\sim 10^7$  was observed near 75 K followed by some recovery at lower temperatures. Mechanical deformations in the dynode system were suggested as the most likely reason for the gain variations. In the same test, the relative photon detection efficiency (photocathode quantum efficiency times photoelectron collection efficiency to the first dynode) decreased by only 25% and at a higher temperature — about 100 K. The dark count rate initially decreased down to 250 K, then rose gradually with further cooling and eventually reached a 3-fold increase relative to the value measured at room temperature.

A 3-inch diameter ETL D747/9361 FLB photomultiplier tube was used successfully to detect scintillation from liquid neon although the tube was kept at about 155 K in this experiment [84].

Recently, a special type of bialkali photocathode has been developed for low temperature applications [247]. It is characterized by a lower sheet resistance, obviating the need for metal strips or platinum backing of the sensitive layer. A more recent version of the 2-inch Hamamatsu R7724Q-MOD is an example designed for operation at LXe temperatures with quantum efficiency of  $\approx 25\%$  at 178 nm. The 3-inch models R11065 and R11410 (shown in Figure 20 c) have been developed specifically for low background experiments with LXe and LAr [248, 249, 250].

Another important achievement is the development of new ‘superbialkali’ photocathodes with significantly enhanced quantum efficiency by Photonis and Hamamatsu [247]. This progress was achieved by using extremely pure photocathode materials and process tuning. Hamamatsu quotes a typical value of 43% at 350 nm for Ultrabialkali (UBA) and 35% for Superbialkali (SBA) phototubes [248]. A peak value of 55% is advertised by Photonis [251]. At the time of writing, there was no information available on the quantum efficiency of these photocathodes below 200 nm. Operation at low temperature is also not guaranteed due to high sheet resistance. Deposition of a metal pattern, as for normal bialkali photocathodes, might help extend the range to LXe temperature.

Good definition of the single photoelectron signal is also an important requirement for reliable detection of faint luminous signals. For a good photomultiplier, the spectrum of anode pulses due to single photoelectrons emitted from the photocathode should present a well defined peak, separated from the exponential noise with a peak-to-valley ratio of about 2 or higher. As an example we present the single electron spectrum measured with a 2-inch R7724Q-MOD tube (Figure 21 a). A technique for *in-situ* calibration of single photoelectron responses in photomultiplier arrays under exact data conditions is described in [252].

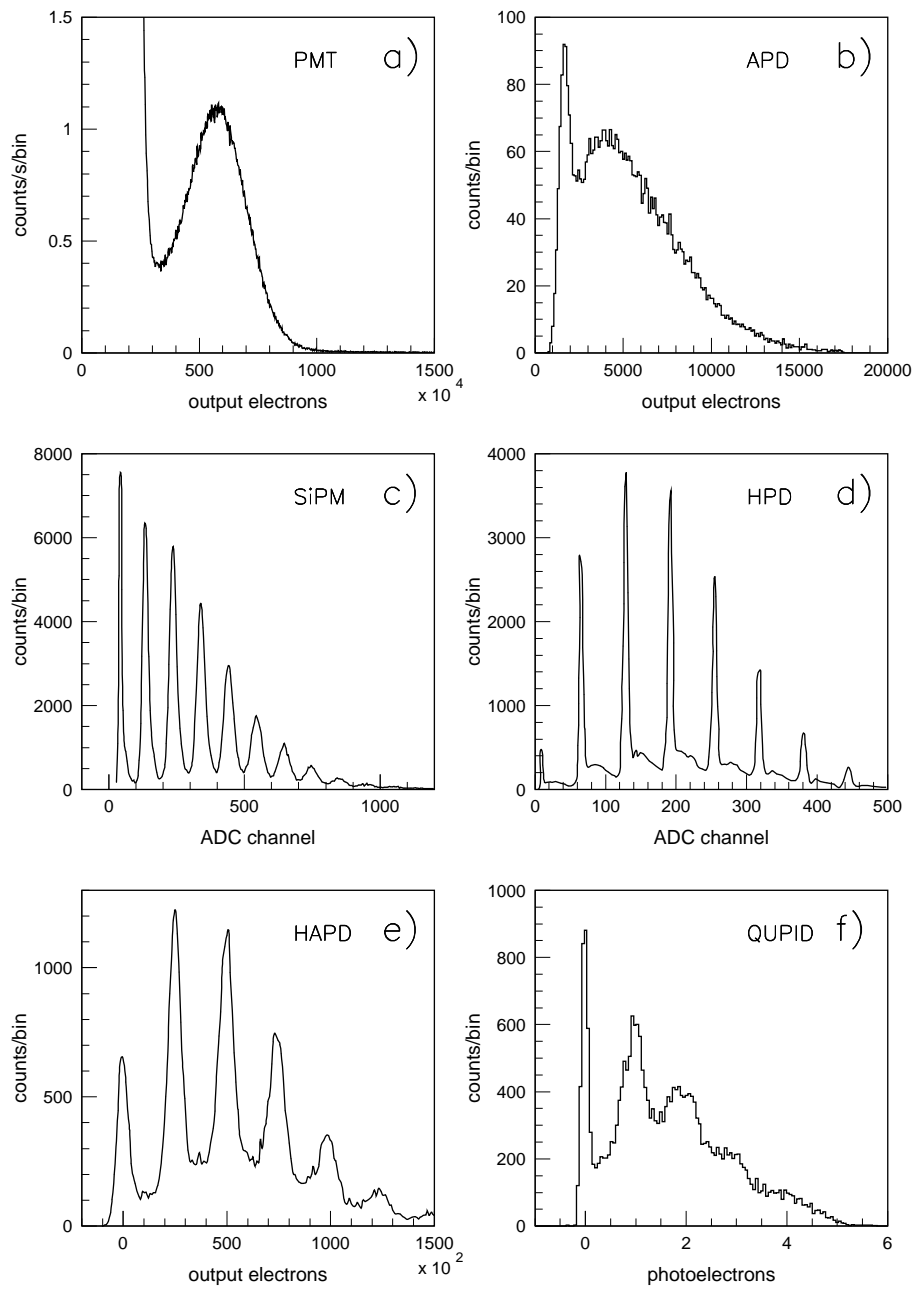


**Figure 21.** Low signal response of several photon detectors discussed in the text: (a) Single photoelectron response (dark counts) measured with a 2-inch Hamamatsu R7724Q-MOD photomultiplier with quartz window and Al fingers under a bialkali photocathode (courtesy V. Solovov and L. de Viveiros); (b) Response of a 5-mm diameter LAAPD from Advanced Photonix to faint light pulses generating a mean of 4.3 electron-hole pairs after pedestal subtraction (adapted from [253]; with permission from Elsevier); (c)  $1 \times 1 \text{ mm}^2$  SiPM, Hamamatsu S10362-11-100U (courtesy F. Neves) (d) HPD from Delft Electronic Products, PP0270K with Amptek 250 preamplifier (adapted from [254]; with permission from Elsevier); (e) 13-inch HAPD (adapted from [255]; with permission from Elsevier); (f) QUPID (adapted from [256]; with permission from Elsevier).

Radioactivity of the photomultiplier components is a key concern in low background experiments. In fact, PMTs can dominate the total radioactivity of a detector. For a model with glass envelope, the emission rate of  $^{40}\text{K}$   $\gamma$ -rays can be quite significant (up to  $\sim 10$  Bq per device for normal glass [257]). Trace amounts of radioisotopes from the U/Th decay chains contribute to both  $\gamma$ -ray and neutron background (the latter through  $(\alpha, n)$  reactions and spontaneous fission of  $^{238}\text{U}$ ). Quartz has  $\sim 10^4$  lower content of  $^{40}\text{K}$  and  $\sim 10^2$  less  $^{232}\text{Th}$  and  $^{238}\text{U}$  than normal glass, and so PMTs with quartz window are preferable from this point of view, too. An all-quartz envelope would be ideal, but practically unattainable due to difficulties in welding the contact pins. A significant effort is being made by manufacturers and research teams to reduce the background from photomultiplier tubes by rigorous choice of the raw materials used for all components. For example,  $\sim 10^3$   $\gamma$ -rays/day and  $\sim 10^{-3}$  neutrons/day have been achieved in the 2-inch Hamamatsu R8778 [258, 259], and a factor of  $\sim 3$  higher for the ETEL D766Q [202] (shown in Figure 20 b). A significant further reduction of radioactive backgrounds has been reported recently: a prototype of a 3-inch R11410-MOD, developed by Hamamatsu, exhibits 24 times lower content of  $^{238}\text{U}$ , 9 times less  $^{232}\text{Th}$  and 8 times less  $^{40}\text{K}$  per PMT when compared with the R8778; this would result in a reduction of PMT-induced nuclear recoil background by a factor of 36 in the LUX350 experiment, adding to a further reduction of electron recoil background [249].

Traces of radioactive nuclei are encountered also in the metal and ceramic parts of the electron multiplication system. A typical 2-inch photomultiplier contains about 70 g of glass, 20 g of metal and 10 g of ceramic [257]. Hybrid photomultiplier vacuum tubes, which do not use dynode structures for amplification and in which the variety (and total mass) of the required materials can be significantly reduced, are an attractive solution. In this type of device, photoelectrons emerging from the photocathode are accelerated in a strong electric field up to energies of 10 to 20 keV and focused onto a silicon detector. As silicon is virtually free of radioactivity and the mass of the photodiode can be very small, the background from the inner part of the tube can be significantly reduced (by a factor of  $\sim 100$  according to [260]). In addition, all non-metal parts can be made of quartz. We shall discuss some hybrid devices in Section 5.1.4.

The exciting and fast-paced history of recent developments in photon detectors, including vacuum-based, solid-state and their combinations, can be found in the review articles [261, 262, 251, 263].

### 5.1.2 Large area avalanche photodiodes

Silicon photodiodes with intrinsic amplification are an attractive alternative to photomultiplier tubes. Their great advantage is much lower intrinsic radioactive background and smaller mass. Moreover, higher quantum efficiency than can be achieved with PMTs is possible, especially in the VUV wavelength region. Among the disadvantages one should mention lower amplification gain, higher noise, and high cost per unit area. At present, two types of silicon photodiode with amplification are being considered as possible candidates to replace photomultiplier tubes: Large Area Avalanche Photodiodes (LAAPD) operating in proportional mode, and multipixel devices operating in Geiger mode; the latter are frequently called Silicon Photomultipliers (SiPM) or Multi-Pixel Photon Counters (MPPC).

A comprehensive review on advances in solid state photon detectors has been published recently [263]. We therefore refer the reader to this work for detailed information on the subject and

will consider here only some of the aspects that seem to us to be the most relevant for applications in liquefied rare gas detectors.

In a silicon avalanche photodiode, photons are absorbed in an intrinsic (undoped) absorption region which is sandwiched between a metal contact and a  $p-n$  junction. A reverse-bias voltage of  $\sim 0.2-2$  kV is applied to the photodiode thus creating a field of  $>10^5$  V/cm across the depletion region near the junction. Electrons drifting through this region acquire sufficient energy to produce secondary electron-hole pairs by impact ionization so that an avalanche is developed and thus the initial photocurrent is amplified. In silicon, both electrons and holes can produce secondary ionization.

The multiplication gain is a very steep function of the applied voltage, and dependent also on temperature. Typically, gains  $\sim 100-1000$  are achieved at room temperature, being limited by breakdown. At low temperature, higher gains can be achieved: values of  $4 \cdot 10^3$  at 193 K [253] and even  $\sim 2 \cdot 10^4$  at 40 K [264] have been reported in the literature (the APD models were different in these works). The practical gain is, however, limited by noise, which also increases with the applied voltage.

In avalanche devices noise has two components of distinct nature. One is due to dark current fluctuations, while the other results from the statistics of the multiplication process. The dark current increases with voltage (i.e. with gain) but, on the other hand, it depends strongly on temperature. For example, a reduction by almost a factor of  $10^5$  was observed with a 5 mm diameter LAAPD from Advanced Photonix (API) [265] when cooled from room temperature down to  $-100^\circ\text{C}$  [266]. At this temperature, corresponding to the typical operation point of liquid xenon detectors, the dark current was less than 1 pA, while in normal conditions it was measured to be of the order of tens of nA. The electronic noise was found to be practically independent of gain for  $T < -40^\circ\text{C}$  and gains  $>5$  [253], thus indicating that fluctuations of the dark current do not contribute significantly in these regimes.

The random nature of the multiplication process results in additional fluctuations of the output signal of avalanche devices, which is characterized by the excess noise factor  $F = \langle m^2 \rangle / M^2$ , where  $m$  is the stochastic multiplication gain and  $M = \langle m \rangle$  is its mean value. For gains  $M \gg 1$ , the excess noise factor is approximately linear with gain and therefore at high gains and low temperature the noise is determined by gain fluctuations.

Several models of avalanche photodiode have been investigated as candidates for detection of scintillation signals in liquefied rare gases. LAAPDs from API with 5 mm and 16 mm diameter active areas were found to perform very well whilst immersed into liquid xenon [267, 268]. Scintillation signals from 5 MeV  $\alpha$ -particles and conversion electrons were successfully detected with energy resolution comparable to that measured with photomultiplier tubes. The quantum efficiency for xenon scintillation light was found to be  $>100\%$  [267], suggesting a non-negligible contribution from multiple electron-hole pair production by a single VUV photon (each photon carries  $\approx 7$  eV, while the Si band gap is 1.12 eV). The authors are not aware of any published results on quantum efficiency for argon scintillation light; however, efforts are ongoing to extend the sensitivity to shorter wavelengths. In liquid xenon, a maximum gain of  $\sim 1000$  was obtained with API devices [267], above which degradation of the energy resolution due to excess noise became noticeable. A gain of  $\sim 10^4$  has been reported [269, 270] for  $13 \times 13$  mm<sup>2</sup> LAAPDs from Radiation Monitoring Devices [271]. In all instances the photodiodes were directly immersed into the LXe.

The same model from RMD was tested from 77 K down to liquid helium temperature [264]. A similar tendency of gain-voltage dependence was observed — the lower the temperature, the steeper the dependence becomes, and the lower the breakdown voltage. Between 77 K down to 40 K multiplication gains up to  $\sim 2 \cdot 10^4$  were obtained. However, with further cooling breakdown appears at a bias voltage of only 500 V, even before appreciable amplification sets in. Moreover, an abrupt degradation of quantum efficiency to about 15% of that at room temperature was observed between 50 K and 35 K. These measurements were carried out with a red LED.

In contrast to photomultiplier tubes, avalanche photodiodes do not present a well defined single photoelectron peak — signal amplitudes due to a single electron-hole pair have nearly exponential distribution Figure 21 b). The reason resides in the multiplication process, different for a photodiode and a PMT (quasi continuous with gain of 2 at each step for the APD, versus a discrete process with gain of 5–10 at each dynode in the case of a PMT). This makes detection of single photons, a strong requirement for DM searches and CNS experiments, more problematic as it becomes more difficult to discriminate electronic and other exponential like noise without losing a significant fraction of the single photon signals. Yet, good discrimination seems possible given the fact that the quantum efficiency of the photodiode can be as high as  $\sim 100\%$  (for xenon light at least). This can allow setting rather high a discrimination threshold so that even if 2/3 of the single photon signals are below threshold, the remaining 1/3 would provide the same single photon detection efficiency as with a PMT with good single electron spectrum and  $\sim 30\%$  photocathode quantum efficiency [272] (equal sensitive areas are assumed).

The first large-scale application of these devices was in the EXO-200  $\beta\beta$ -decay experiment, which features Advanced Photonix LAAPDs (model SD630-70-75-500) used as bare dies, without the standard ceramic encapsulation; these experiments require also extremely low background levels and excellent energy resolution around the  $Q$ -value for  $^{136}\text{Xe}$  (2,458 keV), but not as low a scintillation threshold; 468 such devices operate submerged in the LXe to readout the scintillation light from a chamber with 110 kg active mass [273].

### 5.1.3 Silicon photomultipliers

An excellent single photoelectron response can be obtained with silicon photodiodes operated in the Geiger mode Figure 21 c). The voltage applied across the depleted region in these devices is set above the breakdown limit so that a single electron or hole entering the multiplication region can initiate a breakdown, similarly to what happens in a conventional gaseous Geiger counter. Thus, a large pulse of fixed amplitude determined by the stored charge is produced. A built-in resistor limits the restoration current so that the voltage drops rapidly below the multiplication threshold and the discharge ceases. In this mode, two or more electrons at the beginning of the multiplication region would produce signals of the same amplitude as a single electron, typically yielding  $10^4$  to  $10^6$  electrons. The solution for obtaining proportionality between the output signal and the number of photons is to pixellate the device and make each pixel work as an independent counter [274]. Then, the number of detected photons is simply proportional to the number of pixels which present signals or, more conveniently, to the amplitude of the sum signal over all pixels.

In silicon, the photon attenuation length is  $>100$  nm in the visible region for  $\lambda \gtrsim 400$  nm, but it drops abruptly for shorter wavelengths, being only  $\sim 6$  nm in the region of  $\lambda$  between 300 nm to 150 nm (Figure 22). For a conventional  $n^+/p/p^+$  structure (in the sequence encountered by

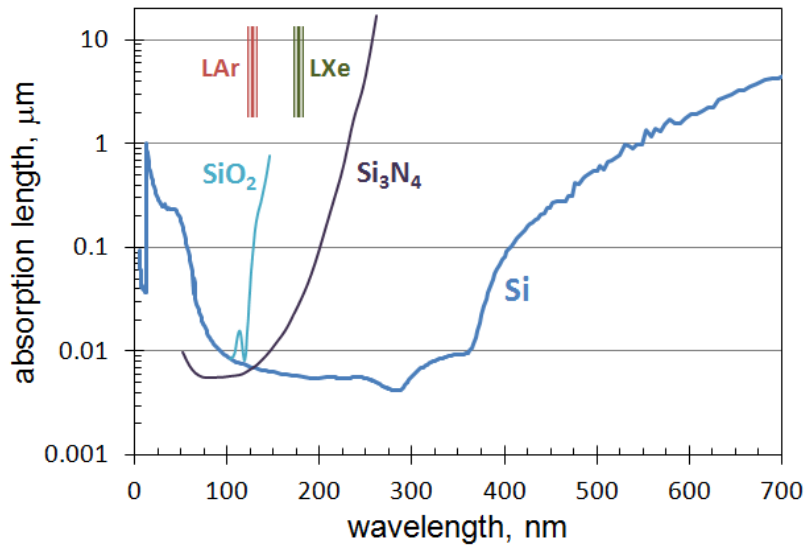


**Figure 22.** Absorption length in bulk silicon and its thermal oxide and nitride, which are typical device passivation materials (note that other native silicon oxides, with different absorption spectra, can also form). Calculated with extinction coefficients from [275] and [276].

incident photons), the short wavelength photons are absorbed at the very front of the undepleted  $n^+$  region, which has typically a thickness of  $\sim 100$  nm and where recombination is quite strong [277]. This is one of the main reasons for the low quantum efficiency of these devices for short wavelengths. Photon absorption in the native  $\text{SiO}_2$  and protective  $\text{Si}_3\text{N}_4$  layers frequently used in these devices is also critical, especially for argon light.

The SiPM is a pixel device and, therefore, some dead space between pixels is necessary to obtain electrical and optical isolation (the latter is to avoid optical cross-talk induced by photons generated during the multiplication process). Although the quantum efficiency of each individual pixel, i.e. the probability of conversion of a photon into an electron-hole pair, can be as high as 50% to 80% in the visible wavelength region, from a practical point of view a more relevant quantity is the photon detection efficiency (PDE), defined as  $\eta_{\text{SiPM}} = Q \cdot F \cdot \epsilon_d$ , where  $Q$  is the quantum efficiency,  $F$  is the so called ‘fill factor’ (the ratio of the sensitive area to total area) and  $\epsilon_d$  is the probability for a charge carrier to trigger an avalanche. For example, Hamamatsu Photonics quotes fill factors of 0.3–0.8 for different models [278] depending on the pixel size (generally higher for larger pixels).

The probability to initiate an avalanche depends on the wavelength (and on the applied voltage, naturally) and is different for electrons and holes. For holes,  $\epsilon_d$  is about half of that for electrons [277, 279] and here is another factor affecting the sensitivity in the short wavelength region. Visible photons are absorbed predominantly in the wide absorption region of intrinsic silicon or lowly doped  $p$ -type material, which sits beyond the multiplication region, and the avalanche is triggered by an electron upon reaching the depletion region (traveling backwards relative to the photon); in this instance  $\epsilon_d$  approaches unity at sufficiently high voltage. On the other hand, short wavelength photons are absorbed at short distances from the surface. The electron drifts away from the junction and does not reach the multiplication region at all. The avalanche can still develop trig-

gered by the hole (if it does not recombine instead of entering the multiplication region) but with a lower probability.

For visible light, a photon detection efficiency of up to  $\eta_{\text{SiPM}} \sim 0.6$  can be achieved. This should be compared with the corresponding value for a photomultiplier tube:  $\eta_{\text{PMT}} = Q \cdot \varepsilon_1$ , where  $\varepsilon_1$  is the collection efficiency of photoelectrons to first dynode, typically  $\varepsilon_1 \approx 0.7 - 0.8$ . Hence, for a good PMT ( $Q=30\%$ ) the photon detection efficiency is  $\eta_{\text{PMT}} \sim 0.20-0.25$ . This comparison shows that silicon photomultipliers have a great advantage over vacuum tubes (equal areas being assumed). At present, the area of commercially available single-crystal SiPMs is at best  $6 \times 6 \text{ mm}^2$ . Arrays of 16 SiPMs and a matrix of 16 such arrays (i.e. 256 SiPMs) became available recently [280]. The  $61 \times 61 \text{ mm}^2$  total area is already comparable to that of a conventional PMT. Hamamatsu offers arrays of  $4 \times 4$  and  $8 \times 8$  arrays of SiPMs  $3 \times 3 \text{ mm}^2$  each (models S11064 and S11834).

The low temperature performance of a  $1 \times 1 \text{ mm}^2$  SiPM from SensL [280] has been studied in [281]. It was found to perform well down to liquid nitrogen temperature at gains up to  $2 \cdot 10^6$ . Similarly to an APD operated in proportional mode, the gain at fixed voltage also depends on temperature and, therefore, a correction of the applied voltage on temperature is necessary in order to keep the gain stable. However, in contrast with an APD, where the gain is a steeper-than-exponential function of the voltage, in the Geiger mode the gain depends on the voltage linearly (because the output signal is limited by the charge stored in the cell capacitance) and, therefore, its variation with temperature is not so dramatic as for APDs. The gain was found to vary at the rate of about  $0.5\%/^\circ\text{C}$  for gains of  $M \sim 2 \cdot 10^6$ . As liquefied gas detectors require temperature stabilization with precision much better than  $\pm 1^\circ\text{C}$  anyway, the gain stability should not be a serious issue during operation of the detector, although a gain monitoring system and, probably, a temperature compensation circuit might be desirable. To compare, a regular APD operating at  $M = 100$  exhibited a gain temperature coefficient of  $\approx 4\%$  per  $^\circ\text{C}$ , while for  $M = 1000$  this rose to as much as  $15\%$  per  $^\circ\text{C}$  [272]. Therefore, APDs require much more tight temperature control and a gain stabilization mechanism becomes indispensable.

The dark noise count rate of a SiPM at room temperature is very high and very sensitive to the bias voltage. For example, values of  $10^6 \text{ Hz}$  and  $10^5 \text{ Hz}$  were measured with  $1 \times 1 \text{ mm}^2$  devices from SensL and Hamamatsu [281, 282]. Cooling results in a significant reduction of the dark noise: by reducing the temperature down to  $-100^\circ\text{C}$  the noise counts were suppressed by a factor of  $\sim 1000$  in [281] and, for the other model, to a level of  $\sim 1 \text{ Hz}$  [282]. The effect of further cooling was found to be much less significant [281]: cooling down from  $-100^\circ\text{C}$  to  $-200^\circ\text{C}$  gives another factor of  $\sim 10$  only.

Silicon photomultipliers from other manufacturers have also been tested at low temperature. A  $2 \times 2 \text{ mm}^2$  G-APD (Geiger APD, according to the manufacturer's terminology) CPTA model 149-35 (Russia) was successfully operated in liquid argon [283]; a  $1 \times 1 \text{ mm}^2$  SiPM from FBK-IRST (Italy) was found to perform well down to approximately  $-150^\circ\text{C}$  [284].

The sensitivity of silicon photomultipliers in the VUV wavelength region has been questioned, with existing results being contradictory. According to the manufacturers, there should be no significant sensitivity below  $\approx 400 \text{ nm}$  or  $\approx 300 \text{ nm}$  depending on the structure ( $n^+/p/\pi/p^{++}$  or  $p^+/n/v/n^{++}$ , respectively); this is largely related to the photon absorption depth argument laid out above. Nevertheless, a number of attempts to detect xenon light have been made.



One of the earliest versions of silicon photomultiplier from Pulsar (Russia) has been tested in liquid xenon to detect primary scintillation light from  $\alpha$ -particles [285]. A quantum efficiency of 22% and a photon detection efficiency of  $\sim 5.5\%$  due to a poor fill factor has been estimated for the xenon wavelength.

Three different models from Russian companies MEPhi/Pulsar and CPTA have been tested with light emitted by gaseous and liquid xenon under  $\alpha$ -particles. A photon detection efficiency of  $< 1\%$  has been reported [286]. A windowless version of a  $3 \times 3 \text{ mm}^2$  MPPC from Hamamatsu was tested with a VUV light source and a narrow 175 nm optical filter in [282]. A total PDE of  $\approx 2.0\%$  has been measured against a calibrated photomultiplier tube, which gives a quantum efficiency of  $\approx 2.6\%$  taking into account the fill factor of 78.5%. The PDE obtained with the VUV light source agreed well with that measured in liquid xenon excited by  $\alpha$ -particles. The MPPC was immersed into the liquid in these measurements [282].

A serious issue with SiPMs is afterpulsing due to release of the charges trapped in the high field region during avalanche development. The probability for an afterpulse to occur can be as high as 20% and can depend on temperature. For example, for FBK-IRST SiPMs the afterpulsing probability was observed to be constant from room temperature down to 120 K but increased by a factor of 8 with further cooling down to 70 K [284]. An active quenching circuit, which reduces temporarily the bias voltage shortly after the main pulse, can help mitigate this problem. At the same time, the manufacturing process also seems to be evolving to reduce this drawback.

#### 5.1.4 Hybrid devices

A combination of a vacuum phototube with a silicon device acting as a photoelectron detector can bring significant advantages from the point of view of radioactive background from the photon detector, as already mentioned in Section 5.1.1. The light sensitive part of this type of device is a semitransparent photocathode deposited onto a quartz window, just like in a conventional photomultiplier tube (and hence the same variety of photocathode and window dimensions can be used). Photoelectrons emitted from the photocathode are accelerated (in vacuum) in a strong electric field, which focuses them onto the silicon detector. Under 10 to 20 kV accelerating voltage each photoelectron creates several thousand electron-hole pairs in Si, thus providing a gain of  $\sim 10^3$  [287]. These devices are commonly known as Hybrid Photon Detectors (HPD).

The gain is not high and requires additional amplification, but with a good low noise external preamplifier a very good spectrum for low intensity light pulses can be obtained and individual photoelectrons can be clearly distinguished [288, 254]. It should be pointed out that the amplification mechanism in HPDs is based on energy dissipation by an accelerated photoelectron in the anode rather than on a sequential multiplication of electrons with a gain of 4–6 at each step as in photomultiplier tubes, thus reducing significantly the statistical fluctuations. An example of such spectrum is shown in Figure 21 d.

Obviating the need for a resistive chain required for operation of conventional PMTs is also an advantage, but the high voltage required to bias an HPD is a clear drawback (although no significant current is consumed). Several HPD models with windows up to 72 mm diameter have been developed commercially, e.g. by Photonis [289], including the multi-pixel model developed for the LHCb experiment [290].

Clearly, a higher gain would bring a significant advantage to this hybrid solution. This became possible with the development of avalanche diodes. Using one of these devices instead of a silicon diode adds another factor of  $\sim 300$  to the total gain, thus raising it to  $\sim 10^5$ . A 13-inch HAPD (Hybrid Avalanche Photo-Detector) based on that principle has been developed by several Japanese institutes together with Hamamatsu for use in large Cherenkov detectors for neutrino experiments [255]. It features good timing resolution, photocathode uniformity and excellent single electron response (Figure 21 e).

A collaborative effort between UCLA and Hamamatsu has been developing a dedicated hybrid photosensor for dark matter experiments with special requirements of low radioactivity content, capability to operate at liquid xenon temperature, high quantum efficiency and good single electron response. This device is known as the ‘QUPID’ — Quartz Photon Intensifying Detector [260, 291, 256]. The QUPID is made of a quartz tube of 71 mm diameter with a hemispherical photocathode window (Figure 23). The photocathode is kept at  $-6$  kV while the APD is at ground potential. The sealing between the different parts is made by indium bonding. The version described in [256] uses a special low temperature bialkali photocathode, which does not require metal strips or an underlay to reduce the resistance, although previous versions were provided with metal fingers under normal bialkali photocathodes. A quantum efficiency of  $(34\pm 2)\%$  has been measured for xenon light at room temperature for several samples. The QUPID has also been tested in liquid xenon at  $-100^\circ\text{C}$  and 1.6 bar being fully immersed into the liquid. The liquid xenon scintillation signals from 122 keV  $\gamma$ -rays and  $\alpha$ -particles were recorded [256]. Tests at even lower temperature described in [291] have confirmed that the QUPID can operate down to  $-175^\circ\text{C}$ . An example of an amplitude spectrum measured with weak light pulses, showing that single photoelectrons are clearly resolved, is shown in Figure 21 f.

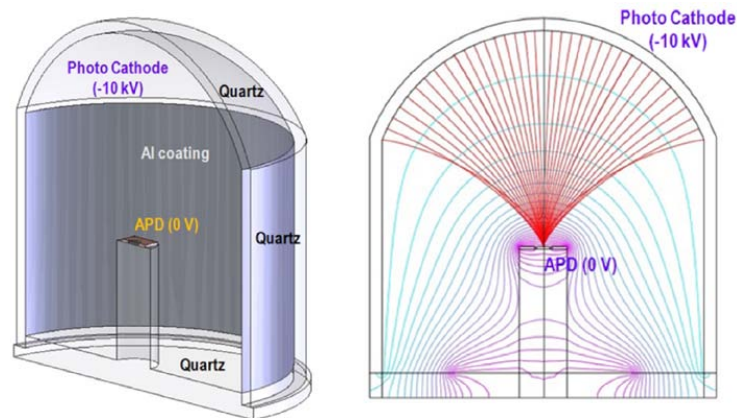


**Figure 23.** The Quartz Photon Intensifying Detector (QUPID) developed by a collaboration of the University of California, Los Angeles and Hamamatsu. (Courtesy K. Arisaka.)

## 5.2 Alternative techniques for light and charge signal detection

### 5.2.1 Electron multiplication with micro-pattern structures

The double-phase technology, with measurement of both primary scintillation in the liquid and secondary scintillation in the gas phase with photomultiplier tubes, has proven to be reliable and capable of providing high nuclear/electron recoil discrimination capability down to keV energies. Nevertheless, significant effort is being put into development of alternative read-out configurations aiming ultimately at reducing the cost of instrumenting very large underground detectors, keeping low radioactive background associated with the readout system as well as providing spatial resolution of  $\sim 1$  mm, which is important for target fiducialization and multi-vertex resolution (in dark matter searches) or for full track reconstruction (for high energy neutrino experiments). This effort is taking the following directions: a) attempting to measure the ionization signal in the gas phase through electron multiplication; b) developing new, low mass photon detectors for VUV light, other than photodiodes, capable of substituting expensive photomultiplier tubes (silicon photodiodes, discussed in the previous section, cannot be considered as a cost effective alternative, at the time of writing at least); c) combining a micro-pattern device with an array of SiPMs (or other photon detectors) to enhance the secondary scintillation signal (in double- or single-phase configuration); and d) search for single phase solutions whilst retaining the concept of measuring two signals for each interaction.

Most existing and planned experiments aiming at WIMP search with liquid noble gas detectors rely on detection of the two signals — primary scintillation and ionization charge. The ionization signal can, in principle, be measured in several ways, with secondary scintillation in the gas phase being one but not the only option. An alternative can be amplification of the ionization charge extracted from the liquid through the avalanche process. In this respect, much of the attention is turned to micro-pattern avalanche detectors of various kinds, such as GEM and GEM-like detectors and Micromegas (GEM stands for Gaseous Electron Multiplier and Micromegas for MICROMEsh Gaseous Structure). One should note that efficient detection of a single electron extracted from a nuclear recoil track is very desirable for sensitivity to a light WIMP scenario and is probably indispensable for detection of coherent neutrino scattering. Existing double-phase xenon DM detectors have already proven the capability to measure single electrons emitted from the liquid [64, 37], with very good signal-to-noise ratio (see Figure 6), and this sets the bar to judge any alternatives.

Two main problems are associated with operation of an avalanche device in a pure double-phase medium: strong VUV photon emission results in positive feedback and thus leads to early onset of discharging; and high gas density, which affects the maximum achievable multiplication gain. In the gaseous avalanche detectors the first problem is usually mitigated by adding a small concentration of quenching molecules (at percent level), which suppress VUV emission through excitation relaxation (also through the Penning effect in some cases). However, this does not appear viable in the double-phase detectors (at least from our present understanding) due to the strong purity concern and constraints on the quencher choice imposed by low temperature. As for the second concern, the lowest saturated gas density achievable in a liquid/gas system (at the triple point) is higher than that at NTP conditions by a factor of 1.5 for xenon and 2.5 for argon. At more convenient vapor pressures, say 1.5 bar, the equivalent gas densities correspond to 2.7 bar and 5.1 bar for Xe and Ar at room temperature, respectively [225]. Solid/gas detectors would allow

operation at much lower equilibrium pressures, but more significant challenges arise in growing crystals with the required quality in very large detectors.

The GEM structure and details on its design and operation are thoroughly described in the literature, e.g. [292]. Essentially, it is a two-electrode system formed by two copper layers on either side of a thin ( $\sim 50 \mu\text{m}$ ) dielectric foil with thousands of fine through-holes across the whole structure ( $\sim 50 \mu\text{m}$  diameter, at  $\sim 150 \mu\text{m}$  pitch). A significant advantage of this approach is the possibility of stacking several devices to achieve higher gains.

The maximum attainable gain in pure noble gases is, in general, lower than in gases with quenchers [293] and decreases rapidly with the gas pressure [294, 295] (see Figure 24). At several bar the advantage of using a triple-GEM structure against a single GEM becomes less important as the difference between the maximum attainable gains becomes smaller. For xenon above 4 bar the single GEM configuration is even better than the cascade of three GEMs (although gains are very low). The effect was explained by the authors in terms of a more significant contribution from the positive ion backflow to the secondary electron emission in a cascaded structure [296]. Better performance at high pressures was found by combining a GEM with microstrip electrodes etched on its back surface, so that the electron multiplication occurs in two steps — first in the GEM holes and then near the anode strips [297].

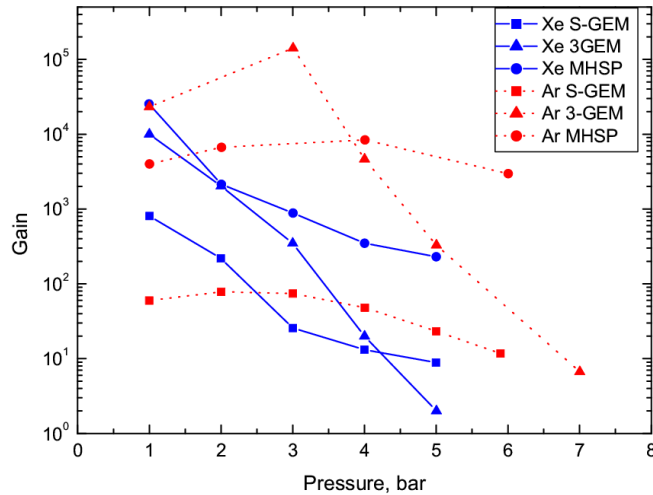


**Figure 24.** Maximum effective gain (i.e. measured at an external collector) as a function of gas pressure for a single GEM (S-GEM) [295], a cascade of 3 GEMs (3-GEM) [294] and a micro-hole strip plate (MHSP) [297]. (Adapted from [295]; with permission from Elsevier.)

Operation of a triple-GEM combination in the gas phase of a double-phase detector was studied in [300, 301, 302] (see also references therein and a recent review article [303]). It was found that significantly higher maximum gain can be achieved in argon than in xenon:  $G_{max} \approx 3000$  as opposed to  $G_{max} \approx 200$ , respectively [300]. Subsequently, the same authors achieved gains of up to  $10^4$  in argon with an improved setup [302]. Figure 25 shows data for both media. A similar maximum gain,  $G_{max} \approx 150$ , was measured with a single GEM in high purity xenon [299] at the same gas density as in [300] (at room temperature, the same density would occur at  $P_{eq} \approx 1.87$  bar).

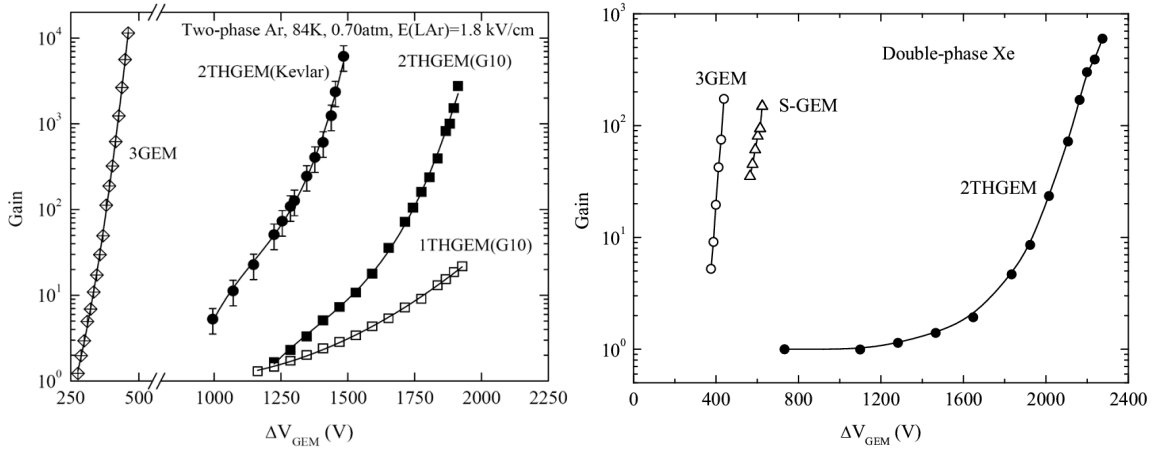


**Figure 25.** Gain as a function of voltage for triple-GEM and several configurations of THGEM. Left: in double-phase Ar (from [298]; with permission from IOP Publishing). Right: in double-phase Xe ( $T = 164$  K,  $P = 1$  bar); data for single GEM (S-GEM) from [299]; for triple-GEM (3GEM) from [300] and for a double-THGEM system (2THGEM) from [283] (with permission from IOP Publishing).

It was also observed that the liquid temperature had a significant effect on gain — higher gains could be achieved at lower temperature [304, 299], which is consistent with the vapor density considerations. An increase from 165 K to 171 K (from  $P_{eq} \approx 1.87$  bar to  $P_{eq} \approx 2.6$  bar) resulted in the decrease of  $G_{max}$  from 150 to about 25. This highlights the importance of good temperature stabilization both for avoiding discharges and for gain stability. It is worth noting that the temperature stability requirement for an avalanche device is more severe than in the case of secondary scintillation given that secondary photon production is linear with  $E/n$  ( $n$  is the number density) while the avalanche process depends on it exponentially.

The maximum gain achieved to date with these structures operating in double-phase xenon is far from sufficient for detection of single electrons extracted from the liquid. On the other hand, one would expect this to be possible in argon, where gains of  $\sim 10^4$  have been realized. Indeed, single electron signals have been observed with a triple-GEM structure [301], although with an exponential spectrum as expected from the statistics of the avalanche process, as illustrated in Figure 26. The authors estimate the probability to detect a single electron as  $\sim 50\%$ .

More robust ‘macroscopic’ versions of GEM, proposed more recently [305, 306, 307], are similar to GEM with all dimensions scaled up by a factor of 5 to 20. This device, known as LEM (Large Electron Multiplier) or THGEM (THick GEM), can be produced both by etching techniques and by purely mechanical means using precise CNC machining. Other technologies are also being explored. These devices operate at higher voltages than GEMs but are more resistant to discharges. The LEM/THGEM structures can benefit from a better confinement of the electron avalanche if channels with a smaller aspect ratio are used. This reduces photon feedback and, therefore, the probability of photon-induced discharges to occur. The extent of the multiplication region is larger than in GEMs, which is also an advantage because the same gain can be obtained at a lower field. We refer to review articles [308, 309, 310] and references therein for more detailed information on the operation and present status of these devices.

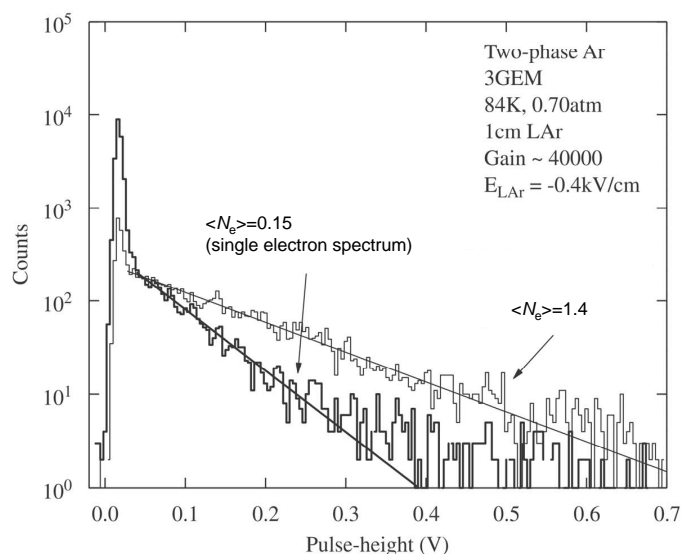


**Figure 26.** Pulse height spectra measured with triple-GEM in double-phase Ar in the few electron regime. The liquid under a reversed field ( $E_{LAr} = 0.4$  kV/cm) was irradiated with low intensity X-rays so that electrons at the input of the multiplication system are produced by photoelectric effect on the copper electrode of the lower GEM by the LAr scintillation. The authors estimate that, for each X-ray absorbed in LAr,  $\sim 0.1$  photoelectrons are produced on average. By adjusting the intensity of the X-ray tube they were able to vary the mean number of primary electrons at the entrance of the triple-GEM system ( $\langle N_e \rangle$  in the plot). The gain is  $4 \cdot 10^4$  in these measurements. (From [301]; with permission from Elsevier.)

LEM/THGEM structures have been extensively tested in various gas mixtures achieving gains of up to  $10^5$  and even  $10^6$  at low pressure [307]. They were also proven to operate in pure noble gases at room temperature and pressures of a few bar [311]. In normal conditions, maximum gains of  $\sim 4 \cdot 10^4$  were achieved with a double-THGEM system in purified Ar, Xe and Ar-Xe (95%+5%) mixtures. In xenon, the amplification gain was also measured as a function of pressure: as the pressure increased the maximum gain dropped gradually down to a few hundred for  $P = 2.9$  bar. For a single THGEM, the respective gain was generally a factor of 2 to 4 lower than for a chain of two devices. Much weaker dependence on pressure was found for the Ar+Xe Penning mixture: similar maximum gains of  $\sim 2 \cdot 10^4$  are reported both for 1 bar and for 2 bar.

Several types of THGEM were tested in double-phase argon at 84 K and  $P = 0.7$  bar and compared with a triple-GEM system [298]: THGEM with G10 as insulator, Kevlar-based THGEM and RETGEM (see next paragraph). It was observed that only the G10-based THGEM showed stable operation with a maximum gain of 200 for a single device and  $\sim 3 \cdot 10^3$  for a double-THGEM system (compare with  $10^4$  for triple-GEM). About 18% *r.m.s.* energy resolution was measured for 60 keV  $\gamma$ -rays ( $\sim 1000$  primary electrons in LAr) with the triple-GEM and the double G10-based THGEM assemblies. The two systems were shown to operate at low detection threshold of 4 and 20 primary electrons for the triple-GEM and double-THGEM, respectively, the spectra being exponential. A strong charging effect was observed for the Kevlar-based THGEM both at room temperature and in double-phase argon. The noise rates of GEM and THGEM multipliers

have also been measured in double-phase argon [298]: for a threshold corresponding to 4 primary electrons the noise rate was found to be  $\sim 0.2$  counts/s per  $\text{cm}^2$  of detector active area; a value of  $0.007$  counts/(s $\cdot\text{cm}^2$ ) was reported for a 20-electron threshold.

In a larger scale system, operation of a  $10\times 10$   $\text{cm}^2$  double-LEM structure in pure Ar gas and in the double-phase regime has been reported [312]. The LEMs, placed 3 mm apart, were 1.6 mm thick with 0.5 mm diameter holes at 0.8 mm pitch. They were operated with an electric field inside the holes of  $\sim 25$  kV/cm. A gain of  $\sim 10^3$  in the gas at normal temperature and pressure was reached, while in the double-phase system the LEMs were operated at a gain of 10 [313]. It was found that segmentation of the LEM upper electrode to obtain avalanche position significantly distorted the electric field thus leading to premature discharges. More recently, the same group reported on operation of a single unsegmented LEM in double-phase argon at an effective gain of 30 (measured at a separate electrode placed behind the LEM to which electrons are collected) [314]. The collector (termed a ‘projective readout anode’) had two sets of orthogonal strips, which allowed determination of the avalanche position. The LEM and the 2D readout system were placed above a 30 cm thick LAr layer. At the time of writing, no record of higher gains in a medium- or large-scale double-phase argon system, in which electron drift across long distances is required, could be found in the literature.

In order to increase the resilience of micro-hole structures to discharges and thus increase the maximum achievable gain, the use of resistive electrodes instead of metallic ones has been proposed [315]. Thanks to the low conductivity of the resistive electrodes, a spark leads to a rapid drop of local voltage. The discharge current is thus limited and the ability to produce damage is significantly reduced. Thick GEMs with resistive electrodes received the abbreviated name RETGEM (Resistive Electrode Thick GEM). Several versions have been developed and shown to operate in pure argon and neon at gains of  $\sim 6\cdot 10^3$  (single plate) or  $\sim 10^5$  in a cascade of two in Ar, and up to  $\sim 7\cdot 10^5$  with a double RETGEM in Ne [315]. The performance of 1 mm thick RETGEM with very thin copper electrodes coated with a CuO resistive layer has also been studied in argon at low temperature. The gain was observed to decrease gradually from  $\sim 6\cdot 10^3$  at room temperature to  $\sim 10^3$  at 100 K ( $P = 1$  bar in both cases) and to  $\sim 400$  in saturated gas at 89 K ( $\sim 2\cdot 10^3$  in a cascade of two). On the other hand, the authors of [298] could not observe any multiplication with a RETGEM in a double-phase argon chamber, and suggested argon condensation in the holes and increased resistance of the resistive layers at low temperature as possible reasons. In neon, a gain of  $\sim 3\cdot 10^4$  was achieved at room temperature with a single RETGEM with metal strips for position readout; the gain decreased only slightly when the temperature was lowered to 78 K [316].

Charge multiplication has been observed also using Micromegas with 50  $\mu\text{m}$  gap in the gas phase of a double-phase xenon chamber filled with a Xe+2%CH<sub>4</sub> mixture [317]. Micromegas stands for MICROMesh Gaseous Structure [318] and consists of two parallel electrodes — a micromesh cathode and an anode plate placed at a short distance from each other — so that the electron multiplication takes place in a very strong quasi-uniform field between the electrodes. A gain of about 500 was reported for the double-phase Xe+2%CH<sub>4</sub> system [317] albeit only for short periods of time — the amplification disappeared after 10 to 30 min of operation, a fact attributed by the authors to condensation of xenon in the amplification gap. Xenon condensation in the region of strong electric field (some 140 kV/cm in that experiment) is favored by the high polarizability of xenon atoms.

Gas condensation in the holes of avalanche devices has been reported as a likely reason for temporary failure of GEMs [304], LEMs [312] and RETGEMs [298], for double-phase argon as well as xenon. In some instances this could be reversed with thermal cycling. Contrary to what was observed with Micromegas, this seemed to occur mostly at the initial stage of the chamber filling and could disappear after a couple of hours of temperature stabilization. A carefully chosen temperature gradient in the chamber may help, but a reliable recipe to avert this effect has not been developed yet.

Generally, one can conclude that the avalanche micro-pattern devices considered here work better in argon than in xenon and better still in neon than in argon. This is not surprising given that the Townsend coefficient in xenon is the lowest among the three gases due to the higher ratio of the number of excitations to the number of ionizations per collision [319]. Another aspect to mention is the much larger field required for electron extraction from liquid xenon than from liquid argon [320, 207]. High electric field in front of a GEM or similar structure placed above the liquid surface reduces the efficiency of electron collection into the holes and therefore the observable amplification gain is also lower.

More information can be found in a recently published comprehensive review on operation of micro-pattern avalanche detectors at cryogenic temperatures [303].

### 5.2.2 Photon detection with micro-pattern structures

To find a feasible alternative to existing WIMP detector designs, which use photomultiplier tubes to detect primary scintillation along with the ionization signal via secondary scintillation in gas, one must find a reliable way to detect the prompt VUV light emitted from the liquid. Considerable effort has been put into trying to couple a photocathode to an electron multiplication system, which can be operated in gas (ideally, in the liquid too). This concept is usually referred to in the literature as the ‘gaseous photomultiplier’ (see, for example, review papers [321, 322]).

The idea of such coupling is intrinsically a contradictory one since a high photoelectric conversion coefficient, required for efficient detection of incoming photons, would also mean high probability of positive feedback due to photons emitted in the avalanche. One can imagine several solutions to this problem. One is to suppress photon emission during the avalanche development by a suitable choice of gas composition and/or by shifting the wavelength of the unwanted photons to the wavelength region where the sensitivity of the photocathode is low (CsI, for example, has a sensitivity cutoff for  $\lambda > 200$  nm). In the case of double-phase detectors this, however, would mean separation of the avalanche region from the principal volume of the detector with a sealed VUV-transparent window [323, 324]. Although not impossible technically, it remains to be established that this approach can outperform traditional photomultiplier tubes. We shall discuss recent efforts in this direction at the end of this section.

On the other hand, windowless solutions with both the avalanche device and the photocathode operated in pure noble gas would suffer from strong photon emission during the avalanche process, occurring at the same wavelength to which the photocathode is supposed to be most sensitive. In this situation, feedback might be reduced by preventing illumination of the photocathode by the avalanche photons by way of a careful geometrical arrangement. In other words, one requires the photocathode to be ‘visible’ for photons coming from the detector volume but not for those generated in the avalanche. Some micro-hole structures seem well suited for this purpose: the



avalanches are mostly confined within the holes while the photocathode can be deposited on the surface of the structure turned down to the detector volume, thus being geometrically shielded from the direct avalanche photons. However, there is still the matter of reflected photons, which becomes more problematic as one tries to enhance the VUV reflectivity of all inner surfaces of the detector to improve the light collection efficiency in the chamber.

Concerning the choice of photocathode material, work has focused mostly on cesium iodide due to its sensitivity in the VUV wavelength region but also for technological reasons: the relative easiness of deposition of CsI on metallic and glass surfaces and its capability to recover after exposure to air. Much work has been done since the first successful experiments [325, 326] and the literature on CsI is quite extensive [327]. The most immediate application of these devices is in Cherenkov imaging detectors [328]. Cesium iodide has been proven to operate in several gas mixtures with quenchers as well as in pure noble gases and liquids [325, 327, 293, 329]. Practically all of the above mentioned microstructures have been experimented in combination with a CsI photocathode (see, for example, [321] and references therein).

The quantum efficiency of reflective CsI photocathodes in vacuum has been measured to be up to 30% for xenon light and up to 60% for VUV from argon, depending on the sample preparation [330] (see Figure 27). The photocurrent in a uniform electric field, measured with an electrometer, was found to saturate at a field of about 1.7 kV/cm. A lower quantum efficiency of 15% has also been reported for 175 nm [331].

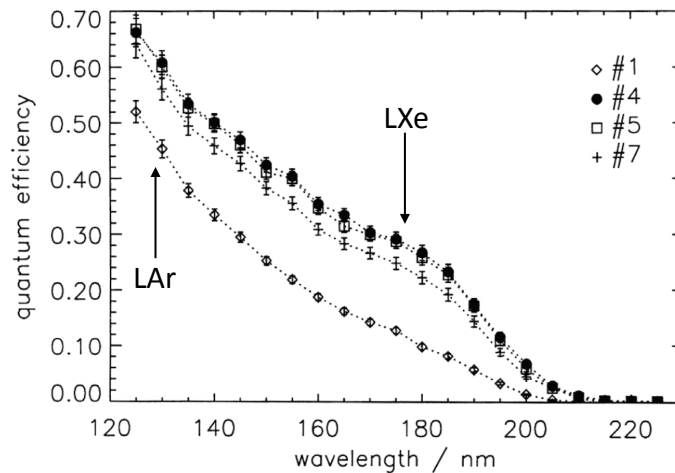


**Figure 27.** Quantum efficiency of reflective CsI photocathodes in vacuum as a function of the photon wavelength for four different samples. The arrows indicate the emission wavelengths for liquid argon and xenon. (Adapted from [330]; with permission from Elsevier.)

When the photocathode is operated in gas, photoelectrons can suffer backscattering off the gas atoms and return to the photocathode [332, 333, 334]. Frequent collisions with gas atoms can also result in insufficient energy gained from the electric field between collisions to overcome the image potential of the photocathode. Both factors lead to reduction of the photoelectron extraction efficiency. Backscattering is more significant in noble gases than in molecular gases. Its probability increases with the gas density and the energy of incident photons. The latter is because the elastic

scattering cross section increases with electron energy in the eV region [335, 336, 337]. At atmospheric pressure, the photoelectron collection efficiency in xenon was found to be about half of that in argon and neon at fields of a few kV/cm. For example, for  $E = 1$  kV/cm it is about 0.47 in Ar, 0.4 in Ne and Kr, 0.25 in Xe and 0.22 in He [333] (measured as gas/vacuum photocurrent ratio for a given illumination intensity and, therefore, includes possible difference in quantum efficiency). Measurements of quantum efficiency of semi-transparent CsI photocathodes in vacuum have also shown some dependence on the temperature. For 165 nm VUV light it changed from 33% at room temperature to 29% at 130 K and to 26% at 77 K [338].

In [306], several micro-hole systems, including LEMs, were experimented within pure argon, krypton and xenon with CsI photocathodes. A gain of  $10^4$  was obtained with LEM without a photocathode (apparently in pure Xe, but the authors are not explicit on this point), but with a CsI coating the maximum gain decreased by an order of magnitude, which can be explained by ion feedback. VUV photons from xenon scintillation were detected with  $\sim 1\%$  efficiency (including quantum efficiency of the photocathode, the probability for a photoelectron to escape and to produce an avalanche in the LEM hole). A better efficiency between 2.5% and 8% (for 130 K and 293 K, respectively) was measured for 165 nm with CsI deposited on top of a GEM and operated in pure Ar [338]. An even higher value of 15% was reported by the same authors for a photocathode deposited on a GEM operated in Ar+10%CH<sub>4</sub> gas mixture at 1 bar and at room temperature [339]. At 170 K the efficiency decreased to 11%, the effect being attributed to back-diffusion of the photoelectrons. The maximum achievable gain was found to be practically independent on temperature, being about 500 for a double GEM with CsI (when CsI was deposited on the surface of a capillary plate, a gain of  $\sim 10^3$  was measured).

A triple-GEM structure with a CsI photocathode deposited on the bottom surface of the first GEM was tested in double-phase argon at 84 K and  $P = 0.7$  bar [340, 302]. Primary scintillation from 60 keV  $\gamma$ -rays was detected at a gain of  $1.4 \cdot 10^3$ , however with surprisingly low efficiency (about 2 photoelectrons at the entrance of the first GEM).

RETGEMs also were tested with CsI [315], including a version with segmented electrodes S-RETGEM (standing for strip-RETGEM) [341]. In argon at room temperature and  $P = 1$  bar, the S-RETGEM was operated with gains up to  $3 \cdot 10^3$ . By reversing the drift field, to avoid the ionization charge to drift to the multiplication structure and observe only scintillation signals, a higher gain of up to  $10^4$  could be reached with a single plate. Much higher gains were obtained with neon:  $\sim 2 \cdot 10^4$  with a single GEM,  $\sim 10^5$  with single GEM and reversed drift field,  $\sim 3 \cdot 10^5$  with double GEM and reversed field (obviously, the reversed field option cannot be used if one intends to detect the ionization signal). A detection efficiency for 185 nm photons of  $\sim 13\%$  was reported for Ar, Ne and Ar+CO<sub>2</sub> mixture.

We refer to the review article [303] for more information on these devices.

The development of sealed gaseous photomultipliers has also progressed, using reflective or semi-transparent CsI (for VUV) or bialkali photocathodes (for VUV or visible light) — see [342] and references therein. Recently, a 500 day run with stable operation of a sealed device with bialkali photocathode and a Pirex glass GEM was reported [343] (the authors also refer to this glass GEM as a ‘micro blasting glass plate’ — MB-GP). A Kapton-based GEM was found incompatible with bialkali photocathodes due to the high absorption of alkali vapors by Kapton during the pho-

tocathode activation. Gains  $\sim 10^5$  have been reached with a double MB GP multiplication structure in Ne/isobutane (10%) and Ne/CF<sub>4</sub> (10%) mixtures without significant ion or photon feedback. A quantum efficiency of 14% was reported for Ne, versus 20% in vacuum at 350 nm. On the other hand, for a semi-transparent CsI photocathode deposited onto a quartz window, and the same multiplication structure and gas mixtures, the same group reported similar gains but only  $\sim 0.5\%$  quantum efficiency at 170 nm light [344]. All the above results were obtained at room temperature.

Detection of liquid xenon scintillation due to  $\alpha$ -particles with a gaseous photomultiplier was reported in [324]. The photomultiplier was coupled to a liquid xenon chamber through a MgF<sub>2</sub> window and operated at 173 K under continuous flow of He or Ne based gas mixtures at 1.1 bar; CH<sub>4</sub> and CF<sub>4</sub> were used as admixtures to avoid condensation at low temperature. A reflective CsI photocathode was deposited on one side of a THGEM. Two multiplication structures were experimented with: double THGEM and THGEM followed by a Parallel Ionization Multiplier (PIM) and a Micromegas. Gains up to  $\sim 10^4$  were attained. For both structures, instabilities were observed at low temperature, rather significant in the case of the second configuration. The authors do not provide enough information to allow the number of photoelectrons extracted from the photocathode to be estimated, but refer that it was significantly lower than expected assuming 22% extraction efficiency. As a possible reason, photocathode degradation due to condensation of impurities is mentioned.

### 5.2.3 Optical readout from micro-pattern structures

Given the difficulties involved in operating micro-pattern detectors in the avalanche mode, attention has been recently turned to their operation at lower voltages, insufficient for developing significant avalanche but high enough to produce secondary scintillation in the detector holes. The general idea is to obtain a higher light gain (defined usually as the total number of photons per primary electron extracted from the liquid) than in a uniform field as presently done in the current double-phase DM detectors and to use highly segmented solid-state photon detectors to enable efficient multi-vertex resolution (especially important for future CNS experiments).

Production of the secondary light within the THGEM holes in double-phase argon system was studied in [345]. A 1 mm<sup>2</sup> SiPM was positioned directly above the center of a 65 mm diameter THGEM, aligned with one of the holes, 5 mm above it. In order to render it sensitive to the argon VUV light, a special gel containing TPB wavelength shifter, re-emitting the absorbed VUV light at 460 nm, was used. The light yield per primary electron increased exponentially with the voltage across the THGEM up to charge gain of  $\sim 100$ , above which a steeper-than-exponential rise was observed (although the charge gain continued on an exponential trend) accompanied by degradation of the energy resolution. According to authors' estimates,  $\sim 600$  photons per primary electron were generated in the THGEM holes at a gain of  $\sim 100$ . Given the low  $\gamma$ -ray energy used to ionize the liquid (5.9 keV from <sup>55</sup>Fe), charge gain determination at low gain values was difficult. We cannot, therefore, estimate the light yield in the absence of charge multiplication.

The authors of [346] studied avalanche scintillation<sup>12</sup> in double-phase argon using a double THGEM multiplication structure and a 4.4 mm<sup>2</sup> SiPM (termed by the manufacturer G-APD —

---

<sup>12</sup>The term 'avalanche scintillation' is employed by the authors in order to distinguish the light emitted in the avalanche from that produced at lower fields below the charge multiplication threshold, commonly called secondary or proportional scintillation.

‘Geiger APD’) placed behind a glass window at a distance of 4 mm from the top THGEM. The G-APD was sensitive only in the visible and near infrared regions up to 950 nm with an average quantum efficiency of 15%. The chamber was irradiated with 60 keV  $\gamma$ -rays from  $^{241}\text{Am}$ . For a charge multiplication gain of 400 (total gain for the two THGEMs), about 0.7 photoelectrons per primary electron was measured. For a gain of 60 this value was 0.14, indicating that the charge gain increased faster with voltage than the light gain. From these data, one can estimate that each electron extracted from the liquid resulted in  $\sim 1800$  photons emitted in  $4\pi$  if the system is operated at gain of 400 and  $\sim 350$  photons for a gain of 60. Unfortunately, the authors are not explicit on the charge calibration procedure that may result in by a factor of about 3 lower yields per primary electron taking into account the known  $W$ -value for liquid argon. Even so, the avalanche light yield is very high, comparable to that observed in [345] with a wavelength shifter.

Using the same setup, avalanche scintillation in xenon was also studied [347]. The THGEMs were operated in gaseous Xe at  $T = 200$  K ( $-73^\circ\text{C}$ ) and  $P = 0.73$  bar (i.e. not in saturated vapor) at charge gains of up to 600. The light yield in the NIR region was found to be significantly lower than in argon. Thus, for a charge gain of 350, each primary electron resulted in 0.071 photoelectrons in the SiPM (compare with 0.7 for Ar). Taking into account all inefficiencies, a value of  $\sim 250$  NIR photons/primary electron emitted in  $4\pi$  can be estimated.

Secondary light from a GEM in double-phase xenon has been observed with a LAAPD sensitive to xenon light [348]. The GEM foil was placed 3 mm above the liquid surface and operated at vapor pressure of 1.4 bar. The voltage across the GEM (400 V) was well below the multiplication threshold (see Figure 25, right panel [299]). Normalized to  $4\pi$ , the number of secondary photons produced in the GEM channels was a factor of  $\sim 2$  higher than in the uniform field between the liquid surface and the GEM. The authors estimate that number to be about 200 VUV photons per primary electron [349].

An array of 19 G-APDs,  $2 \times 2$  mm<sup>2</sup> each, was used to detect secondary light from a single THGEM and also from a stack of 2 THGEMs in double-phase Xe [350]. As the G-APDs are not sensitive in the VUV region a 140 nm layer of *p*-terphenyl wavelength shifter was deposited on a sapphire window placed in front of them. To avoid contamination of xenon, the *p*-terphenyl layer was either enclosed in a vacuum tight cell between two sapphire windows and filled with Ar or a 1  $\mu\text{m}$  poly-para-xylylene protective layer was deposited on top of it. An electron lifetime in liquid xenon of  $\sim 10$   $\mu\text{s}$  was reported. The measured PDE agreed rather well with that expected from the device specification ( $\sim 15\%$  for 370 nm) assuming 100% re-emission efficiency for *p*-terphenyl. At the voltages used in this work, a comparable (within a factor of 1.5) number of secondary photons were produced in the THGEM channels at 1.6 kV and in the uniform field between the liquid surface and the first THGEM (5 mm drift distance; 4.9 kV/cm). For a more compact G-APD packing the authors anticipate a total response of  $\sim 10$  photoelectrons per primary electron. Instabilities on THGEMs were also reported.

The authors of [351] are exploring new techniques for rendering wavelength shifters harmless to the purity of the xenon: besides the protective layer over the *p*-terphenyl, as described above, a new *p*-terphenyl-based nanostructured organosilicon luminophore is also being examined: besides conversion of the xenon emission to longer wavelengths ( $\approx 370$  nm instead of  $\approx 330$  nm for pure *p*-terphenyl), this would also be less volatile and could perhaps be used in a clean environment without a protective layer.

#### 5.2.4 Back to single phase?

The double-phase technology has already been amply demonstrated for detection of low energy signals. However, design constraints due to the need to keep the liquid surface quiet and level, pressure and temperature stable and uniform, and other technical challenges, inspire some thinking about single-phase alternatives [352, 353], which may be cheaper to operate in the case of very large detectors. The solution must evidently pass through realization of an amplification process in the condensed medium. Charge multiplication and secondary scintillation have been observed in liquid xenon and argon long ago, but the achievable gains are far from sufficient and the fields required are extremely high,  $\sim 10^5$  to  $10^6$  V/cm.

The first observation of electron multiplication in condensed noble gases belongs to Hutchinson in 1948 [1]. He observed multiplication in solid argon with a gain of  $>12$  but it was transient and disappeared in a short time — the effect was attributed to polarization of the solid. No multiplication was found in the liquid with anode wires as thin as  $15\ \mu\text{m}$ . Later, using much thinner wires of a few  $\mu\text{m}$  diameter, multiplication in liquid xenon was observed with gains of  $\sim 10$  to  $\sim 100$  [354, 355, 356, 357, 358]. An attempt to build a multiwire proportional chamber for medical  $\gamma$ -ray imaging has been undertaken [359, 360]. However, it was found impractical because of low gain but also due to wire fragility, being unable to withstand the electrostatic repulsion between individual wires in the multiwire anode arrangement.

Attempts to obtain stable electron multiplication in liquid argon were unsuccessful [361]. Although the avalanche did develop in LAr, it was unstable and not reproducible. In addition, correlation between the signal amplitude and the deposited energy was not obvious — an observation later confirmed by other authors [362]. This group used a single sharp needle as an anode to study electron avalanches in LAr. In pure argon, the avalanche behavior was erratic, in part due to strong optical feedback owing to the short wavelength of avalanche photons. This is consistent with the fact that the avalanche could be stabilized by adding a small amount of xenon; a gain of  $\sim 100$  was reported for this mixture. In tension with these results, a gain in excess of 100 was reported for pure argon in [363], using an array of microtips with bending radius of  $\sim 0.25\ \mu\text{m}$ .

Several micro-pattern detectors have also been tested in pursuit of electron multiplication. A gain of  $\approx 15$  was reported for microstrips immersed in liquid xenon [364, 365]. Attempts to obtain multiplication with field emission arrays (Spindt cathodes) were unsuccessful in argon [366], and this was also confirmed in xenon by one of us (VC).

Secondary scintillation was first observed in high-pressure liquid xenon in a uniform electric field [367]. With increasing field strength, the scintillation yield induced by  $\alpha$ -particles was found to decrease by about 15% up to  $E \sim 70$  kV/cm, as expected from the suppression of recombination. At higher fields, a steady increase of luminescence was observed, reaching the zero-field value at  $E \sim 120$  kV/cm. The measurements were conducted at two temperatures of the liquid,  $-5^\circ\text{C}$  and  $+10^\circ\text{C}$ , corresponding to liquid densities of about 2.0 and  $1.7\ \text{g/cm}^3$ , respectively.

Later, proportional scintillation was observed in the non-uniform field in the vicinity of very thin wires [368, 358, 369, 370]. For example, with a wire of  $4\ \mu\text{m}$  diameter a light yield of  $\sim 10$ – $100$  photons per primary electron was obtained [369]. The highest yield was measured at a charge gain of  $\sim 50$ . It has also been shown that it is possible to obtain secondary scintillation with thicker wires: a yield of  $\sim 5$  photons/electron has been estimated for a wire of  $20\ \mu\text{m}$  diameter [371] at an

anode voltage of 5 kV; for a 50  $\mu\text{m}$  wire,  $\sim 30$  photons/electron was estimated to be achievable at 12 kV [372].

The ratio of secondary to primary scintillation in single-phase liquid xenon was originally proposed to discriminate between nuclear and electron recoils in a dark matter detector some two decades ago [48].

Much less information is available on secondary light in liquid argon. To our knowledge this was observed only recently, in the channels of a THGEM immersed into this liquid [345]. At a THGEM voltage of about 10 kV, signals of  $\sim 100$  photoelectrons were recorded from 5.9 keV X-rays with a 1  $\text{mm}^2$  SiPM placed behind a THGEM hole, at a distance of 5 mm. The VUV photons were converted to the visible range with a wavelength shifter deposited onto the SiPM. A light yield of  $\sim 300$  VUV photons per primary electron has been estimated (this value is similar to that used in double-phase xenon systems). The amount of detected light increased linearly with applied voltage indicating the absence of charge multiplication up to at least 10.2 kV. Poor amplitude spectra, much worse than for the double-phase regime with the THGEM operated in the gas phase, tarnish these otherwise encouraging results. The reason for that is not quite clear yet. Optimization of the THGEM geometry can probably bring about some improvement.

In spite of several rather significant efforts, for now the only viable alternative to double-phase systems seems to be to explore scintillation pulse shape discrimination in liquid systems, at zero electric field, as described in Section 3. However, losing the ionization response has consequences for the achievable energy threshold for nuclear recoil detection and for event localization in three dimensions.

We refer to [6, 7] and references therein for a more complete survey on electron multiplication and secondary scintillation in the liquid phase.

## 6. Direct dark matter search experiments

In this section we review briefly some dark matter search projects, aiming to illustrate how noble liquid technologies are implemented in real experiments. We focus on those which have published WIMP search results recently or have operated detectors underground, but some large systems which we consider significant and are close to deployment are also described. Other technologies, namely cryogenic bolometers, room temperature scintillators and bubble/droplet chambers will not be covered here.

With tonne-scale target masses required to probe the whole range of scattering cross sections favored by theory, a critical consideration is how these designs can be scaled up whilst maintaining very low energy threshold for nuclear recoils. As the system size increases, self-shielding of an inner, fiducial volume from external backgrounds becomes increasingly effective, and this is one of the key advantages of the noble liquids. On the other hand, particle discrimination can be impaired, for example due to increasing difficulty in applying strong electric fields, which is another important consideration.

We note that noble liquid detectors, some much larger than those discussed here, have been applied to other physics measurements — for example, the MEG experiment features a 2.2 tonne liquid xenon scintillation calorimeter to search for the lepton-flavor violating decay  $\mu^+ \rightarrow e^+ \gamma$  [373]; and ICARUS is a 760-tonne liquid argon time projection chamber (TPC) to study cosmic rays, neutrino oscillations and search for proton decay [374]. The energy scale of these processes is in the MeV region or higher. On the other hand, our goals are the detection of nuclear recoils with energy up to 100 keV at most and hopefully achieve their discrimination from electron recoil backgrounds. These are, therefore, very distinct requirements.

### 6.1 Liquid xenon detectors

At the time of writing, five collaborations have operated liquid xenon detectors built for dark matter searches. We begin by overviewing these programs, referencing published instrument descriptions and main WIMP scattering results where appropriate, before describing the latest experiments in more detail. Other surveys of application of this technology to WIMP searches have been published [8].

The DAMA team built and operated the first liquid xenon WIMP detector, DAMA/LXe, at the Gran Sasso Underground Laboratory (LNGS) in Italy, from the mid 1990s. This was a scintillation chamber with 6.5 kg of xenon enriched in  $^{129}\text{Xe}$ , read out by three 3.5-inch photomultipliers [42]. WIMP elastic scattering results using pulse shape discrimination were published in 1998 [375]. The collaboration then opted to pursue room temperature sodium iodide detectors (DAMA/NaI).

The ZEPLIN program at the Boulby mine (UK) followed from the late 1990s, with ZEPLIN-I publishing final results in 2005 [44]; it featured at its core a PTFE-lined 5-kg chamber with three 8-cm diameter photomultipliers viewing the liquid xenon scintillation. ZEPLIN-II and ZEPLIN-III were the first double-phase systems to be conceived for dark matter searches, and were essentially developed in parallel and exploiting different technological solutions. ZEPLIN-II became the first liquid/gas system to operate in the world, completing in 2007 [49]; it utilized a deep, high-reflectance PTFE chamber containing 31 kg of liquid xenon with readout from seven 13-cm diameter PMTs in the gas phase. ZEPLIN-III concluded the liquid xenon program at Boulby, with

science runs in 2008 [376] and, following an upgrade phase, in 2010/11 [56]; its design featured 31 2-inch PMTs immersed in the liquid, viewing a thin disc geometry of 12 kg of liquid xenon under high electric field [50].

The XENON Collaboration deployed XENON10 at LNGS in 2006. This double-phase detector contained 14 kg of active xenon in a deep PTFE-walled chamber, viewed by two arrays of 1-inch PMTs located in the liquid and gas phases (41 and 48 units, respectively) [201]. Main WIMP results were published in 2008 [377]. This design was essentially scaled up for XENON100, in which 62 kg of active mass are viewed by 178 PMTs [197]. A first run of 100 live days of acquisition in 2010 yielded a world leading result on WIMP-nucleon elastic scattering [57]. This sensitivity lead has been extended with data from a further 225 live days reported recently [215]. The XENON team is working on the next generation tonne-scale experiment XENON1T, which will be built at LNGS starting in 2013.

The LUX350 team has just completed construction of a double-phase detector with 300 kg active mass, featuring 122 2-inch PMTs equally divided in bottom and top arrays. The system has been tested in a surface facility, in preparation for underground deployment in the Davis complex of the Sanford Underground Laboratory at the Homestake mine (US) [170, 378]. In collaboration with the ZEPLIN-III groups, the multi-tonne LZ program is being developed to occupy the same infrastructure after LUX [379].

The latest XMASS detector has the largest liquid xenon WIMP target running at present: 800 kg. The spherical scintillation chamber is 80 cm in diameter and is instrumented with 642 2-inch PMTs. The rationale behind this program is to compensate for the poorer nuclear recoil discrimination achievable in a scintillation-only system with the significant self-shielding for external backgrounds enabled by the large target mass; the expected fiducial mass of 100 kg is, however, comparable to that anticipated in LUX350. XMASS-800 has been fully operational at the Kamioka Observatory (Japan) since 2011 [380]. The Collaboration plans a 26 tonne future detector aimed also at detecting solar neutrinos and  $\beta\beta$ -decay.

The PANDA-X (Particle AND Astrophysical Xenon TPC) is an emerging effort aiming to deploy a three-stage experiment at the new JinPing Laboratory (China), the deepest underground facility in the world (2,513 m depth, 7,500 m water equivalent) [353]. Initially, the experiment will feature a 25 kg fiducial LXe mass in a planar geometry with 5 kV/cm drift field. The next stage, with 500 kg fiducial, will reuse the outer infrastructure, but some internal components will be replaced. A tonne-scale target would require a larger inner vessel. To reduce background and cost, the team may also replace the double-phase system by direct readout of proportional scintillation around thin wires in a liquid-only detector. The light readout for PANDA-1T might feature gaseous photomultipliers instead of conventional PMTs.

Finally, we mention briefly DARWIN (DARK matter WImp search with Noble liquids), a design study for a next-generation, multi-tonne detector in Europe [381]. The project focuses on double-phase LAr and/or LXe targets and is investigating, among other issues, alternative ionization readouts with LEMs and CMOS pixel detectors (GridPix [382]) coupled to electron multipliers, or via proportional scintillation in the gas phase using gaseous photomultipliers [383].

We now describe in more detail the most competitive systems already operated or at an advanced stage of construction, highlighting various design features and how the main technological challenges were addressed in each detector.



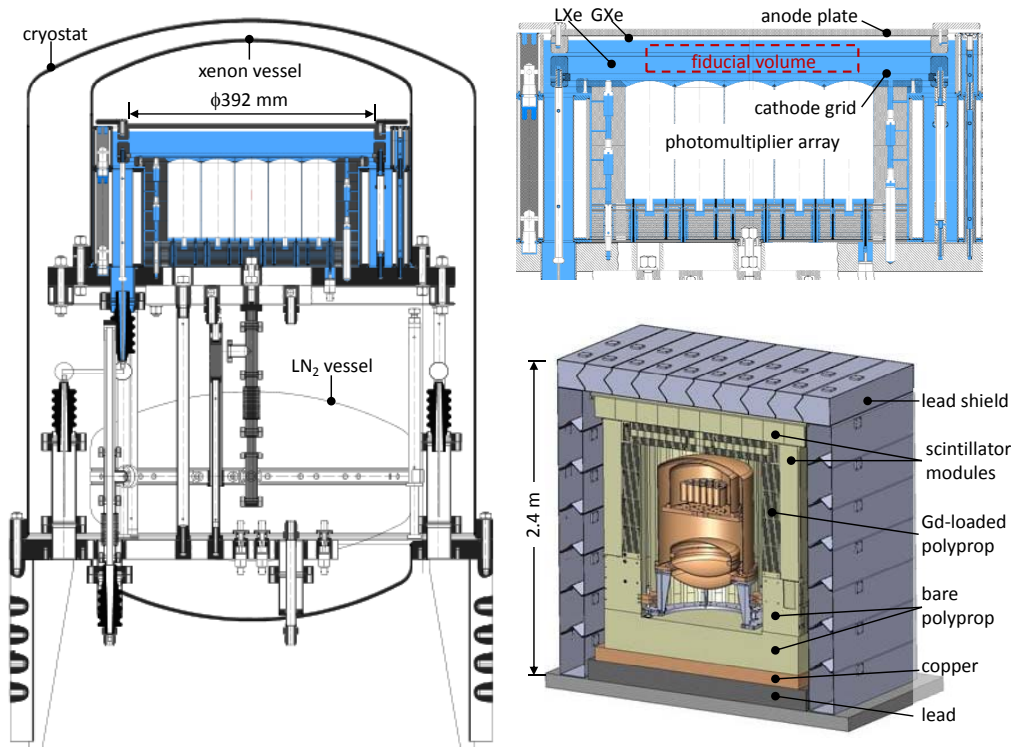


**Figure 28.** Schematic drawings of the ZEPLIN-III experiment. The WIMP target is shown left, with liquid xenon in blue; the double-phase chamber is detailed on the right, with an approximate fiducial volume indicated by the dashed red rectangle. Also shown on the right is the fully-shielded configuration at Boulby (including a veto instrument surrounding the WIMP target). (Adapted from [50] and [40]; courtesy ZEPLIN-III Collaboration; with permission from Elsevier.)

**The ZEPLIN Collaboration** operated its third liquid xenon detector, shown in Figure 28, at the Boulby Underground Laboratory in the UK (ZEPLIN stands for ZonEd Proportional scintillation in LIquid Noble gases). The instrument construction is described in detail in [50]. Most elements were built from high purity copper to minimize background. The outer cryostat vessel enclosed two chambers; the lower one contained the LN<sub>2</sub> coolant, which boiled off through a heat-exchanger attached to the xenon vessel above it. The latter housed a 12 kg liquid xenon WIMP target, with immersed photomultipliers (viewing upward) to maximize detection efficiency for faint primary scintillation signals. The working volume was formed by an anode disc 39 cm in diameter and a multi-wire cathode located 4 cm below it, a few mm above the hexagonal array of 31 PMTs. This volume was mostly filled with liquid xenon — leaving a gap of 4 mm above it where secondary scintillation took place in the cold vapor.

Contrary to ZEPLIN-II, where a wire-grid just below the liquid surface helped with cross-phase emission, in ZEPLIN-III the planar geometry allowed application of a strong field to the whole liquid phase with only two electrodes, thus enhancing the efficiency for charge extraction from the particle tracks. Typical operation fields were 3–4 kV/cm in the liquid and approximately twice as strong in the gas [376, 56]. A second wire-grid, just above the photomultiplier windows, shielded the photon detectors from the external field and also provided a reverse field region to sup-

press secondary scintillation signals from low-energy background photons from the PMTs. Only xenon-friendly, low-outgassing materials were used within this chamber, in particular avoiding large amounts of PTFE, in order to maintain sufficient electron lifetime in the liquid without the need for continuous re-purification. This was achieved, with that parameter actually improving over one year of operation in the closed system: from 14  $\mu\text{s}$  to 45  $\mu\text{s}$  by the end of the run [193].

In the first science run custom-made photomultipliers D730Q/9829QA from ETEL were used; these had bi-alkali photocathodes with metal fingers deposited on quartz windows under the photocathode for low temperature operation. The average (cold) quantum efficiency for xenon light was 30% [239]. For the second dark matter run, those tubes were replaced with another pin-by-pin compatible model with 40 times lower radioactivity per unit, lowering the overall electromagnetic background of the experiment to 750 mdr at low energy ( $1 \text{ dru} = 1 \text{ kg}^{-1}\text{day}^{-1}\text{keV}^{-1}$ ) [202]. Unfortunately, their optical performance was poorer, with only 26% mean quantum efficiency and large gain dispersion [193]. In ZEPLIN-III the PMT array was biased from a common external voltage ladder, connected to a stack of copper disks powering each set of PMT dynodes (these can be seen in Figure 28 just below the photomultipliers). Although this reduces the number of feedthroughs required (lower background), and the need for internal electronics (better xenon purity and reliability), it does not allow for gain equalization at the PMT anodes.

Between the two science runs a veto instrument was retrofitted around the WIMP target, as also shown in Figure 28, replacing some of the hydrocarbon shielding. This veto included 52 plastic scintillator modules surrounding a Gd-loaded polypropylene structure tailored for neutron moderation and efficient radiative capture [40, 41]. The use of anti-coincidence systems around WIMP targets is increasingly recognized as important: besides lowering the effective background of the experiment they provide an independent measurement of the neutron (and other) background, which can reduce the systematic error associated with a potential discovery.

As in other double-phase systems, accurate position reconstruction of particle interactions in three dimensions allows for a very precise fiducial volume to be defined, well away from any surfaces and avoiding outer regions with non-uniform electric field and light collection. The depth coordinate is obtained with precision of a few tens of  $\mu\text{m}$  from the drift time of the ionization (measured by the time separation between the primary and the secondary scintillation signals — see Figure 3). The horizontal coordinates are reconstructed from S2 signals from all PMTs; a spatial resolution of 1.6 mm (FWHM) was achieved for 122 keV  $\gamma$ -rays [199]. A fiducial volume containing 6.5 kg of liquid xenon was defined for the 83-day long first run of ZEPLIN-III [376], decreasing to 5.1 kg for the 319-day second run owing to the poorer PMT performance.

The scintillation threshold for WIMP searches was  $\approx 7$  keV in both runs [56] — using recent data for the relative scintillation efficiency of nuclear recoils [67]. An ionization threshold corresponding to the electroluminescence of 5 electrons was defined by the trigger hardware; although ZEPLIN-III could detect the signature from a single ionization electron — as shown in Figure 6 — in practice these signals could not be used due to a large single electron background which generated too high a trigger rate [37]. An electron recoil rejection efficiency of 99.99% was achieved at WIMP-search energies in the first run, which remains the best reported for double-phase xenon. In both datasets a handful of events were observed within the signal acceptance region, consistent with background expectations in both cases. The combined result excluded a WIMP-nucleon scalar cross section above  $3.9 \cdot 10^{-8}$  pb ( $3.9 \cdot 10^{-44}$  cm<sup>2</sup>) at 90% CL for 50 GeV WIMP mass [56, 376].

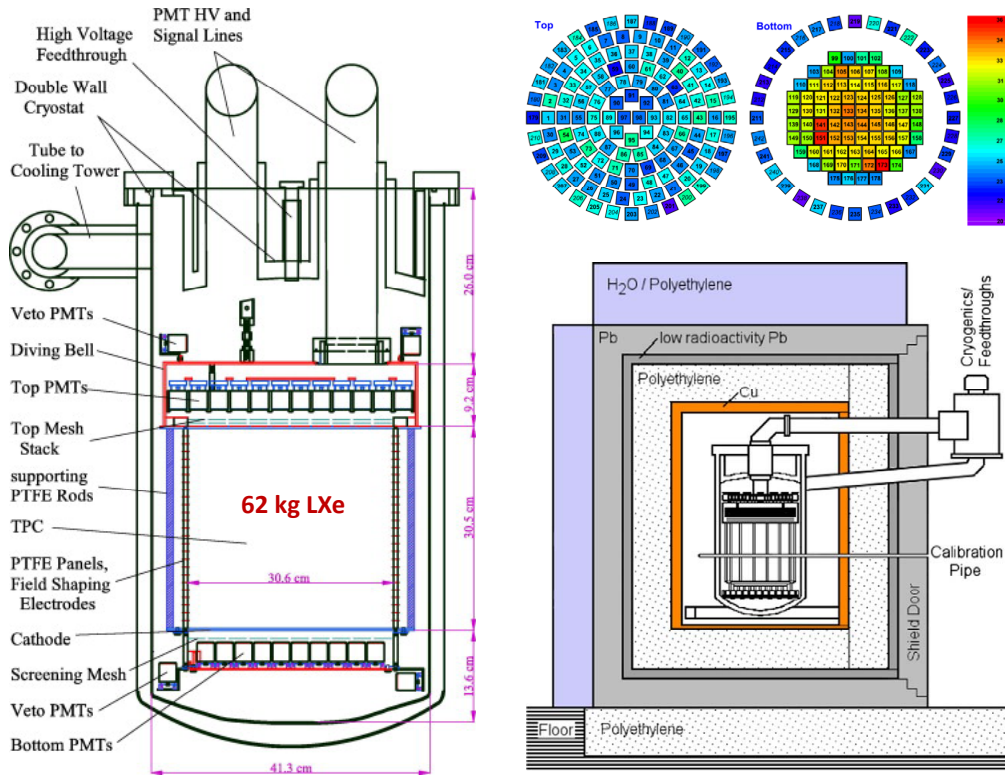


**Figure 29.** Schematic diagrams of the XENON100 experiment. The main instrument is shown left; it contains 62 kg of liquid xenon in the active TPC region and an additional 99 kg in a surrounding ‘veto’ region. The VUV readout uses two arrays of 1-inch square PMTs with  $\sim 30\%$  quantum efficiency; the QE distribution and PMT layout are shown top right. The shielding configuration around the instrument is also shown on the right. (Adapted from [197]; courtesy E. Aprile; with permission from Elsevier.)

The **XENON Collaboration** has chosen a bulk detector concept for XENON10 and its successor XENON100, the latter shown schematically in Figure 29. The two detectors, very similar in design, are described in [201] and [197], respectively. They were deployed at LNGS (Italy) in sequence, with XENON100 designed to fit the existing shielding enclosure. Results from a first run of 100 live days in 2010 have been published [57] and the Collaboration has just reported from a second run with 225 live-days of science data [215], following additional purification to lower further the  $^{85}\text{Kr}$  background.

In XENON100, the 62 kg WIMP target is 31 cm in diameter by 31 cm in height and is contained within a PTFE cylinder with field shaping rings enclosed within its walls. Five meshes provide the necessary electric fields. The cathode at the bottom of the chamber and another (the ‘gate’) just below the liquid surface define a drift field of 0.53 kV/cm. At this field the ionization drift time for events near the cathode is  $176 \mu\text{s}$ , demanding very high purity of the liquid. A strong extraction field of  $\sim 12 \text{ kV/cm}$  is formed between the gate electrode and the anode mesh a few mm above the liquid surface. Secondary scintillation develops in the gas gap between these two electrodes. Two additional meshes close to each PMT array are used to close the electric field lines and thus shield the photomultiplier tubes. The thickness of the gas phase is defined with the help

of a diving bell, indicated in red in Figure 29, which is pressurized by the gas recirculation line. This also allows liquid to be filled to above the bell for shielding purposes (see below). The active volume is viewed by two arrays of photomultipliers Hamamatsu R8520-06-A1, one below the cathode mesh viewing upward and detecting mostly primary scintillation signals, and the other placed in the gas phase and viewing downward. The layout of the two arrays is also shown in Figure 29. The 178 PMTs were selected for low U/Th radioactivity content; they have 1-inch square window and alkali photocathodes with aluminum fingers underneath.

Approximately 4 cm of liquid surrounding the time projection chamber from all sides (totaling 99 kg of xenon) establishes an active scintillation ‘veto’ detector for external  $\gamma$ -rays; this volume is optically isolated from the main chamber and is viewed by an additional set of 64 PMTs operated in anti-coincidence with the WIMP target. The average energy threshold of this volume is  $\sim 100$  keV for electron recoils.

Cooling is provided by a pulsed tube refrigerator [384] and delivered from outside the shield to minimize background. Very good thermal stability is achieved over several months of operation. The liquid xenon purity is maintained with active recirculation through a hot getter.

Very low rates of electron recoil background were achieved at the core of XENON100 in a preliminary run, with  $< 5$  mdr reported at low energy whilst retaining a fiducial mass of 40 kg [385]. If maintained, this rate would lead to only a few background events per year of operation with a discrimination efficiency at the level of 99.5%.

Initial WIMP results were derived from 100.9 live days with a 48 kg fiducial volume, above an 8 keV nuclear recoil threshold. Three candidate events were observed in the signal region with an expected background of  $1.8 \pm 0.6$  events, thus excluding a spin-independent elastic interaction above  $7.0 \cdot 10^{-9}$  pb ( $7.0 \cdot 10^{-45}$  cm<sup>2</sup>) for a 50 GeV WIMP with 90% confidence [57].

The sensitivity of this dataset was limited by a higher concentration of <sup>85</sup>Kr than had been achieved in the preliminary run, which was attributed to an air leak [57, 386]. After further cryogenic distillation a second long run was started in 2011 and accumulated 225 live days [215]. An electron recoil background rate of  $\sim 5$  mdr was recovered in a 34 kg fiducial mass. Two events were observed in the 6.6–30.5 keV recoil energy range in this exposure, which is consistent with a background expectation of  $1.0 \pm 0.2$  events. This excludes at 90% CL a scalar interaction above  $2.0 \cdot 10^{-9}$  pb ( $2.0 \cdot 10^{-45}$  cm<sup>2</sup>) for a 55 GeV WIMP, which constitutes the strongest experimental constraint on spin-independent WIMP-nucleon scattering to date.

A larger system, XENON1T, is being developed by the Collaboration; this features a 1-m long TPC containing 2.2 tonnes of xenon. The original design featured 3-inch QUPID photon detectors (Section 5.1.4), but the new 3-inch Hamamatsu R11410 PMTs are also being considered. The system will be housed in a 10-m diameter water tank at LNGS, with construction beginning soon.

**The LUX Collaboration** (LUX stands for Large Underground Xenon experiment) has built a 350 kg liquid xenon detector to operate at the Sanford Underground Laboratory (SURF) at the Homestake mine in South Dakota [170, 244]. The detector, shown in Figure 30, exploits the same double-phase principle with measurement of primary scintillation in the liquid and secondary scintillation in the gas; the chamber configuration is in general similar to the ZEPLIN-II and XENON TPCs. The active volume is a cylinder of 49 cm diameter and 59 cm height equipped with 122 Hamamatsu R8778 PMTs (2-inch diameter), equally distributed in top and bottom arrays.

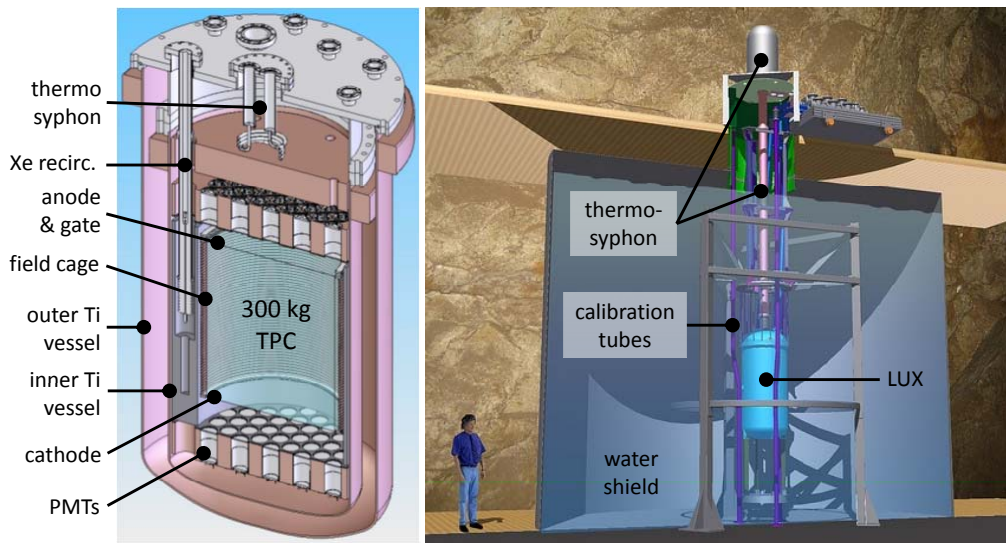


**Figure 30.** Illustration of the LUX detector and its deployment in the water tank shield in the Davis complex of the Sanford Underground Laboratory. The 300-kg time projection chamber, installed within a double-vessel titanium cryostat, is viewed by two arrays of 61 photomultipliers each. (Adapted from [244]; courtesy LUX Collaboration.)

LUX350 is expected to reach  $< 0.8$  mdr of electron recoil background (before discrimination) in an inner 100 kg fiducial mass. Besides self-shielding, this very low background level is afforded by a thin-walled titanium cryostat design and operation within an 8-m diameter water tank. Containing 300 tonnes of ultrapure water instrumented with 20 ten-inch PMTs (Hamamatsu R7081), this will provide passive shielding for external  $\gamma$ -rays and neutrons as well as an active muon veto.

Cooling and temperature regulation are achieved primarily by closed-loop  $N_2$  thermosyphons connected to a liquid nitrogen reservoir located above the water tank [387]. The cryogenic system has been designed with the cooling power requirements of next-generation detectors in mind. The xenon is purified by continuous circulation and a heat-exchanger system is employed to allow higher recirculation rates, with the outgoing gas cooling the incoming xenon.

The detector has been tested in a dedicated surface facility at SURF, within a 3-m diameter water tank, which provided useful shielding for detector characterization and allowed full system verification in realistic underground conditions [170]. In these tests the center of the chamber yielded a very impressive 8 photoelectrons per keV in scintillation for electron recoils at zero electric field. At the time of writing the experiment is being commissioned underground in the redeveloped Davis complex at SURF; initial WIMP results are expected early in 2013.

For the next phase the LUX and ZEPLIN-III teams are planning the LZ program at Homestake, where a detector with active mass of several tonnes can be deployed within the infrastructure developed for LUX350 [379]. A TPC similar in design to LUX is envisaged, viewed by Hamamatsu R11410 3-inch photomultipliers, and containing up to 7 tonnes of active xenon. A liquid scintillator veto is being designed to fit around a thin-walled titanium cryostat to further decrease internal backgrounds. Construction is expected to start around 2014.

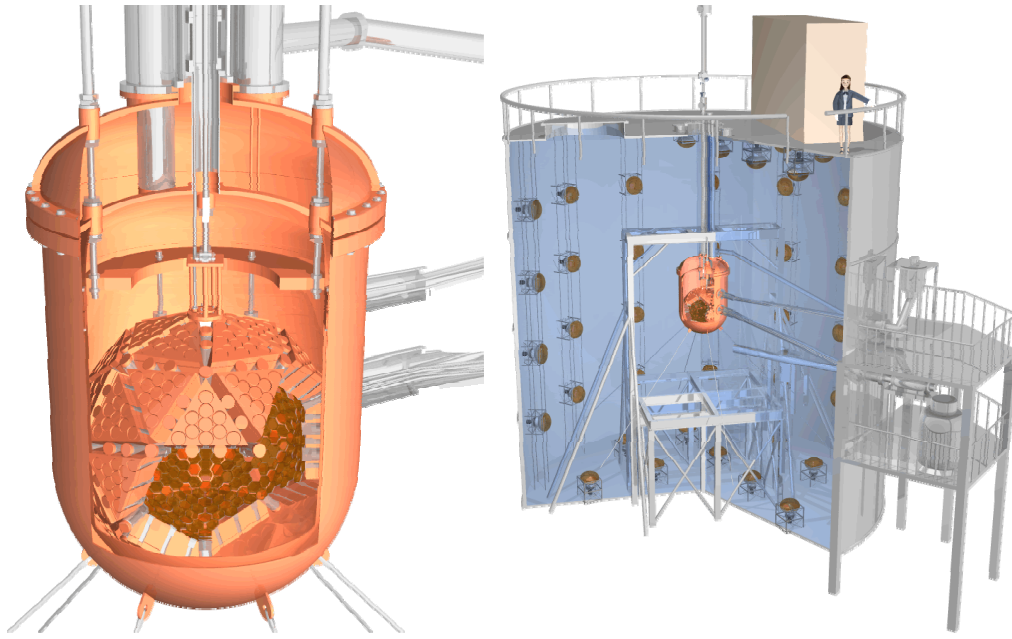


**Figure 31.** The XMASS scintillation detector is shown left; 800 kg of liquid xenon are viewed by 642 photomultipliers arranged in a pentakis dodecahedron geometry. The chamber is located within a 10-m diameter water shield at Kamioka. (Credits: Kamioka Observatory, ICRR (Institute for Cosmic Ray Research), The University of Tokyo.)

**The XMASS Collaboration** based in Japan has chosen a different approach, which relies on efficient measurement of primary scintillation in a single-phase liquid xenon detector (Figure 31). Without the need to apply strong electric fields internally, the design of the target chamber is less constrained and a spherical geometry, optimal to exploit self-shielding, becomes possible. XMASS is a multipurpose experimental program which aims to study solar neutrinos,  $\beta\beta$ -decay and WIMPs [39]. Following several years of R&D work with an 80-kg prototype [164], an 800 kg detector has been built and installed at the Kamioka Observatory; engineering data-taking started in 2011.

The detector is a sphere of 80 cm internal diameter made from OFHC copper with 642 Hamamatsu R10789 photomultipliers closely packed into a honeycombed structure. These have hexagonal windows (65 mm diagonal) and were expressly optimized for low background for this experiment. They have bi-alkali photocathodes with metal fingers under the quartz windows, and quantum efficiencies for xenon light of up to 39% at liquid xenon temperature. The photocathode coverage fraction in the chamber is 64% [380]. A preliminary signal yield of 15.9 photoelectrons per keV has been reported for  $^{57}\text{Co}$  at the center of the detector [388] — 3 times higher than had been assumed by the XMASS team [380]. This will improve the previously stated threshold of 5 keV for electron recoils.

The only possibility for electron recoil background rejection is pulse shape discrimination, as only the scintillation signal is measured. Therefore, the requirements for both external  $\gamma$ -ray shielding and intrinsic contamination are even more stringent than in double-phase detectors. The

planned fiducial volume includes only the central  $\sim 100$  kg, with a 20-cm thick outer shell being sacrificed for shielding from external  $\gamma$ -rays and neutrons, as well as from  $\beta$ - and  $\alpha$ -particles emitted from the detector walls. Intrinsic backgrounds, notably  $^{85}\text{Kr}$  and  $^{222}\text{Rn}$ , then become a critical consideration, and the XMASS Collaboration has devoted much effort to mitigate these [27, 380]. In order to shield the detector from external radiation, XMASS is immersed into a 10-m diameter tank filled with 800 tonnes of ultrapure water instrumented with 72 20-inch PMTs. The water shield absorbs  $\gamma$ -rays and thermalizes fast neutrons from the rock, besides providing a Cherenkov muon veto. Overall, an electronic background rate below 0.1 mdr is expected in the inner 100 kg fiducial volume and neutron backgrounds are negligible there [380].

The possibility of using pulse shape discrimination, as in early xenon dark matter detectors, has been carefully investigated [389]. The difference in scintillation decay times for electrons and nuclear recoils is small, as discussed in Section 4.2.1, but useful nonetheless. That study, conducted with a small prototype chamber with a high light yield of 20.9 photoelectrons per keV, reports an electron rejection efficiency of 92% near 5 keV, improving to 99.9% for 15 keV electrons — both retaining 50% nuclear recoil acceptance. A second measurement was performed with some scintillation light deliberately masked to provide a lower photoelectron yield, in line with what had been expected for XMASS, and this confirmed significantly poorer discrimination. However, the actual performance achieved by XMASS warrants, in our view, a comparison with the above (unmasked) result. This suggests that only a few undiscriminated electron recoil events would remain per year of operation if the claimed nominal background rate can be confirmed.

The 800 kg system is primarily a WIMP detector. As the next step, the Collaboration plans to scale up the detector to a 2.5 m sphere containing 20 tonnes of liquid xenon (10 tonnes fiducial). This mass will allow also detection of solar neutrinos and study  $\beta\beta$ -decay of  $^{136}\text{Xe}$  as originally planned [39].

## 6.2 Liquid argon detectors

Dark matter searches with liquid argon have not progressed as quickly as with liquid xenon, but there has been renewed interest in this medium in recent years. Experience from large projects, namely ICARUS, propelled ambitious efforts over a decade ago, but these lost ground to liquid xenon programs, which adopted a more incremental approach. Yet, the field is a vibrant area of research once again, involving double-phase systems as well as scintillation-only detectors (pulse shape discrimination is very effective in liquid argon, as discussed in Sections 3 and 4.2.1). Two collaborations have built dark matter systems, two other detectors are at an advanced stage of construction, and a new effort is emerging. As in the previous section, we begin by outlining the main experiments before describing the most competitive systems in more detail.

The WARP Collaboration started their program at LNGS in the late 1990s, building on R&D experience from ICARUS, and published in 2008 the only set of dark matter results from liquid argon to date [55]; their 2.3-liter prototype chamber featured photomultiplier readout and exploited both ionization/scintillation ratio as well as pulse shape discrimination. A detector with 140 kg active mass was subsequently built and commissioned at Gran Sasso in 2009 [390], but no published information on the present status of the project could be found.

The ArDM Collaboration started development of a tonne-scale double-phase chamber in 2004 [391]; this is presently being deployed at the Canfranc Underground Laboratory (Spain) [392] fol-

lowing construction and extensive testing at CERN. The original design features photomultiplier readout of scintillation in the liquid and detection of emitted ionization using Large Electron Multipliers in the gas.

Two single-phase detectors are being built by the DEAP/CLEAN Collaboration to operate at SNOLab (Canada). MiniCLEAN is a 500 kg scintillation detector using cold PMTs over  $4\pi$  solid angle [393]. It has a multiple-target mission: after an initial 2-year run with natural argon, the Collaboration proposes to replace the working medium with liquid neon to explore how the rate of a hypothetical signal varies with atomic mass under similar backgrounds. The second system, DEAP-3600, features 3.6 tonnes of liquid argon in a transparent acrylic vessel viewed by warm photomultipliers [394]. It proposes to operate with natural argon for the first three years followed by use of underground argon depleted in  $^{39}\text{Ar}$ . MiniCLEAN is due to start data-taking in late 2012, followed by DEAP-3600 one year later.

Finally, the DarkSide team have returned to double-phase argon but starting on a smaller scale. A 10 kg prototype has been operated at LNGS [395] and a low-background 50-kg device (33 kg fiducial) is under construction [396].

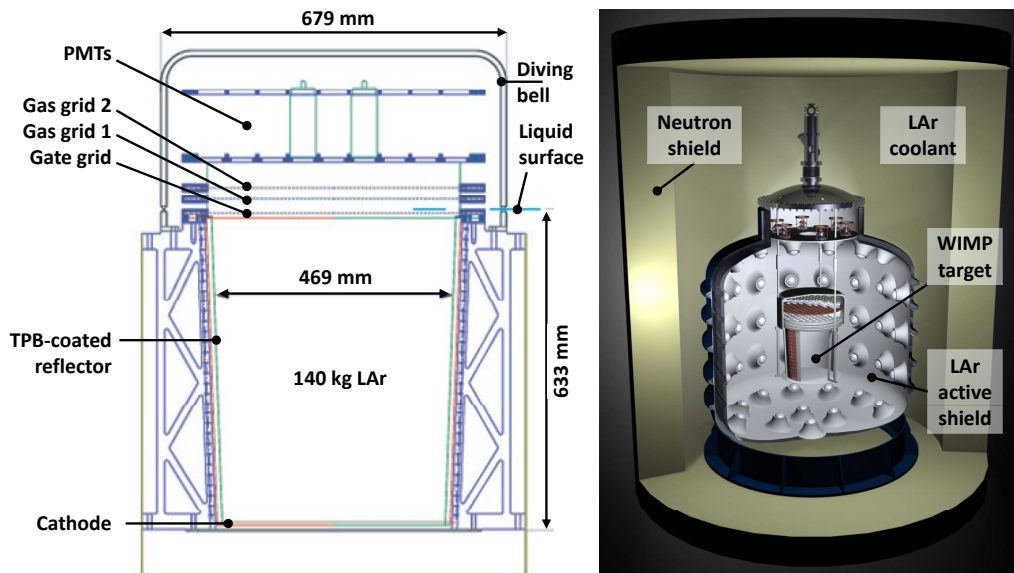


**Figure 32.** The WARP140 dark matter experiment. The 100-liter WIMP target is represented left, viewed by 37 PMTs (only two are shown). The target is surrounded by an active scintillator shield sharing the same ultra-pure LAr; a stainless steel cryostat (not shown) filled with LAr coolant contains the nested vessels; this is lined with a polyethylene layer to shield against cryostat neutrons. (Adapted from [397].)

**The WIMP Argon Programme (WARP)** was proposed in 2004, emerging from R&D activities with liquid xenon and liquid argon for the ICARUS experiment. It consisted initially of two stages: an existing double-phase test chamber with 2.3-liter capacity was modified and deployed at LNGS; this would prototype a 100-liter detector built from low background components and using 140 kg of isotopically purified argon [397]. A future 1.4 tonne detector was envisaged, occupying some of the infrastructure developed for WARP140, the 100-liter chamber. WIMP search data



from the 2.3-liter prototype were acquired in 2005. With the help of dual parameter discrimination (S2/S1 ratio and S1 pulse shape, as shown in Figure 5, right), a WIMP-nucleon cross-section limit of  $1 \cdot 10^{-6}$  pb ( $1 \cdot 10^{-42}$  cm<sup>2</sup>) was published in 2008 [55].

The WARP140 target, shown schematically in Figure 32, has a 60 cm long drift region designed to operate at 0.5–1 kV/cm; the electric field is conditioned by field-shaping rings embedded in the chamber walls. The electroluminescence region is defined by two grids either side of the liquid surface, with the liquid height determined by a diving bell. The target is viewed by an array of 37 PMTs with 2- and 3-inch diameter looking down from the gas phase into the active volume; these models (ETL D750UKFLA and D757UKFLA) have low-temperature bialkali photocathodes developed by Electron Tubes to operate at LAr temperature. The voltage divider chains are made from Kapton printed circuit boards with discrete components selected for operation at LAr temperature. To wavelength-shift the VUV photons emitted by the prompt and proportional scintillations of LAr, TPB was evaporated onto highly reflective plastic foil coating all internal surfaces. A light yield of 1.6 photoelectrons per keV was reported at zero electric field with this configuration [390].

This chamber is immersed in a much larger LAr volume of 8 tonnes, totally surrounding the inner detector and working as an active veto; this is viewed by 2- and 3-inch photomultiplier tubes of the above models, 300 in total. Liquid argon circulates through the WIMP target and the active shield, driven by an external purification system. The cryogen is contained within a double-walled stainless steel cryostat, 2.9 m in diameter and 4.45 m in height, lined internally with an additional 10 cm of polyethylene to shield against neutrons from stainless steel. External hydrocarbon and lead enclosures complete the shield.

Construction of the 100-liter detector started in 2005 and by 2009 the detector had been commissioned at LNGS [390]. However, problems with high voltage delivery and with the stability of the wavelength shifting layers halted the first technical run; a second test was conducted in 2010, but high voltage problems persisted. No update on WARP140 has been reported recently.

**The ArDM (Argon Dark Matter) experiment** aims to search for WIMPs with a tonne-scale double-phase liquid argon detector deployed at the Canfranc underground facility (Spain) [391]. Its conceptual design is shown in Figure 33. The detector contains 850 kg of active mass of LAr shaped as a cylinder of 80 cm diameter and 120 cm height; the estimated fiducial mass is not known. The active volume is viewed by 14 hemispherical 8-inch photomultipliers placed at the bottom (Hamamatsu R5912-02MOD bialkali tubes with platinum underlay to operate at LAr temperature). TPB is used to wavelength-shift the argon light; a thin transparent layer is deposited over the PMT windows, while all other surfaces are covered with a PTFE fabric (Tetratex) coated with an opaque TPB layer, which works also as a reflector [234]. A light yield of 1 photoelectron per keV at zero electric field was predicted for the completed chamber based on tests with 7 out of 14 PMTs [398], which would enable a nuclear recoil energy threshold of 30 keV as originally planned.

The ionization charge is drifted away from the interaction site under a strong electric field ( $>3$  kV/cm) and emitted into the vapor phase with the help of two electrodes located either side of the liquid surface. A distinguishing feature of this experiment is the aim to measure directly the charge extracted from the liquid with Large Electron Multipliers (LEM) placed in the gas phase [391]. A gain of 27 has been achieved in a dedicated prototype with a 1-mm thick LEM operating in double-phase argon, with the amplified charge collected by a two-dimensional projec-

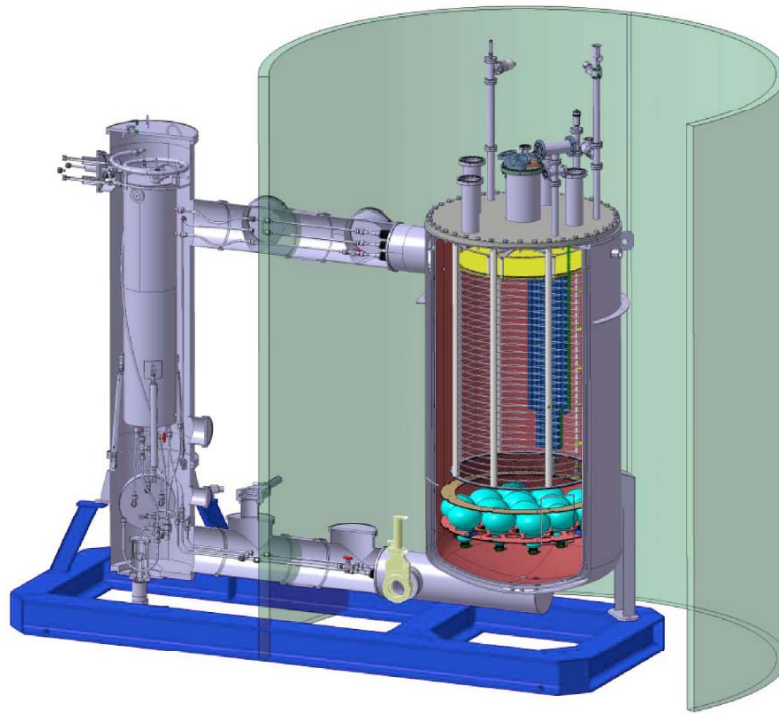


**Figure 33.** The ArDM inner cryostat containing the 850-kg LAr WIMP target connected to the liquid argon purification column to the left. These elements are located within a LAr bath held in an outer vessel (not shown). 14 PMTs at the bottom of the WIMP chamber view the wavelength-shifted scintillation light; the ionization charge is amplified by LEMs in the vapor phase. The HV multiplier can be seen in dark blue at the back of the chamber. The inner cryostat is surrounded by a neutron shield. (From [399]; with permission from IOP Publishing.)

tive readout anode providing orthogonal views with 3 mm position resolution [314]. A cascaded two-stage LEM is expected to provide readout sensitivity to a few ionization electrons.

Another innovative feature in ArDM is the use of a high voltage (HV) Greinacher multiplier (also known as Cockcroft-Walton) working in the LAr to bias the electrode grids as well as the field shaping rings located along the internal walls [400]. If stable HV operation is successful this may obviate the need for low-background, cryogenic HV feedthroughs in future large experiments, which are a common technical challenge in double-phase detectors. The ArDM multiplier has been successfully operated at 70 kV, corresponding to a drift field of 0.5 kV/cm; the stated goal is nearly 400 kV [399].

The double-phase detector is contained in a 1-m diameter, 2-m tall cryostat shown in Figure 33. This is surrounded by an internal neutron shield. A cryogenic pump drives a LAr purification column containing CuO, shown to the left of the cryostat. Electrons have to travel up to 120 cm in the ArDM TPC, which will take  $\sim 1$  ms even at high electric field; liquid purity is therefore a critical issue. The vessel and purification system are fully immersed in a separate LAr cooling bath, contained within a stainless steel cryostat (not shown). The temperature of the cooling bath is maintained with the aid of cryocoolers installed in a recondenser unit sitting on top of the recirculation/purification section [399].

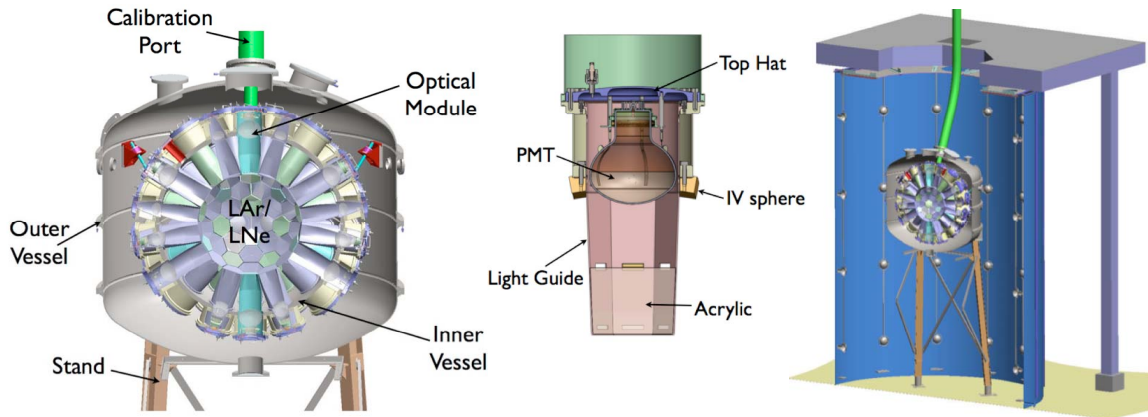


**Figure 34.** Schematic views of the MiniCLEAN experiment. Left: Cut-out of outer and inner vessels to reveal the arrangement of optical cassettes which view the 500 kg LAr (or LNe) WIMP target in  $4\pi$ . Center: detail of optical cassette (here termed ‘module’), including a photomultiplier attached to a stainless steel light guide with an acrylic plug covered in TPB at the front. Right: integrated experiment immersed in water tank. (From [393], courtesy A. Hime.)

The dominant background in ArDM will be the  $\beta$  decay of  $^{39}\text{Ar}$  present in atmospheric argon, which eventually will limit the sensitivity of the experiment. The rate of these electron recoils ( $\sim 1$  kBq) demands extremely high discrimination factors, but this may be compromised by event confusion within the  $\sim 1$  ms drift time. Operation with underground argon is envisaged by the collaboration [399].

The ArDM detector operated with liquid argon on a surface laboratory at CERN. A number of tests have been carried out and most sub-systems have been demonstrated. Commissioning underground at Canfranc is under way [392].

**The DEAP/CLEAN Collaboration** is pursuing a single-phase LAr program at SNOLab, exploiting pulse shape discrimination to overcome the dominant background of electron recoils from  $^{39}\text{Ar}$  [401]. This requires discrimination of at least a few parts in  $10^9$  for low energy electrons. This program emerged from the proposal to use LNe and LHe for low energy neutrino detection [38, 402]. Several R&D chambers, including MicroCLEAN and DEAP-1, have been built specifically to address the discrimination and other key issues, such as the scintillation efficiency for nuclear recoils in LAr [54, 102, 117].

Two experiments, MiniCLEAN and DEAP-3600, are presently being installed at SNOLab, with first data expected by the end of 2012 [403] and 2013 [394], respectively. Both have spherical targets containing natural argon — in the first instance — with the wavelength-shifted LAr scintillation viewed by photomultipliers over  $4\pi$  solid angle. There are similarities between the two designs, for which reason we describe the two systems in parallel, but there are also important differences, with technological solutions being explored for the design of the much larger instrument: a future CLEAN experiment (standing for Cryogenic Low Energy Astrophysics with Noble liquids) may contain 40–120 tonnes of active target [402, 393].

MiniCLEAN features a 45 cm diameter target containing 500 kg of liquid argon, with an expected fiducial mass of 100 kg defined by reconstruction of the scintillation vertex [393]. The Collaboration consider replacing the working medium with liquid neon for a subsequent run in order to exploit the different scaling of event rates from a possible WIMP signal ( $A^2$  dependence) and from backgrounds. This would also enable sensitivity to solar p-p neutrinos, which is another stated scientific goal. The optical readout employs 92 individual ‘cassettes’, each containing an 8-inch Hamamatsu R5912-02MOD photomultiplier viewing an acrylic plug coated with TPB wavelength shifter, as shown schematically in Figure 34. These are mounted onto a stainless steel inner vessel. The cryostat is completed by an outer vessel with 2.6 m diameter for thermal insulation and containment. The photomultipliers operate cold within the cryogen [246]. Shielding against PMT neutrons, one of the dominant backgrounds, is provided by the cryogen and acrylic layers in front of the PMTs. A second important background comes from the plating of radon daughters on the wavelength shifter, with emitters ejecting nuclear recoils into the active volume. This is mitigated by a strict cleaning procedure performed on the PMT cassettes *ex situ* and transfer to the detector under vacuum.

DEAP-3600 (Dark matter experiment with Argon and Pulse shape discrimination) has been under development since 2005 and is also at an advanced stage of construction [394]. Its 3,600 kg target (1,000 kg fiducial) of natural LAr is expected to be the first tonne-scale WIMP detector to operate. The geometry is depicted in Figure 35. The spherical volume is 85 cm in diameter, defined by a transparent acrylic vessel coated internally with TPB wavelength shifter. 255 PMTs (8-inch Hamamatsu R5912) view the target behind 50-cm long acrylic light guides, which keep the PMTs relatively warm and shield the target against their radioactivity. Plate-out of radon progeny on the inner surface of the acrylic vessel will be eliminated before first cool-down by use of a purpose-developed resurfacer device to remove the top few  $\mu\text{m}$  of acrylic prior to deposition of the TPB *in situ*. An outer containment vessel made from stainless steel completes the cryostat.

The two instruments will be installed within individual water tanks side by side at SNOLab’s Cube Hall. MiniCLEAN is cooled with a pulse-tube refrigerator with heat exchanger, whereas DEAP-3600 employs a liquid nitrogen thermosyphon to liquefy the argon. Both water tanks are instrumented with photomultipliers to provide a muon veto.

The success of these experiments is predicated on the achievement of sufficient discrimination power for the efficient rejection of the very high rate of electron recoils expected from the decay of  $^{39}\text{Ar}$  — a total activity of 3.6 kBq is expected in DEAP-3600, for example. Work with the MicroCLEAN and DEAP-1 prototypes has established useful levels of discrimination ( $\sim 10^{-6}$ ) but the baseline levels required for the full scale WIMP experiments have so far only been inferred through model-based extrapolations of statistically-limited datasets [404, 102]. Work with DEAP-1 underground is still ongoing, exploring more sophisticated pulse shape analyses than the fraction of prompt light used initially.

Pulse shape discrimination depends critically on the number of detected photoelectrons and so the light yield of these chambers is extremely important. From the performance achieved in the prototype chambers, along with Monte Carlo simulations of their experimental set-up, MiniCLEAN expect  $\sim 6$  photoelectrons per keV for electron recoils [403] and aim for a 50 keV WIMP-search threshold for  $10^{-9}$  discrimination. For DEAP-3600 the baseline is 8 photoelectrons per keV, along with a 60 keV threshold for nuclear recoils required to achieve  $10^{-10}$  discrimination [394].

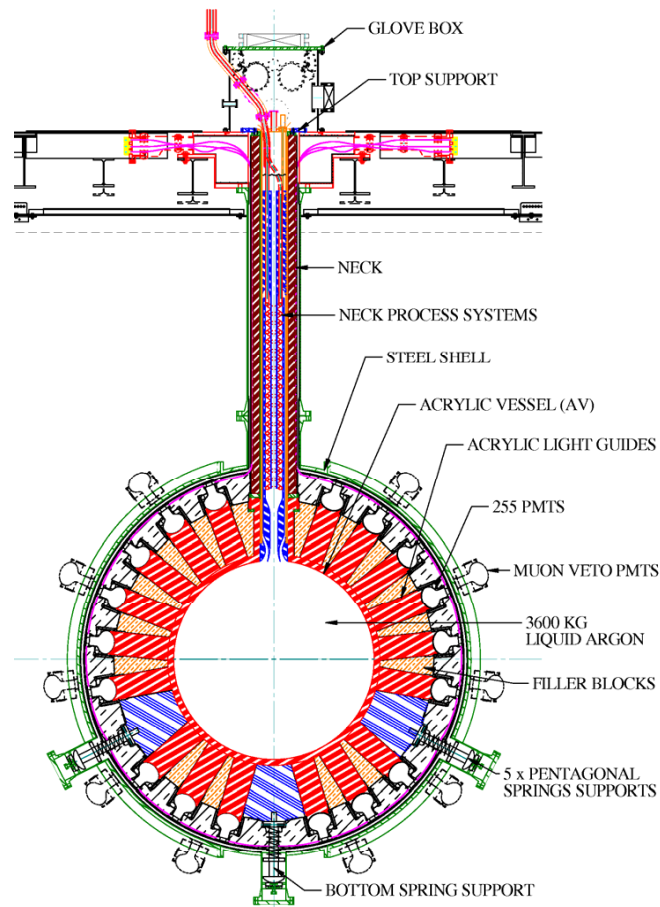


**Figure 35.** Schematic view of the DEAP-3600 single-phase liquid argon experiment. The acrylic vessel holds 3,600 kg of LAr, which is viewed by 255 8-inch photomultipliers through 50-cm light guides. These provide neutron shielding and thermal insulation between the cryogenic acrylic vessel and the ‘warm’ PMTs. The inner detector is housed in a large stainless steel spherical vessel, which itself is immersed in an 8-meter diameter water shielding tank. (From [394], courtesy M. Boulay; image credit K. Dering.)

After a 3-year run of DEAP-3600, expected to be free of background, the project may operate the detector with underground-sourced argon, affording some gain in WIMP-search threshold due to the lower requirements on discrimination, and so confirm any signal hints observed in the first run. MiniCLEAN have adopted a different strategy: a first 2-year long run with natural argon might be followed by operation with liquid neon, from which a lower WIMP signal rate is expected in the canonical elastic scattering model. This will provide a distinct signature from dominant background sources, which are expected to increase in rate (e.g. neutrons) or to remain constant (surface contamination).

## 7. Detecting coherent neutrino scattering with the noble liquids

Some progress towards a first measurement of coherent neutrino-nucleus elastic scattering using liquefied noble gases has also taken place in recent years. Efforts have focused on two types of very intense source of low and intermediate energy neutrinos: nuclear reactors and accelerator-driven neutron spallation sources.

Nuclear power reactors produce an average of 6 antineutrinos per  $^{235}\text{U}$  fission, with a total of  $5 \cdot 10^{20}$   $\bar{\nu}$ /s emitted from a facility with 3 GW thermal output — of which several dozen operate presently around the world [405]. At standoff distances of 30 m down to 10 m the antineutrino flux is  $\sim 5\text{--}50 \cdot 10^{12}$   $\bar{\nu}/\text{cm}^2/\text{s}$ . Antineutrinos offer interesting prospects for nuclear non-proliferation activities since no amount of line-of-sight shielding can mask the count rates observed by a nearby detector; direct monitoring of the rate of production of fissile material or the degree of fuel burn-up becomes possible [406].

A few suitable spallation sources exist around the world and, to our knowledge, CNS has been considered only at two, namely the new Spallation Neutron Source (SNS) at Oak Ridge National Laboratory (US) and the ISIS facility at the Rutherford Appleton Laboratory (UK). The potential for neutrino physics at such facilities — including CNS — has long been recognized (e.g. [407, 408, 23, 409]). The SNS yields  $\sim 10^{15}$   $\nu/\text{s}$  (a factor of  $\sim 10$  higher than at ISIS). These neutrinos (equal fluxes of  $\nu_e, \nu_\mu, \bar{\nu}_\mu$ ) come from the decay-at-rest of pions and muons produced by the interaction of high-energy protons on a spallation target. Although reactors provide much higher fluxes, the pulsed nature of the proton beam (typically  $\sim 0.1\text{--}1$   $\mu\text{s}$  pulse width at 40–60 Hz repetition) and higher neutrino energies (e.g. 30 MeV for  $\nu_\mu$  versus a few MeV for reactor  $\bar{\nu}$ ) are clear advantages in this instance. Similar distances to the spallation target are viable, but shielding against the very penetrating spallation neutrons must be a prime consideration, influencing the distance as well as angle to the incident proton beam.

In nature, core-collapse supernovae radiate the overwhelming majority of their energy as neutrinos and, were one to occur in our galaxy, a multi-second burst containing multiple events would be observed by the next generation of DM detectors operating underground [410]. In general,  $^8\text{B}$  solar neutrinos will pose a nuclear recoil background for low-threshold DM searches ( $\leq 3$  keV) already at WIMP-nucleon cross sections of  $\sim 10^{-10}$  pb ( $10^{-46}$   $\text{cm}^2$ ) [411]. For higher thresholds, atmospheric neutrinos and diffuse supernova neutrino background (DSNB) — the past history of all supernova explosions — will dominate below  $\sim 10^{-12}$  pb ( $10^{-48}$   $\text{cm}^2$ ) [412].

The experimental challenge is manifest in Figure 1, which depicts expected CNS event rates at ISIS and at a nuclear reactor. Extremely low thresholds are required to achieve sensible event rates at either location. The trade-off mentioned in Section 3 between scattering rate ( $\propto E_\nu^2 N^2/A$ ) and the recoil spectrum ( $E_r^{\text{max}} \propto E_\nu^2/A$ ), with  $N$  and  $A$  the neutron and atomic numbers of the target, respectively, is patent in the figure. Xenon works best with the harder neutrino spectrum of the spallation source ( $E_\nu < 53$  MeV), whereas argon (or, better still, neon) would be better suited for reactor antineutrinos ( $E_\nu \lesssim 10$  MeV).

Naturally, both types of facility are extremely powerful neutron sources too. Extensive shielding is required, and an anti-coincidence neutron detector is probably essential. Difficulties associated with a surface deployment compound the problem. Atmospheric muons may be disruptive, especially for double-phase detectors: a relatively small detector with 60 cm diameter would expe-

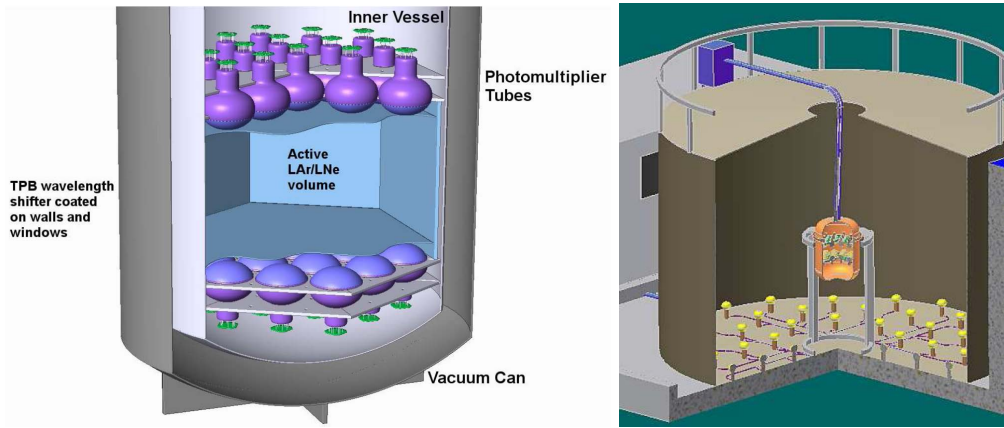


**Figure 36.** Diagram of the CLEAR experiment proposed for SNS at Oak Ridge. Left: the LAr/LNe scintillation target is defined by a TPB-coated chamber viewed by 38 PMTs immersed in the liquid, contained in a vacuum cryostat (image credit J. Nikkel). Right: the detector would be located in an instrumented water tank for shielding and muon veto (image credit J. Fowler). (From [413], courtesy K. Scholberg.)

rience  $\sim 50 \mu\text{s}$  depositing tens of MeV per event, whilst conducting a search for rare events at keV energies. In addition, cosmic-ray neutrons as well as those arising in muon-initiated cascades are serious backgrounds too.

The prospect of deploying noble liquid detectors specifically for measuring CNS has been studied by a few groups around the world. We mention briefly the most advanced below — whilst noting that other measurement technologies, notably cryogenic germanium, are also contenders for a first observation.

**The CLEAR Experiment** (Coherent Low Energy A (Nuclear) Recoils) was conceived for deployment at SNS, at a distance of 46 m to the spallation target and in the backward direction with respect to the proton beam. A single-phase, scintillation-only design was adopted, allowing interchangeable liquid argon and liquid neon targets (456 kg and 391 kg, respectively), within an active volume 60 cm in diameter and 44 cm in height [413]. Significant recoil energies can result in these targets, especially in LNe where the recoil spectrum extends to  $>100$  keV, allowing use of pulse shape discrimination from the scintillation signal. The VUV light is wavelength-shifted by TPB evaporated onto the PTFE chamber walls as well as two fused silica or acrylic plates, and detected by 38 Hamamatsu R5912-02MOD photomultipliers (Figure 36). The detector would be located inside an instrumented water tank for shielding and cosmic-ray veto.

A significant event rate is expected in this configuration. Assuming SNS operation at a power of 1.4 MW, a live running time of  $2.4 \cdot 10^7$  s/yr for each target material, and a beam timing cut of  $6 \cdot 10^{-4}$  efficiency, CLEAR should register  $\sim 600$  events/year with LAr above a 20 keV nuclear recoil threshold, and  $\sim 250$  events/year for a LNe run with 30 keV threshold (including 50% recoil acceptance after pulse shape discrimination). The dominant background is from  $^{39}\text{Ar}$ , PMT  $\gamma$ -rays, radon daughters and neutrons produced from beam loss in the transport line (which were found to be higher than those from the spallation target itself). Although there has been no progress recently due to lack of funding, the Collaboration still deem the project to be technically viable.

A very different and innovative approach was proposed in 2004 [24]: if measurement of single ionization electrons could be achieved through proportional scintillation in double-phase argon, this would open the way to utilizing these detectors in electron counting mode (i.e. sub-threshold in S1). This started a LAr-based programme at Lawrence Livermore National Laboratory (US) aimed specifically at nuclear reactor monitoring. Deployment in the ‘tendon gallery’ of a 3.4 GW<sub>th</sub> reactor, 25 m away from the core, is being considered. A schematic of a possible prototype detector is shown in Figure 37. This might achieve  $\sim 80$  counts/day above a threshold of 2 ionization electrons measured by proportional scintillation.  $^{39}\text{Ar}$  is again a problematic background also in this regime, which would require use of underground argon. Preliminary work with a smaller chamber is underway, in order to characterize the response to single electrons and to measure the ionization yield in LAr at very low energies [414, 415].

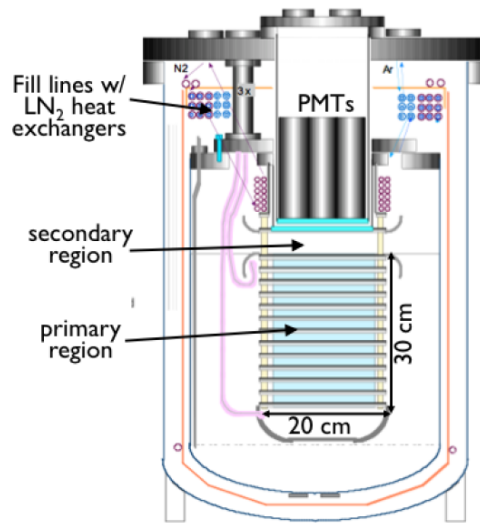


**Figure 37.** Possible design of a 10-kg double-phase Ar detector for deployment at a nuclear power reactor. Measurement of CNS will be attempted in the 1–10 ionization electron regime. (Courtesy A. Bernstein.)

With this type of measurement in mind, the ZEPLIN program characterized the single electron signature and its production mechanisms in double-phase xenon: first using ZEPLIN-II data [64], then with ZEPLIN-III [37] (see also Figure 6). Similar work with a surface prototype was conducted at ITEP (Russia) [416]. The excellent signal-to-noise ratio achieved on the single electron signature and the low background measured at two electrons and above led the ZEPLIN-III Collaboration to explore further a deployment of this detector at a nuclear reactor and at the ISIS facility (UK) [37]. The predicted CNS signal and dominant internal backgrounds, as measured through proportional scintillation with a yield of 30 photoelectrons per electron, are reproduced in Figure 38. These assume ionization yields as measured down to 4 keV recoil energy [67] and extrapolated to zero in an *ad hoc* way below that.

It was found that the reactor signal was salient over background above a 3-electron threshold, with  $\gtrsim 2,000$  events expected in 10 kg·yr live exposure (at 10 m from a 3 GW<sub>th</sub> reactor core). These signals are below the scintillation threshold, so no discrimination can be relied upon.



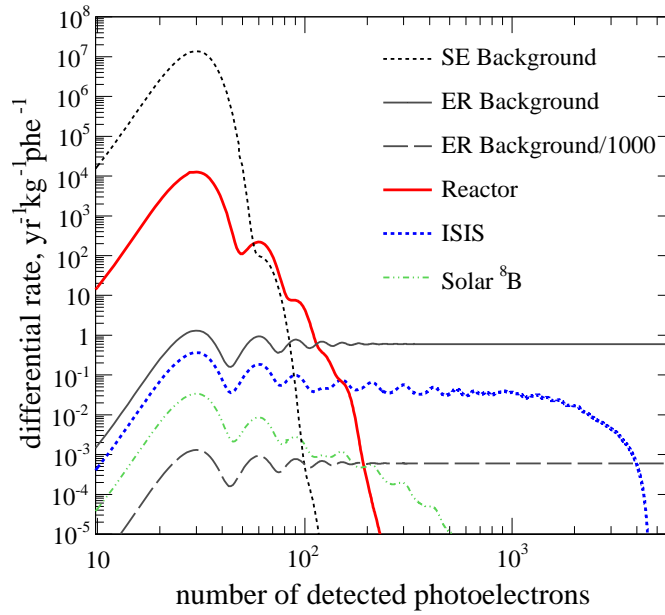


**Figure 38.** Neutrino-induced ionization spectra expected in the liquid target of ZEPLIN-III at a nuclear reactor and at the ISIS stopped pion source. CNS from solar  $^8\text{B}$  is also shown for reference. The peak structure reflects discrete numbers of ionization electrons measured by electroluminescence. Single electron background and internal electron recoil backgrounds (1 dru) are also shown; the latter is reduced by  $\sim 1000$  times at ISIS due to the beam-coincident measurement [37]. (Courtesy ZEPLIN-III Collaboration; with permission from Springer Science and Business Media.)

The prospects for detecting this signature with a beam-coincident measurement at the stopped pion source seemed also encouraging (at 10 m from the spallation target, with a neutrino flux of  $\sim 3.6 \cdot 10^6 \text{ cm}^{-2} \text{ s}^{-1}$  per flavor). Owing to the much harder energy spectrum, approximately half of the detected events should produce measurable S1 and S2 signals, thus allowing three-dimensional position reconstruction and electron/nuclear recoil discrimination; this would provide an important cross-check for the part of the spectrum detected through ionization only. At ISIS, non-beam related backgrounds could be significantly reduced with a beam coincidence cut with  $10^{-3}$  efficiency — corresponding to a measurement window of  $20 \mu\text{s}$  every 20 ms:  $\sim 700$  signal events were expected above 3 emitted electrons in a 10 kg-yr exposure.

The possibility of an ISIS deployment was subsequently studied in more detail by one of us (HA), after a possible location for the experiment was identified near the spallation target, at  $90^\circ$  to the proton beam. The target-target distance would be 8.66 m, with the line-of-sight shielding including an existing  $\approx 5$  m of iron and  $\approx 1$  m of concrete; additional neutron shielding would be added to the full shield used underground at Boulby (including the neutron veto). With realistic parameters considered for the accelerator, the spallation target and the experiment, the signal rate expected in a 6 kg fiducial LXe volume was only 52 events/year. Cosmogenic and internal neutrons were studied by Monte Carlo simulation; they were found to contribute  $\sim 30$  unvetoes events/year in the recoil energy range 0.1–10 keV within the beam coincidence window, but these could be further subtracted with an off-beam measurement. Electron recoils backgrounds would

add a further  $\sim 10$  events/year before discrimination. However, beam-coincident spallation neutrons above 20 MeV were found to overwhelm a measurement at that location, irrespective of any additional shielding. A 1- $\mu$ s delayed measurement targeting follow-on muon-decay neutrinos only (pion decay neutrinos are essentially prompt) was proposed to solve this problem for SNS neutrino studies [417]. This would eliminate high-energy beam-induced backgrounds, as delayed neutrons can be shielded effectively. However, this is only possible for events containing both S1 and S2 pulses (since S1 carries the event timing information). The overall timing cut would retain  $\sim 25\%$  signal acceptance, leaving 13 events per year. This rate was deemed too low to justify pursuing the experiment further at that particular location — at least with that target mass, which was the main limiting factor in this instance.

**Finally, the RED Collaboration** (Russia) is pursuing a promising effort for a first detection of CNS. They propose a LXe/LAr experiment named RED-100 (Russian Emission Detector). The baseline design features 200 kg of liquid xenon, with approximately 100 kg of fiducial mass; liquid argon is also a possible target, with 100 kg of total mass for a 50 kg fiducial.

The detector design is illustrated in Figure 39. The sensitive volume is 45 cm in diameter and 45 cm in height, defined by optically transparent mesh electrodes and lateral field-shaping rings. The envisaged drift field is 0.5–1 kV/cm in the liquid and 7–10 kV/cm in the 1-cm thick gas phase. The team plan to use two arrays of low-background Hamamatsu R11410-10 photomultipliers (19 phototubes each). The mean expected number of photoelectrons per electron in the secondary scintillation region is 80 [418].

To study the response of LXe and LAr to sub-keV nuclear recoils, the teams are preparing a setup at the MEPHI research reactor. This will include a neutron filter to prepare a quasi-monochromatic 24 keV neutron beam, irradiating a smaller double-phase chamber (this was one of

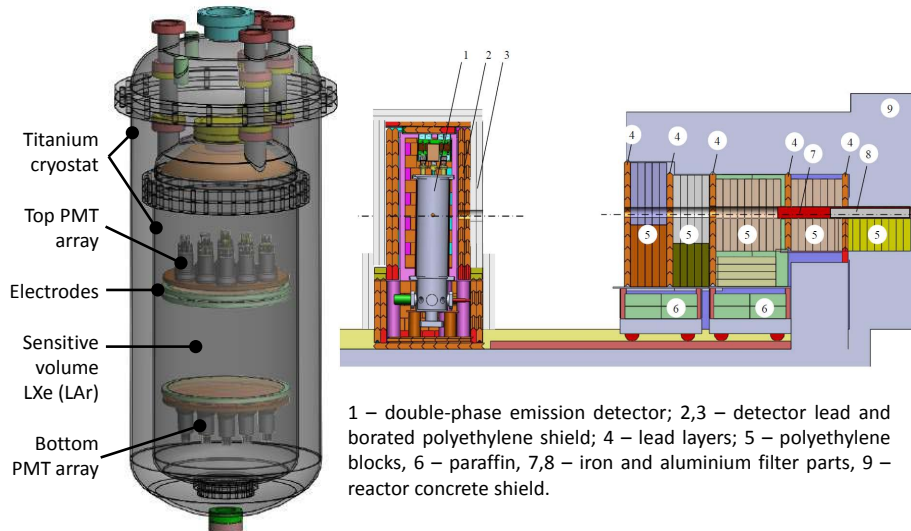


**Figure 39.** The RED-100 double-phase detector is shown left; it will contain 200(100) kg of LXe(LAr). The right panel shows the smaller prototype chamber exposed to 24 keV neutrons at the MEPHI nuclear reactor, to study the response to very low energy nuclear recoils. (Courtesy RED Collaboration.)

the prototypes for ZEPLIN-III, with 7 photomultipliers). This experiment will allow the measurement of the ionization and scintillation yields with maximum recoil energies of  $\sim 0.7$  keV for Xe and  $\sim 2.3$  keV for Ar.

Two deployments of RED-100 are envisaged. Firstly, at 19 m from the core of the Kalininskaya nuclear power station, where the antineutrino flux is  $1.35 \cdot 10^{13} \text{ cm}^{-2}\text{s}^{-1}$ ;  $\sim 20$  events/day are expected in 100 kg of LXe above a 2 ionization electron threshold, and  $\sim 200$  events/day in 100 kg of LAr. An experiment at SNS is also being considered, 40 m from the spallation target and 10 m underground; the neutrino flux there would be  $5 \cdot 10^6 \text{ cm}^{-2}\text{s}^{-1}$  (per flavor). The expected count rates are  $\sim 1,400$  and  $\sim 400$  events/100 kg/year for LXe and LAr, respectively.

## 8. Conclusion

Liquefied noble gas technology has been developed into well established radiation and particle detection techniques, having found a wide range of application. Technical challenges have been overcome over the last decade to demonstrate that these media can provide low energy threshold, low background, target mass scalability and stable operation over long periods. In particular, double-phase liquid/gas detectors are now at the forefront of low energy particle physics. They are top contenders for a first direct detection of WIMP dark matter as well as of coherent neutrino-nucleus elastic scattering.

In dark matter searches, xenon detectors have made the most progress so far, but liquid argon experiments are also close to data-taking underground; liquid neon setups are being considered. We present in Figure 40 WIMP-nucleon exclusion limits reported by liquid noble gas experiments. These have covered over three orders of magnitude in scalar cross-section sensitivity in just over a decade, and there are signs that this rate is accelerating as self-shielding begins to pay off with the larger target masses now being deployed. XENON100 offers presently the tightest experimental constraint from any technology.

Prospects for a first detection of CNS have also improved due to the excellent sensitivity afforded by the ionization response in double-phase detectors. This quest goes hand in hand with the search for light WIMPs, both involving sub-keV detection thresholds in scalable target technologies. A first measurement of CNS may be close, although some challenges remain in controlling neutron backgrounds at the neutrino sources.

Practically all current dark matter experiments using the double-phase technique rely on measurement of the ionization signal via secondary scintillation in a uniform electric field detected by a large number of photomultiplier tubes. The quest for sensitivity stimulated development of new PMTs capable of operating at cryogenic temperatures and having high quantum efficiency for xenon VUV light. In the last two decades, the quantum efficiency at these wavelengths has doubled. Progress in reducing the radioactivity background has been even more remarkable — a factor of  $\sim 1,000$  has been achieved over this period.

Alternative readout techniques, such as solid state photon detectors and micro-pattern detectors for charge amplification, have continued to be developed. The case for these approaches over the traditional PMT readout has not been made so far — at least at low energies. However, at higher energies and especially for very large detectors new solutions may be advantageous or even necessary (e.g. LAr TPCs for neutrino detection).

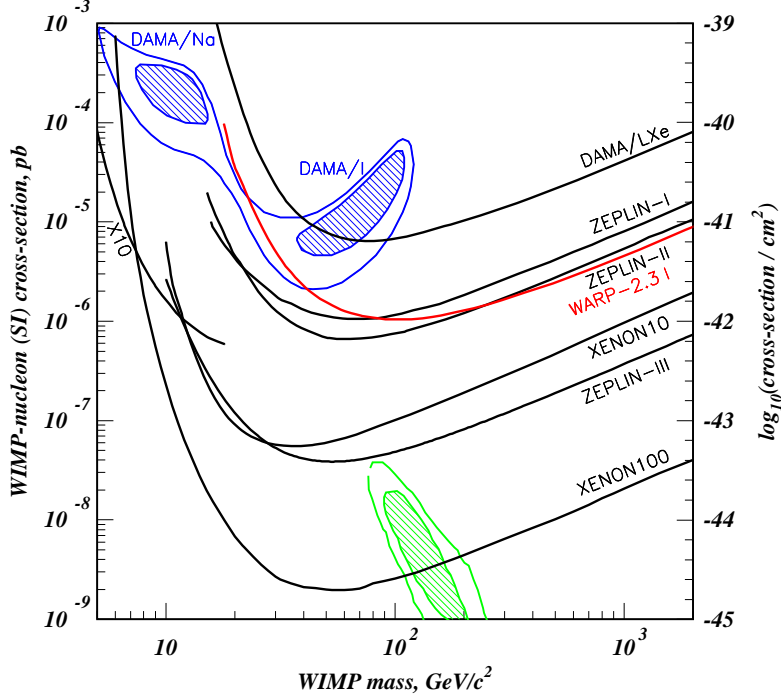


**Figure 40.** Spin-independent WIMP-nucleon scattering cross-section limits (90% CL) published from liquid xenon (black) and liquid argon experiments (red); in order of publication: DAMA/LXe [375], ZEPLIN-I [44], ZEPLIN-II [49], WARP 2.3-I [55], XENON10 [377, 126] (low energy analysis [210]), ZEPLIN-III [56] and XENON100 [215]. The parameter space favored by Constrained MSSM after  $1 \text{ fb}^{-1}$  of LHC data is shown in green [419]. The DAMA/NaI annual modulation result [420] interpreted as a nuclear recoil WIMP signal in [421] is also shown (in blue) for reference.

The success of experiments that rely on the double-phase technique depends on a good understanding of the physics involved in the detection process. In our view most processes are now well understood; nevertheless, some knowledge gaps remain in the keV and sub-keV energy regions, in particular regarding the response to nuclear recoils. Exploration of this energy regime will be essential to enable a first measurement of CNS, and these experiments are now contributing to this effort.

In the year 2012 we celebrated the silver jubilee of direct dark matter searches [422]. The noble liquids have now taken a clear lead in trying to answer this most important of scientific questions. The authors conclude by reaffirming their belief that the double-phase technique will maintain a strong position in low energy particle physics in the future.

## Acknowledgments

The authors are grateful to E. Aprile, D. McKinsey, A. Mangiarotti and A. Hitachi for fruitful discussions. We also wish to thank R. Ferreira Marques, P. Mendes, A. Currie and C. Ghag for reading the manuscript and for useful suggestions. A special thank you is due to A. Breskin, who inspired this work and patiently supported it through the whole writing process.

## References

- [1] G. W. Hutchinson, *Ionization in liquid and solid argon*, *Nature* **162** (1948) 610.
- [2] J. H. Marshall, *A liquid argon ionization chamber measurement of the shape of the beta-ray spectrum of  $^{40}\text{K}$* , *Phys. Rev.* **91** (1953) 905–909.
- [3] J. A. Northrop and R. A. Nobles, *Some aspects of gas scintillation counters*, *IRE Trans. Nuc. Sci.* **3** (1956) 59–61.
- [4] J. A. Northrop, J. M. Gursky, and A. E. Johnsruud, *Further work with noble element scintillators*, *IRE Trans. Nuc. Sci.* **5** (1958) 81–87.
- [5] A. S. Barabash and A. I. Bolozdynya, *Liquid Ionization Detectors*. Energoatomizdat, 1993. (in Russian).
- [6] M. I. Lopes and V. Chepel, *Rare gas liquid detectors*, in *Electronic Excitations in Liquefied Rare Gases* (W. Schmidt and E. Illenberger, eds.), pp. 331–388, American Scientific Publishers, 2005.
- [7] E. Aprile, A. E. Bolotnikov, A. I. Bolozdynya, and T. Doke, *Noble Gas Detectors*. Wiley-VCH Verlag, 2006.
- [8] E. Aprile and T. Doke, *Liquid xenon detectors for particle physics and astrophysics*, *Rev. Mod. Phys.* **82** (2010) 2053–2097.
- [9] A. I. Bolozdynya, *Emission Detectors*. World Scientific, 2010.
- [10] D. Y. Akimov, *Techniques and results for the direct detection of dark matter (review)*, *Nucl. Instrum. Meth. A* **628** (2011) 50–58.
- [11] G. Bertone, *Particle Dark Matter: Observations, Models and Searches*. Cambridge University Press, 2010.
- [12] M. W. Goodman and E. Witten, *Detectability of certain dark-matter candidates*, *Phys. Rev. D* **31** (1985) 3059–3063.
- [13] D. Y. Akimov, *Experimental methods for particle dark matter detection (review)*, *Instrum. Exp. Tech.* **44** (2001) 575–617.
- [14] T. J. Sumner, *Experimental searches for dark matter*, *Living Rev. Relativ.* **5** (2002) 4.
- [15] R. J. Gaitskell, *Direct detection of dark matter*, *Ann. Rev. Nucl. Part. Science* **54** (2004) 315–359.
- [16] V. A. Ryabov, V. A. Tsarev, and A. M. Tskhovrebov, *The search for dark matter particles*, *Physics-Uspekhi* **51** (2008) 1091–1121.
- [17] E. Figueroa-Feliciano, *Direct detection searches for WIMP dark matter*, *Prog. Part. Nuc. Phys.* **66** (2011) 661–673.
- [18] M. Cirelli, *Indirect searches for dark matter*, *Pramana* **79** (2012) 1021–1043.
- [19] P. S. Barbeau, J. I. Collar, and O. Tench, *Large-mass ultralow noise germanium detectors: performance and applications in neutrino and astroparticle physics*, *J. Cosmol. Astropart. Phys.* **9** (2007) 9.
- [20] A. Drukier and L. Stodolsky, *Principles and applications of a neutral-current detector for neutrino physics and astronomy*, *Phys. Rev. D* **30** (1984) 2295–2309.
- [21] J. D. Lewin and P. F. Smith, *Review of mathematics, numerical factors, and corrections for dark matter experiments based on elastic nuclear recoil*, *Astropart. Phys.* **6** (1996) 87–112.

- [22] A. Bueno, M. C. Carmona, J. Lozano, and S. Navas, *Observation of coherent neutrino-nucleus elastic scattering at a beta beam*, *Phys. Rev. D* **74** (2006) 033010.
- [23] K. Scholberg, *Prospects for measuring coherent neutrino-nucleus elastic scattering at a stopped-pion neutrino source*, *Phys. Rev. D* **73** (2006) 033005.
- [24] C. Hagmann and A. Bernstein, *Two-phase emission detector for measuring coherent neutrino-nucleus scattering*, *IEEE Trans. Nuc. Sci.* **51** (2004) 2151–2155.
- [25] EXO collaboration, N. Ackerman, B. Aharmim, M. Auger, D. J. Auty, P. S. Barbeau, K. Barry, et al., *Observation of two-neutrino double-beta decay in  $^{136}\text{Xe}$  with the EXO-200 detector*, *Phys. Rev. Lett.* **107** (2011) 212501.
- [26] KAMLAND-ZEN collaboration, A. Gando, Y. Gando, H. Hanakago, H. Ikeda, K. Inoue, R. Kato, et al., *Measurement of the double- $\beta$  decay half-life of  $^{136}\text{Xe}$  with the KamLAND-Zen experiment*, *Phys. Rev. C* **85** (2012) 045504.
- [27] XMASS collaboration, K. Abe, J. Hosaka, T. Iida, M. Ikeda, K. Kobayashi, Y. Koshio, et al., *Distillation of liquid xenon to remove krypton*, *Astropart. Phys.* **31** (2009) 290–296.
- [28] A. I. Bolozdynya, P. P. Brusov, T. Shutt, C. E. Dahl, and J. Kwong, *A chromatographic system for removal of radioactive  $^{85}\text{Kr}$  from xenon*, *Nucl. Instrum. Meth. A* **579** (2007) 50–53.
- [29] D. Acosta-Kane, R. Acciarri, O. Amaize, M. Antonello, B. Baibussinov, M. B. Ceolin, et al., *Discovery of underground argon with low level of radioactive  $^{39}\text{Ar}$  and possible applications to WIMP dark matter detectors*, *Nucl. Instrum. Meth. A* **587** (2008) 46–51.
- [30] D. G. Cerdeño and A. M. Green, *Direct detection of WIMPs*, in *Particle Dark Matter: Observations, Models and Searches* (G. Bertone, ed.), p. 347, Cambridge University Press, Feb., 2010. arXiv:1002.1912.
- [31] R. H. Helm, *Inelastic and elastic scattering of 187-MeV electrons from selected even-even nuclei*, *Phys. Rev.* **104** (1956) 1466–1475.
- [32] J. Engel, *Nuclear form factors for the scattering of weakly interacting massive particles*, *Phys. Lett. B* **264** (1991) 114–119.
- [33] G. Duda, A. Kemper, and P. Gondolo, *Model-independent form factors for spin-independent neutralino-nucleon scattering from elastic electron scattering data*, *J. Cosmol. Astropart. Phys.* **2007** (2007) 012.
- [34] R. L. Burman, A. C. Dodd, and P. Plischke, *Neutrino flux calculations for the ISIS spallation neutron facility*, *Nucl. Instrum. Meth. A* **368** (1996) 416–424.
- [35] D. Z. Freedman, *Coherent effects of a weak neutral current*, *Phys. Rev. D* **9** (1974) 1389–1392.
- [36] D. Akimov, A. Bondar, A. Burenkov, and A. Buzulutskov, *Detection of reactor antineutrino coherent scattering off nuclei with a two-phase noble gas detector*, *JINST* **4** (2009) P06010.
- [37] E. Santos, B. Edwards, V. Chepel, H. Araújo, D. Akimov, E. Barnes, et al., *Single electron emission in two-phase xenon with application to the detection of coherent neutrino-nucleus scattering*, *JHEP* **2011** (2011) 1–20.
- [38] D. N. McKinsey and J. M. Doyle, *Liquid helium and liquid neon – sensitive, low background scintillation media for the detection of low energy neutrinos*, *ArXiv e-prints* (July, 1999) , [9907314].

- [39] Y. Suzuki, *Low energy solar neutrino detection by using liquid xenon*, in *Low Energy Solar Neutrino Detection, Proc. 2nd Int. Workshop, 4-5 December 2000, Tokyo, Japan* (Y. Suzuki, M. Nakahata, and S. Moriyama, eds.), pp. 81–90, World Scientific, 2002. DOI.
- [40] ZEPLIN-III collaboration, D. Y. Akimov, H. M. Araújo, E. J. Barnes, V. A. Belov, A. A. Burenkov, V. Chepel, et al., *The ZEPLIN-III anti-coincidence veto detector*, *Astropart. Phys.* **34** (2010) 151–163.
- [41] C. Ghag, D. Y. Akimov, H. M. Araújo, E. J. Barnes, V. A. Belov, A. A. Burenkov, et al., *Performance of the veto detector incorporated into the ZEPLIN-III experiment*, *Astropart. Phys.* **35** (2011) 76–86.
- [42] R. Bernabei, P. Belli, A. Bussolotti, F. Cappella, R. Cerulli, C. J. Dai, et al., *The liquid xenon set-up of the DAMA experiment*, *Nucl. Instrum. Meth. A* **482** (2002) 728–743.
- [43] R. Lüscher, *Dark matter search at Boulby mine*, *Eur. Phys. J. C* **33** (2004) s968–s970.
- [44] ZEPLIN-I collaboration, G. J. Alner, H. Araújo, G. J. Arnison, J. C. Barton, A. Bewick, C. Bungau, et al., *First limits on nuclear recoil events from the ZEPLIN-I galactic dark matter detector*, *Astropart. Phys.* **23** (2005) 444–462.
- [45] N. J. C. Spooner, *The UKDMC dark matter xenon programme – new WIMP limits and progress towards 1 tonne*, in *Technique and Application of Xenon Detectors, Proc. Int. Workshop XENON01, Kashiwa, Japan 2001* (Y. Suzuki, M. Nakahata, Y. Koshio, and S. Moriyama, eds.), pp. 68–77, World Scientific, 2003. DOI.
- [46] B. A. Dolgoshein, V. N. Lebedenko, and B. U. Rodionov, *New method of registration of ionising particle tracks in condensed matter*, *Sov. Phys. JETP Lett.* **11** (1970) 351–353.
- [47] A. S. Barabash and A. I. Bolozdynya, *How to detect the dark matter of the galaxy if it is made up of weakly interacting neutral particles with masses 1-10 GeV/c<sup>2</sup>*, *Sov. Phys. JETP Lett.* **49** (1989) 356–359.
- [48] P. Benetti, E. Calligarich, R. Dolfini, A. G. Berzolari, F. Mauri, L. Mazzone, et al., *Detection of energy deposition down to the keV region using liquid xenon scintillation*, *Nucl. Instrum. Meth. A* **327** (1993) 203–206.
- [49] ZEPLIN-II collaboration, G. J. Alner, H. M. Araújo, A. Bewick, C. Bungau, B. Camanzi, M. J. Carson, et al., *First limits on WIMP nuclear recoil signals in ZEPLIN-II: A two-phase xenon detector for dark matter detection*, *Astropart. Phys.* **28** (2007) 287–302.
- [50] ZEPLIN-III collaboration, D. Y. Akimov, G. J. Alner, H. M. Araújo, A. Bewick, C. Bungau, A. A. Burenkov, et al., *The ZEPLIN-III dark matter detector: Instrument design, manufacture and commissioning*, *Astropart. Phys.* **27** (2007) 46–60.
- [51] S. Suzuki, *A new liquid xenon scintillation detector to detect and study low energy signals from WIMPs*, *Butsuri (Membership Journal of the Physical Society of Japan)* **53** (1998) 181. (In Japanese).
- [52] H. Wang, *Xenon as a detector for dark matter search*, *Phys. Rep.* **307** (1998) 263–267.
- [53] E. Aprile, C. E. Dahl, L. de Viveiros, R. J. Gaitskell, K. L. Giboni, J. Kwong, et al., *Simultaneous measurement of ionization and scintillation from nuclear recoils in liquid xenon for a dark matter experiment*, *Phys. Rev. Lett.* **97** (2006) 081302.
- [54] W. H. Lippincott, K. J. Coakley, D. Gastler, A. Hime, E. Kearns, D. N. McKinsey, et al., *Scintillation time dependence and pulse shape discrimination in liquid argon*, *Phys. Rev. C* **78** (2008) 035801.

- [55] WARP collaboration, P. Benetti, R. Acciarri, F. Adamo, B. Baibussinov, M. Baldo-Ceolin, M. Belluco, et al., *First results from a dark matter search with liquid argon at 87 K in the Gran Sasso underground laboratory*, *Astropart. Phys.* **28** (2008) 495–507.
- [56] ZEPLIN-III collaboration, D. Y. Akimov, H. M. Araújo, E. J. Barnes, V. A. Belov, A. Bewick, A. A. Burenkov, et al., *WIMP-nucleon cross-section results from the second science run of ZEPLIN-III*, *Phys. Lett. B* **709** (2012) 14–20.
- [57] XENON100 collaboration, E. Aprile, K. Arisaka, F. Arneodo, A. Askin, L. Baudis, A. Behrens, et al., *Dark matter results from 100 live days of XENON100 data*, *Phys. Rev. Lett.* **107** (2011) 131302.
- [58] L. W. Kastens, S. B. Cahn, A. Manzur, and D. N. McKinsey, *Calibration of a liquid xenon detector with  $^{83m}\text{Kr}$* , *Phys. Rev. C* **80** (2009) 045809.
- [59] A. Manalaysay, T. Marrodán Undagoitia, A. Askin, L. Baudis, A. Behrens, A. D. Ferella, et al., *Spatially uniform calibration of a liquid xenon detector at low energies using  $^{83m}\text{Kr}$* , *Rev. Sci. Instrum.* **81** (2010) 073303.
- [60] E. Aprile, R. Budnik, B. Choi, H. A. Contreras, K.-L. Giboni, L. W. Goetzke, et al., *Measurement of the scintillation yield of low-energy electrons in liquid xenon*, *ArXiv e-prints* (2012) , [1209.3658].
- [61] A. Manzur, A. Curioni, L. Kastens, D. N. McKinsey, K. Ni, and T. Wongjirad, *Scintillation efficiency and ionization yield of liquid xenon for monoenergetic nuclear recoils down to 4 keV*, *Phys. Rev. C* **81** (2010) 025808.
- [62] J. F. Ziegler, J. P. Biersack, and M. D. Ziegler, *SRIM – The Stopping Power and Range of Ions in Matter*. SRIM Co, 2008. Available at <http://www.srim.org>.
- [63] T. Doke, *Ionization and excitation by high energy radiation*, in *Electronic Excitations in Liquefied Rare Gases* (W.F.Schmidt and E.Illenberg, eds.), pp. 71–93, American Scientific Publishers, 2005.
- [64] B. Edwards, H. M. Araújo, V. Chepel, D. Cline, T. Durkin, J. Gao, et al., *Measurement of single electron emission in two-phase xenon*, *Astropart. Phys.* **30** (2008) 54–57.
- [65] P. F. Sorensen, *A Position-Sensitive Liquid Xenon Time-Projection Chamber for Direct Detection of Dark Matter: The XENON10 Experiment*. PhD thesis, Brown University, 2008.
- [66] P. Sorensen, A. Manzur, C. E. Dahl, J. Angle, E. Aprile, F. Arneodo, et al., *The scintillation and ionization yield of liquid xenon for nuclear recoils*, *Nucl. Instrum. Meth. A* **601** (2009) 339–346.
- [67] M. Horn, V. A. Belov, D. Y. Akimov, H. M. Araújo, E. J. Barnes, A. A. Burenkov, et al., *Nuclear recoil scintillation and ionisation yields in liquid xenon from ZEPLIN-III data*, *Phys. Lett. B* **705** (2011) 471–476.
- [68] R. L. Platzman, *Total ionization in gases by high-energy particles: An appraisal of our understanding*, *Int. J. Appl. Rad. Isot.* **10** (1961) 116–127.
- [69] T. Doke, A. Hitachi, S. Kubota, A. Nakamoto, and T. Takahashi, *Estimation of Fano factors in liquid argon, krypton, xenon and xenon-doped liquid argon*, *Nucl. Instrum. Meth.* **134** (1976) 353–357.
- [70] G. Baldini, *Ultraviolet absorption of solid argon, krypton, and xenon*, *Phys. Rev.* **128** (1962) 1562–1567.
- [71] U. Asaf and I. T. Steinberger, *Photoconductivity and electron transport parameters in liquid and solid xenon*, *Phys. Rev. B* **10** (1974) 4464–4468.



- [72] T. Takahashi, S. Konno, T. Hamada, M. Miyajima, S. Kubota, A. Nakamoto, et al., *Average energy expended per ion pair in liquid xenon*, *Phys. Rev. A* **12** (1975) 1771–1775.
- [73] T. Doke, A. Hitachi, J. Kikuchi, K. Masuda, H. Okada, and E. Shibamura, *Absolute scintillation yields in liquid argon and xenon for various particles*, *Jap. J. Appl. Phys.* **41** (2002) 1538–1545.
- [74] P. Sorensen and C. E. Dahl, *Nuclear recoil energy scale in liquid xenon with application to the direct detection of dark matter*, *Phys. Rev. D* **83** (2011) 063501.
- [75] C. E. Dahl, *The physics of background discrimination in liquid xenon, and first results from XENON10 in the hunt for WIMP dark matter*. PhD thesis, Princeton University, 2009.
- [76] A. Hitachi, T. Takahashi, N. Funayama, K. Masuda, J. Kikuchi, and T. Doke, *Effect of ionization density on the time dependence of luminescence from liquid argon and xenon*, *Phys. Rev. B* **27** (1983) 5279–5285.
- [77] A. Hitachi, T. Doke, and A. Mozumder, *Luminescence quenching in liquid argon under charged-particle impact: Relative scintillation yield at different linear energy transfers*, *Phys. Rev. B* **46** (1992) 11463–11470.
- [78] A. Mangiarotti, M. I. Lopes, M. L. Benabderrahmane, V. Chepel, A. Lindote, J. Pinto da Cunha, et al., *A survey of energy loss calculations for heavy ions between 1 and 100 keV*, *Nucl. Instrum. Meth. A* **580** (2007) 114–117.
- [79] J. Lindhard, M. Scharff, and H. E. Schiøtt, *Range concepts and heavy ion ranges*, *Mat. Fys. Medd. Dan. Vid. Selsk.* **33** (1963), no. 14 .
- [80] J. Lindhard, V. Nielsen, and M. Sharff, *Approximation method in classical scattering by screened Coulomb fields*, *Mat. Fis. Medd. Dan. Vid. Selsk.* **36** (1968), no. 10 .
- [81] J. Lindhard, V. Nielsen, M. Sharff, and P. V. Thomsen, *Integral equations governing radiation effects*, *Mat. Fis. Medd. Dan. Vid. Selsk.* **33** (1963), no. 10 1–42.
- [82] A. Hitachi, *Properties of liquid xenon scintillation for dark matter searches*, *Astropart. Phys.* **24** (2005) 247–256.
- [83] S. Kubota, M. Hishida, and J. Raun, *Evidence for a triplet state of the self-trapped exciton states in liquid argon, krypton and xenon*, *J. Phys. C: Solid State Phys.* **11** (1978) 2645.
- [84] J. A. Nikkel, R. Hasty, W. H. Lippincott, and D. N. McKinsey, *Scintillation of liquid neon from electronic and nuclear recoils*, *Astropart. Phys.* **29** (2008) 161–166.
- [85] D. N. McKinsey, C. R. Brome, J. S. Butterworth, S. N. Dzhosyuk, P. R. Huffman, C. E. H. Mattoni, et al., *Radiative decay of the metastable  $He_2(a^3\Sigma_u^+)$  molecule in liquid helium*, *Phys. Rev. A* **59** (1999) 200–204.
- [86] G. Bressi, G. Carugno, E. Conti, D. Iannuzzi, and A. T. Meneguzzo, *Infrared scintillation in liquid Ar and Xe*, *Nucl. Instrum. Meth. A* **440** (2000) 254–257.
- [87] G. Bressi, G. Carugno, E. Conti, C. Del Noce, and D. Iannuzzi, *Infrared scintillation: a comparison between gaseous and liquid xenon*, *Nucl. Instrum. Meth. A* **461** (2001) 378–380.
- [88] T. Heindl, T. Dandl, M. Hofmann, R. Kracken, L. Oberauer, W. Potzel, et al., *The scintillation of liquid argon*, *Europhys. Lett.* **91** (2010) 62002.
- [89] A. Buzulutskov, A. Bondar, and A. Grebenuk, *Infrared scintillation yield in gaseous and liquid argon*, *Europhys. Lett.* **94** (2011) 52001.

- [90] P. Lindblom and O. Solin, *Atomic near-infrared noble gas scintillations I: optical spectra*, *Nucl. Instrum. Meth. A* **268** (1988) 204–208.
- [91] G. Bressi, G. Carugno, E. Conti, D. Iannuzzi, and A. T. Meneguzzo, *A first study of the infrared emission in argon excited by ionizing particles*, *Phys. Lett. A* **278** (2001) 280–285.
- [92] S. Belogurov, G. Bressi, G. Carugno, E. Conti, D. Iannuzzi, and A. T. Meneguzzo, *Measurement of the light yield of infrared scintillation in xenon gas*, *Nucl. Instrum. Meth. A* **452** (2000) 167–169.
- [93] T. Doke, *Fundamental properties of liquid argon, krypton and xenon as radiation detector media*, *Portugal. Phys.* **12** (1981) 9–48.
- [94] S. Kubota, M. Hishida, M. Suzuki, and J.-z. Ruan(Gen), *Dynamical behavior of free electrons in the recombination process in liquid argon, krypton, and xenon*, *Phys. Rev. B* **20** (1979) 3486–3496.
- [95] U. Sowada, J. M. Warman, and M. P. de Haas, *Hot-electron thermalization in solid and liquid argon, krypton, and xenon*, *Phys. Rev. B* **25** (1982) 3434–3437.
- [96] S. Kubota, A. Nakamoto, T. Takahashi, T. Hamada, E. Shibamura, M. Miyajima, et al., *Recombination luminescence in liquid argon and in liquid xenon*, *Phys. Rev. B* **17** (1978) 2762–2765.
- [97] S. Kubota, M. Hishida, M. Suzuki, and J.-z. Ruan(Gen), *Liquid and solid argon, krypton and xenon scintillators*, *Nucl. Instrum. Meth.* **196** (1982) 101–105.
- [98] E. Morikawa, R. Reininger, P. Gürtler, V. Saile, and P. Laporte, *Argon, krypton, and xenon excimer luminescence: From the dilute gas to the condensed phase*, *J. Chem. Phys.* **91** (1989) 1469–1477.
- [99] R. Acciarri, M. Antonello, B. Baibussinov, M. Baldo-Ceolin, P. Benetti, F. Calaprice, et al., *Effects of nitrogen contamination in liquid argon*, *JINST* **5** (2010) P06003.
- [100] R. Acciarri, M. Antonello, B. Baibussinov, M. Baldo-Ceolin, P. Benetti, F. Calaprice, et al., *Oxygen contamination in liquid argon: combined effects on ionization electron charge and scintillation light*, *JINST* **5** (2010) P05003.
- [101] S. Kubota, M. Suzuki, and J.-z. Ruan(Gen), *Specific-ionization-density effect on the time dependence of luminescence in liquid xenon*, *Phys. Rev. B* **21** (1980) 2632–2634.
- [102] M. G. Boulay, B. Cai, M. Chen, V. V. Golovko, P. Harvey, R. Mathew, et al., *Measurement of the scintillation time spectra and pulse-shape discrimination of low-energy beta and nuclear recoils in liquid argon with DEAP-I*, *ArXiv e-prints* (Apr., 2009), [0904.2930].
- [103] M. Szydagis, N. Barry, K. Kazkaz, J. Mock, D. Stolp, M. Sweany, et al., *NEST: a comprehensive model for scintillation yield in liquid xenon*, *JINST* **6** (2011) P10002.
- [104] V. Chepel, M. I. Lopes, and V. Solovov, *Primary scintillation yield and  $\alpha/\beta$  ratio in liquid xenon*, *Rad. Phys. Chem.* **74** (2005) 160–167.
- [105] J. Jortner, L. Meyer, S. A. Rice, and E. G. Wilson, *Localized excitations in condensed Ne, Ar, Kr, and Xe*, *J. Chem. Phys.* **42** (1965) 4250–4253.
- [106] T. Doke and K. Masuda, *Present status of liquid rare gas scintillation detectors and their new application to gamma-ray calorimeters*, *Nucl. Instrum. Meth. A* **420** (1999) 62–80.
- [107] T. Doke, K. Masuda, and E. Shibamura, *Estimation of absolute photon yields in liquid argon and xenon for relativistic (1 MeV) electrons*, *Nucl. Instrum. Meth. A* **291** (1990) 617–620.

- [108] T. Shutt, C. E. Dahl, J. Kwong, A. Bolozdynya, and P. Brusov, *Performance and fundamental processes at low energy in a two-phase liquid xenon dark matter detector*, *Nucl. Phys. B: Proc. Suppl.* **173** (2007) 160–163.
- [109] L. Lavoie, *Liquid xenon scintillators for imaging of positron emitters*, *Med. Phys.* **3** (1976) 283–293.
- [110] R. van Sonsbeek, C. W. E. van Eijk, and R. W. Hollander, *Light yield of liquid and solid xenon irradiated with  $\gamma$ -rays*, *Nucl. Instrum. Meth. A* **367** (1995) 362–366.
- [111] A. Braem, A. Gonidc, D. Schinzel, W. Seidl, E. F. Clayton, G. Davies, et al., *Observation of the UV scintillation light from high energy electron showers in liquid xenon*, *Nucl. Instrum. Meth. A* **320** (1992) 228–237.
- [112] J. Séguinot, G. Passardi, J. Tischhauser, and T. Ypsilantis, *Liquid xenon ionization and scintillation studies for a totally active-vector electromagnetic calorimeter*, *Nucl. Instrum. Meth. A* **323** (1992) 583–600.
- [113] J. Séguinot, J. Tischhauser, and T. Ypsilantis, *Liquid xenon scintillation: photon yield and Fano factor measurements*, *Nucl. Instrum. Meth. A* **354** (1995) 280–287.
- [114] P. Belli, R. Bernabei, C. Dai, A. Incicchitti, D. Prospero, and C. Bacci, *Liquid xenon detector for dark matter search at Gran Sasso*, *Nucl. Instrum. Meth. A* **336** (1993) 336–342.
- [115] M. Miyajima, S. Sasaki, and E. Shibamura, *Absolute number of photons produced by alpha-particles in liquid and gaseous xenon*, *Nucl. Instrum. Meth. B* **63** (1992) 297–308.
- [116] E. Aprile, R. Mukherjee, and M. Suzuki, *A study of the scintillation light induced in liquid xenon by electrons and alpha particles*, *IEEE Trans. Nuc. Sci.* **37** (1990) 553–558.
- [117] D. Gastler, E. Kearns, A. Hime, L. C. Stonehill, S. Seibert, J. Klein, et al., *Measurement of scintillation efficiency for nuclear recoils in liquid argon*, *Phys. Rev. C* **85** (2012) 065811.
- [118] S. Suzuki and A. Hitachi, *Application of rare gas liquids to radiation detectors*, in *Charged Particles and Photon Interactions with Matter: Recent Advances, Applications, and Interfaces* (Y. Hatano, Y. Katsumura, and A. Mozumder, eds.), pp. 879–922, CRC Press, 2011.
- [119] A. Hitachi, *Properties of liquid rare gas scintillation for WIMP search*, in *Identification of Dark Matter, Proc. of the 5th Int. Workshop IDM2004*, p. 396, World Scientific, 2005.
- [120] T. Doke, H. J. Crawford, A. Hitachi, J. Kikuchi, P. J. Lindstrom, K. Masuda, et al., *LET dependence of scintillation yields in liquid argon*, *Nucl. Instrum. Meth. A* **269** (1988) 291–296.
- [121] *ESTAR – Stopping power and range tables for electrons*, National Institute of Standards and Technology. <http://physics.nist.gov/PhysRefData/Star/Text/ESTAR.html>.
- [122] M. Tanaka, T. Doke, A. Hitachi, T. Kato, J. Kikuchi, K. Masuda, et al., *LET dependence of scintillation yields in liquid xenon*, *Nucl. Instrum. Meth. A* **457** (2001) 454–463.
- [123] F. Arneodo, B. Baiboussinov, A. Badertscher, P. Benetti, E. Bernardini, A. Bettini, et al., *Scintillation efficiency of nuclear recoil in liquid xenon*, *Nucl. Instrum. Meth. A* **449** (2000) 147–157.
- [124] D. Akimov, A. Bewick, D. Davidge, J. Dawson, A. S. Howard, I. Ivaniouchenkov, et al., *Measurements of scintillation efficiency and pulse shape for low energy recoils in liquid xenon*, *Phys. Lett. B* **524** (2002) 245–251.
- [125] E. Aprile, K. L. Giboni, P. Majewski, K. Ni, M. Yamashita, R. Hasty, et al., *Scintillation response of liquid xenon to low energy nuclear recoils*, *Phys. Rev. D* **72** (2005) 072006.

- [126] E. Aprile, L. Baudis, B. Choi, K. L. Giboni, K. Lim, A. Manalaysay, et al., *New measurement of the relative scintillation efficiency of xenon nuclear recoils below 10 keV*, *Phys. Rev. C* **79** (2009) 045807.
- [127] G. Plante, E. Aprile, R. Budnik, B. Choi, K.-L. Giboni, L. W. Goetzke, et al., *New measurement of the scintillation efficiency of low-energy nuclear recoils in liquid xenon*, *Phys. Rev. C* **84** (2011) 045805.
- [128] V. Chepel, V. Solovov, F. Neves, A. Pereira, P. J. Mendes, C. P. Silva, et al., *Scintillation efficiency of liquid xenon for nuclear recoils with the energy down to 5 keV*, *Astropart. Phys.* **26** (2006) 58–63.
- [129] GEANT4 collaboration, S. Agostinelli, J. Allison, K. Amako, J. Apostolakis, H. Araújo, P. Arce, et al., *Geant4 – A simulation toolkit*, *Nucl. Instrum. Meth. A* **506** (2003) 250–303.
- [130] R. Brunetti, E. Calligarich, M. Cambiaghi, F. Carbonara, A. Cocco, C. de Vecchi, et al., *WARP liquid argon detector for dark matter survey*, *New Astron. Rev.* **49** (2005) 265–269.
- [131] C. Regenfus, Y. Allkofer, C. Amsler, W. Creus, A. Ferella, J. Rochet, et al., *Study of nuclear recoils in liquid argon with monoenergetic neutrons*, *J. Phys.: Conf. Ser.* **375** (2012) 012019.
- [132] W. H. Lippincott, K. J. Coakley, D. Gastler, E. Kearns, D. N. McKinsey, and J. A. Nikkel, *Scintillation yield and time dependence from electronic and nuclear recoils in liquid neon*, *Phys. Rev. C* **86** (2012) 015807.
- [133] D.-M. Mei, Z.-B. Yin, L. C. Stonehill, and A. Hime, *A model of nuclear recoil scintillation efficiency in noble liquids*, *Astropart. Phys.* **30** (2008) 12–17.
- [134] A. Mozumder, *Free-ion yield and electron-ion recombination rate in liquid xenon*, *Chem. Phys. Lett.* **245** (1995) 359–363.
- [135] A. Mozumder, *Free-ion yield in liquid argon at low-LET*, *Chem. Phys. Lett.* **238** (1995) 143–148.
- [136] M. Miyajima, T. Takahashi, S. Konno, T. Hamada, S. Kubota, H. Shibamura, et al., *Average energy expended per ion pair in liquid argon*, *Phys. Rev. A* **9** (1974) 1438–1443.
- [137] L. C. Northcliffe and R. F. Schilling, *Range and stopping-power tables for heavy ions*, *Atom. Data Nucl. Data* **7** (1970) 233–463.
- [138] J. Thomas and D. A. Imel, *Recombination of electron-ion pairs in liquid argon and liquid xenon*, *Phys. Rev. A* **36** (1987) 614–616.
- [139] J. Thomas, D. A. Imel, and S. Biller, *Statistics of charge collection in liquid argon and liquid xenon*, *Phys. Rev. A* **38** (1988) 5793–5800.
- [140] R. A. Holroyd and W. F. Schmidt, *Transport of electrons in nonpolar fluids*, *Annu. Rev. Phys. Chem.* **40** (1989) 439–468.
- [141] Y. Hatano, *Electron-ion recombination in dense molecular media*, in *Linking the Gaseous and Condensed Phases of Matter* (L. G. Christophorou, E. Illenberger, and W. F. Schmidt, eds.), vol. 326 of *NATO ASI Series B: Physics*, pp. 467–486, Plenum Press, New York, 1994.
- [142] W. F. Schmidt, *Liquid State Electronics of Insulating Liquids*. CRC Press, New York, 1997.
- [143] W. M. Bartczak and A. Hummel, *Computer simulation of ion recombination in high-energy charged particles tracks*, in *Electronic Excitations in Liquefied Rare Gases* (W. F. Schmidt and E. Illenberger, eds.), p. 443, American Scientific Publishers, 2005.
- [144] M. Tachiya, *Breakdown of the Debye theory of bulk ion recombination*, *J. Chem. Phys.* **87** (1987) 4108–4113.

- [145] K. Shinsaka, M. Codama, T. Srithanratana, M. Yamamoto, and Y. Hatano, *Electron-ion recombination rate constants in gaseous, liquid, and solid argon*, *J. Chem. Phys.* **88** (1988) 7529–7536.
- [146] P. Sorensen, J. Angle, E. Aprile, F. Arneodo, L. Baudis, A. Bernstein, et al., *Lowering the low-energy threshold of xenon-based detectors*, *PoS (IDM2010) 017* (2010), [[arXiv:1011.6439](https://arxiv.org/abs/1011.6439)]. (Proc. Int. Workshop on Identification of Dark Matter IDM2010).
- [147] E. Aprile, R. Mukherjee, and M. Suzuki, *Ionization of liquid xenon by  $^{241}\text{Am}$  and  $^{210}\text{Po}$  alpha particles*, *Nucl. Instrum. Meth. A* **307** (1991) 119–125.
- [148] H. D. Pruett and H. P. Broida, *Free-carrier drift-velocity studies in rare-gas liquids and solids*, *Phys. Rev. C* **164** (1967) 1138–1144.
- [149] E. Aprile, R. Mukherjee, and M. Suzuki, *Performance of a liquid xenon ionization chamber irradiated with electrons and gamma-rays*, *Nucl. Instrum. Meth. A* **302** (1991) 177–185.
- [150] A. S. Barabash, A. A. Golubev, O. V. Kazachenko, V. M. Lobashev, B. M. Ovchinnikov, and B. E. Stern, *A pulsed liquid ionization chamber filled with Xe, Ar and  $\text{CH}_4$* , *Nucl. Instrum. Meth. A* **236** (1985) 69–81.
- [151] T. Y. Voronova, M. A. Kirsanov, A. A. Kruglov, I. M. Obodobskii, S. G. Pokashalov, V. A. Shilov, et al., *Ionization yield from electron tracks in liquid xenon*, *Sov. Phys. Tech. Phys.* **34** (1989) 825–827.
- [152] U. Fano and W. Lichten, *Interpretation of  $\text{Ar}^+$ -Ar collisions at 50 keV*, *Phys. Rev. Lett.* **14** (1965) 627–629.
- [153] F. Bezrukov, F. Kahlhoefer, and M. Lindner, *Interplay between scintillation and ionization in liquid xenon dark matter searches*, *Astropart. Phys.* **35** (2011) 119–127.
- [154] A. Baldini, C. Bemporad, F. Ceci, T. Doke, M. Grassi, A. A. Grebenuk, et al., *Absorption of scintillation light in a 100 l liquid xenon  $\gamma$ -ray detector and expected detector performance*, *Nucl. Instrum. Meth. A* **545** (2005) 753–764.
- [155] V. Chepel, M. Lopes, R. Ferreira Marques, and A. Policarpo, *Purification of liquid xenon and impurity monitoring for a PET detector*, *Nucl. Instrum. Meth. A* **349** (1994) 500–505.
- [156] N. Ishida, M. Chen, T. Doke, K. Hasuike, A. Hitachi, M. Gaudreau, et al., *Attenuation length measurements of scintillation light in liquid rare gases and their mixtures using an improved reflection suppresser*, *Nucl. Instrum. Meth. A* **384** (1997) 380–386.
- [157] V. N. Solovov, V. Chepel, M. I. Lopes, A. Hitachi, R. Ferreira Marques, and A. J. P. L. Policarpo, *Measurement of the refractive index and attenuation length of liquid xenon for its scintillation light*, *Nucl. Instrum. Meth. A* **516** (2004) 462–474.
- [158] G. M. Seidel, R. E. Lanou, and W. Yao, *Rayleigh scattering in rare-gas liquids*, *Nucl. Instrum. Meth. A* **489** (2002) 189–194.
- [159] A. Baldini, C. Bemporad, F. Ceci, T. Doke, M. Grassi, T. Haruyama, et al., *Liquid xenon scintillation calorimetry and Xe optical properties*, *IEEE Trans. Dielect. Elect. Insul.* **13** (2006) 547–555.
- [160] R. P. Madden, L. R. Canfield, and G. Hass, *On the vacuum-ultraviolet reflectance of evaporated aluminum before and during oxidation*, *J. Opt. Soc. Am.* **53** (1963) 620.
- [161] L. R. Canfield and G. Hass, *Reflectance and Optical Constants of Evaporated Copper and Silver in the Vacuum Ultraviolet from 1000 to 2000 Å*, *J. Opt. Soc. Am.* **55** (1965) 61.

- [162] G. Hass, W. R. Hunter, and R. Tousey, *Reflectance of evaporated aluminum in the vacuum ultraviolet*, *J. Opt. Soc. Am.* **46** (1956) 1009–1012.
- [163] M. Fernández-Perea, J. I. Larruquert, J. A. Aznárez, A. Pons, and J. A. Méndez, *Vacuum ultraviolet coatings of Al protected with MgF<sub>2</sub> prepared both by ion-beam sputtering and by evaporation*, *Appl. Opt.* **46** (2007) 4871–4878.
- [164] A. Minamino, K. Abe, Y. Ashie, J. Hosaka, K. Ishihara, K. Kobayashi, et al., *Self-shielding effect of a single phase liquid xenon detector for direct dark matter search*, *Astropart. Phys.* **35** (2012) 609–614.
- [165] S. Bricola, A. Menegolli, M. Prata, M. C. Prata, G. Raselli, M. Rossella, et al., *Noble-gas liquid detectors: measurement of light diffusion and reflectivity on commonly adopted inner surface materials*, *Nucl. Phys. B: Proc. Suppl.* **172** (2007) 260–262.
- [166] C. Silva, J. Pinto da Cunha, A. Pereira, M. I. Lopes, V. Chepel, V. Solovov, et al., *A model of the reflection distribution in the vacuum ultra violet region*, *Nucl. Instrum. Meth. A* **619** (2010) 59–62.
- [167] C. F. P. Silva, *Study of the Reflectance Distributions of Fluoropolymers and Other Rough Surfaces with Interest to Scintillation Detectors*. PhD thesis, University of Coimbra, 2009.
- [168] M. Yamashita, T. Doke, K. Kawasaki, J. Kikuchi, and S. Suzuki, *Scintillation response of liquid Xe surrounded by PTFE reflector for gamma rays*, *Nucl. Instrum. Meth. A* **535** (2004) 692–698.
- [169] F. Neves, V. Chepel, V. Solovov, A. Pereira, M. I. Lopes, J. Pinto da Cunha, et al., *Performance of a chamber for studying the liquid xenon response to  $\gamma$ -rays and nuclear recoils*, *IEEE Trans. Nuc. Sci.* **52** (2005) 2793–2800.
- [170] LUX collaboration, D. S. Akerib, X. Bai, E. Bernard, A. Bernstein, A. Bradley, D. Byram, et al., *Technical results from the surface run of the LUX dark matter experiment*, *ArXiv e-prints* (Oct., 2012), [1210.4569].
- [171] C. P. Silva, J. Pinto da Cunha, V. Chepel, A. Pereira, V. Solovov, P. Mendes, et al., *Measuring the angular profile of the reflection of xenon scintillation light*, *Nucl. Instrum. Meth. A* **580** (2007) 322–325.
- [172] C. Silva, J. Pinto da Cunha, A. Pereira, V. Chepel, M. I. Lopes, V. Solovov, et al., *Reflectance of polytetrafluoroethylene for xenon scintillation light*, *J. Appl. Phys.* **107** (2010) 064902.
- [173] U. Rössler, *Band structure and excitons*, in *Rare Gas Solids* (M. L. Klein and J. A. Venables, eds.), p. 505, Academic Press, London, 1976.
- [174] I. T. Steinberger, *Band structure parameters of classical rare gas liquids*, in *Electronic Excitations in Liquefied Rare Gases* (W. F. Schmidt and E. Illenberger, eds.), p. 51, American Scientific Publishers, 2005.
- [175] L. S. Miller, S. Howe, and W. E. Spear, *Charge transport in solid and liquid Ar, Kr, and Xe*, *Phys. Rev.* **166** (1968) 871–878.
- [176] T. H. Dey and T. J. Lewis, *Ion mobility and liquid motion in liquefied argon*, *J. Phys. D: Appl. Phys.* **1** (1968) 1019–1029.
- [177] O. Hilt and W. F. Schmidt, *Positive hole mobility in liquid xenon*, *Chem. Phys.* **183** (1994) 147–153.
- [178] O. Hilt, W. F. Schmidt, and A. G. Khrapak, *Ionic mobilities in liquid xenon*, *IEEE Trans. Dielect. Elect. Insul.* **1** (1994) 648–656.
- [179] G. Jaffé, *Zur Theorie der Ionisation in Kolonnen*, *Annalen der Physik (Leipzig)* **347** (1913) 303–344.

- [180] E. Shibamura, A. Hitachi, T. Doke, T. Takahashi, S. Kubota, and M. Miyajima, *Drift velocities of electrons, saturation characteristics of ionization and W-values for conversion electrons in liquid argon, liquid argon-gas mixtures and liquid xenon*, *Nucl. Instrum. Meth.* **131** (1975) 249–258.
- [181] I. M. Obodovskii and S. G. Pokachalov, *Average ion pair formation energy in liquid and solid xenon*, *Sov. J. Low Temp. Phys* **5** (1979) 393–396.
- [182] E. M. Gushchin, A. A. Kruglov, and I. M. Obodovskii, *Electron dynamics in condensed argon and xenon*, *Sov. Phys. JETP* **55** (1982), no. 4 650.
- [183] A. G. Khrapak, W. F. Schmidt, and E. Illenberger, *Localized electrons, holes and ions*, in *Electronic Excitations in Liquefied Rare Gases* (W. F. Schmidt and E. Illenberger, eds.), pp. 317–330, American Scientific Publishers, 2005.
- [184] P. G. Le Comber, R. J. Loveland, and W. E. Spear, *Hole transport in the rare-gas solids Ne, Ar, Kr, and Xe*, *Phys. Rev. B* **11** (1975) 3124–3130.
- [185] P. Sorensen, *Anisotropic diffusion of electrons in liquid xenon with application to improving the sensitivity of direct dark matter searches*, *arXiv e-prints* (Feb., 2011), [1102.2865v2].
- [186] A. M. Atrazhev, A. V. Berezhnov, D. O. Dunikov, I. V. Chernysheva, V. V. Dmitrenko, and G. Kapralova, *Electron transport coefficients in liquid xenon*, in *Proc. 2005 IEEE Int. Conf. on Dielect. Liquids ICDL2005; Coimbra, Portugal, Jun 26 – Jul 1, 2005*, pp. 329–332, 2005.
- [187] W.-T. Chen, H. Carduner, J.-P. Cussonneau, J. Donnard, S. Duval, A.-F. Mohamad-Hadi, et al., *Measurement of the transverse diffusion coefficient of charge in liquid xenon*, *ArXiv e-prints* (Sept., 2011), [1109.3300].
- [188] E. Shibamura, T. Takahashi, S. Kubota, and T. Doke, *Ratio of diffusion coefficient to mobility for electrons in liquid argon*, *Phys. Rev. A* **20** (1979) 2547–2554.
- [189] P. Cennini, S. Cittolin, J.-P. Revol, C. Rubbia, W.-H. Tian, P. Picchi, et al., *Performance of a three-ton liquid argon time projection chamber*, *Nucl. Instrum. Meth. A* **345** (1994) 230–243.
- [190] S. Amerio, S. Amoruso, M. Antonello, P. Aprili, M. Armenante, F. Arneodo, et al., *Design, construction and tests of the ICARUS T600 detector*, *Nucl. Instrum. Meth. A* **527** (2004) 329–410.
- [191] A. Dobi, C. Hall, S. Slutsky, Y.-R. Yen, B. Aharmin, M. Auger, et al., *Xenon purity analysis for EXO-200 via mass spectrometry*, *Nucl. Instrum. Meth. A* **675** (2012) 40–46.
- [192] G. Bakale, U. Sowada, and W. F. Schmidt, *Effect of an electric field on electron attachment to sulfur hexafluoride, nitrous oxide, and molecular oxygen in liquid argon and xenon*, *J. Chem. Phys.* **80** (1976) 2556–2559.
- [193] P. Majewski, V. N. Solovov, D. Y. Akimov, H. M. Araújo, E. J. Barnes, V. A. Belov, et al., *Performance data from the ZEPLIN-III second science run*, *JINST* **7** (2012) C03044.
- [194] D. Schinzel and W. F. Schmidt, *Principles of production and ultrapurification*, in *Electronic Excitations in Liquefied Rare Gases* (W. F. Schmidt and E. Illenberger, eds.), pp. 317–330, American Scientific Publishers, 2005.
- [195] P. Benetti, A. Bettini, E. Calligarich, F. Casagrande, P. Casoli, C. Castagnoli, et al., *A simple and effective purifier for liquid xenon*, *Nucl. Instrum. Meth. A* **329** (1993) 361–364.
- [196] B. Baibussinov, M. B. Ceolin, E. Calligarich, S. Centro, K. Cieslik, C. Farnese, et al., *Free electron lifetime achievements in liquid argon imaging TPC*, *JINST* **5** (2010) P03005.

- [197] E. Aprile, K. Arisaka, F. Arneodo, A. Askin, L. Baudis, A. Behrens, et al., *The XENON100 dark matter experiment*, *Astropart. Phys.* **35** (2012) 573–590.
- [198] E. Conti, R. DeVoe, G. Gratta, T. Koffas, S. Waldman, J. Wodin, et al., *Correlated fluctuations between luminescence and ionization in liquid xenon*, *Phys. Rev. B* **68** (2003) 054201.
- [199] V. N. Solovov, V. A. Belov, D. Y. Akimov, H. M. Araújo, E. J. Barnes, A. A. Burenkov, et al., *Position reconstruction in a dual phase xenon scintillation detector*, *IEEE Trans. Nuc. Sci.* **59** (2012) 3286–3293.
- [200] E. Aprile, K. L. Giboni, P. Majewski, K. Ni, and M. Yamashita, *Observation of anticorrelation between scintillation and ionization for MeV gamma rays in liquid xenon*, *Phys. Rev. B* **76** (2007) 014115.
- [201] E. Aprile, J. Angle, F. Arneodo, L. Baudis, A. Bernstein, A. Bolozdynya, et al., *Design and performance of the XENON10 dark matter experiment*, *Astropart. Phys.* **34** (2011) 679–698.
- [202] H. M. Araújo, D. Y. Akimov, E. J. Barnes, V. A. Belov, A. Bewick, A. A. Burenkov, et al., *Radioactivity backgrounds in ZEPLIN-III*, *Astropart. Phys.* **35** (2012) 495–502.
- [203] EXO collaboration, M. Auger, D. J. Auty, P. S. Barbeau, E. Beauchamp, V. Belov, C. Benitez-Medina, et al., *Search for neutrinoless double-beta decay in  $^{136}\text{Xe}$  with EXO-200*, *Phys. Rev. Lett.* **109** (2012) 032505.
- [204] A. Bolozdynya, V. Egorov, B. Rodionov, and V. Miroshnichenko, *Emission detectors*, *IEEE Trans. Nuc. Sci.* **42** (1995) 565–569.
- [205] Y. Sakai, *Hot electrons*, in *Electronic Excitations in Liquefied Rare Gases* (W. F. Schmidt and E. Illenberger, eds.), pp. 275–294, American Scientific Publishers, 2005.
- [206] A. I. Bolozdynya, *Two-phase emission detectors and their applications*, *Nucl. Instrum. Meth. A* **422** (1999) 314–320.
- [207] E. M. Gushchin, A. A. Kruglov, and I. M. Obodovskii, *Emission of "hot" electrons from liquid and solid argon and xenon*, *Sov. Phys. JETP* **55** (1982), no. 5 860.
- [208] A. F. Borghesani, G. Carugno, M. Cavenago, and E. Conti, *Electron transmission through the Ar liquid-vapor interface*, *Phys. Lett. A* **149** (1990) 481–484.
- [209] A. Bondar, A. Buzulutskov, A. Grebenuk, D. Pavlyuchenko, and Y. Tikhonov, *Electron emission properties of two-phase argon and argon-nitrogen avalanche detectors*, *JINST* **4** (2009) P09013.
- [210] XENON10 collaboration, J. Angle, E. Aprile, F. Arneodo, L. Baudis, A. Bernstein, A. I. Bolozdynya, et al., *Search for light dark matter in XENON10 data*, *Phys. Rev. Lett.* **107** (2011) 051301.
- [211] H. Zaklad, S. E. Derenzo, T. F. Budinger, and L. W. Alvarez, *Liquid xenon multiwire proportional chambers for nuclear medicine applications*, in *First World Congress on Nuclear Medicine, Tokyo, Japan, 1974*. (Lawrence Berkeley Laboratory Report LBL-3000).
- [212] A. I. Bolozdynya, *Emission particle detectors*, *Instrum. Exp. Tech.* **28** (1985) 265.
- [213] V. V. Egorov, *Position-sensitive detection of nuclear gamma radiation by the emission method (in Russian)*. PhD thesis, Moscow Engineering and Physics Institute, 1982.
- [214] V. V. Egorov, V. P. Miroshnichenko, B. U. Rodionov, A. I. Bolozdynya, S. D. Kalashnikov, and V. L. Krivoshein, *Electroluminescence emission gamma-camera*, *Nucl. Instrum. Meth.* **205** (1983) 373–374.



- [215] XENON100 collaboration, E. Aprile, M. Alfonsi, K. Arisaka, F. Arneodo, C. Balan, L. Baudis, et al., *Dark matter results from 225 live days of XENON100 data*, *Phys. Rev. Lett.* **109** (2012) 181301.
- [216] M. Salet S. C. P. Leite, *Radioluminescence of rare gases*, *Portugal. Phys.* **11** (1980) 53–100.
- [217] A. J. P. L. Policarpo, *Light production and gaseous detectors*, *Phys. Scripta* **23** (1981) 539–549.
- [218] T. Takahashi, S. Himi, M. Suzuki, J. Ruan(Gen), and S. Kubota, *Emission spectra from Ar-Xe, Ar-Kr, Ar-N<sub>2</sub>, Ar-CH<sub>4</sub>, Ar-CO<sub>2</sub> and Xe-N<sub>2</sub> gas scintillation proportional counters*, *Nucl. Instrum. Meth.* **205** (1983) 591–596.
- [219] C. A. N. Conde, L. Requicha Ferreira, and M. F. A. Ferreira, *The secondary scintillation output of xenon in a uniform field gas proportional scintillation counter*, *IEEE Trans. Nuc. Sci.* **24** (1977) 221–224.
- [220] C. M. B. Monteiro, L. M. P. Fernandes, J. A. M. Lopes, L. C. C. Coelho, J. F. C. A. Veloso, J. M. F. dos Santos, et al., *Secondary scintillation yield in pure xenon*, *JINST* **2** (2007) P05001.
- [221] M. M. F. R. Fraga, C. M. Ferreira, J. Loureiro, and M. Salet S. C. P. Leite, *Electron excitation cross sections in Kr and Xe*, in *ESCAMPIG'90 – 10th European Section Conf. on the Atomic and Molecular Physics of Ionised Gases, Orléans, France (Europhys. Conf. Abstracts)* (B. Dubreuil, ed.), vol. 14E, pp. 72–73, Aug., 1990.
- [222] F. P. Santos, T. H. V. T. Dias, A. D. Stauffer, and C. A. N. Conde, *Three-dimensional Monte Carlo calculation of the VUV electroluminescence and other electron transport parameters in xenon*, *J. Phys. D: Appl. Phys.* **27** (1994) 42.
- [223] A. C. Fonseca, R. Meleiro, V. Chepel, A. Pereira, V. Solovov, and M. I. Lopes, *Study of secondary scintillation in xenon vapour*, *IEEE Nuc. Sci. Symp. Conf. Record* **1** (2004) 572–576.
- [224] C. M. B. Monteiro, J. A. M. Lopes, J. F. C. A. Veloso, and J. M. F. dos Santos, *Secondary scintillation yield in pure argon*, *Phys. Lett. B* **668** (2008) 167–170.
- [225] National Institute of Standards and Technology, *Thermophysical properties of fluid systems, NIST Chemistry WebBook*. <http://webbook.nist.gov/chemistry/fluid/>.
- [226] M. M. R. Fraga, C. C. Bueno, J. A. C. Goncalves, F. A. F. Fraga, R. Ferreira Marques, and A. J. P. L. Policarpo, *Pressure dependence of secondary NIR scintillation*, *IEEE Nuc. Sci. Symp. Conf. Record* **1** (2000) 145–149.
- [227] G. Carugno, *Infrared emission in gaseous media induced by ionizing particles and by drifting electrons*, *Nucl. Instrum. Meth. A* **419** (1998) 617–620.
- [228] B. Schneider and J. S. Cohen, *Ground and excited states of Ne<sub>2</sub> and Ne<sub>2</sub><sup>+</sup> – II. spectroscopic properties and radiative lifetimes*, *J. Chem. Phys.* **61** (1974) 3240–3243.
- [229] I. B. Berlman, *Handbook of Fluorescence Spectra of Aromatic Molecules*. Academic Press, 1965.
- [230] C. H. Lally, G. J. Davies, W. G. Jones, and N. J. T. Smith, *UV quantum efficiencies of organic fluors*, *Nucl. Instrum. Meth. B* **117** (1996) 421–427.
- [231] D. N. McKinsey, C. R. Brome, J. S. Butterworth, R. Golub, K. Habicht, P. R. Huffman, et al., *Fluorescence efficiencies of thin scintillating films in the extreme ultraviolet spectral region*, *Nucl. Instrum. Meth. B* **132** (1997) 351–358.
- [232] V. M. Gehman, S. R. Seibert, K. Rielage, A. Hime, Y. Sun, D.-M. Mei, et al., *Fluorescence efficiency and visible re-emission spectrum of tetraphenyl butadiene films at extreme ultraviolet wavelengths*, *Nucl. Instrum. Meth. A* **654** (2011) 116–121.

- [233] P. Benetti, C. Montanari, G. L. Raselli, M. Rossella, and C. Vignoli, *Detection of the VUV liquid argon scintillation light by means of glass-window photomultiplier tubes*, *Nucl. Instrum. Meth. A* **505** (2003) 89–92.
- [234] ARDM collaboration, V. Boccone, P. K. Lightfoot, K. Mavrokoridis, C. Regenfus, C. Amsler, A. Badertscher, et al., *Development of wavelength shifter coated reflectors for the ArDM argon dark matter detector*, *JINST* **4** (2009) 6001.
- [235] A. I. Bolozdynya, A. W. Bradley, P. P. Brusov, C. E. Dahl, J. Kwong, and T. Shutt, *Using a wavelength shifter to enhance the sensitivity of liquid xenon dark matter detectors*, *IEEE Trans. Nuc. Sci.* **55** (2008) 1453–1457.
- [236] M. Ichige, T. Doke, Y. Doi, and Y. Yoshimura, *Operating characteristics of photomultipliers at low temperature*, *Nucl. Instrum. Meth. A* **327** (1993) 144–147.
- [237] H. M. Araújo, V. Y. Chepel, M. I. Lopes, R. Ferreira Marques, and A. J. P. L. Policarpo, *Low temperature performance of photomultiplier tubes illuminated in pulsed mode by visible and vacuum ultraviolet light*, *Rev. Sci. Instrum.* **68** (1997) 34–40.
- [238] H. M. Araújo, V. Y. Chepel, M. I. Lopes, J. van der Marel, R. Ferreira Marques, and A. J. P. L. Policarpo, *Study of bialkali photocathodes below room temperature in the UV/VUV region*, *IEEE Trans. Nuc. Sci.* **45** (1998) 542–549.
- [239] H. M. Araújo, A. Bewick, D. Davidge, J. Dawson, T. Ferbel, A. S. Howard, et al., *Low-temperature study of 35 photomultiplier tubes for the ZEPLIN-III experiment*, *Nucl. Instrum. Meth. A* **521** (2004) 407–415.
- [240] R. J. Hollingworth and J. E. McMillan, *Low temperature tests of photomultipliers for use in liquid xenon experiments*, in *The Identification of Dark Matter, Proc. 5th Int Workshop IDM2004* (N. J. C. Spooner and V. Kudryavtsev, eds.), pp. 402–407, World Scientific, 2005. DOI.
- [241] E. Aprile, M. Beck, K. Bokeloh, R. Budnik, B. Choi, H. A. Contreras, et al., *Measurement of the quantum efficiency of Hamamatsu R8520 photomultipliers at liquid xenon temperature*, *JINST* **7** (2012) P10005.
- [242] M. Yamashita, *R&D results and status of the XENON dark matter experiment*, in *Applications of Rare Gas Xenon to Science And Technology (XeSAT2005)*, (Waseda University, Tokyo, Japan), Mar., 2005.
- [243] Y. Suzuki, *XMASS experiment*, in *Identification of Dark Matter 2008*, PoS(IDM2008)001, 2008.
- [244] LUX collaboration, D. S. Akerib, X. Bai, S. Bedikian, E. Bernard, A. Bernstein, A. Bolozdynya, et al., *The large underground xenon (LUX) experiment*, *ArXiv e-prints* (Nov., 2012), [1211.3788].
- [245] A. Ankowski, M. Antonello, P. Aprili, F. Arneodo, A. Badertscher, B. Baiboussinov, et al., *Characterization of ETL 9357FLA photomultiplier tubes for cryogenic temperature applications*, *Nucl. Instrum. Meth. A* **556** (2006) 146–157.
- [246] J. A. Nikkel, W. H. Lippincott, and D. N. McKinsey, *Demonstration of photomultiplier tube operation at 29 K*, *JINST* **2** (2007) 11004.
- [247] K. Nakamura, Y. Hamana, Y. Ishigami, and T. Matsui, *Latest bialkali photocathode with ultra high sensitivity*, *Nucl. Instrum. Meth. A* **623** (2010) 276–278.
- [248] Hamamatsu Photonics, *Photonic devices – Electron tube devices and applied products*, Jan., 2011.
- [249] D. S. Akerib, X. Bai, E. Bernard, A. Bernstein, A. Bradley, D. Byram, et al., *An ultra-low background PMT for liquid xenon detectors*, *ArXiv e-prints* (May, 2012), [1205.2272].

- [250] K. Lung, K. Arisaka, A. Bargetzi, P. Beltrame, A. Cahill, T. Genma, et al., *Characterization of the Hamamatsu R11410-10 3-inch photomultiplier tube for liquid xenon dark matter direct detection experiments*, *ArXiv e-prints* (2012), [1202.2628].
- [251] D. Renker, *New developments on photosensors for particle physics*, *Nucl. Instrum. Meth. A* **598** (2009) 207–212.
- [252] F. Neves, V. Chepel, D. Y. Akimov, H. M. Araújo, E. J. Barnes, V. A. Belov, et al., *Calibration of photomultiplier arrays*, *Astropart. Phys.* **33** (2010) 13–18.
- [253] V. N. Solovov, F. Neves, V. Chepel, M. I. Lopes, R. Ferreira Marques, and A. J. P. L. Policarpo, *Low-temperature performance of a large area avalanche photodiode*, *Nucl. Instrum. Meth. A* **504** (2003) 53–57.
- [254] C. P. Datema, I. B. Pleasants, and D. Ramsden, *Hybrid photodiodes in scintillation counter applications*, *Nucl. Instrum. Meth. A* **387** (1997) 100–103.
- [255] H. Nakayama, A. Kusaka, H. Kakuno, T. Abe, M. Iwasaki, H. Aihara, et al., *Development of a 13-in. hybrid avalanche photo-detector (HAPD) for a next generation water cherenkov detector*, *Nucl. Instrum. Meth. A* **567** (2006) 172–175.
- [256] A. Teymourian, D. Aharoni, L. Baudis, P. Beltrame, E. Brown, D. Cline, et al., *Characterization of the quartz photon intensifying detector (QUPID) for noble liquid detectors*, *Nucl. Instrum. Meth. A* **654** (2011) 184–195.
- [257] R. M. McAlpine, *Photomultipliers for low background applications*, Tech. Rep. RP/092, Electron Tubes Ltd, 1992. <http://www.et-enterprises.com/files/file/technical-information/rp092colour.pdf>.
- [258] S. Fiorucci, D. S. Akerib, S. Bedikian, A. Bernstein, A. Bolozdynya, A. Bradley, et al., *Status of the LUX dark matter search*, in *American Institute of Physics Conference Series* (G. Alverson, P. Nath, and B. Nelson, eds.), vol. 1200 of *AIP Conf. Ser.*, pp. 977–980, Feb., 2010. arXiv:0912.0482. DOI.
- [259] L. de Viveiros, *Optimization of Signal versus Background in Liquid Xe Detectors Used for Dark Matter Direct Detection Experiments*. PhD thesis, Brown University, Providence, RI, 2009.
- [260] K. Arisaka, H. Wang, P. F. Smith, D. Cline, A. Teymourian, E. Brown, et al., *XAX: A multi-ton, multi-target detection system for dark matter, double beta decay and pp solar neutrinos*, *Astropart. Phys.* **31** (2009) 63–74.
- [261] K. Arisaka, *New trends in vacuum-based photon detectors*, *Nucl. Instrum. Meth. A* **442** (2000) 80–90.
- [262] D. Renker, *New trends on photodetectors*, *Nucl. Instrum. Meth. A* **571** (2007) 1–6.
- [263] D. Renker and E. Lorenz, *Advances in solid state photon detectors*, *JINST* **4** (2009) 4004.
- [264] L. Yang, S. N. Dzhosyuk, J. M. Gabrielse, P. R. Huffman, C. E. H. Mattoni, S. E. Maxwell, et al., *Performance of a large-area avalanche photodiode at low temperature for scintillation detection*, *Nucl. Instrum. Meth. A* **508** (2003) 388–393.
- [265] API – Advanced Photonix Inc., 2925 Boardwalk, Ann Arbor, MI 48104, USA.
- [266] V. N. Solovov, V. Chepel, M. I. Lopes, R. Ferreira Marques, and A. J. P. L. Policarpo, *Study of large area avalanche photodiode for detecting liquid xenon scintillation*, *IEEE Trans. Nuc. Sci.* **47** (2000) 1307–1310.

- [267] V. N. Solovov, A. Hitachi, V. Chepel, M. I. Lopes, R. Ferreira Marques, and A. J. P. L. Policarpo, *Detection of scintillation light of liquid xenon with a LAAPD*, *Nucl. Instrum. Meth. A* **488** (2002) 572–578.
- [268] K. Ni, E. Aprile, D. Day, K. L. Giboni, J. A. M. Lopes, P. Majewski, et al., *Performance of a large area avalanche photodiode in a liquid xenon ionization and scintillation chamber*, *Nucl. Instrum. Meth. A* **551** (2005) 356–363.
- [269] U. Oberlack, C. Olsen, P. Shagin, E. Aprile, K. L. Giboni, and R. Santorelli, *R&D towards a liquid xenon advanced compton telescope (LXeACT)*, in *APS Meeting Abstracts*, p. 11005, Apr., 2007.
- [270] P. Shagin, R. Gomez, U. Oberlack, P. Cushman, B. Sherwood, M. McClish, et al., *Avalanche photodiode for liquid xenon scintillation: quantum efficiency and gain*, *JINST* **4** (2009) 1005.
- [271] RMD – Radiation Monitoring Devices, Inc., 44 Hunt Street, Watertown, MA 02472, USA.
- [272] V. Chepel, V. N. Solovov, F. Neves, M. I. Lopes, A. Lindote, J. Pinto da Cunha, et al., *Liquid xenon scintillation: Light propagation and detection with avalanche photodiodes*, in *Identification of Dark Matter, Proc. Int. Workshop IDM2002* (N. J. C. Spooner and V. Kudryavtsev, eds.), pp. 377–382, World Scientific, 2003. DOI.
- [273] R. Neilson, F. Leport, A. Pocar, K. S. Kumar, A. Odian, C. Y. Prescott, et al., *Characterization of large area APDs for the EXO-200 detector*, *Nucl. Instrum. Meth. A* **608** (2009) 68–75.
- [274] G. Bondarenko, P. Buzhan, B. Dolgoshein, V. Golovin, E. Guschin, A. Ilyin, et al., *Limited Geiger-mode microcell silicon photodiode: new results*, *Nucl. Instrum. Meth. A* **442** (2000) 187–192.
- [275] “Tabulated optical constants, photonics.” Briham Young University, 44 Hunt Street, Watertown, MA 02472, USA; [www.photonics.byu.edu/tabulatedopticalconstants.phtml](http://www.photonics.byu.edu/tabulatedopticalconstants.phtml).
- [276] H. R. Philipp and E. A. Taft, *An optical characterization of native oxides and thin thermal oxides on silicon*, *J. Appl. Phys.* **53** (1982) 5224–5229.
- [277] C. Piemonte, *A new silicon photomultiplier structure for blue light detection*, *Nucl. Instrum. Meth. A* **568** (2006) 224–232.
- [278] Hamamatsu Photonics Inc., Solid State Division, “MPPC – multipixel photon counters.” [http://sales.hamamatsu.com/assets/applications/SSD/mppc\\_kapd0002e08.pdf](http://sales.hamamatsu.com/assets/applications/SSD/mppc_kapd0002e08.pdf).
- [279] W. G. Oldham, R. R. Samuelson, and P. Antognetti, *Triggering phenomena in avalanche diodes*, *IEEE Trans. Electron. Dev.* **ED-19** (1972) 1056–1060.
- [280] SensL, Lee House, Riverview Business Park, Bessboro Road, Blackrock, Cork, Ireland.
- [281] P. K. Lightfoot, G. J. Barker, K. Mavrokoridis, Y. A. Ramachers, and N. J. C. Spooner, *Characterisation of a silicon photomultiplier device for applications in liquid argon based neutrino physics and dark matter searches*, *JINST* **3** (2008) 10001.
- [282] F. Neves, F. Balau, V. Solovov, V. Chepel, R. Martins, A. Pereira, et al., “Characterization of Hamamatsu MPPC for use in liquid xenon scintillation detectors.” Presented at Int. Workshop on New Photon Detectors, PhotoDet 2012, June 13-15, LAL Orsay, France, 2012.
- [283] A. Bondar, A. Buzulutskov, A. Grebenuk, A. Sokolov, D. Akimov, I. Alexandrov, et al., *Geiger mode APD performance in a cryogenic two-phase Ar avalanche detector based on THGEMs*, *Nucl. Instrum. Meth. A* **628** (2011) 364–368.
- [284] G. Collazuol, M. G. Bisogni, S. Marcatili, C. Piemonte, and A. D. Guerra, *Studies of silicon photomultipliers at cryogenic temperatures*, *Nucl. Instrum. Meth. A* **628** (2011) 389–392.

- [285] E. Aprile, P. Cushman, K. Ni, and P. Shagin, *Detection of liquid xenon scintillation light with a silicon photomultiplier*, *Nucl. Instrum. Meth. A* **556** (2006) 215–218.
- [286] D. Akimov, A. Akindinov, A. Burenkov, Y. Grishkin, M. Danilov, A. Kovalenko, et al., *Tests of multipixel Geiger photodiodes in liquid and gaseous xenon*, *Instrum. Exp. Tech.* **52** (2009) 345–351.
- [287] R. DeSalvo, W. Hao, Y. You, Y. Wang, and C. Xu, *First results on the hybrid photodiode tube*, *Nucl. Instrum. Meth. A* **315** (1992) 375–384.
- [288] R. DeSalvo, *Why people like the hybrid photodiode*, *Nucl. Instrum. Meth. A* **387** (1997) 92–96.
- [289] Photonis Technologies S.A.S., Domaine de PELUS, Axis Buiseness Park – Bat E, 18 Avenue de Pythagore, 33700 Merignac, France.
- [290] LHCb-RICH GROUP collaboration, T. Gys, *Production of 500 pixel hybrid photon detectors for the RICH counters of LHCb*, *Nucl. Instrum. Meth. A* **567** (2006) 176–179.
- [291] A. Fukasawa, K. Arisaka, H. Wang, and M. Suyama, *QUPID, a single photon sensor for extremely low radioactivity*, *Nucl. Instrum. Meth. A* **623** (2010) 270–272.
- [292] F. Sauli, *GEM: A new concept for electron amplification in gas detectors*, *Nucl. Instrum. Meth. A* **386** (1997) 531–534.
- [293] A. Buzulutskov, A. Breskin, R. Chechik, G. Garty, F. Sauli, and L. Shekhtman, *The GEM photomultiplier operated with noble gas mixtures*, *Nucl. Instrum. Meth. A* **443** (2000) 164–180.
- [294] A. Bondar, A. Buzulutskov, and L. Shekhtman, *High pressure operation of the triple-GEM detector in pure Ne, Ar and Xe*, *Nucl. Instrum. Meth. A* **481** (2002) 200–203.
- [295] F. D. Amaro, A. S. Conceição, J. F. C. A. Veloso, L. C. C. Coelho, L. M. P. Fernandes, L. F. Requicha Ferreira, et al., *Operation of a single-GEM in noble gases at high pressures*, *Nucl. Instrum. Meth. A* **579** (2007) 62–66.
- [296] A. Buzulutskov, *Physics of multi-GEM structures*, *Nucl. Instrum. Meth. A* **494** (2002) 148–155.
- [297] F. D. Amaro, J. F. C. A. Veloso, A. Breskin, R. Chechik, and J. M. F. dos Santos, *Operation of MHSP multipliers in high pressure pure noble-gas*, *JINST* **1** (2006) 4003.
- [298] A. Bondar, A. Buzulutskov, A. Grebenuk, D. Pavlyuchenko, Y. Tikhonov, and A. Breskin, *Thick GEM versus thin GEM in two-phase argon avalanche detectors*, *JINST* **3** (2008) 7001.
- [299] F. Balau, V. Solovov, V. Chepel, A. Pereira, and M. I. Lopes, *Gem operation in double-phase xenon*, *Nucl. Instrum. Meth. A* **598** (2009) 126–129.
- [300] A. Bondar, A. Buzulutskov, A. Grebenuk, D. Pavlyuchenko, R. Snopkov, and Y. Tikhonov, *Two-phase argon and xenon avalanche detectors based on Gas Electron Multipliers*, *Nucl. Instrum. Meth. A* **556** (2006) 273–280.
- [301] A. Bondar, A. Buzulutskov, A. Grebenuk, D. Pavlyuchenko, R. Snopkov, Y. Tikhonov, et al., *A two-phase argon avalanche detector operated in a single electron counting mode*, *Nucl. Instrum. Meth. A* **574** (2007) 493–499.
- [302] A. Bondar, A. Buzulutskov, A. Grebenuk, D. Pavlyuchenko, and Y. Tikhonov, *Recent results on the properties of two-phase argon avalanche detectors*, *Nucl. Instrum. Meth. A* **598** (2009) 121–125.
- [303] A. Buzulutskov, *Advances in cryogenic avalanche detectors*, *JINST* **7** (2012) C2025.
- [304] V. Solovov, F. Balau, F. Neves, V. Chepel, A. Pereira, and M. I. Lopes, *Operation of gas electron multipliers in pure xenon at low temperatures*, *Nucl. Instrum. Meth. A* **580** (2007) 331–334.

- [305] H. K. Kim, K. Jackson, W. S. Hong, I. J. Park, S. H. Han, J. Kadyk, et al., *Application of the LIGA process for fabrication of gas avalanche devices*, *IEEE Trans. Nuc. Sci.* **47** (2000) 923–927.
- [306] L. Periale, V. Peskov, P. Carlson, T. Francke, P. Pavlopoulos, P. Picchi, et al., *Detection of the primary scintillation light from dense Ar, Kr and Xe with novel photosensitive gaseous detectors*, *Nucl. Instrum. Meth. A* **478** (2002) 377–383.
- [307] R. Chechik, A. Breskin, C. Shalem, and D. Mormann, *Thick GEM-like hole multipliers: properties and possible applications*, *Nucl. Instrum. Meth. A* **535** (2004) 303–308.
- [308] C. Shalem, R. Chechik, A. Breskin, and K. Michaeli, *Advances in thick GEM-like gaseous electron multipliers – Part I: Atmospheric pressure operation*, *Nucl. Instrum. Meth. A* **558** (2006) 475–489.
- [309] C. K. Shalem, R. Chechik, A. Breskin, K. Michaeli, and N. Ben-Haim, *Advances in thick GEM-like gaseous electron multipliers – Part II: Low-pressure operation*, *Nucl. Instrum. Meth. A* **558** (2006) 468–474.
- [310] A. Breskin, R. Alon, M. Cortesi, R. Chechik, J. Miyamoto, V. Dangendorf, et al., *A concise review on THGEM detectors*, *Nucl. Instrum. Meth. A* **598** (2009) 107–111.
- [311] R. Alon, J. Miyamoto, M. Cortesi, A. Breskin, R. Chechik, I. Carne, et al., *Operation of a Thick Gas Electron Multiplier (THGEM) in Ar, Xe and Ar-Xe*, *JINST* **3** (2008) 1005.
- [312] A. Badertscher, L. Knecht, M. Laffranchi, A. Marchionni, G. Natterer, P. Otiougova, et al., *Construction and operation of a double phase lar large electron multiplier time projection chamber*, *ArXiv e-prints* (Nov., 2008), [0811.3384].
- [313] A. Badertscher, L. Knecht, M. Laffranchi, D. Lussi, A. Marchionni, G. Natterer, et al., *Operation of a double-phase pure argon large electron multiplier time projection chamber: Comparison of single and double phase operation*, *Nucl. Instrum. Meth. A* **617** (2010) 188–192.
- [314] A. Badertscher, A. Curioni, L. Knecht, D. Lussi, A. Marchionni, G. Natterer, et al., *First operation of a double phase lar large electron multiplier time projection chamber with a 2D projective readout anode*, *Nucl. Instrum. Meth. A* **641** (2011) 48–57.
- [315] V. Peskov, B. Baibussinov, S. Centro, A. di Mauro, B. Lund-Jensen, P. Martinengo, et al., *Development and first tests of GEM-like detectors with resistive electrodes*, *IEEE Trans. Nuc. Sci.* **54** (2007) 1784–1791.
- [316] P. Martinengo, E. Nappi, R. Oliveira, V. Peskov, F. Pietropaolo, and P. Picchi, *A new generation of GEM detectors and their applications*, *Nucl. Instrum. Meth. A* **604** (2009) 8–10.
- [317] P. K. Lightfoot, R. Hollingworth, N. J. C. Spooner, and D. Tovey, *Development of a double-phase xenon cell using micromegas charge readout for applications in dark matter physics*, *Nucl. Instrum. Meth. A* **554** (2005) 266–285.
- [318] Y. Giomataris, P. Rebourgeard, J. P. Robert, and G. Charpak, *MICROMEGAS: a high-granularity position-sensitive gaseous detector for high particle-flux environments*, *Nucl. Instrum. Meth. A* **376** (1996) 29–35.
- [319] A. A. Kruithof, *Townsend’s ionization coefficients for neon, argon, krypton and xenon*, *Physica* **7** (1940) 519–540.
- [320] E. M. Gushchin, A. A. Kruglov, V. V. Litskevich, A. N. Lebedev, I. M. Obodovskii, and S. V. Somov, *Electron emission from condensed noble gases*, *Sov. J. Exp. Th. Phys.* **49** (1979) 856.
- [321] R. Chechik and A. Breskin, *Advances in gaseous photomultipliers*, *Nucl. Instrum. Meth. A* **595** (2008) 116–127.

- [322] A. Buzulutskov, *Gaseous photodetectors with solid photocathodes*, *Phys. Part. Nucl.* **39** (2008) 424–453.
- [323] L. Periale, V. Peskov, A. Braem, Di Mauro, P. Martinengo, P. Picchi, et al., *Development of new sealed UV sensitive gaseous detectors and their applications*, *Nucl. Instrum. Meth. A* **572** (2007) 189–192.
- [324] S. Duval, A. Breskin, R. Budnik, W. T. Chen, H. Carduner, M. Cortesi, et al., *On the operation of a micropattern gaseous UV-photomultiplier in liquid xenon*, *JINST* **6** (2011) 4007.
- [325] J. Séguinot, G. Charpak, Y. Giomataris, V. Peskov, J. Tischhauser, and T. Ypsilantis, *Reflective UV photocathodes with gas-phase electron extraction: solid, liquid, and adsorbed thin films*, *Nucl. Instrum. Meth. A* **297** (1990) 133–147.
- [326] D. F. Anderson, S. Kwan, V. Peskov, and B. Hoeneisen, *Properties of CsI and CsI-TMAE photocathodes*, *Nucl. Instrum. Meth. A* **323** (1992) 626–634.
- [327] A. Breskin, *CsI UV photocathodes: history and mystery*, *Nucl. Instrum. Meth. A* **371** (1996) 116–136.
- [328] F. Piuz, *Ring Imaging Cherenkov systems based on gaseous photo-detectors: trends and limits around particle accelerators*, *Nucl. Instrum. Meth. A* **502** (2003) 76–90.
- [329] E. Aprile, A. Bolotnikov, D. Chen, R. Mukherjee, F. Xu, D. F. Anderson, et al., *Electron extraction from a CsI photocathode into condensed Xe, Kr, and Ar*, *Nucl. Instrum. Meth. A* **343** (1994) 129–134.
- [330] H. Rabus, U. Kroth, M. Richter, G. Ulm, J. Friese, R. Gernhäuser, et al., *Quantum efficiency of cesium iodide photocathodes in the 120-220 nm spectral range traceable to a primary detector standard*, *Nucl. Instrum. Meth. A* **438** (1999) 94–103.
- [331] B. Azmoun, A. Caccavano, Z. Citron, M. Durham, T. Hemmick, J. Kamin, et al., *Collection of photoelectrons and operating parameters of CsI photocathode GEM detectors*, *IEEE Trans. Nuc. Sci.* **56** (2009) 1544–1549.
- [332] A. Breskin, A. Buzulutskov, R. Chechik, A. D. Mauro, E. Nappi, G. Paic, et al., *Field-dependent photoelectron extraction from CsI in different gases*, *Nucl. Instrum. Meth. A* **367** (1995) 342–346.
- [333] L. C. C. Coelho, H. M. N. B. L. Ferreira, J. A. M. Lopes, T. H. V. T. Dias, L. F. R. Ferreira, J. M. F. Dos Santos, et al., *Measurement of the photoelectron-collection efficiency in noble gases and methane*, *Nucl. Instrum. Meth. A* **581** (2007) 190–193.
- [334] D. S. Covita, C. D. R. Azevedo, C. C. Caldas, and J. F. C. A. Veloso, *Photoelectron extraction efficiency from cesium iodide photocathodes in a pressurized atmosphere of argon and xenon up to 10 bar*, *Phys. Lett. B* **701** (2011) 151–154.
- [335] J. K. Theobald, *Investigation of back diffusion of photoelectrons in various standard gases as it affects secondary electron emission coefficients*, *J. Appl. Phys.* **24** (1953) 123–127.
- [336] V. D. Peskov, *Secondary processes in gas-filled counters: II.*, *Sov. Phys. Tech. Phys.* **22** (1977) 335.
- [337] A. di Mauro, E. Nappi, F. Posa, A. Breskin, A. Buzulutskov, R. Chechik, et al., *Photoelectron backscattering effects in photoemission from CsI into gas media*, *Nucl. Instrum. Meth. A* **371** (1996) 137–142.
- [338] L. Periale, V. Peskov, C. Iacobaeus, T. Francke, B. Lund-Jensen, N. Pavlopoulos, et al., *The development of gaseous detectors with solid photocathodes for low-temperature applications*, *Nucl. Instrum. Meth. A* **535** (2004) 517–522.

- [339] L. Periale, V. Peskov, C. Iacobaeus, T. Francke, B. Lund-Jensen, P. Pavlopoulos, et al., *The successful operation of hole-type gaseous detectors at cryogenic temperatures*, *IEEE Trans. Nuc. Sci.* **52** (2005) 927–931.
- [340] A. Bondar, A. Buzulutskov, A. Grebenuk, D. Pavlyuchenko, R. Snopkov, and Y. Tikhonov, *First results of the two-phase argon avalanche detector performance with CsI photocathode*, *Nucl. Instrum. Meth. A* **581** (2007) 241–245.
- [341] V. Peskov, P. Martinengo, E. Nappi, R. Oliveira, G. Paic, F. Pietropaolo, et al., *Photosensitive strip RETHGEM*, *ArXiv e-prints* (July, 2008) , [0807.2718].
- [342] R. Chechik, M. Balcerzyk, A. Breskin, A. Buzulutskov, G. P. Guedes, D. Mormann, et al., *Progress in GEM-based gaseous photomultipliers*, *Nucl. Instrum. Meth. A* **502** (2003) 195–199.
- [343] T. Sumiyoshi, F. Tokanai, H. Sugiyama, T. Okada, N. Ohishi, T. Ohmura, et al., *Development of a gaseous PMT with micro-pattern gas detectors*, *Nucl. Instrum. Meth. A* **639** (2011) 121–125.
- [344] F. Tokanai, T. Sumiyoshi, H. Sugiyama, T. Okada, N. Ohishi, H. Sakurai, et al., *Sealed gaseous photomultiplier with CsI photocathode*, *Nucl. Instrum. Meth. A* **628** (2011) 190–193.
- [345] P. K. Lightfoot, G. J. Barker, K. Mavrokoridis, Y. A. Ramachers, and N. J. C. Spooner, *Optical readout tracking detector concept using secondary scintillation from liquid argon generated by a thick gas electron multiplier*, *JINST* **4** (2009) 4002.
- [346] A. Bondar, A. Buzulutskov, A. Grebenuk, A. Sokolov, D. Akimov, I. Alexandrov, et al., *Direct observation of avalanche scintillations in a THGEM-based two-phase Ar avalanche detector using Geiger-mode APD*, *JINST* **5** (2010) P08002.
- [347] A. Bondar, A. Buzulutskov, A. Grebenuk, E. Shemyakina, A. Sokolov, D. Akimov, et al., *On the low-temperature performances of THGEM and THGEM/G-APD multipliers in gaseous and two-phase Xe*, *JINST* **6** (2011) 7008.
- [348] V. Solovov, “GEM in double phase liquid xenon detector.” Presented at 5th RD51 Collaboration Meeting, Freiburg, Germany, May, 2010.
- [349] V. Solovov, “Private communication.”
- [350] D. Y. Akimov, A. V. Akindinov, I. S. Alexandrov, V. A. Belov, A. A. Burenkov, M. A. Danilov, et al., “Development of SiPM+WLS photodetection system for readout of THGEM in noble gas detectors.” Presented at NDIP-2011, Lyon, France, July 2011; <http://ndip.in2p3.fr/ndip11/AGENDA/AGENDA-by-DAY/Presentations/3Wednesday/AM/ID123-Akindinov.pdf>.
- [351] D. Y. Akimov, A. V. Akindinov, I. S. Alexandrov, V. A. Belov, O. V. Borshchev, A. A. Burenkov, et al., *Development of VUV wavelength shifter for the use with a visible light photodetector in noble gas filled detectors*, *Nucl. Instrum. Meth. A* **695** (2012) 403–406.
- [352] P. Majewski, “R&D for future ZEPLIN: a multi-ton LXe DM detector.” Presented at CRYODET – Cryogenic Liquid Detectors for Future Particle Physics, LNGS, Italy, Mar, 2006.
- [353] K. Giboni, X. Ji, A. Tan, and L. Zhao, “PANDA-X: A new detector for dark matter search.” Presented at KEK Seminar, Tsukuba, Japan, Nov., 2011.
- [354] R. A. Muller, S. E. Derenzo, G. Smadja, D. B. Smith, R. G. Smits, H. Zaklad, et al., *Liquid-filled proportional counter*, *Phys. Rev. Lett.* **27** (1971) 532–535.
- [355] S. E. Derenzo, T. S. Mast, H. Zaklad, and R. A. Muller, *Electron avalanche in liquid xenon*, *Phys. Rev. A* **9** (1974) 2582–2591.



- [356] J. Prunier, R. Allemand, M. Laval, and G. Thomas, *Some properties of xenon liquid-filled nuclear detectors*, *Nucl. Instrum. Meth.* **109** (1973) 257.
- [357] M. Miyajima, K. Masuda, A. Hitachi, T. Doke, T. Takahashi, S. Konno, et al., *Proportional counter filled with highly purified liquid xenon*, *Nucl. Instrum. Meth.* **134** (1976) 403–405.
- [358] M. Miyajima, K. Masuda, Y. Hoshi, T. Doke, T. Takahashi, T. Hamada, et al., *A self-triggered liquid xenon drift chamber by the use of proportional ionization or proportional scintillation*, *Nucl. Instrum. Meth.* **160** (1979) 239–246.
- [359] H. Zaklad, S. E. Derenzo, R. A. Muller, G. Smadja, R. G. Smits, and L. W. Alvarez, *A liquid xenon radioisotope camera*, *IEEE Trans. Nuc. Sci.* **19** (1972), no.~3 206–213.
- [360] H. Zaklad, S. E. Derenzo, R. A. Muller, and R. G. Smits, *Initial images from a 24-wire liquid xenon  $\gamma$ -camera*, *IEEE Trans. Nuc. Sci.* **20** (1973) 429–431.
- [361] S. E. Derenzo, D. B. Smith, G. R. Smits, H. Zaklad, L. W. Alvarez, and R. A. Muller, *Recent developments in high resolution liquid counters*, tech. rep., Lawrence Radiation Laboratory Report UCRL-20118 and NAL Summer Study Report SS-181, Batavia, Ill., 1970.
- [362] J. G. Kim, S. M. Dardin, K. H. Jackson, R. W. Kadel, J. A. Kadyk, V. Peskov, et al., *Studies of electron avalanche behavior in liquid argon*, *IEEE Trans. Nuc. Sci.* **49** (2002) 1851–1856.
- [363] G. Bressi, M. Cambiaghi, G. Carugno, E. Conti, and E. D’Uscio, *Electron multiplication in liquid argon on a tip array*, *Nucl. Instrum. Meth. A* **310** (1991) 613–617.
- [364] A. J. P. L. Policarpo, V. Chepel, M. I. Lopes, V. Peskov, P. Geltenbort, R. Ferreira Marques, et al., *Observation of electron multiplication in liquid xenon with a microstrip plate*, *Nucl. Instrum. Meth. A* **365** (1995) 568–571.
- [365] A. J. P. L. Policarpo, V. Chepel, M. I. Lopes, and R. Ferreira Marques, *Electron multiplication and secondary scintillation in liquid xenon: new prospects*, *ICFA Instrum. Bulletin* **15** (1997) 51–62. (SLAC-PUB-7718).
- [366] G. Kim, S. M. Dardin, R. W. Kadel, J. A. Kadyk, K. H. Jackson, V. Peskov, et al., *Further studies of electron avalanche gain in liquid argon*, *IEEE Trans. Nuc. Sci.* **50** (2003) 1073–1077.
- [367] B. A. Dolgoshein, V. N. Lebedenko, and B. U. Rodionov, *Luminescence induced by alpha particles in liquid xenon in an electric field*, *Sov. Phys. JETP Lett.* **6** (1967) 224–225.
- [368] A. Lansart, A. Seigneur, J.-L. Moretti, and J.-P. Morucci, *Development research on a highly luminous condensed xenon scintillator*, *Nucl. Instrum. Meth.* **135** (1976) 47–52.
- [369] K. Masuda, S. Takasu, T. Doke, T. Takahashi, A. Nakamoto, S. Kubota, et al., *A liquid xenon proportional scintillation counter*, *Nucl. Instrum. Meth.* **160** (1979) 247–253.
- [370] K. Masuda, T. Doke, and T. Takahashi, *A liquid xenon position sensitive gamma-ray detector for positron annihilation experiments*, *Nucl. Instrum. Meth.* **188** (1981) 629–638.
- [371] T. Doke, *Recent developments of liquid xenon detectors*, *Nucl. Instrum. Meth.* **196** (1982) 87–96.
- [372] A. J. P. L. Policarpo, *Ionization scintillation detectors*, *Nucl. Instrum. Meth.* **196** (1982) 53–62.
- [373] S. Mihara, *MEG liquid xenon detector*, *J. Phys.: Conf. Ser.* **308** (2011) 012009.
- [374] C. Rubbia, M. Antonello, P. Aprili, B. Baibussinov, M. B. Ceolin, L. Barze, et al., *Underground operation of the ICARUS T600 LAr-TPC: first results*, *JINST* **6** (2011) P07011.

- [375] R. Bernabei, P. Belli, F. Montecchia, A. Incicchitti, D. Prosperi, C. J. Dai, et al., *New limits on particle dark matter search with a liquid xenon target-scintillator*, *Phys. Lett. B* **436** (1998) 379–388.
- [376] V. N. Lebedenko, H. M. Araújo, E. J. Barnes, A. Bewick, R. Cashmore, V. Chepel, et al., *Results from the first science run of the ZEPLIN-III dark matter search experiment*, *Phys. Rev. D* **80** (2009) 052010.
- [377] XENON collaboration, J. Angle, E. Aprile, F. Arneodo, L. Baudis, A. Bernstein, A. Bolozdynya, et al., *First results from the XENON10 dark matter experiment at the Gran Sasso National Laboratory*, *Phys. Rev. Lett.* **100** (2008) 021303.
- [378] D. S. Akerib, X. Bai, S. Bedikian, E. Bernard, A. Bernstein, A. Bradley, et al., *Data acquisition and readout system for the LUX dark matter experiment*, *Nucl. Instrum. Meth. A* **668** (2012) 1–8.
- [379] D. C. Malling, D. S. Akerib, H. M. Araújo, X. Bai, S. Bedikian, E. Bernard, et al., *After LUX: The LZ program*, *ArXiv e-prints* (Oct., 2011) , [1110.0103].
- [380] H. Sekiya and the XMASS collaboration, *Xmass*, *J. Phys.: Conf. Ser.* **308** (2011) 012011.
- [381] L. Baudis and DARWIN Consortium, *DARWIN dark matter WIMP search with noble liquids*, *J. Phys.: Conf. Ser.* **375** (2012) 012028.
- [382] V. Blanco Carballo, M. Chefdeville, M. P. Decowski, M. Fransen, H. van der Graaf, W. J. C. Koppert, et al., *Applications of GridPix detectors*, *JINST* **5** (2010) P02002.
- [383] S. Duval, L. Arazi, A. Breskin, R. Budnik, W.-T. Chen, H. Carduner, et al., *Hybrid multi-micropattern gaseous photomultiplier for detection of liquid-xenon scintillation*, *Nucl. Instrum. Meth. A* **695** (2011) .
- [384] T. Haruyama, K. Kasami, Y. Matsubara, T. Nishitani, Y. Maruno, K. Giboni, et al., *High-power pulse tube cryocooler for liquid xenon particle detectors*, in *Cryocoolers 13* (R. G. Ross, ed.), pp. 689–694. Springer US, 2005. DOI.
- [385] XENON100 collaboration, E. Aprile, K. Arisaka, F. Arneodo, A. Askin, L. Baudis, A. Behrens, et al., *First dark matter results from the XENON100 experiment*, *Phys. Rev. Lett.* **105** (2010) 131302.
- [386] XENON100 collaboration, E. Aprile, K. Arisaka, F. Arneodo, A. Askin, L. Baudis, A. Behrens, et al., *Study of the electromagnetic background in the XENON100 experiment*, *Phys. Rev. D* **83** (2011) 082001.
- [387] D. S. Akerib, X. Bai, S. Bedikian, A. Bernstein, A. Bolozdynya, A. Bradley, et al., *The LUX prototype detector*, *ArXiv e-prints* (July, 2012) , [1207.3665].
- [388] J. Liu and the XMASS collaboration, *The XMASS 800 kg detector*, *J. Phys.: Conf. Ser.* **375** (2012) 012022.
- [389] XMASS collaboration, K. Ueshima, K. Abe, K. Hiraide, S. Hirano, Y. Kishimoto, K. Kobayashi, et al., *Scintillation-only based pulse shape discrimination for nuclear and electron recoils in liquid xenon*, *Nucl. Instrum. Meth. A* **659** (2011) 161–168.
- [390] R. Acciarri, M. Antonello, B. Baibussinov, P. Benetti, F. Calaprice, E. Calligarich, et al., *The WArP experiment*, *J. Phys.: Conf. Ser.* **308** (2011) 012005.
- [391] L. Kaufmann and A. Rubbia, *The ArDM project: a dark matter direct detection experiment based on liquid argon*, *J. Phys.: Conf. Ser.* **60** (2007) 264.
- [392] “Canfranc experiment report EXP-08-2011.”  
[http://www.lsc-canfranc.es/Docs/Experiments/ArDM\\_eng.pdf](http://www.lsc-canfranc.es/Docs/Experiments/ArDM_eng.pdf), 2011.

- [393] A. Hime, *The miniCLEAN dark matter experiment*, *ArXiv e-prints* (Oct., 2011), [1110.1005].
- [394] M. G. Boulay and the DEAP Collaboration, *DEAP-3600 dark matter search at SNOLab*, *J. Phys.: Conf. Ser.* **375** (2012) 012027.
- [395] D. Akimov, T. Alexander, D. Alton, K. Arisaka, H. O. Back, P. Beltrame, et al., *Light yield in DarkSide-10: a prototype two-phase liquid argon TPC for dark matter searches*, *ArXiv e-prints* (Apr., 2012), [1204.6218].
- [396] P. D. Meyers, C. Galbiati, and F. Calaprice, “DarkSide-50: A direct search for dark matter with new techniques for reducing background.” <http://lartpc-docdb.fnal.gov/cgi-bin/ShowDocument?docid=581>, 2010.
- [397] R. Brunetti, E. Calligarich, M. Cambiaghi, C. D. Vecchi, R. Dolfini, L. Grandi, et al., “WARP: WIMP Argon Programme (Experimental Proposal).” <http://warp.lngs.infn.it/papers/proposal.pdf>, Mar., 2004.
- [398] ARDM collaboration, C. Amsler, A. Badertscher, V. Boccone, A. Bueno, M. C. Carmona-Benitez, W. Creus, et al., *First results on light readout from the 1-ton ArDM liquid argon detector for dark matter searches*, *JINST* **5** (2010) 1003P.
- [399] A. Marchionni, C. Amsler, A. Badertscher, V. Boccone, A. Bueno, M. C. Carmona-Benitez, et al., *ArDM: a ton-scale LAr detector for direct dark matter searches*, *J. Phys.: Conf. Ser.* **308** (2011) 012006.
- [400] S. Horikawa, A. Badertscher, L. Kaufmann, M. Laffranchi, A. Marchionni, M. Messina, et al., *Feasibility of high-voltage systems for a very long drift in liquid argon TPCs*, *J. Phys.: Conf. Ser.* **308** (2011) 012027.
- [401] M. G. Boulay and A. Hime, *Technique for direct detection of weakly interacting massive particles using scintillation time discrimination in liquid argon*, *Astropart. Phys.* **25** (2006) 179–182.
- [402] D. N. McKinsey and K. J. Coakley, *Neutrino detection with CLEAN*, *Astropart. Phys.* **22** (2005) 355–368.
- [403] K. Rielage and MiniCLEAN Collaboration, *Status and prospects of the MiniCLEAN dark matter experiment*, in *AIP Conf. Series* (S. G. Steadman, G. S. F. Stephans, and F. E. Taylor, eds.), vol. 1441, pp. 518–520, Apr., 2012. DOI.
- [404] W. H. Lippincott, S. B. Cahn, D. Gastler, L. W. Kastens, E. Kearns, D. N. McKinsey, et al., *Calibration of liquid argon and neon detectors with  $^{83m}\text{Kr}$* , *Phys. Rev. C* **81** (2010) 045803.
- [405] “IAEA power reactor information system.” <http://pris.iaea.org/pris/>.
- [406] A. Bernstein, Y. Wang, G. Gratta, and T. West, *Nuclear reactor safeguards and monitoring with antineutrino detectors*, *J. Appl. Phys.* **91** (2002) 4672–4676.
- [407] B. Armbruster, I. Blair, M. Becker, A. Benen, B. A. Bodmann, N. E. Booth, et al., *KARMEN at ISIS: The advantage of a pulsed neutrino source in the search for neutrino oscillations and neutrino nuclear interactions*, *Nucl. Phys. A* **629** (1998) 507–516.
- [408] F. T. Avignone III and Y. V. Efremenko, *Neutrino nucleus cross-section measurements at intense, pulsed spallation sources*, *J. Phys. G: Nuc. Phys.* **29** (2003) 2615–2628.
- [409] A. Bolozdynya, F. Cavanna, Y. Efremenko, G. T. Garvey, V. Gudkov, A. Hatzikoutelis, et al., *Opportunities for neutrino physics at the spallation neutron source: A white paper*, *ArXiv e-prints* (Nov., 2012), [1211.5199].

- [410] C. Horowitz, K. Coakley, and D. McKinsey, *Supernova observation via neutrino-nucleus elastic scattering in the CLEAN detector*, *Phys. Rev. D* **68** (2003) 023005.
- [411] J. Monroe and P. Fisher, *Neutrino backgrounds to dark matter searches*, *Phys. Rev. D* **76** (2007) 033007.
- [412] L. E. Strigari, *Neutrino coherent scattering rates at direct dark matter detectors*, *New J. Phys.* **11** (2009) 105011.
- [413] K. Scholberg, T. Wongjirad, E. Hungerford, A. Empl, D. Markoff, P. Mueller, et al., *The CLEAR experiment*, *ArXiv e-prints* (Oct., 2009) , [0910.1989].
- [414] C. D. Winant, A. Bernstein, C. Haggmann, N. Madden, and W. Stoeffl, *Dual-phase argon ionization detector for measurement of coherent elastic neutrino scattering and medium-energy nuclear recoils*, *Nucl. Phys. B: Proc. Suppl.* **221** (2011) 413.
- [415] S. Sangiorgio, A. Bernstein, M. Foxe, C. Haggmann, T. Joshi, I. Jovanovic, et al., *The hunt for coherent neutrino-nucleus scattering with ionization argon detectors*, *IEEE Nuc. Sci. Symp. Conf. Rec.* (Nov., 2010) 102–104.
- [416] A. A. Burenkov, D. Y. Akimov, Y. L. Grishkin, A. G. Kovalenko, V. N. Lebedenko, V. N. Solovov, et al., *Detection of a single electron in xenon-based electroluminescent detectors*, *Phys. At. Nuc.* **72** (2009) 653–661.
- [417] *v-SNS Collaboration*, 2005. <http://www.phy.ornl.gov/workshops/nusns/proposal.pdf>.
- [418] RED collaboration, D. Y. Akimov, I. S. Alexandrov, V. I. Aleshin, V. A. Belov, A. I. Bolozdynya, A. A. Burenkov, et al., *Perspectives to measure neutrino-nuclear neutral current coherent scattering with two-phase emission detector*, *ArXiv e-prints* (Dec., 2012) , [1212.1938].
- [419] O. Buchmueller, R. Cavanaugh, D. Colling, A. De Roeck, M. J. Dolan, J. R. Ellis, et al., *Supersymmetry and dark matter in light of LHC 2010 and XENON100 data*, *Eur. Phys. J. C* **71** (2011) 1722.
- [420] R. Bernabei, P. Belli, F. Cappella, R. Cerulli, C. J. Dai, A. D'Angelo, et al., *First results from DAMA/LIBRA and the combined results with DAMA/NaI*, *Eur. Phys. J. C* **56** (2008) 333.
- [421] C. Savage, K. Freese, P. Gondolo, and D. Spolyar, *Compatibility of DAMA/LIBRA dark matter detection with other searches in light of new galactic rotation velocity measurements*, *J. Cosmol. Astropart. Phys.* **9** (2009) 36.
- [422] S. P. Ahlen, F. T. Avignone, R. L. Brodzinski, A. K. Drukier, G. Gelmini, and D. N. Spergel, *Limits on cold dark matter candidates from an ultralow background germanium spectrometer*, *Phys. Lett. B* **195** (1987) 603–608.